Experimental Study of Plasma Transport Using X-ray Imaging Spectroscopy in Alcator C-Mod

by

Chi Gao

B.S. Physics, University of Science and Technology of China (2009)

Submitted to the Department of Nuclear Science and Engineering
in partial fulfillment of the requirements for the degree of
Doctor of Philosophy in Nuclear Science and Engineering
at the
MASSACHUSETTS INSTITUTE OF TECHNOLOGY
September 2015

Author ..... Signature redacted

Chi Gao
Department of Nuclear Science and Engineering
June 26, 2015

Certified by... Signature redacted .....

Dr. John E. Rice
Senior Research Scientist, Plasma Science and Fusion Center
Thesis Supervisor

Certified by.....

Prof. Anne E. White
Associate Professor of Nuclear Science and Engineering
Thesis Reader

Certified by..... Signature redacted .....

Prof. Ronald R. Parker
Professor of Nuclear Science and Engineering, Emeritus
Thesis Reader

Accepted by.. Signature redacted .....

Prof. Mujid S. Kazimi
TEPCO Professor of Nuclear Engineering
Chairman, Department Committee on Graduate Students

Experimental Study of Plasma Transport Using X-ray Imaging Spectroscopy in Alcator C-Mod

by

Chi Gao

Submitted to the Department of Nuclear Science and Engineering
on June 26, 2015, in partial fulfillment of the
requirements for the degree of
Doctor of Philosophy in Nuclear Science and Engineering

Abstract

The high resolution X-ray spectrometer with spatial resolution (HiReX–Sr) is intensively used in the studies of impurity, momentum and energy transport in Alcator C-Mod. This thesis investigates three phenomena using HiReX–Sr: (1) Non-local heat transport (the breakdown of a local expression for the heat flux) is observed in linear Ohmic confinement (LOC) regime plasmas in cold pulse injection experiments. This effect disappears in saturated Ohmic confinement (SOC) regime plasmas. The plasma rotation reverses direction across this transition. Transport analysis show that a transient internal transport barrier (ITB) forms in the core plasma. Cold pulse modulation experiments suggest a non-diffusive heat transport behavior. The change of dominant turbulence mode from electron mode dominance in LOC plasmas to ion mode dominance in SOC plasmas is proposed to be the underlying mechanism for the correlations among the disappearance of the non-local effect, the rotation reversals and the LOC/SOC transitions. This work extends the understanding of non-local phenomena in the tokamak plasmas. (2) Evidence of inward momentum pinch in ICRF modulation experiments. The momentum transport coefficients are calculated based on a simplified model. It is found that within $0.1 < r/a < 0.5$, the momentum diffusivity is lower than the ion thermal diffusivity and the momentum pinch is inward. (3) ICRF induced argon pumpout in hydrogen-deuterium plasma is observed in Alcator C-Mod when the H-to-D level is relatively high ($n_H/n_D \approx 35\% - 50\%$). The pumpout effect is maximal when $n_H/n_D \approx 40\% \pm 5\%$, at which level the hydrogen-deuterium hybrid layer is close to the Ar^{16+} 2^{nd} harmonic resonant layer. This suggests that the pumpout of argon could be due to the energy absorbed from the enhanced left-hand polarized electric field through 2nd harmonic resonance. Further experiments are proposed to verify this impurity-wave interaction mechanism, which is potentially useful for active impurity control in fusion devices.

Thesis Supervisor: Dr. John E. Rice

Title: Senior Research Scientist, Plasma Science and Fusion Center

Thesis Reader: Prof. Anne E. White
Title: Associate Professor of Nuclear Science and Engineering

Thesis Reader: Prof. Ronald R. Parker
Title: Professor of Nuclear Science and Engineering, Emeritus

Acknowledgments

The thesis work cannot be completed without the help from an enormous number of people during my six years at MIT. I would like to acknowledge some of them below.

I would express the deepest gratitude to my supervisor, Dr. John Rice for guiding me in the past six years. He provided me with interesting projects and was patient with my slow progress. His expertise in spectroscopy and plasma rotation was an invaluable treasure in the whole path of my thesis. He was always ready to discuss with me and able to provide me with valuable advice not only on the research projects but also on my graduate life. I am sincerely grateful for his continuous guidance and encouragements.

I would like to thank my thesis readers Prof. Anne White and Prof. Ron Parker. Prof. White and Prof. Parker gave my tremendously valuable advices on my thesis work. I am deeply grateful for their time devoted on my thesis committee meetings and on reading through this thesis. Prof. White also acted as my academic advisor in NSE department for the past few years and oversaw my academic records. Prof. Ron Parker and Dr. Earl Marmar have supported me financially, for which I am sincerely thanksful. I would thank Prof. Jeff Freidberg to be my committee chair. The knowledge I learned from his classes and from his book *Plasma Physics and Fusion Energy* cannot be more helpful in writing this thesis.

I would also like to thank the spectroscopy group in Alcator C-Mod. Dr. Yuri Podpaly tough me how to operate the HiReX–Sr. Each time I was stuck by some issue on the spectrometer, he was the best person I can look for help, even after his graduation from the Alcator C-Mod project. Dr. Luis F. Delgado-Aparicio from PPPL brought and test great ideas to the group and helped the operation of HiReX–Sr. In addition I sincerely thank Dr. Delgado-Aparicio for the great help on my job search. Dr. Matt Reinke devoted countless time on developing the THACO code, without which the thesis work is impossible. His high standard of scientific work impressed me and my future career work will benefit from it. I take this opportunity to show my respect to Dr. Manfred Bitter and Dr. Ken Hill who

pioneered the X-ray imaging spectroscopy work, and thank Dr. Alex Ince-Cushman for building the core system for this thesis. I also thank Dr. Hongjuan Sun in Max-Planck-Institut für Plasmaphysik for the collaboration and enlightening discussions on my thesis work.

I wish to express my thanks to Dr. David Mikkelsen, Dr. Nathan Howard, Dr. Catherine Fiore and Dr. Matt Reinke for the help on running TRANSP, GYRO and STRAHL, and thanks to Dr. Darin Ernst for developing the fiTs code and co-maintaining the LOKI cluster, and thanks to Dr. Yijun Lin for teaching me running the ICRF wave code. I am also grateful to the physics operators of my experiments: Dr. Jim Irby, Prof. Ron Parker, Dr. Jerry Hughes, Dr. Steve Wolfe and Prof. Ian Hutchinson.

I recognized the help from the faculty, scientists and graduate students in PSFC: Dr. Seung Gyou Baek, Dr. Paul Bonoli, Dr. Dan Brunner, Prof. Bruno Coppi, Mark Chilenski, Dr. Michael Churchill, Paul Ennever, Ian Faust, Dr. Theodore Golfinopoulos, Dr. Robert Granetz, Dr. Martin Greenwald, Christian Haakonsen, Dr. Zachary Hartwig, Dr. Amanda Hubbard, Dr. Brian LaBombard, Dr. Jungpyo Lee, Dr. Bruce Lipschultz, Dr. Yunxing Ma, Dr. Bob Mumgaard, Prof. Felix Parra-Diaz, Prof. Miklos Porkolab, Dr. Bill Rowan, Dr. Steve Scott, Dr. Syuinichi Shiraiwa, Dr. Choongki Sung, Dr. Jim Terry, Dr. Greg Wallace, Dr. John Walk, Prof. Dennis Whyte, Kevin Woller and Dr. Steve Wukitch. Thanks are also due to the engineers and technicians in Alcator C-Mod who made the machine running and helped me with great kindness and patiences, especially, Lee Berkowitz, Bill Byford, Bill Cochran, Tim Davis, Gary Dekow, Ed Fitzgerald, Felix Kreisel, Mark London, Bill Parkin, Samuel Pierson, Andy Pfeiffer, Ron Rosati, Brandon Savage, Maria Silveira, Josh Stillerman, Roza Tesfaye, Thomas Toland and Lihua Zhou. I would also like to thank the administrative personnel in PSFC and NSE department: Heather Barry, Alisa Cabral, Valerie Censabella, Jessica Coco, Clare Egan, Amy Frizzi, Lee Keating, Nancy Masley, Marcia Mora, Elizabeth Parmelee, Paul Rivenberg and Jason Thomas.

Thanks to my undergraduate advisors, Prof. Changxuan Yu, Dr Jinlin Xie and

Prof. Tao Lan, who encouraged my study at MIT.

Finally I would thank my parents for their continuous and selfless support for almost thirty years. I also thank my parents-in-law for their consistent assistance. Specially thanks to my wife Xiaonan for her endless support throughout all these days, and for giving birth to our son Xuhang. Xuhang has become the source of happiness and joy for the family.

THIS PAGE INTENTIONALLY LEFT BLANK

Contents

List of Figures

List of Tables

THIS PAGE INTENTIONALLY LEFT BLANK

Chapter 1

Introduction

1.1 Thesis Goal and Outlines

Energy shortage has been one of the most significant international concerns for decades. Thermonuclear Fusion is a potential ultimate solution due to its high efficiency, large fuel reserves and cleanliness. Among the efforts devoted to fusion research, the tokamak is considered to be the most promising device to achieve controllable thermonuclear fusion for commercial use. Great progress has been made during the past few decades on Tokamak experiments, but there is a variety of outstanding physics and technical questions yet to be solved. Of these questions, the transport properties of plasma in tokamaks constitute an active research area, but are still lacking fully understanding. The goal of this thesis is to study the plasma transport phenomena using a high resolution X-ray imaging spectroscopy. This thesis work is carried out in the Alcator C-Mod tokamak located at the MIT Plasma Science and Fusion Center.

The thesis consists of six chapters, which are arranged as follows:

Chapter 1 introduces the concepts of thermonuclear fusion, plasma, confinement and tokamaks in Section 1.2. The major diagnostic used in this thesis work, HIgh REsolution X-ray imaging spectroscopy (HiReX), is described in Section 1.3. Other diagnostics aiding the thesis are described in Section 1.4.

Chapter 2 discusses the theoretical background related to the thesis. Section 2.1

gives an overview of plasma anomalous transport theory. The drift-wave instabilities (ITG, TEM, ETG) will be discussed, as they are related to the energy confinement, non-local heat transport (the breakdown of a local expression for the heat flux) and momentum transport in Chapter 3. Section 2.2 introduces the Coriolis pinch in momentum transport, which is later compared with the experimental pinch obtained in ICRF modulation experiment in Chapter 4. Section 2.3 introduces the ICRF wave theory and wave-impurity interaction, which is related to the study of the argon pumpout effect in Chapter 5. Numerical codes (STRAHL, TRANSP and GYRO) used in the thesis will be introduced in Section 2.4.

Chapter 3 studies the non-local heat transport phenomenon and its correlation with rotation reversals and the LOC/SOC transition in Alcator C-Mod. Although the non-local phenomenon was first observed two decades ago, the experiment in C-Mod sheds new light on the subject with the measurement of ion temperature dynamics and plasma rotation from HiReX–Sr. The correlation among the non-local effect, rotation reversals and the LOC/SOC transition is revealed in this study, which suggests a unified explanation of multi-channel transport.

Chapter 4 presents the study of momentum transport with ICRF modulation. The toroidal momentum transport coefficients, diffusivity χ_ϕ and pinch V_ϕ, are deduced from the modulated toroidal rotation profiles. These coefficients (more specifically, the normalized momentum pinch RV_ϕ/χ_ϕ) are compared with the theory on momentum pinch due to the Coriolis effect.

Chapter 5 studies the argon impurity transport with ICRF waves. An argon pumpout effect has been observed recently in Alcator C-Mod during ICRF operation. This pumpout happens only when the H/D ratio is relatively high ($n_H/n_D \approx 35\% - 50\%$), at which level the H-D mode conversion layer is close to the Ar^{16+} 2^{nd} harmonic resonance layer. This chapter will introduce this observation, explain the phenomenon in the views of impurity-wave interaction and edge source effect, and present the comparison between STRAHL simulations and experimental results.

Chapter 6 summaries the thesis work and proposes the future works.

1.2 Nuclear Fusion

1.2.1 Fusion and Plasma

Fusion is the process in which two or more light atomic nuclei collide and fuse into a heavy atomic nucleus. Mass is not conserved and energy is released in this process. Fusion powers the stars. The goal of fusion research is to make controlled fusion energy possible for human society. Three fusion reactions are studied mostly and are considered to be most attractive:

D–D reaction:

$$^{2}_{1}\mathrm{D} + ^{2}_{1}\mathrm{D} \rightarrow ^{3}_{2}\mathrm{He} + ^{1}_{0}\mathrm{n} + 3.27 \ \ \mathrm{MeV} \tag{1.1}$$

D–^{3}He reaction:

$$^{2}_{1}\mathrm{D} + ^{3}_{2}\mathrm{He} \rightarrow ^{4}_{2}\alpha + ^{1}_{1}\mathrm{p} + 18.3 \ \ \mathrm{MeV} \tag{1.2}$$

D–T reaction:

$$^{2}_{1}\mathrm{D} + ^{3}_{1}\mathrm{T} \rightarrow ^{4}_{2}\alpha + ^{1}_{0}\mathrm{n} + 17.6 \ \ \mathrm{MeV} \tag{1.3}$$

Among them the D–T reaction is the most favorable one for controlled fusion due to its high energy gain and larger cross section as is shown in Fig. 1-1. But it still requires a temperature of a few 10s keV to get sufficient fusion reactions and to produce energy. At this high temperature, the fuel atoms are fully ionized, forming a cluster of unbounded positively charged nuclei and negatively charged electrons. This electrically neutral medium of positive and negative particles is called a plasma, the fourth state of matter. An important feature of plasmas (ions and electrons) is the response to long-ranged electromagnetic fields; this feature gives rise to some distinct characteristics.

1.2.2 Confinement and Lawson Criterion

The unbounded electrons and ions must be confined within a sufficient amount of time to ensure enough fusion reactions to balance the energy loss due to bremsstrahlung and thermal conduction. This power balance condition

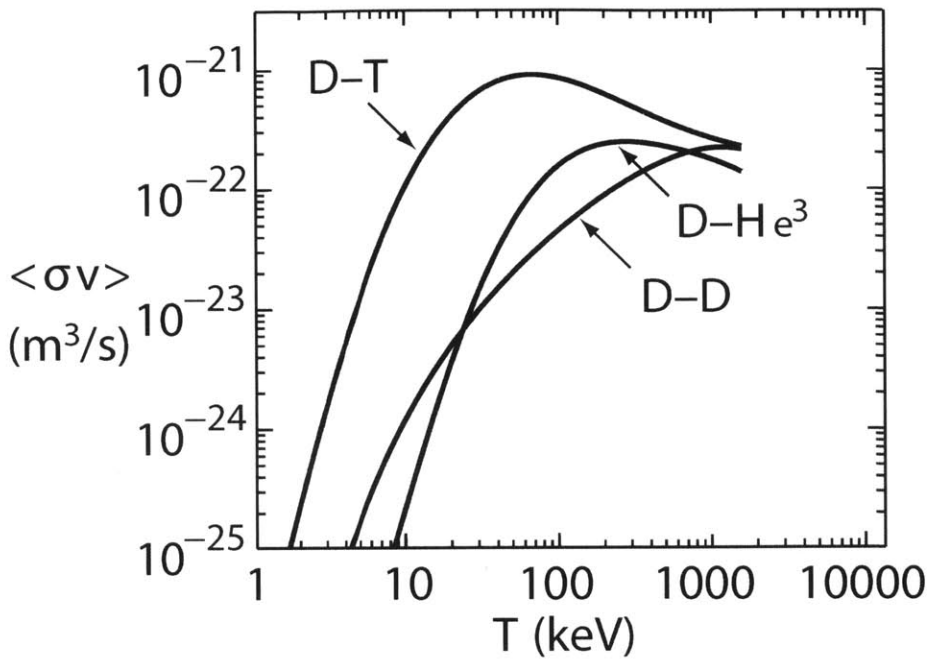

Figure 1-1: Velocity averaged cross section for D–D, D–T or D–^{3}He reactions as a function of temperature. Figure from [1].

($P_{out} = P_{loss}$) is called "ignition". It means without external heating, the heating of plasma from fusion products (mostly α particles for D–T reactions) is sufficient to maintain the plasma temperature against all energy losses. Ignition is the minimum requirement for a fusion reaction to maintain steady-state operation. More specifically, the ignition condition (Lawson criterion) for D–T reaction is minimal at $T = 15$ keV:

$$(p\tau_E)_{min} = 8.3 \text{ atm s} = 5.2 \times 10^{21} \text{ m}^{-3} \text{ keV s} \tag{1.4}$$

where $T = T_i = T_e$ is the plasma temperature, $p \equiv nT = p_i + p_e = (n_i + n_e)T$ is the total pressure, and τ_E is the energy confinement time which characterize how long the plasma temperature can be maintained. The energy confinement time can be calculated by

$$\frac{\partial W}{\partial t} = P - \frac{W}{\tau_E} \tag{1.5}$$

$$\tau_E = \frac{W}{P - \frac{\partial W}{\partial t}} \tag{1.6}$$

where $W = \int \frac{3}{2} p dV$ is the plasma stored energy, and $P = P_{\text{Ohmic}} + P_{\text{auxiliary}}$ is the heating power including Ohmic and auxiliary heating. For a plasma at $T = 15$ keV with an energy confinement time of 1 s, a pressure of 8 atm, a density of $n = 1.7 \times 10^{20}$ m^{-3}, is required for ignition. It is worth noting that the required $(p\tau_E)_{\text{min}}$ is higher at other temperatures.

The confinement time is determined by the transport properties of plasmas. The transport can be either collisional or turbulent. A widely accepted conclusion is that turbulent transport is the dominant mechanism responsible for most of the energy and particle transport in tokamaks. These transport mechanisms will be briefly introduced in Section. 2.1.

1.2.3 Tokamaks

The extremely high temperature required excludes the possibility to use any container to confine the plasmas. There are basically three ways to confine plasma under conditions to satisfy the Lawson criterion: (1) gravitational confinement, (2) inertial confinement, (3) magnetic confinement. The last approach, magnetic confinement, uses magnetic fields to confine the plasma. Because plasmas consist of free negatively charged electrons and positively charged ions, these charged particles will rotate around the magnetic field line, called gyro-motion. Ideally, the particle's perpendicular motion (i.e., motion with velocity that is perpendicular to the magnetic field) is confined within a Larmor radius:

$$\rho_L = \frac{m v_\perp}{qB} \tag{1.7}$$

The stronger the magnetic field is, the better the particles are confined. However, the motion of particles is the superposition of perpendicular gyro-motion and free parallel motion. In addition to the gyro-motion, particles also move freely along the field line with velocity $v_\parallel = \mathbf{v} \cdot B$. In a linear machine, particles will leak out in the open ends of magnetic field lines. The solution to avoid the end losses is to bend the magnetic field and make it closed, using a torus-shaped chamber. The tokamak,

an acronym of Russian words "toroidal chamber with axis magnetic field", is such a device. The first tokamak was built at the Kurchatov Institute in Moscow in the 1950s. The concept proved to be practical and other countries followed to build more.

Fig. 1-2 is a schematic diagram of a tokamak. The toroidal field coils produce a toroidal magnetic field B_t around the torus, which is used to confine the plasma. A toroidal field alone cannot guarantee the confinement in torus geometry due to the inhomogeneity of magnetic field and plasma pressure. A poloidal magnetic field B_p is required to balance the plasma pressure and reach equilibrium. This poloidal field can be produced by the toroidal current in plasma itself. The central solenoid, shown in the diagram of Fig. 1-2, acts like a transformer primary to induce such plasma current. The plasma current is also used for heating the plasma itself, called Ohmic heating. As the plasma temperature increases, the resistivity drops quickly $\left(\propto T^{-3/2}\right)$, and Ohmic heating solely is not sufficient to bring the temperature to fusion conditions, so other auxiliary heating schemes (RF or beam heating) must be used. From Maxwell's equations (more specifically, Ampère's law and Faraday's law), to have a steady inductive plasma current, the current in the solenoid primary must be linear in time. This applies a limitation for steady-state operation. Non-inductive current drive is proposed as a solution. The combined toroidal and poloidal magnetic field ($B_t \gg B_p$) gives rise to a helical magnetic field around the torus, as is shown by the dark line of Fig. 1-2. The poloidal field coils are used for position and shape control of the plasma, by providing additional poloidal magnetic field (the main poloidal field is provided by the plasma current). The central solenoid can also assist in plasma positioning and shaping.

Great progress has been made after 60 years of research, as Fig. 1-3 shows the triple product ($nT\tau_E$) achieved from different tokamaks. For now, there are around 30 Tokamaks are operating around the world. ITER (International Thermonuclear Experimental Reactor), the largest and most advanced tokamak, is under construction and expected to operate in the next decade.

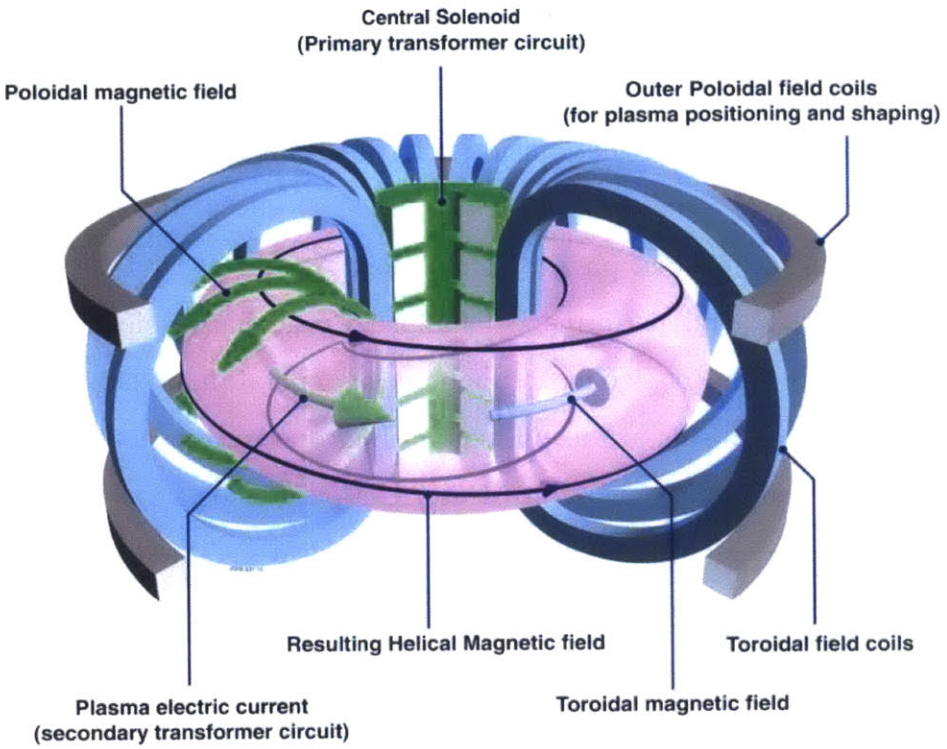

Figure 1-2: Schematic diagram of a tokamak shows the toroidal and poloidal magnetic field coils and magnetic fields. Figure is adapted from euro-fusion.org.

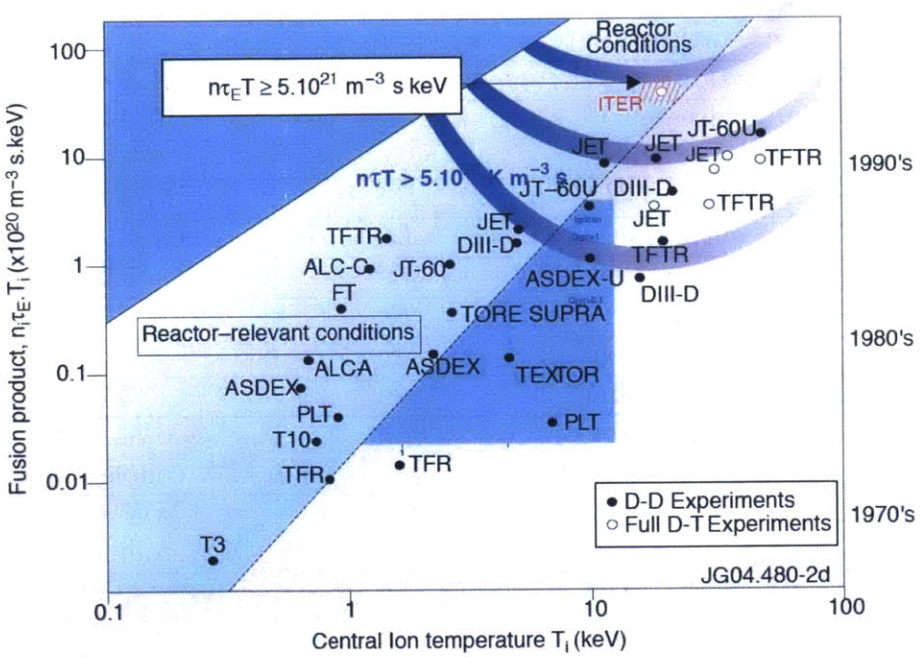

Figure 1-3: Triple product ($nT\tau_E$) achieved from different tokamaks. Figure from [2] P179.

1.2.4 Alcator C-Mod Tokamak

Alcator C-Mod [24, 25, 26, 27] is a compact high magnetic field tokamak. As of today, it has the highest toroidal magnetic field (8 T) in tokamaks. Alcator C-Mod began operation since 1991, as a successor of Alcator A [28, 29, 30, 31] and Alcator C [32, 33, 34, 35]. Although compact in physical dimension, Alcator C-Mod can be operated with high parameters and performance similar to other larger devices. The high magnetic field with compact size makes high density operation possible, under which condition ions and electrons are in full equilibrium due to frequent collisions. The high particle flux and power density in Alcator C-Mod provide a unique environment for the scrape-off layer (SOL) and divertor studies. Alcator C-Mod holds the current record for average plasma pressure in tokamaks (1.8 atm) [25].

Table 1.1: Operation Parameters of Alcator C-Mod

Quantity	Symbol	Value
Major radius	R_0	0.66 m
Minor radius	a	0.22 m
Plasma volume	V_p	1 m^3
Plasma surface area	A_p	7 m^2
Aspect ratio	$1/\epsilon = R_0/a$	3
Elongation	κ	1.3 - 1.9
Triangularity	δ_{upper}	0.2 - 0.4
	δ_{lower}	0.4 - 0.8
Toroidal magnetic field at $R = R_0$	B_0	2.7 - 8.1 T
Plasma current	I_p	0.3 - 2 MA
Line average plasma density	$\overline{n}_e$	$0.2 - 5.0 \times m^{-3}$
Plasma temperature	T	$1 - 10$ keV
Maximum pulse length	t_{pulse}	5 s
Energy confinement time	τ_E	$\sim$ 50 ms
Maximum ICRF power	P_{RF}	8 MW sources 6 MW coupled to plasma
Maximum LHCD power	P_{LH}	3 MW sources 1.2 MW coupled to plasma
Normalized plasma pressure	$\beta = \frac{P}{B^2/2\mu_0}$	$< 1\%$

Basic engineering and physics parameters of Alcator C-Mod are listed in Table 1.1. Fig. 1-4 illustrates the poloidal cross section of Alcator C-Mod. The major radius R_0 is

defined as the distance from plasma geometrical axis to the machine(central solenoid) axis. The color curves (green, red and blue) are contours of poloidal magnetic flux. The red contour separates closed magnetic field (green contours) and open magnetic field (blue contours). For diverted plasmas, the point with $B_p = 0$ is called "X-point", and the flux surface crossing the X-point is called the separatrix (red contour). For limited plasma, there is no such X-point, and the red contour is the Last Closed Flux Surface (LCFS). The open field line region is called the Scrape-Off Layer (SOL). Particles are poorly confind in the SOL. Most of the particle and energy in plasma will be carried out of the SOL at the divertors.

The minor radius a is defined as the half length of the distance between the most inner and most outer LCFS. Aspect ratio $(1/\epsilon)$ is the ratio of major radius to minor radius. Small aspect ratio is helpful in improving the β value (ratio of plasma pressure to magnetic field pressure, $\beta = \frac{nT}{B^2/2\mu_0}$), a measure of magnetic confinement efficiency. However the reduction of aspect ratio is constrained by the space limit of toroidal field coils. 2.5 – 3 is the typical aspect ratio for conventional tokamaks. Spherical tokamaks like NSTX can achieve an aspect ratio of 1.26 [36].

The cross section of original tokamaks was circular. Later it was realized that a non-circular cross-section is more optimal for confinement. Shaping coils (poloidal field coils) are installed in most modern tokamaks. These coils are used to control the plasma shape, which is characterized by elongation, κ, and triangularity ,δ:

$$\kappa = \frac{b}{a} \tag{1.8}$$

$$\delta_{upper} = \frac{d_{upper}}{a} \tag{1.9}$$

$$\delta_{lower} = \frac{d_{lower}}{a} \tag{1.10}$$

where a is the plasma minor radius, $2b$ is the distance between the X point and the highest point on LCFS, d_{upper} is the distance between the geometrical axis and the highest point on LCFS, d_{lower} is the distance between the geometrical axis and the X-point, as shown in Fig. 1-4.

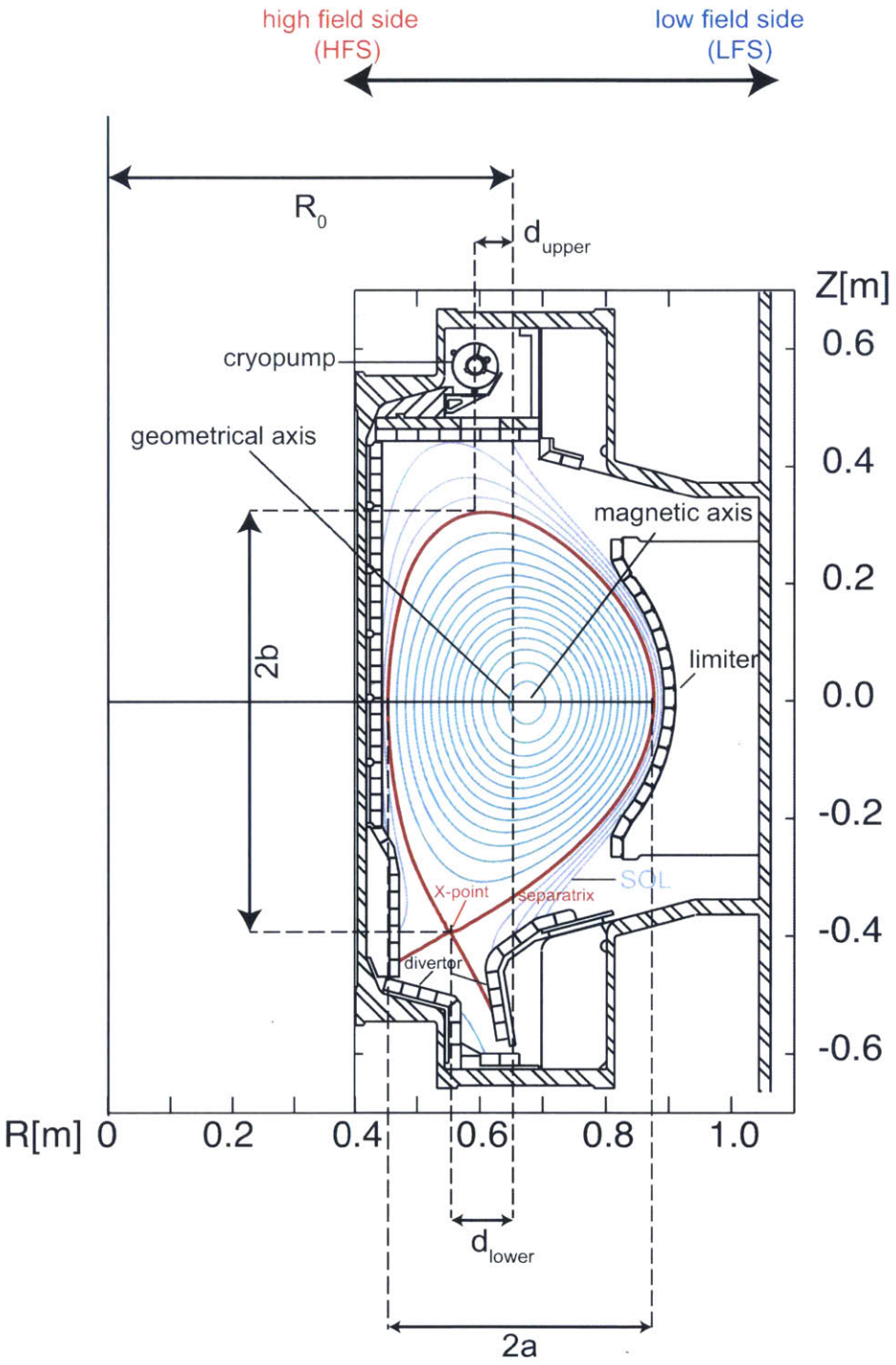

Figure 1-4: A cross section view of standard lower single null (LSN) divertor plasma. The magnetic axis, separatrix, scrape-off layer (SOL) and divertor are indicated.

Auxiliary Heating

As was mentioned previously, the efficiency of Ohmic heating drops as $T^{-3/2}$. Ohmic heating can effectively heat the plasma up to a few keV. Above that temperature, auxiliary heating is necessary. Neutral beam injection (NBI) and radio frequency (RF) heating are two main methods of auxiliary heating. For NBI, neutral beams (normally D_2) injected into a plasma feel no force from the magnetic field and travel in a straight line. Then they are ionized through charge exchange or collisions with plasma particles, and get confined by the magnetic field. During this process, the energy of neutral beams is gradually transferred to the plasma ions and electrons through Coulomb collisions. The neutral beams are slowed down and become a component of the plasma. NBI has proven to be efficient in plasma heating [37, 38] and momentum generation [39, 40, 41, 42, 43] on multiple machines. However the application of NBI on future reactor-size machines ($a > 2-3$ m, like ITER) is limited due to the large machine size, high plasma density and limitations on beam energy. In Alcator C-Mod, a neutral beam is utilized for diagnostic purpose, instead of heating.

Ion cyclotron range of frequency (ICRF) waves are used as the main auxiliary heating method in Alcator C-Mod. When the wave frequency ($f = \omega/2\pi$) equals to the ion gyro-motion's cyclotron frequency $\left(f_{ci} = \omega_{ci}/2\pi = \frac{ZeB}{2\pi m_i}\right)$, wave can transfer energy to ions through resonant absorption. As the magnetic field varies in a plasma $\left(B_t \propto \frac{1}{R}\right)$, the resonance happens at a specific position, called the resonance layer. At a field of 5.2 T on the magnetic axis, the deuterium cyclotron frequency is 40 MHz. In order to efficiently heat the ions, the wave needs to be circularly polarized and rotate in the same direction as the ions. This is called left-hand polarization with notation E_+. However, as the wave travels from the launcher (LHS launcher in Alcator C-Mod) to the resonance layer, the left-hand circularly polarized component is perfectly screened. For this reason, RF waves at twice the cyclotron frequency of deuterium (i.e., 80 MHz) can be used. This heating method proves to be very efficient while from theory second harmonic absorption should be much weaker. Later it was realized that most of the RF power is actually absorbed by the residual hydrogen

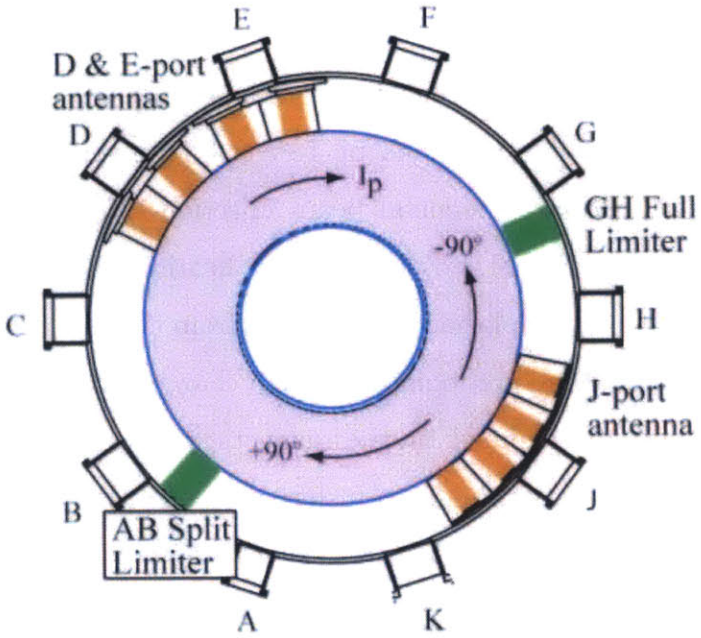

Figure 1-5: Locations of D, E and J ICRF antennas in Alcator C-Mod. J antenna launches waves in co-current direction for 90° phasing, and in counter-current direction for −90° phasing. Figure from [3].

through a fundamental resonance with RF wave, although typically the amount of residual hydrogen is small ($n_H/n_D \sim 1-5\%$). This heating mechanism is call minority heating.

In Alcator C-Mod, three antennas are utilized [3] for ICRF heating, as shown in Fig. 1-5. Table 1.2 is the configuration of these three antennas. The two two-strap D and E antennas have fixed dipole phase and fixed frequency (80.5 MHz and 80 MHz, respectively). They can deliver up to 4 MW of source power, out of which 3.5 MW can be coupled into plasma. The four-strap J antenna has variable frequency between 50 - 78 MHz, source power of 4 MW (3 MW can be coupled into plasma) and the tunable phasing can be set at

- $[0, 0, 0, 0]$: monopole, $n_{\|} = \pm 4$
- $[0, \pi, 0, \pi]$: dipole, $n_{\|} = \pm 13$
- $[0, \pi, \pi, 0]$: $180°, n_{\|} = \pm 10$
- $[0, \pi/2, \pi, 3\pi/2]$: $90°, n_{\|} = 7$

- $[0, -\pi/2, -\pi, -3\pi/2] : -90°, n_{\|} = -7$

Here $n_{\|} = ck_{\|}/\omega$ is the parallel index of refraction, and $k_{\|}$ is the launched wave's parallel wavenumber.

78 MHz J antenna, together with D (80.5 MHz) and E (80 MHz) antennas, are operated to heat D majority - H minority plasmas at 5.2 T, or D majority - ^{3}He minority plasmas at 7.8 T. RF waves with frequency of 50 MHz from J antenna is also used to heat D majority - ^{3}He minority plasmas at 5 T.

Table 1.2: ICRF antenna configuration in Alcator C-Mod

Antenna	Phasing	Frequency (MHz)	Source Power (MW)
D	2 straps, dipole	80.5	2
E	2 straps, dipole	80.0	2
J	4 straps, variable	40 - 80	4

In addtion to heating, ICRF waves can drive strong toroidal and poloidal flow through mode conversion of injected fast magneto-sonic waves into shortwavelength modes [ion Bernstein waves (IBWs) and ion cyclotron waves (ICWs)] [44, 45, 46]. Up to 90 km/s of toroidal flow has been observed in D-^{3}He plasma ($n_{^3\mathrm{He}}/n_D \sim 10\%$). The mode conversion flow drive offers the possibility of momentum control for ITER and future large size reactors, where neutral beams may not be efficient.

ICRF wave theory will be revisited in Chapters 2 and Appendix B.

1.2.5 L-, H- and I-mode in Tokamaks

Three major plasma confinement regimes have been identified in tokamak experiments: low confinement mode (L-mode), high confinement mode (H-mode) and improved confinement mode (I-mode).

L-mode was studied in early tokamak experiments. A widely used scaling for this confinement regime is the ITER89-p scaling [47]

$$\tau_E^{\text{ITER89-p}}\,[\text{ms}] = 48 I_{\text{MA}}^{0.85} R^{1.2} a^{0.3} \kappa^{0.5} B_{\text{T}}^{0.2} A^{0.5} \overline{n}_{e,20}^{0.1} P_{\text{MW}}^{-0.5} \tag{1.11}$$

where I is the current in MA, R, a in meters, B in tesla, A is the main ion mass number, n_e in 10^{20} m^{-3}, P is the total input heating power in MW.

H-mode was discovered in ASDEX in 1982 [37] by applying heating power over a threshold. The widely used confinement time scaling associated with H-mode is

$$\tau_E^{\mathrm{ITER89(y,2)}}\,[\mathrm{ms}] = 145 I_{\mathrm{MA}}^{0.93} R^{1.39} a^{0.58} \kappa^{0.78} B_{\mathrm{T}}^{0.15} A^{0.19} \overline{n}_{e,20}^{0.41} P_{\mathrm{MW}}^{-0.69} \tag{1.12}$$

With the same parameters, the confinement time in H-mode is typically twice that in L-mode. The appearance of edge temperature and density pedestals (region with large radial gradient) is the signature to distinguish H-mode and L-mode, as is shown in Fig. 1-6.

The I-mode regime was discovered in Alcator C-Mod recently [48, 49]. It features H-mode-like energy confinement and L-mode-like particle confinement. I-mode has a pedestal in the temperature profile, but no pedestal in the density profile, as is shown in Fig. 1-6. This characteristic is beneficial in avoiding impurity accumulation in the core plasma.

The thesis mainly focuses on the transport phenomena in Alcator C-Mod Ohmic L-mode plasmas.

1.3 X-ray Imaging Spectroscopy

X-ray imaging spectroscopy is the main diagnostic used in this thesis. Due to its ability of measuring the impurity emissivity, ion rotation, ion and electron temperature, it is extensively used for plasma transport studies. In Alcator C-Mod, the system is called HIgh REsolution Spectroscopy (HiReX). There are two HiReX systems: HiReX–Jr [50] and HiReX–Sr [51, 52, 7, 53, 54].

1.3.1 HiReX–Jr

HiReX–Jr is the prodeccessor of HiReX–Sr. It is a one channel spectrometer constructed to measure ion temperature, electron temperature, and ion rotation at

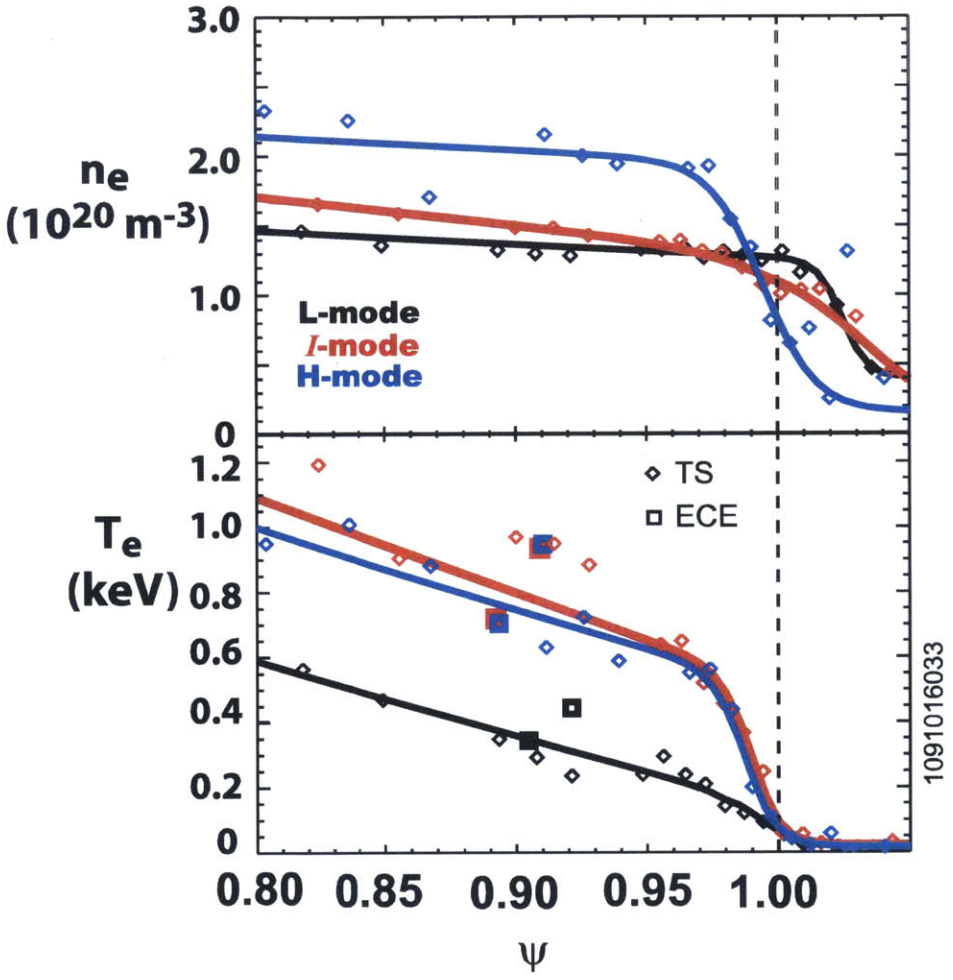

Figure 1-6: The edge n_e and T_e profiles in L-mode (black), H-mode (blue) and I-mode (red). Figure is from [4].

the core of the plasma. HiReX–Jr uses the von Hamos geometry [55]: a quartz crystal flat in the diffractive direction and cylindrically curved in the non-dispersive direction, as shown in Fig. 1-7. Flatness in the diffractive direction requires a slit aperture to avoid degeneracy of X-rays of different energies satisfying the Bragg condition at different angles and being reflected to the same position on the detector. The wavelength resolution is thus guaranteed by reflecting X-rays of different energies (wavelengths) into different horizontal (meridional) planes. The presence of a slit will significantly reduce the photon throughput. To work around this drawback, the crystal is cylindrically bent in the vertical (sagittal) direction, and X-rays of same energy that originate from different locations in the plasma will focus on the detector. The trade-off of the focusing is that the von Hamos geometry spectrometer doesn't have spatial resolution. The detector used for HiReX–Jr is made up of pressurized ethane (20%) and krypton (80%) filling a single proportional counter and a delay line, where the gas is ionzied by X-rays and causes a charge collected by the wire. HiReX–Jr is actively used in the studies of momentum transport ([56, 57, 58, 59, 60, 61, 5, 62, 63, 64, 65, 66]) and energy transport ([67, 68, 69, 70, 71]). Despite the developement of its successor HiReX–Sr, HiReX–Jr is still under operation for the reasons that (1) it doesn't have velocity drift during operation and doesn't require frequent wavelength calibration, (2) the tangential view geometry yields better measurement of toroidal rotation. So HiReX–Jr can be used as a calibration reference against HiReX–Sr.

1.3.2 HiReX–Sr

HiReX–Sr adapted the Johann geometry [72] as shown in Fig. 1-8. The dashed circle in Fig. 1-8 is called the Rowland circle. The radius of curvature of the crystal is equal to the diameter of the Rowland circle. This equality guarantees that all rays coming from the same point on the Rowland circle have the same incident angle. So this point corresponds to a specific photon wavelength, λ, whose value is determined by the Bragg condition. This cylindrically bent crystal geometry (cylindrically bent in the diffractive direction and flat in the non-dispersive direction) avoids the necessity

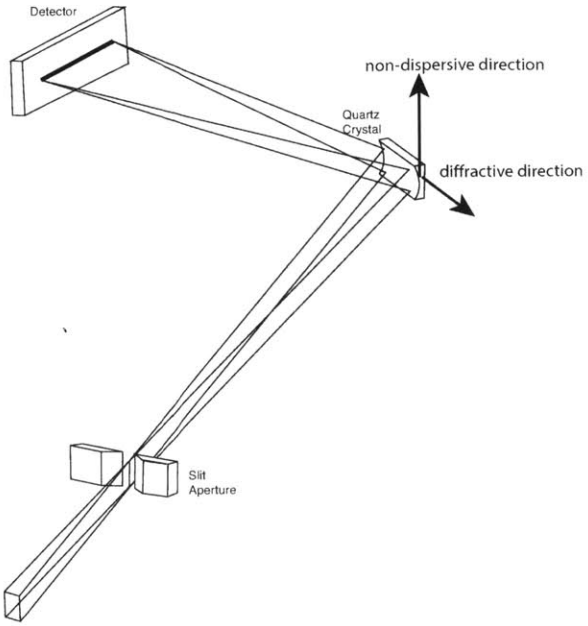

Figure 1-7: Schematic of the von Hamos spectrometer geometry used by HiReX–Jr. Figure is adapted from [5].

of a slit, which increases the photon throughout. But it only provides a signle line of sight and has no spatial resolution.

A spherically bent crystal is necessary to provide spatial resolution in the meridional plane, as shown in Fig. 1-9(a). In this geometry, photons originating above the meridional plane will arrive at the detector below the meridional plane, and vice versa. The meridional plane focusing length (F_m) and sagittal plane focusing length (F_s) are:

$$F_m = R_c \sin\theta_b \tag{1.13}$$

$$F_s = -F_m / \cos 2\theta_b \tag{1.14}$$

where R_c is the radius of the crystal curvature (or diameter of the Rowland circle) and θ_b is the Bragg angle.

In Alcator C-Mod, argon is used as the diagnostic gas for two reasons. First, as a noble gas, argon is chemically inert and doesn't react with wall materials, so to control its concentration in plasma is easier. Secondly, the typical electron temperature in Alcator C-Mod is 0.5 - 5 keV, within this range of temperature helium-like argon

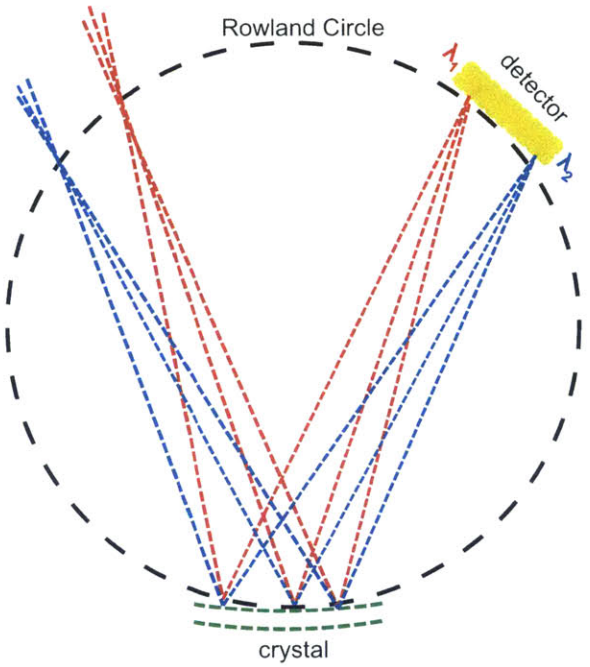

Figure 1-8: Schematic of the Johann spectrometer geometry.

(Ar^{16+}) and hydrogen-like argon (Ar^{17+}) offer a relatively high fraction in coronal equilibrium as shown in Fig. 1-10. For these reasons, emission lines from He-like and H-like argon are ideal for spectroscopic analysis.

HiReX–Sr has two branches: He-like branch (Branch A) and H-like branch (Branch B), as shown in Fig. 1-11 (a). Branch A is a 3-detector system which covers the whole vertical range of plasma (up-down). It uses a rectangular crystal with a 2d spacing of 4.56225 Å. The Bragg angle for 3.9494 Å(He-like argon w line) is 59.96°. Branch B is a 1-detector system which mainly covers the core of plasma. It uses a circular crystal with 2d spacing of 4.56225 Å. The Bragg angle for 3.7311 (H-like argon Ly-α1 line) Åis 54.87°. HiReX–Sr has a tilted tangential view ($\sim 8°$) of the plasma (Fig. 1-11(b)), which provides both toroidal rotation and poloidal rotation measurement.

Examples of He-like and H-like spectra as shown in Fig. 1-12. The transitions and wavelengths of He-like argon emission lines and satellites in the Gabriel notation [73] are listed in Table 1.3. The transitions and wavelengths of H-like argon and molybdenum emission lines are listed in Table 1.4.

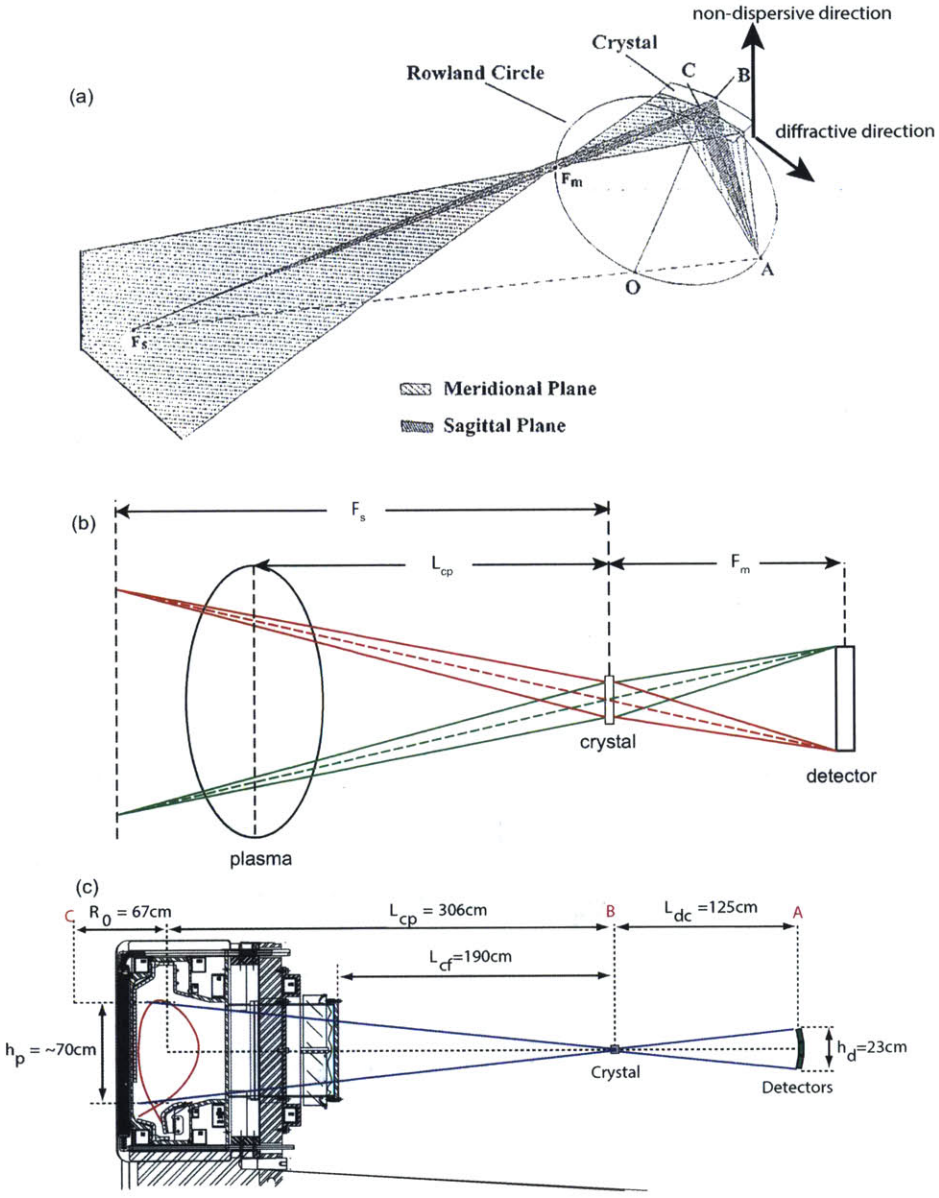

Figure 1-9: (a) Demonstration of X-ray reflection properties for a spherically bent crystal geometry, figure adapted from [6]. (b) Illustration of spatial resolution for the spherically bent cyrstal geometry. (c) Side view of hirex–sr in Alcator C-Mod, figure from [7]

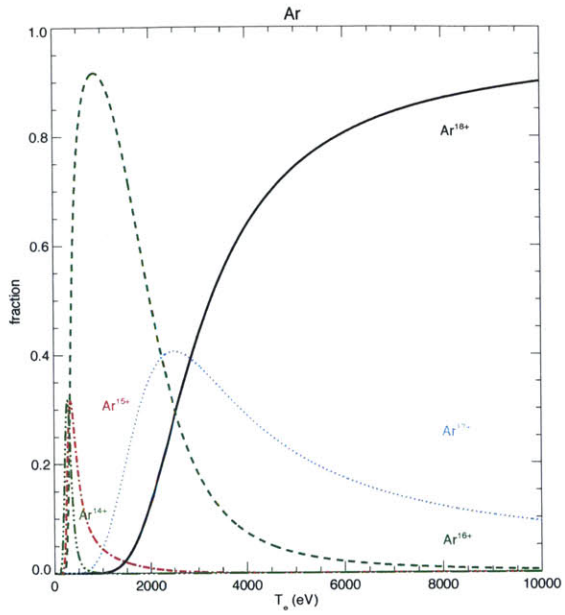

Figure 1-10: Fractional charge states for argon in coronal equilibrium.

Table 1.3: He-like argon (Ar^{16+}) emission lines. Wavelength data are from [21].

Label	Transition	Wavelength (Å)
w	$1s2p\ ^1P_1 \rightarrow 1s^2\ ^1S_0$	3.9492
x	$1s2p\ ^3P_2 \rightarrow 1s^2\ ^1S_0$	3.9659
y	$1s2p\ ^3P_1 \rightarrow 1s^2\ ^1S_0$	3.9692
q	$1s2s2p\ ^2P_{3/2} \rightarrow 1s^22s\ ^2S_{1/2}$	3.9815
r	$1s2s2p\ ^2P_{1/2} \rightarrow 1s^22s\ ^2S_{1/2}$	3.9839
a	$1s2p^2\ ^2P_{3/2} \rightarrow 1s^22p\ ^2P_{3/2}$	3.9864
k	$1s2p^2\ ^2D_{3/2} \rightarrow 1s^22p\ ^2P_{1/2}$	3.9903
j	$1s2p^2\ ^2D_{5/2} \rightarrow 1s^22p\ ^2P_{3/2}$	3.9932
z	$1s2p\ ^3S_1 \rightarrow 1s^2\ ^1S_0$	3.9943

Table 1.4: He-like argon (Ar^{16+}) emission lines and molybdenum lines. He-like argon lines' wavelength data are from [22], molybdenum lines' wavelength data are from [23].

Label	Transition [upper state]	Wavelength (Å)
Lyα_1	$2p_{3/2} \rightarrow 1s_{1/2}$	3.731142
Lyα_2	$2p_{1/2} \rightarrow 1s_{1/2}$	3.736514
T	$2s2p\ ^1P_1 \rightarrow 1s2s\ ^1S_0$	3.75526
Q	$2s2s2p\ ^3P_2 \rightarrow 1s2s\ ^3S_1$	3.76106
J	$2p^2\ ^1D_2 \rightarrow 1s2p\ ^1P_1$	3.77179
Mo^{32+}	$2p \rightarrow 4d\ \left[(2p-)^2\,(2p+)^3\,4d + J = 1\right]$	3.7398
Mo^{31+}_{*}	$2p \rightarrow 4d\ \left[2p + [3s]\,4d + J = \frac{3}{2}\right]$	3.7857
$Mo^{31+}_{\#}$	$2p \rightarrow 4d\,(3p) + \left[2p + [3p+]\,4d + J = \frac{3}{2}+\right]$	3.7874

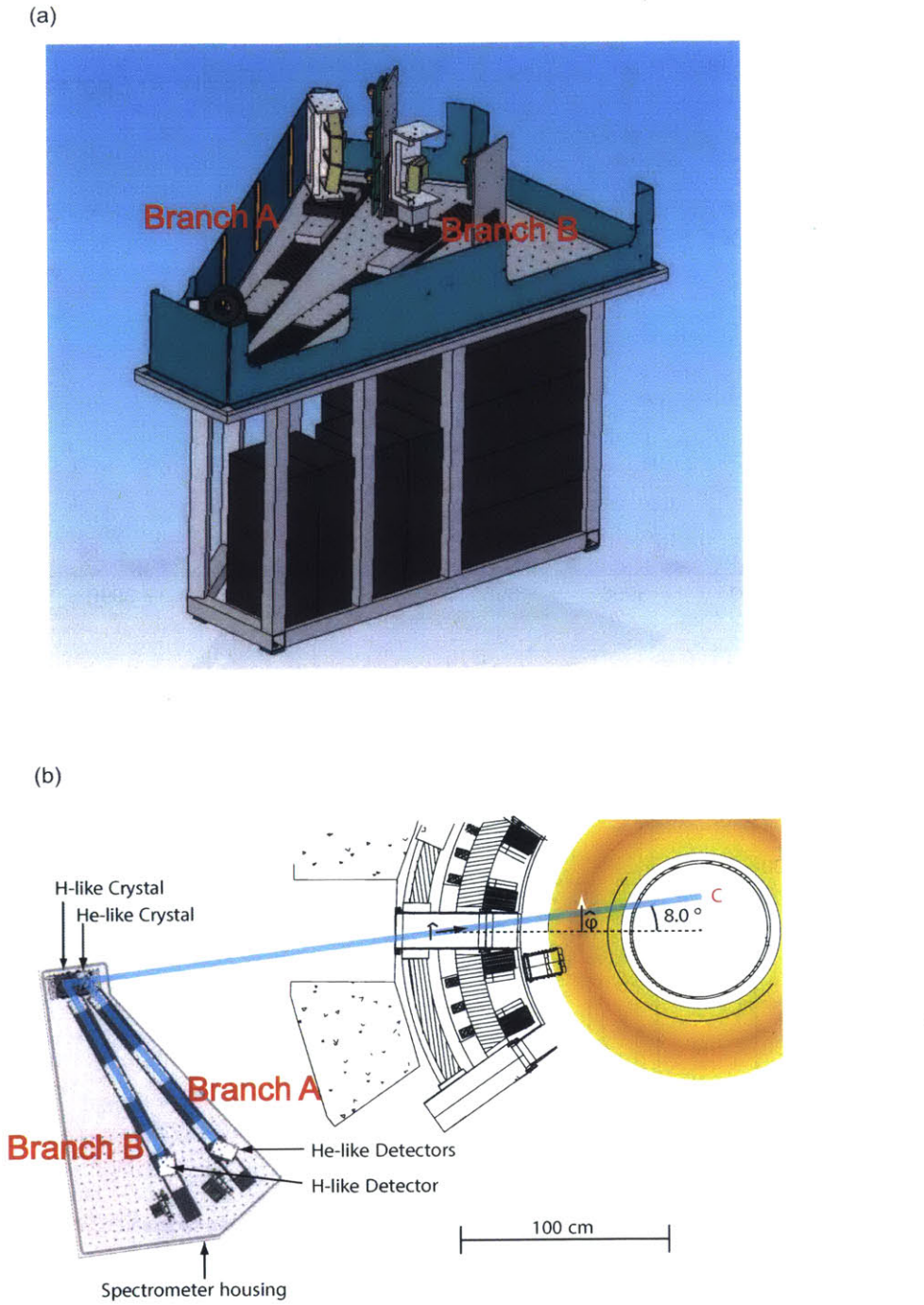

Figure 1-11: (a)Engineering drawing of the HiReX–Sr spectrometer. (b) Top view of HiReX–Sr spectrometer and Alcator C-Mod. Figure is adapted from [7].

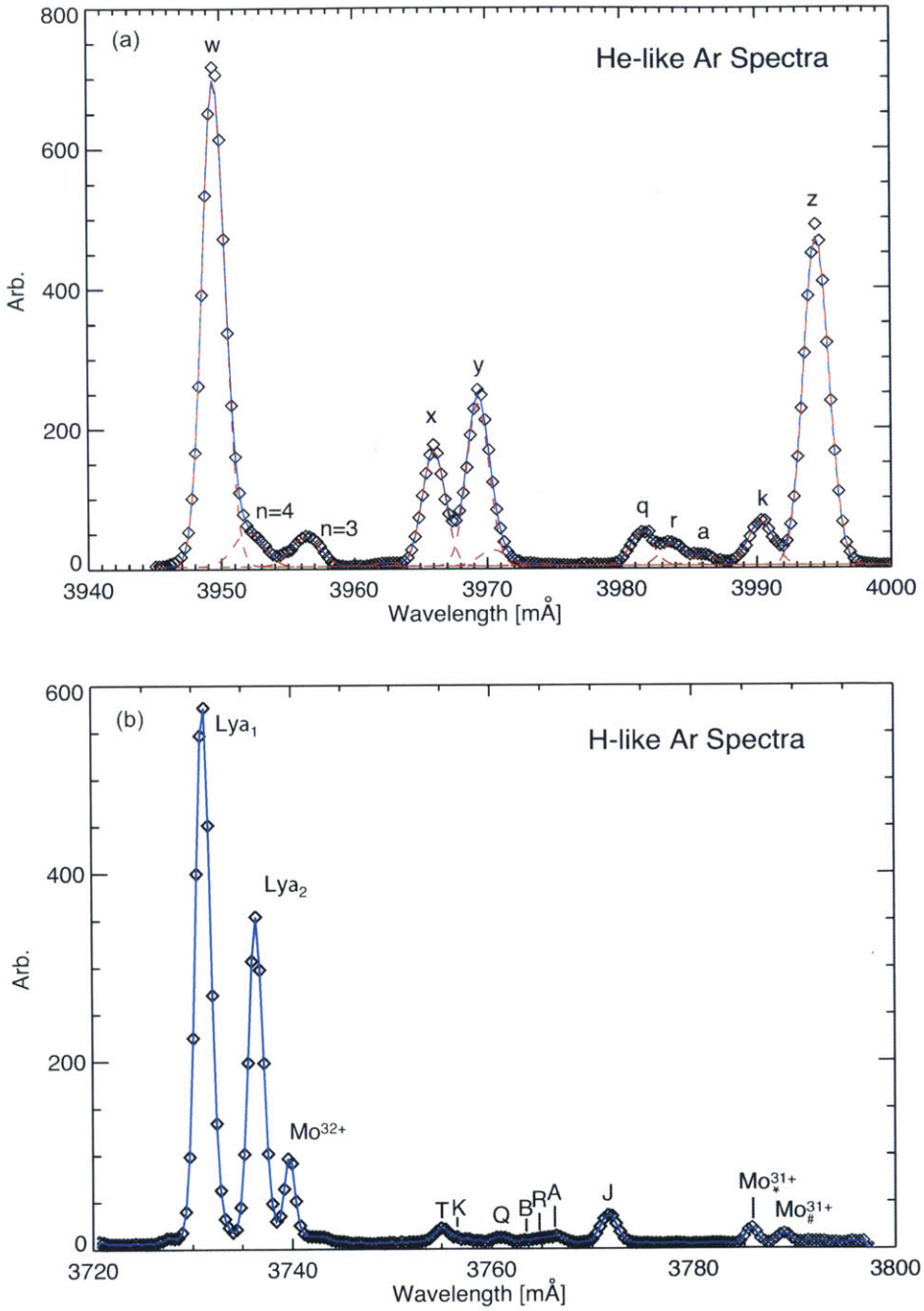

Figure 1-12: (a) He-like and (b) H-like argon spectra from HiReX–Sr. Figure is adapted from [8].

Local plasma quantities (emissivity, rotation and temperature) can be deduced from the measured brightness, defined as the chord integrated spectra. With the assumption that electron and ion distribution functions are Maxwellian, the measured brightness can be expressed as:

$$B_j^{\lambda} = \int dl \frac{\varepsilon_0(l)}{\sqrt{2\pi} w(l)} e^{-\frac{\left(\lambda - \lambda_0 - \frac{\lambda_0}{c}\hat{l}\cdot\mathbf{v}(l)\right)^2}{2w(l)^2}} \tag{1.15}$$

where B_j^{λ} is the spectral brightness of photons with wavelength λ along the j^{th} chord; l is the distance along the line of sight; $\hat{l}$ is the unit vector along the line of sight; λ_0 is the wavelength in the lab frame; $\varepsilon_0(l)$ is the emissivity at l; $\mathbf{v}(l)$ is the impurity ion velocity at l; w, defined as $w(l)^2 = \lambda_0^2 k T_I(l)/mc^2$, is the full width half maximum (FWHM) of the spectra; $T_I(l)$ is the impurity ion temperature at l.

Define the n^{th} moment of brightness at j^{th} chord as:

$$M_{n,j} = \int d\lambda (\lambda - \lambda_0)^n B_j^{\lambda} \tag{1.16}$$

The first three moments of B_j^{λ} can be used to get $\varepsilon_0(l), \mathbf{v}(l)$ and $T_I(l)$:

$$M_{0,j} = \int dl\ \varepsilon_0(l) \tag{1.17}$$

$$M_{1,j} = \frac{\lambda_0}{c} \int dl\ \left[\hat{l}\cdot\mathbf{v}(l)\right]\ \varepsilon_0(l) \tag{1.18}$$

$$M_{2,j} = \int dl \left[\frac{\lambda_0^2}{c^2}\left(\hat{l}\cdot\mathbf{v}(l)\right)^2 + w(l)^2\right] \tag{1.19}$$

MHD theory shows that the density and temperature are functions of poloidal magnetic flux ψ, and the first order rotation approximation from neoclassical theory claims that plasma rotation can be decomposed into a rotation along the magnetic field line and a toroidal rotation [74]. The emissivity excited by electron recombination and impact is a function of n_e, n_I and T_e, thus is also a flux function. The following assumptions can be made:

$$\varepsilon_0 = \varepsilon_0(\psi) \tag{1.20}$$

$$T = T(\psi) \tag{1.21}$$

$$\mathbf{v} = u(\psi)\,\mathbf{B} + \omega(\psi)\,R\hat{\phi} \tag{1.22}$$

where $\hat{\phi}$ is the toroidal unit vector, $\mathbf{B}$ is the magnetic field, ω is the toroidal angular velocity. With the assumptions in Eqs.1.20–1.22, matrix inversions can be performed on Eqs.1.17–1.19 to get local parameters $\varepsilon_0(\psi), u(\psi), \omega(\psi)$ and $T(\psi)$. A dedicated code to perform spectroscopic analysis for HiReX–Sr has been developed and discussed in great detail in [54, 75].

The main ion temperature is inferred by the measured argon temperature. The time scale for impurity-deuterium thermal equilibration is [53]

$$\tau_{eq}^{ID} \approx 2 \times 10^{-4} \frac{T_k^{3/2}}{Z_I n_{20}} \text{ s} \tag{1.23}$$

where T_k is ion temperature in keV, n_{20} is electron density in 10^{20} m^{-3}. For a typical C-Mod L-mode plasma ($T \approx 2$ keV, $n_e \approx 10^{20}$ m^{-3}), $\tau_{eq}^{ID} \approx 40$ μs; the upper limit of τ_{eq}^{ID} is about 0.3 ms, obtained from a low density high temperature discharge ($T \approx 5$ keV, $n_e \approx 0.5 \times 10^{20}$ m^{-3}). Therefore with typical plasma parameters in tokamaks, the ion-impurity thermal equilibration time is much shorter than the energy confinement time ($\sim$ 10s of ms). This indicates that the argon and main ion temperatures are well coupled and the measured argon temperature is a good proxy of the main ion temperature, and it is verified by the simultaneous measurements of impurity and main ion temperatures in DIII-D tokamak [76].

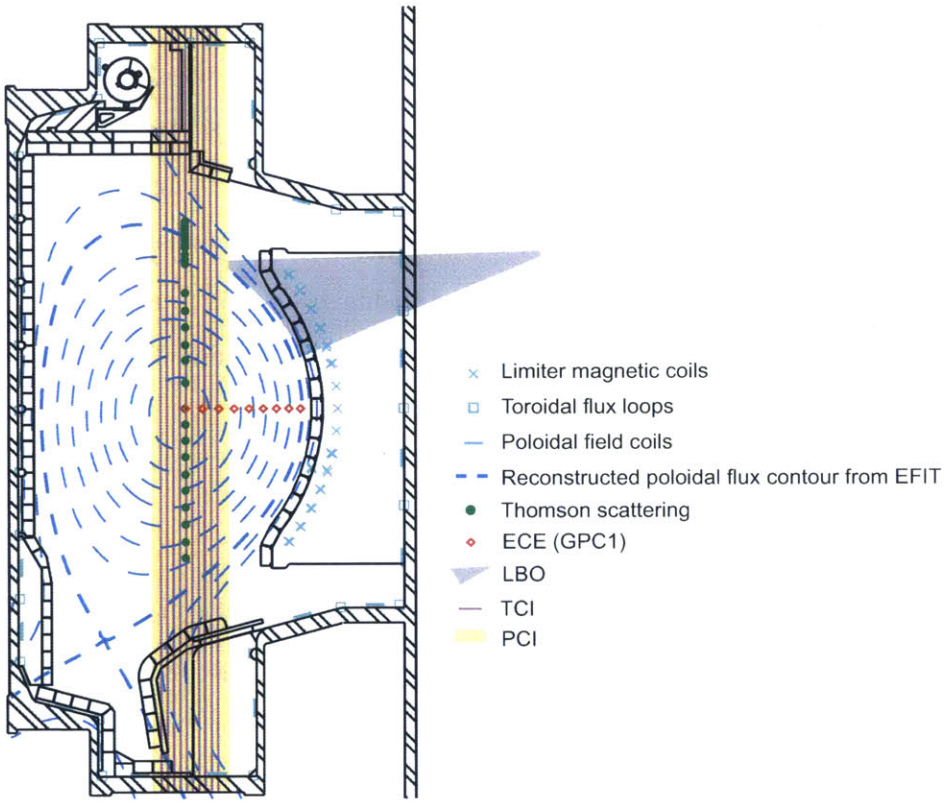

Figure 1-13: Poloidal view of Alcator C-Mod cross section shows some of the diagnostics: magnetic coils, Thomson scattering (1.4.1), electron cyclotron emission (ECE, 1.4.2), laser blow-off (LBO), two-color interferometetry (TCI, 1.4.3) and phase-contrast imaging (PCI, 1.4.4).

1.4 Other Diagnostics in Alcator C-Mod

1.4.1 Thomson Scattering

The Thomson scattering system [77, 78, 79, 80] measures the electron density and temperature profiles by detecting the laser photon scattering from plasma electrons. The system use two identical Nd:YAG lasers ($\lambda_0 = 1064$nm). The laser beams are vertically fired into the plasma alternatively, each at a rate of 50 Hz, which translates into a temporal resolution of 10 ms. The green bullets • along the beam path in Fig.1-13 represent scattering volumes, where the photons are scattered. The scattered photons are collected by optics with a horizontal view of the plasma. The ability to locally measure electron temperature and density simultaneously makes Thomson scattering an essential diagnostic for fusion plasma research. The measured density and temperature profiles are smoothly fitted numerically using FiTs or quickFit [4] and then they are used for transport or turbulence studies.

1.4.2 Electron Cyclotron Emission (ECE)

Electron cyclotron emission (ECE) measures the local electron temperature using the fact that the observed photon intensity of a specific frequency is proportional to the local electron temperature. Alcator C-Mod has a set of several diagnostics measuring the ECE: Michelson interferometer, grating polychromators (GPCs) and Fusion Research Center heterodyne ECE (FRCECE). All ECE instruments use second-harmonic extraordinary (X) mode emission.

The Michelson interferometer [81] has a frequency resolution of 5 GHz and temporal resolution up to 33 Hz with low vibration. Its optic system has a large-aperture Gaussian telescope which makes the in-situ calibration possible. For this reason, the Michelson interferometer is used as a benchmark against which other ECE instruments are calibrated.

Higher temporal resolution measurements are provided by two grating polychromators: 9-channel system GPC1 [82] and 19 channel system GPC2 [83].

The GPC systems have a coverage on the low field side (LFS) mid-plane ($\diamond$ in Fig.1-13). They can measure the electron temperature profiles with a typical temporal resolution of 10 μs (100 kHz) and low noise levels of $\sim$ 10 eV [84].

FRCECE uses separate viewing optics and emission is detected by a 32-channel radiometer [85]. This enables higher spatio-temporal resolution of electron temperature. The profile measurements' radial resolution can be up to 4 mm with a temporal resolution of 1 μs (1 MHz).

The high temporal resolution of ECE measurements makes it a very attractive electron temperature diagnostic. But its application suffers when the electrons are non-thermal (non-Maxwellian). In operations with lower-hybrid waves which create high energy electron tails, ECE measurement is not feasible and Thomson scattering is required.

1.4.3 TCI

The two color interferometer (TCI) is a vertically viewing 10-chord interferometer system (||| in Fig.1-13) using a 20 W, 10.6 μm CO_2 laser and a 17 mW, 0.632 μm HeNe laser to measure the line-integrated electron density [86]. The typical temporal resolution for line-integrated density is 2 - 10 kHz (0.5 - 0.1 ms). A recent upgrade of fast TCI [87] enables TCI to simultaneously measure the density fluctuations at a rate of 2 MHz. The TCI can detect fluctuations with radial wavenumber k_R up to 2.83 cm^{-1} and the wavenumber resolution Δk_R is 0.71 cm^{-1}.

1.4.4 PCI

The phase contrast imaging (PCI) [88, 89] measures line-integrated electron density fluctuations. It is a vertically viewing 32-channel system using a 25 W CO_2 laser with $\lambda_0 = 10.6\mu$m (in Fig.1-13). The PCI data acquisition rate is 5 MHz, which is sufficient to study a broad variety of density fluctuation frequencies in Alcator C-Mod. The chord spacing is about 4 mm, which covers 13 cm of plasma radius. The PCI can detect fluctuations with radial wavenumber k_R up to 11.7 cm^{-1} and the

wavenumber resolution Δk_R is 0.73 cm^{-1}.

1.4.5 Reflectrometry

Reflectrometry is used to measure the electron density profile and fluctuations. It consists of 7 channels at frequencies 50, 60, 75, 88, 110, 132 and 140 GHz [90]. The reflectrometry launches ordinary (O) mode RF waves into plasma at the A-port mid-plane. These waves will be cut-off and reflected at different plasma radii determined by the wave frequency and local electron density. The electron density and fluctuation information can be obtained by measuring the refleted waves' phase difference.

1.5 Summary

This section provides an experimental background for this thesis. Although compact in size, Alcator C-Mod provides a unique opportunity for plasma transport research in an ITER-like high field and high density environment. HiReX–Sr is a powerful tool to study plasma transport in multiple channels: impurity, momentum and energy, but a comprehensive transport analysis is impossible without the other diagnostics.

Chapter 2

Related Transport and Wave Theories

This chapter will discuss the theories related to the thesis. Section 2.1 introduces the anomalous transport and drift-wave instabilities. Section 2.2 is about the Coriolis pinch in momentum transport. Section 2.3 discusses mechanism of impurity-wave interaction. Section 2.4 introduces the numerical codes used in this thesis.

2.1 Anomalous Transport & Drift-wave Instability

Transport takes an important position in fusion plasmas. Its major purpose is to study the macro transport properties of plasmas. Quantities such as diffusivity and convectivity are calculated from mechanics and electromagnetism. The objects of plasma transport study are the particle, momentum and energy channnels:

$$\frac{\partial n}{\partial t} + \nabla \cdot \mathbf{\Gamma} = S_{\text{particle}} \tag{2.1}$$

$$\frac{\partial \mathbf{P}}{\partial t} + \nabla \cdot \overleftrightarrow{\mathbf{\Pi}} = \mathbf{S}_{\text{momentum}} \tag{2.2}$$

$$\frac{3n}{2}\frac{\partial T}{\partial t} + \nabla \cdot \mathbf{q} = S_{\text{heat}} \tag{2.3}$$

Eq. 2.1 describes the particle transport where n is the particle density (electron n_e , ion n_i or impurity n_I), $\mathbf{\Gamma}$ is the particle flux and S_{particle} is the particle source. Eq. 2.2 describes the momentum (rotation) transport where $\mathbf{P} = nm\mathbf{V} \approx n_i m_i V_i$ is the plasma momentum density (mainly carried by ions due to the high ion-to-electron mass ratio), $\overleftrightarrow{\mathbf{\Pi}}$ is the stress tensor and $\mathbf{S}_{\text{momentm}}$ is the momentum source. Eq. 2.3 describes the heat transport where T is the temperature (electron T_e or ion T_i), $\mathbf{q}$ is the heat flux and S_{heat} is the heat source.

The plasma transport theories try to calculate the flux and stress terms $(\mathbf{\Gamma}, \overleftrightarrow{\mathbf{\Pi}}, \mathbf{q})$ in terms of plasma parameters $n, \mathbf{V}, T$. More specifically, the radial transport coefficients are the quantities of great interest, which can be expressed in form of diffusion-convection equations:

$$\Gamma_r = - D_n \partial_r n + V_n n \tag{2.4}$$

$$\Pi_{\phi,r} = m_i \left(-\chi_\phi \partial_r n_i V_\phi + V_{pinch} n_i V_\phi\right) + \Pi^{\text{res}} \tag{2.5}$$

$$q_r = - n\chi \partial_r T + n V_q T \tag{2.6}$$

where D_n is the particle diffusivity, V_n is the particle pinch, χ_ϕ is the momentum diffusivity, V_{pinch} is the momentum pinch, Π^{res} is the residual stress which characterizes the momentum flux that is independent of the toroidal rotation and its gradient, χ is the heat diffusivity and V_q is the heat pinch. Particle pinch [91] and momentum pinch [41] are widely observed in experiment. A purely diffusive heat flux ($V_q = 0$) is generally adopted to model the heat transport, but there is evidence of inward electron heat flow with off-axis electron cyclotron heating in DIII-D tokamaks [92, 93]. It is the radial transport that determines the confinement performance. For this reason, the subscript r will be omitted in Γ_r, Π_r and q_r for the rest of this thesis unless otherwise specified.

In fusion plasmas, the transport estimated from collisional or neoclassical theory is generally orders of magnitude lower than experimental results [1], except that under some high confinement high β conditions the transport can be reduced to

neoclassical level [94]. It is believed that this enhanced transport (also called anomalous transport) is dominated by turbulent transport, and the turbulence originates from the low-frequency drift-wave fluctuations. Turbulent transport theory considers the transport arising from fluctuations. The plasma can support wave-like motion (instabilities). The instabilities can tap free energy stored in the temperature and density gradients. As the plasma waves grow, they can modify the medium (plasma) in which they propagate through non-linear interaction, which causes the turbulence. As a simple illustration, the quasi-linear particle and energy fluxes from turbulent $E \times B$ drift are:

$$\Gamma = \langle \tilde{n} \tilde{v}_{E\times B} \rangle \tag{2.7}$$

$$q = \frac{3}{2} \left\langle \widetilde{nT} \tilde{v}_{E\times B} \right\rangle \tag{2.8}$$

where $\tilde{\mathbf{v}}_{E\times B} = -\nabla\tilde{\phi} \times \mathbf{B}/B^2$ is the $E \times B$ drift velocity due to the fluctuating potential $\tilde{\phi}$, $\tilde{n}$ is the fluctuating density and $\tilde{T}$ is the fluctuating temperature such that $\widetilde{nT} = \tilde{n}T_0 + n_0\tilde{T}$. $\tilde{\phi}, \tilde{n}, \tilde{T}$ are turbulence driven by drift-wave instabilities. The turbulence is commonly assumed to be electrostatic, which is valid for low β devices like most conventional tokamaks and C-Mod Ohmic L-mode plasmas.

The research of turbulence in plasmas can be divided into stability studies and transport studies. Stability analysis is used to study the dispersion relation of turbulence in plasmas. Its most successful application is to identify the different types of drift-wave instabilities: ITG (ion temperature gradient) modes, TEM (trapped electron modes), ETG (electron temperature gradient) modes, etc. Linear theory can be used for stability analysis to get the dispersion relation. The growth of instabilities gives rise to transport. Quasilinear theory can be used to estimate the transport quantities as in Eq. 2.7 and Eq. 2.8. Although estimation can be made with some assumptions (for example, mixing length model assumes $D \propto \gamma/k^2$), an accurate calculation of the turbulent transport requires solving the kinetic equation with Maxwell equations (Vlasov-Maxwell equations) on turbulence scales. Gyrokinetic analysis is a standard tool for this task [95, 96]. A detailed

discussion of the gyrokinetic method is out of the scope of this thesis.

This section introduces the two types of drift-wave instabilities related to the thesis work: ITG modes and TEMs. The ETG instability will also be discussed as recent multi-scale simulations on Alcator C-Mod plasmas show that ETG modes may play an important role in anomalous transport [97, 98].

2.1.1 Bohm and Gyro-Bohm Diffusion

Classical transport theory considers the diffusion due to Coulomb collisions. It estimates the particle and energy diffusion coefficients as [1]:

$$D_n^{CL} \approx \rho_{L,e}^2 \bar{\nu}_{ei} \approx 2.0 \times 10^{-3} \frac{n_{20}}{B_0^2 T_k^{1/2}} \ \mathrm{m}^2/\mathrm{s} \tag{2.9}$$

$$\chi_i^{CL} \approx \rho_{L,i}^2 \bar{\nu}_{ii} \approx 0.1 \frac{n_{20}}{B_9^2 T_k^{1/2}} \ \mathrm{m}^2/\mathrm{s} \tag{2.10}$$

$$\chi_e^{CL} \approx \rho_{L,e}^2 \bar{\nu}_{ee} \approx 4.8 \times 10^{-3} \frac{n_{20}}{B_9^2 T_k^{1/2}} \tag{2.11}$$

Neoclassical theory [99, 74], taking into account the toroidal magnetic geometry and trapped electron effects, estimates the diffusion coefficients 1 - 2 orders of magnitude larger than classical theory [100, 1]:

$$D_n^{NC} = 2.2 q^2 \left(\frac{R_0}{r}\right)^{3/2} D_n^{CL} \tag{2.12}$$

$$\chi_e^{NC} = 0.89 q^2 \left(\frac{R_0}{r}\right)^{3/2} \chi_e^{CL} \tag{2.13}$$

$$\chi_i^{NC} = 0.68 q^2 \left(\frac{R_0}{r}\right)^{3/2} \chi_i^{CL} \tag{2.14}$$

but they are still smaller than the particle and energy loss observed in experiments $D_n^{exp} \sim \chi_i^{exp} \sim \chi_e^{exp} \sim 10\chi_i^{NC} \sim 1 \ \mathrm{m}^2/\mathrm{s}$. It is widely accepted that this discrepancy arises from the 'anomalous' transport due to turbulence. The diffusion coefficient of

turbulent transport from mixing length theory is

$$D_e^{\text{Bohm}} = \begin{cases} \frac{1}{16}\frac{T}{eB} & (\text{ Bohm form [101]}) \\ 0.21\frac{T}{eB} & (\text{ Spitzer form [102]}) \end{cases} \tag{2.15}$$

But experimental evidence shows that core tokamak plasma transport could be gyro-Bohm type [103, 104, 105]:

$$D_e^{\text{gyro-Bohm}} \approx \frac{\rho_s}{a} D_e^{\text{Bohm}} \tag{2.16}$$

2.1.2 Drift-wave Instabilities

It is believed that the anomalous transport is due to the low-frequency drive-wave instabilities. In magnetically confined plasmas, density and temperature gradients are unavoidable. These gradients give rise to a cross-field diamagnetic current $\mathbf{j}_{da} = \frac{\mathbf{B}\times\nabla p_a}{B^2}$. The drift velocity associated with this diamagnetic current $\mathbf{v}_{da} = \frac{\mathbf{j}_{da}}{e_a n_a} = \frac{1}{e_a n_a}\frac{\mathbf{B}\times\nabla p_a}{B^2}$ will cause collective oscillations called drift waves. The drift waves become unstable by tapping the free energy in the density and temperature gradients. A detailed discussion on how the drift waves arise and propagate in the plasma can be found in [106, 107].

If the ion and electron density respond to fluctuation potential $\tilde{\phi}$ adiabatically

$$\tilde{n}_{i,e} = \frac{q_{i,e}\tilde{\phi}}{T_{i,e}} n_{i0,e0} \tag{2.17}$$

, there will be no cross-field transport due to the 90° phase difference between the $E \times B$ drift velocity in Eq. 2.7. The adiabatic relation is violated in inhomogeneous plasma with temperature or density gradients. A phase shift will be added to the density response

$$\tilde{n}_{i,e} = \frac{q_{i,e}\tilde{\phi}}{T_{i,e}} \left(1 + \delta_{i,e}\right) n_{i0,e0} \tag{2.18}$$

where $\delta_{i,e}$ is a complex function of local plasma parameters. The dispersion relation

can be obtained from quasi-neutrality

$$\tilde{n}_i \approx \tilde{n}_e \tag{2.19}$$

The dispersion relation will provide the real frequency ω_r and growth rate γ of the instability (or damping rate if it is stable mode)

$$\omega = \omega_R + i\gamma \tag{2.20}$$

Depending on the local plasma parameters $(n_e, T_e, T_i, \partial_r n_e, \partial_r T_e, \partial_r T_i, \partial_r V_\phi, ...)$, the mode can be either electron diamagnetic drift mode ($\omega_r > 0$) or ion diamagnetic drift mode ($\omega_r < 0$); and can be either unstable mode ($\gamma > 0$) or stable mode ($\gamma < 0$), with convention that the wave amplitude is proportional to $e^{-i\omega t}$. Three types of drift-wave instabilities, which are considered to be the most important instabilities driving anomalous transport in low β tokamaks, will be introduced. They are: ion temperature gradient (ITG) mode driven by ion temperature gradient, trapped electron mode (TEM) driven by density gradient of trapped electrons, electron temperature gradient (ETG) mode drive by electron temperature gradient.

2.1.3 Ion Temperature Gradient Modes

Ion Temperature Gradient (ITG) modes are instabilities driven by ion temperature gradients (∇T_i). It is also called the η_i mode because historically it is associated with a critical value of the dimensionless parameter $\eta_i \equiv L_n/L_{T_i} = |\nabla \ln T_i| \,/\, |\nabla \ln n|$, where $L_n \equiv n/|\nabla n|$ is the electron density gradient scale length and $L_{T_i} \equiv |T_i/\nabla T_i|$ is the ion temperature gradient scale length. ITG modes are considered to be the most important instability that drives ion energy transport in hot plasmas. ITG modes have long wavelength turbulence $k_\theta \rho_s \sim 0.3$, where k_θ is the poloidal wave vector, $\rho_s = c_s/\Omega_i$ and $c_s = \sqrt{T_e/m_i}$ is the ion sound wave speed. The modes will propagate in the ion diamagnetic drift direction.

Early theoretical work on ITG modes in slab geometry [108, 109, 110, 111] showed that ion temperature gradient can drive instabilities with growth rate $\gamma \propto \eta_i^{1/3}$. If Landau damping, finite Larmor radius (FLR) and toroidal effects are considered, a threshold η_c for ITG instability exists [112, 113, 107]:

- With toroidal geometry

$$\eta_c = \frac{4\epsilon_n}{3}\left(1+\frac{T_i}{T_e}\right)(1+b_i) \tag{2.21}$$

  where $\epsilon_n \equiv L_n/R$ is the toroidicity and $\epsilon_n \not\to 0, b_i \equiv k_\theta^2 \rho_i^2$.

- With small toroidicity $\epsilon_n \to 0$ and $2\epsilon_n\left(1+\frac{T_i}{T_e}\right)(1+b_i) \leq 1$

$$\eta_c = 1 - \frac{2\epsilon_n}{3}\left(1+\frac{T_i}{T_e}\right)(1+b_i) \tag{2.22}$$

For small toroidicity ($\epsilon_n \to 0$), a minimum value $\eta_{c,min} = 2/3$ is required to trigger the instability when $\epsilon_n\left(1+\frac{T_i}{T_e}\right)(1+b_i) = 1$.

An ITG threshold considering the effect of magnetic shear $s = rq'/q$ in a sheared slab is given in [114]

$$\eta_c = 1.9\left(1+\frac{T_i}{T_e}\right)\frac{s\epsilon_n}{q} \tag{2.23}$$

The ion thermal diffusivity can be obtained from quasi-linear fluxes for slab ITG [115, 116, 117] and toroidal ITG [118]. The numerical results are:

$$\chi_i^{\text{slab-ITG}} = 0.3\left(\frac{q}{s\epsilon_n}\right)^{1/2}\frac{\rho_s}{L_n}\frac{T_e}{eB}\left(\eta_i-\eta_c\right)^{1/2} \tag{2.24}$$

$$\chi_i^{\text{toroidal-ITG}} = c_1\frac{q}{s}\frac{\rho_s}{L_n}\frac{T_e}{eB}\left[2\epsilon_n\left(\eta_i-\eta_c\right)\right]^{1/2} \tag{2.25}$$

where c_1 is of order unity.

Taking the typical Ohmic L-mode parameters in C-Mod at $r/a \approx 0.6$: $s \approx 1$, $\epsilon_n \approx 1/3$, $q \approx 1$, $L_n \approx 0.2$ m, $T_e \approx 1$ keV, $B = 5.4$ T, $(\eta_i - \eta_c) \sim 1$, the ion thermal

diffusivity arising from ITG modes will be

$$\chi_i^{\text{slab-ITG}} \approx 1.4 \text{ m}^2/\text{s} \tag{2.26}$$

$$\chi_i^{\text{toroidal-ITG}} \approx 2.1 \text{ m}^2/\text{s} \tag{2.27}$$

which are slightly larger than the experimental values of $\chi_i \sim 0.5 - 1.0 \text{ m}^2/\text{s}$ calculated using power balance equations. One should notice that Eqs. 2.24 and 2.25 are gyro-Bohm type as Eq. 2.16.

2.1.4 Trapped Electron Modes

Trapped electron modes (TEMs) [119, 120, 121] are ion-scale/intermediate-scale ($k_\theta \rho_s \sim 1$) drive-wave instabilities arising from the non-adiabatic response of trapped electrons to the fluctuating potential, i.e.,

$$\tilde{n}_e^{\text{trapped}} = \frac{e\tilde{\phi}}{T_e}(1 - i\delta)\, n_{e0} \tag{2.28}$$

The deviation $\delta \propto \gamma/\omega$ from the adiabatic distribution can be viewed as a phase difference between the fluctuating potential $\tilde{\phi}$ and the responding fluctuating density $\tilde{n}_e^{\text{trapped}}$. It is this phase shift that will produce net convective electron particle and energy fluxes.

Unlike ITG modes which are universal in both slab and toroidal geometry as long as $\eta_i \neq 0$, TEMs, as it is called, are instabilities only in toroidal devices. TEMs are generally categorized as collisionless TEMs (CTEMs) and dissipative TEMs. The former happens in low collisionality plasmas $\nu_{*e} \equiv \frac{\nu_{e,eff}}{\omega_b} = \frac{\nu_e}{\hat{\omega}_t \epsilon^{3/2}} < 1$, where ν_e is the electron-ion collisionality, ν_{eff} is the effective collisionality, ω_b is the trapped particle

bouncing frequency, $\hat{\omega}_t$ is the transit frequency, and ϵ is the inverse aspect ratio:

$$\nu_e = \frac{\sqrt{2}}{12\pi^{3/2}} \frac{Z_i n_e e^4 \ln \Lambda}{\epsilon_0^2 m_e^{1/2} T^{3/2}} \tag{2.29}$$

$$\nu_{eff} = \frac{\nu_e}{\epsilon} \tag{2.30}$$

$$\omega_b = \sqrt{\epsilon} v_T / qR \tag{2.31}$$

$$\hat{\omega}_t = v_T / qR \tag{2.32}$$

$$v_T = \sqrt{\frac{2T}{m}} \tag{2.33}$$

$$\epsilon = \frac{r}{R_0} \tag{2.34}$$

In this low collisionality regime, the trapped electrons can complete a banana orbit, and the driving mechanism for CTEMs results from electron density or temperature gradients. The mode growth rate is estimated to be increasing with collisionality $\gamma \propto \sqrt{\nu_e}$ [119]. As the collisionality increases so that $\nu_{*e} \sim 1$, the trapped electrons cannot complete the banana orbits due to collisions with passing particles, and a dissipative TEM instability will arise. In this regime, the mode growth rate falls rapidly with increasing collisionality, so TEMs become unimportant for high density plasmas.

The diffusivity from the mixing length estimation with consideration of transition from dissipative TEMs to CTEMs [122] is:

$$\chi_e^{TEM} = \frac{5}{2\sqrt{2}} \frac{q\eta_e}{\epsilon_n \nu_{*e}} \left(\frac{m_e}{m_i}\right)^{1/2} \frac{\rho_s}{L_n} \frac{T_e}{eB} \frac{1}{1 + 0.1/\nu_{*e}} \tag{2.35}$$

Taking the typical Ohmic L-mode parameters in C-Mod at mid-radius $r/a \approx 0.6$: $\epsilon_n \approx 1/3$, $q \approx 1$, $\eta_e \approx 3$, $\left(\frac{m_e}{m_i}\right)^{1/2} \sim 1/40$, $T_e = 1$ keV, $B = 5.4$ T, the electron thermal diffusivity arising from TEMs will be

$$\chi_e^{TEM} \approx \frac{1.06}{\nu_{*e} + 0.1} \text{ m}^2/\text{s} \tag{2.36}$$

It is clear that χ_e^{TEM} will decay with ν_{*e} increasing, as shown in Fig. 2-1. For

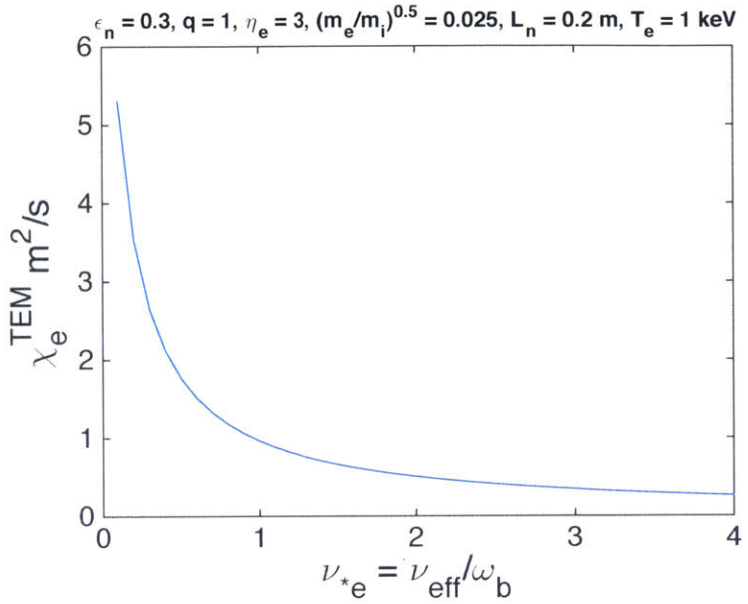

Figure 2-1: The electron thermal diffusivity χ_e^{TEM} as a function of normalized collisionality ν_{*e} calculated based on Eq. 2.36.

$\nu_{*e} \sim 0.3$ at transit between CTEMs and dissipative TEMs, the electron thermal diffusivity will be $\chi_e^{TEM} \approx 3$ m^2/s.

2.1.5 Electron Temperature Gradient Modes

The Electron Temperature Gradient (ETG) modes can be viewed as analogous to ITG modes except on the electron scale $k_\theta \rho_e \sim 1$. It is a drift-wave type instability driven by the electron temperature gradient or $\eta_e = L_n/L_{T_e} = |\nabla \ln T_e| \,/\, |\nabla \ln n|$. Because $\rho_e \sim \sqrt{m_e/m_i}\rho_s$, ETG modes with $k_\theta^{\mathrm{ETG}} \rho_s \gg 1$ are high-k (short wavelength) instabilities comparing to TEMs and ITG modes with $k_\theta^{\mathrm{ITG,TEMs}} \rho_s \sim 1$. Although ETG modes have larger linear growth rate than ITG modes, $\gamma^{ETG} \sim \sqrt{m_i/m_e}\gamma^{ITG}$, the mixing length diffusivity is estimated to be much smaller than ITG:

$$\frac{\chi^{\mathrm{ETG}}}{\chi^{\mathrm{ITG}}} \sim \frac{\gamma^{\mathrm{ETG}} / \left(k^{\mathrm{ETG}}\right)^2}{\gamma^{ITG} / \left(k^{\mathrm{ITG}}\right)^2} \sim \sqrt{\frac{m_e}{m_i}} \sim \frac{1}{60} \tag{2.37}$$

ETG modes were considered to have no effect on ion energy transport due to the high k feature, and little effect on electron energy transport based on the mixing length estimate. However it is shown that radial ETG streamers (radially elongated

turbulence vortices) exist which can produce significant transport [123]. Simulation with reduced mass ratio $\mu = \sqrt{m_i/m_e} = 20 - 30$ shows that ETG turbulence contributes to $\sim 15\%$ of electron energy transport but has little effect on ion energy transport in ITG-dominant Cyclone base case plasma [124]. Recently simulations using Alcator C-Mod parameters and real mass ratio $\mu = \sqrt{m_i/m_e} = 60$ show that ETG modes will increase the electron energy transport by 80% (through contributions from high-k ETG and interactions with low-k TEM/ITG), and increase ion energy transport by 30% (through interactions with low-k ITG) [97]. The role of ETG modes on transport is still not fully understood and it remains an active research topic.

2.2 Momentum Transport and Coriolis Pinch

Momentum transport is important for the reason that rotation plays important roles in turbulence suppression (responsible for the L–H transition [125, 126, 127, 128, 129] and internal transport barrier (ITB) formation [130, 131, 132, 133, 134, 135]) and resistive wall stabilization [39, 136]. It is estimated that an Alfvén Mach number of $M_A = V_\phi/V_A = 0.02$ is required to stabilize RWMs [137] for ITER scenarios, where $V_A = \sqrt{B^2/2\mu_0 n_i m_i}$ is the Alfvén velocity. That is translated into a toroidal rotation of 120 km/s at $B_0 = 5.4$ T and $n_e = 10^{20}$ m^{-3}. In experiments in most existing devices, neutral beam injection (NBI) is used as a momentum source to drive the plasma rotation. However for future reactor-grade fusion devices like ITER, it will probably be momentum source free due to the large dimension, high density and inefficiency of NBI. Plasma self-generated intrinsic rotation without external momentum input will be a major mechanism to provide necessary velocity. The understanding of intrinsic rotation and its radial transport is crucial for fusion research.

In Alcator C-Mod there is no heating neutral beam. Except for plasmas with lower hybrid flow drive (LHFD, [8, 138, 139, 140]) and ICRF mode conversion flow drive (MCFD, [44, 45, 46]), the rotation in all other plasmas is considered to be intrinsic rotation without external momentum input. The evolution of the rotation profile

measured by HiReX–Sr is a powerful tool to study the intrinsic rotation transport, more specifically, the momentum diffusivity χ_ϕ and pinch V_{pinch} in Eq. 2.5.

The momentum diffusivity is usually quantified by Prandtl number $P_r = \chi_\phi/\chi_i$, the ratio of momentum diffusivity and ion energy diffusivity. Theory and gyrokinetic simulation shows the Prandtl number is order of unity [141, 142, 143] in ITG dominated plasmas. The evidence of an inward momentum pinch $V_{\text{pinch}} < 0$ is shown in [5, 144, 41]. A gyro-fluid derivation of the momentum pinch due to the Coriolis effect was performed in ITG plasmas [145]. It predicts an inward momentum pinch

$$\frac{RV_{\text{pinch}}}{\chi_\phi} = -\frac{R}{L_n} - \frac{4}{\tau} \tag{2.38}$$

where $\tau = T_e/T_i$.

In Chapter 4, χ_ϕ and V_{pinch} will be determined in modulation experiments. These values are then compared with the ion energy diffusivity and Coriolis pinch. Appendix A discusses the derivation of the Coriolis pinch Eq. 2.38 in detail.

2.3 Impurity and ICRF Wave Interaction

Chapter 5 studies the ICRF-induced argon pumpout effect, which is probably related to wave-impurity interactions. This section will briefly introduce the mechanism for this interaction.

2.3.1 ICRF Wave Dispersion and Absorption

The dispersion relation of ICRF wave in plasma is:

$$n_\perp^2 = \frac{\left(n_\parallel^2 - R\right)\left(n_\parallel^2 - L\right)}{S - n_\parallel^2} \tag{2.39}$$

where $n_\perp$ and $n_\parallel$ are the wave perpendicular and parallel refractive indexes, respectively; R, L, S are functions of local plasma parameters (n_e, T_e, B) and ICRF wave frequency. Eq. 2.39 is called the ICRF equation. One can find the detailed

derivations and definitions in Appendix B.

The resonance ($n_\perp = \infty$) condition for ICRF wave is

$$n_\parallel^2 = S = 1 - \sum_i \frac{\omega_{pi}^2}{\omega^2 - \Omega_i^2} \tag{2.40}$$

where RF field is enhanced at the resonance location. If the cyclotron layer ($\Omega_i = \omega_{\mathrm{RF}}$) of an ion species overlaps with this resonance layer, the ions could absorb energy from waves through cyclotron resonance damping.

For two-ion species plasmas (for example deuterium majority with hydrogen minority), with a small minority of fraction ($n_H/n_D \sim$ 1s%), the minority cyclotron resonance ($\omega = \Omega_m$) layer is close to the hybrid resonance $\left(n_\parallel^2 = S\right)$ layer. The ICRF waves are absorbed by minority ions through minority cyclotron damping, which is called **minority heating**. The distance between the minority cyclotron resonance layer and the hybrid resonance layer becomes larger as the minority fraction increases ($n_H/n_D > 10\%$), in this regime the waves are mode-converted into ion Bernstein waves (IBW) and absorbed by electrons through Landau damping. This is called the **mode conversion** regime. Meanwhile if the resonance layer of impurity is close to the ion-ion hybrid layer, it is possible that impurity ions absorb power and get energetic. This is what we observed in Alcator C-Mod, which will be discussed in details in Chapter 5. This section generalizes the derivation of overlap between impurity resonance layer and ion-ion hybrid layer.

2.3.2 Impurity Resonance

Ion Cyclotron Resonance Layer

The location of the nth harmonic resonance layer of an impurity with mass number A and charge state Z^+ is

$$R_{resonant} = n\frac{Z}{A}\frac{eB_0}{m_p\omega_{RF}}R_0 \tag{2.41}$$

Hybrid Layer of A-B plasma

Assume the plasma has minority ${}^{A_1}_{Z_1}\mathrm{A}$ and majority ${}^{A_2}_{Z_2}\mathrm{B}$, the ion-ion hybrid resonance (mode conversion) condition $n_\parallel^2 = S$ is

$$n_\parallel^2 = 1 - \frac{\omega_{pA}^2}{\omega_{RF}^2 - \omega_A^2} - \frac{\omega_{pB}^2}{\omega_{RF}^2 - \omega_B^2} \tag{2.42}$$

with notations

$$\begin{aligned}
\gamma &\equiv n_A/n_B \\
n_A &= \frac{\gamma}{\gamma Z_1 + Z_2} n_e \\
n_B &= \frac{1}{\gamma Z_1 + Z_2} n_e \\
\omega_p^2 &\equiv \frac{4\pi n_e e^2}{m_H} \\
\omega_{pA}^2 &= \frac{4\pi n_A Z_1^2 e^2}{m_A} = \frac{Z_1^2}{A_1}\frac{\gamma}{\gamma Z_1 + Z_2}\omega_p^2 \\
\omega_{pB}^2 &= \frac{4\pi n_B Z_2^2 e^2}{m_B} = \frac{Z_2^2}{A_2}\frac{1}{\gamma Z_1 + Z_2}\omega_p^2 \\
\omega_H &\equiv \frac{eB}{m_p} = \frac{eB_0}{m_p}\frac{R_0}{R} \\
\omega_A &= \frac{Z_1 eB}{m_A} = \frac{Z_1}{A_1}\omega_H \\
\omega_B &= \frac{Z_2 eB}{m_B} = \frac{Z_2}{A_2}\omega_H
\end{aligned}$$

In Alcator C-Mod, the typical value of $n_\parallel$ is between 4 and 10, and $\omega_p/2\pi \sim$ GHz, $\omega_{RF}/2\pi \sim \omega_H/2\pi \sim$ 10s MHz. It is safe to approximate

$$1 \sim n_\parallel^2 \ll \frac{\omega_{pA}^2}{\omega_{RF}^2 - \omega_A^2} \sim \frac{\omega_{pB}^2}{\omega_{RF}^2 - \omega_B^2} \tag{2.43}$$

From Eq. 2.42, we have

$$\frac{\omega_{RF}}{\omega_H} = \sqrt{\frac{(\gamma A_1 + A_2)\frac{Z_1^2 Z_2^2}{A_1^2 A_2^2}}{\gamma\frac{Z_1^2}{A_1} + \frac{Z_2^2}{A_2}}} \tag{2.44}$$

The mode conversion layer will be

$$R_{MC} = \frac{eB_0}{m_p \omega_{RF}} \sqrt{\frac{(\gamma A_1 + A_2)\frac{Z_1^2 Z_2^2}{A_1^2 A_2^2}}{\gamma \frac{Z_1^2}{A_1} + \frac{Z_2^2}{A_2}}} R_0 = R_1 \sqrt{\frac{1 + \gamma \frac{A_1}{A_2}}{1 + \gamma \frac{Z_1^2}{Z_2^2}\frac{A_2}{A_1}}} \tag{2.45}$$

where R_1 is the major radius of cyclotron resonance for the first species ${}^{A_1}_{Z_1}\mathrm{A}$:

$$R_1 = \frac{Z_1}{A_1} \frac{eB_0}{m_p \omega_{RF}} R_0 \tag{2.46}$$

$R_{resonant} = R_{MC}$ gives

$$\gamma = \frac{Z_2^2 A_1}{Z_1^2 A_2} \frac{\left(\frac{Z_1}{A_1}\right)^2 - \left(\frac{nZ}{A}\right)^2}{\left(\frac{nZ}{A}\right)^2 - \left(\frac{Z_2}{A_2}\right)^2} \tag{2.47}$$

A positive finite γ requires

$$\min\left(\frac{Z_1}{A_1}, \frac{Z_2}{A_2}\right) < n\frac{Z}{A} < \max\left(\frac{Z_1}{A_1}, \frac{Z_2}{A_2}\right) \tag{2.48}$$

If Eq. 2.47 is satisfied for a specified impurity charge state, the ion-ion hybrid layer overlaps with the impurity n^{th} harmonic resonance layer, then the impurities can gain energy through cyclotron resonance absorption. It is possible that impurities gain sufficient energy that they become too energetic to be confined. This could be the responsible mechanism for the argon pumpout effect discussed in Chaper 5.

H–D Plasma with Argon Impurity

For hydrogen minority and deuterium majority plasmas,

$$Z_1 = Z_2 = 1$$

$$A_1 = 2$$

$$A_2 = 1$$

$$\frac{1}{2} < n\frac{Z}{A} < 1$$

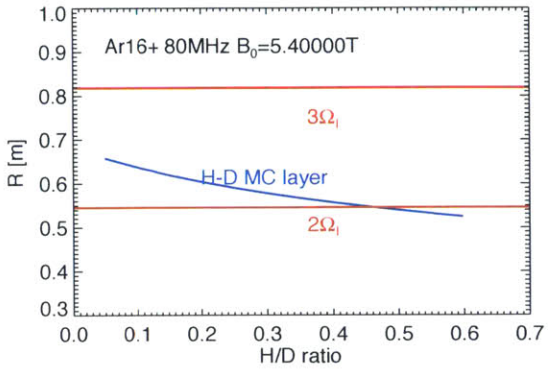

Figure 2-2: The location of H–D mode conversion layer and Ar^{16+} resonance layer as a function of n_H/n_D at 5.4 T in Alcator C-Mod.

If we take $Z = 16, A \approx 40$ as Ar^{16+} is the dominate charge state for C-Mod parameters, we can find the Ar^{16+} 2^{nd} harmonic ($n = 2$) satisfies the requirement Eq. 2.48. The corresponding H–D ratio γ is

$$\gamma = \frac{Z_2^2 A_1}{Z_1^2 A_2} \frac{\left(\frac{Z_1}{A_1}\right)^2 - \left(\frac{nZ}{A}\right)^2}{\left(\frac{nZ}{A}\right)^2 - \left(\frac{Z_2}{A_2}\right)^2} \approx 46\% \tag{2.49}$$

It is worth noting that this ratio is independent of the magnetic field and ICRF frequency. The magnetic field and ICRF frequency only determines where the layers is located in the plasma. Fig.2-2 shows the overlap of Ar^{16+} 2^{nd} harmonic resonance layer and H–D mode conversion layer at H–D ratio of 46%, with $B_0 = 5.4$ T and $f = 80$ MHz.

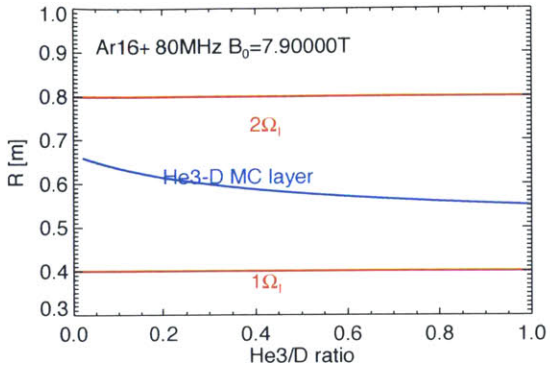

Figure 2-3: The location of ^{3}He–D mode conversion layer and Ar^{16+} resonance layer as a function of n_{He3}/n_D at 7.9 T in Alcator C-Mod.

^{3}He–D Plasma with Argon Impurity

For ^{3}He minority and deuterium majority plasmas,

$$Z_1 = 2$$

$$Z_2 = 1$$

$$A_1 = 3$$

$$A_2 = 2$$

$$\frac{1}{2} < n\frac{Z}{A} < \frac{2}{3}$$

This requirement narrows the available argon charge states. Fig.2-3 shows there is no overlap between the Ar^{16+} 2^{nd} harmonic resonance layer and the ^{3}He–D mode conversion layer.

For other argon charge states, there is no overlap for the fundamental resonance. For the 2^{nd} harmonic resonance, it requires $10 < Z \leq 13$. Take $Z = 13$, we get $\gamma \approx 5\%$, and $R_{\text{res}} \approx R_0$. But few of argon charge states with $Z \leq 13$ exist in the core plasma, as shown in Fig.1-10.

2.4 Numerical Codes

Numerous simulation codes are developed to study the plasma transport properties. This section briefly introduces the codes used in this thesis: STRAHL, TRANSP and GYRO.

2.4.1 STRAHL

STRAHL [146, 147] is a 1-D impurity transport code used to calculate the radial transport and emissions of impurities in the plasma. It solves the radial continuity equation for each ionization stage of the impurity. The background plasma parameters (T_e, n_e) are provided by experimental measurements. An *ansatz* of impurity anomalous diffusivity and convectivity as shown in Eq. 2.4 is specified by user. The neoclassical calculation of diffusion and convection coefficients can also be switched on. STRAHL was developed by IPP-Garching and distributed to Alcator C-Mod with the help of Dr. Ralph Dux and Dr. Thomas Pütterich. It is used for the dedicated analysis of calcium impurity transport in the CaF_2 laser-blowoff experiments [148]. A generic version of STRAHL in C-Mod is implemented by Dr. Matt Reinke for the use on general impurities.

In the predictive mode, the diffusion and convection coefficient profiles are provided as well as electron temperature and density profiles and impurity source. STRAHL calculates each charge state's density profile and the emissivity profiles of emission lines of interest.

A robust method to compare experimental measurements in C-Mod with STRAHL simulation was developed [148]. The diffusion and convection profiles are obtained by running the STRAHL simulation iteratively and minimizing the χ^2 error between the simulated and measured results.

2.4.2 TRANSP

TRANSP is a transport analysis code developed and maintained by PPPL (w3.pppl.gov/transp) [149, 150]. It was facilitated in Alcator C-Mod by Dr.

Schachter [151]. The main purpose of TRANSP is to calculate the local thermal transport coefficients χ_i and χ_e as functions of time and space, given measured profiles and equilibrium. TRANSP assumes the purely diffusive heat flux $q = -n\chi\partial_r T$. The diffusivity $\chi(r,t)$ is calculated using the power balance equation

$$\nabla \cdot \mathbf{q}_j = -\frac{3}{2} n_j \frac{\partial T_j}{\partial t} + Q_j - \mathbf{P}_j : \nabla \mathbf{u}_j + S_E \tag{2.50}$$

and

$$\chi_j(r) = -\frac{\int_0^r dV \nabla \cdot \mathbf{q}_j}{A_{\text{surf}}\, n_j \partial_r T_j} = -\frac{P_{\text{cond},j}}{A_{\text{surf}}\, n_j \partial_r T_j} \tag{2.51}$$

The conducted power P_{cond} is calculated using input profiles, equilibria and some other models. A detailed discussion on the models and calculations of conducted power can be found in [151, Chapter 3].

In Alcator C-Mod, TRANSP is also used to provide input files for GYRO. The main purpose of this intermediate step is to get the radial electric field E_r using the NCLASS module in TRANSP. With the impurity argon toroidal rotation profile $V_\phi(r)$ measured by HiReX–Sr and the neoclassical poloidal rotation profile $V_\theta(r)$ calculated by NCLASS, the E_r profile can be calculated based on force balance

$$E_r = -V_\theta B_\phi + V_\phi B_\theta + \frac{1}{e_\alpha n_\alpha}\frac{\partial p_\alpha}{\partial r} \tag{2.52}$$

where α corresponds to each ion species. The TRANSP simulations in this thesis are run on the PPPL Unix cluster.

2.4.3 GYRO

STRAHL and TRANSP calculate the experimental transport coefficients without considering much about the physical origin of the coefficients. To better understand the plasma transport which is dominated by turbulence, a first principles gyrokinetic analysis is required. It is extremely difficult to get an analytical solution of the Fokker-Planck equation. For this reason numerous gyrokinetic simulation codes have been developed. In this thesis, GYRO is used to study the linear plasma instabilities

of interest in Chapter 3.

GYRO [152, 153] is a δf initial value solver that calculates the fluctuating distribution function δf away from equilibrium (Maxwellian distribution). It can be run with flux-tube boundary conditions (local simulation) or physical boundary conditions (global simulation). In GYRO, the fluctuating quantities are represented by toroidal mode number n by (taking the electrostatic potential as a example)

$$\delta\Phi\left(r,\theta,\phi,t\right)=\sum_{j=-N+1}^{N-1}\delta\Phi_{n}\left(r,\theta,t\right)e^{-in\alpha}e^{-in\omega_{o}t} \tag{2.53}$$

where θ is the poloidal angle, $n = j\Delta n$ is the toroidal mode number, Δn is the user-defined mode spacing, N sets the range of modes considered in the simulation, $\alpha = \phi - q\left(r\right)\theta$ is the Clebsch angle, $\omega_0 = E_r/RB_p$ is the toroidal angular velocity.

For linear simulations, GYRO computes the mode real frequency $\omega_{r,n}$ and growth rate γ_n by assuming

$$\delta\Phi_{n}\left(r,\theta,t\right)=\delta\Phi_{n}\left(r,\theta\right)e^{-i\omega_{r,n}t+\gamma_{n}t} \tag{2.54}$$

The sign of $\omega_{r,n}$ determines the mode (instability) propagation direction. The convention in the thesis is positive $\omega_{r,n}$ means the mode propagates in the electron diamagnetic direction, negative $\omega_{r,n}$ means in the ion diamagnetic direction. The mode is stable when $\gamma_n < 0$; if $\gamma_n > 0$, the mode grows exponentially and it is an unstable mode. The propagation direction of the most unstable mode implies the dominant instability for turbulent transport.

The real frequency and growth rate are typically plotted as a function of $k_\theta\rho_s$, where $k_\theta = \frac{nq}{r}$ is poloidal wavenumber, $\rho_s = c_s/\Omega_i = \sqrt{\frac{T_e}{m_i}}/\Omega_i$ is the ion gyro-radius at the ion sound velocity.

The mode will saturate eventually due to the nonlinear interactions between different modes. The fluxes and transport coefficients can be obtained by running nonlinear simulation in GYRO. These quantities can be compared with the experimental quantities calculated by the transport codes (TRANSP, STRAHL, etc.).

In this thesis, linear GYRO simulations are performed to study the characteristics of dominant turbulent instabilities. The simulations are run in MIT PSFC parallel AMD Opteron/Infiniband cluster Loki.

2.5 Summary

This section provides a brief theoretical background for the thesis. The drift-wave instability analysis is related to the study of several transit phenomena between LOC and SOC plasmas (LOC and SOC will be defined therein) in Chapter 3. The Coriolis momentum pinch will be used to compare with the momentum pinch term obtained in the rotation modulation experiment in Chapter 4. The impurity-wave interaction is proposed to be a possible mechanism for the argon pumpout effect, which is discussed is Chapter 5. As to the numerical codes, STRAHL is used in Chapter 5 to study the impurity transport. TRANSP is used in Chaper 3 and Chaper 4 to calculate the heat diffusivity; and is used in Chaper 3 to provide the input profiles for GYRO. Ion-scale linear GYRO simulation are performed in Chaper 3 to study the turbulence dominance.

Table 2.1: The topics and numerical code in each chaper

Chapter	Topic	Code
3	non-local heat transport	TRANSP, GYRO
4	momentum transport	TRANSP
5	argon pumpout	STRAHL

THIS PAGE INTENTIONALLY LEFT BLANK

Chapter 3

Non-local Heat Transport, Rotation Reversals and the LOC/SOC Transition in Ohmic L-mode Plasmas

For magnetically confined plasmas, it is still challenging to fully understand heat transport, which is important for predictions of the performance of burning plasma tokamaks like ITER. One of these challenges is the explanation of the non-local phenomenon: the breakdown of a local expression for the fluxes, i.e. the fluxes are not functions of local parameters. The most famous example of the non-local effect in electron heat transport is the inward propagation of edge cooling. The first experiment was carried out on TEXT about 20 years ago [154, 155, 9], in which carbon was injected into the edge plasma to induce a temperature perturbation. The edge temperature decreased rapidly as expected, but interestingly the core temperature promptly began to rise, and peaked within a few mili-seconds. This effect cannot be explained by the local transport model which assumes that transport coefficients are functions of local thermodynamic parameters. Similar effects have been observed in TFTR [156, 13], RTP [157, 14, 158], ASDEX Upgrade

[15], Tore Supra [16], JET [159], LHD [160, 161, 162, 163], JT-60U [164, 165, 163], HL-2A [166, 17], Alcator C-Mod [18, 167], etc.

This chapter focuses on the experimental study of non-local heat transport and its correlation with the LOC/SOC transition and rotation reversals in Alcator C-Mod [18, 167]. The chapter is arranged as follows: Section 3.1 introduces the three seemingly unrelated topics: (a) Ohmic confinement regime, (b) rotation reversals and (c) non-local heat transport. In Section 3.2, the experimental setup and major diagnostics are described. In Section 3.4, the experimental results will be presented. The discrepancy between propagation of cold pulses at low and high densities will be shown, as well as the changes in energy confinement and plasma rotation. The data processing methods, FFT and GSVD, will be discussed in Section 3.3. The Fourier transform of electron temperature in repetitive cold pulse experiments will give more insight into the cold pulse propagation and the non-local effect. In Section 3.5, we give a descriptive explanation of the non-local effect in low density L-mode plasmas in Alcator C-Mod. A sudden drop of core electron heat diffusivity can reproduce the experimental observation; the sudden appearance of a heat pinch models the results equally well. This cold pulse induced a transient ITB-like state which is augmented by core fluctuation measurements. In Section 3.6, the results of linear gyrokinetic simulations of low and high density plasmas are presented. We see an obvious difference in the turbulence characteristics, which can be described as TEM dominant at low density and ITG mode dominant at high density. Conclusions and a discussion are presented in Section 3.7.

3.1 Non-local Heat Transport, the LOC/SOC Transition and Rotation Reversals

This section will introduce the transport phenomena related to the research in this chapter. These topics are non-local transport, the LOC/SOC transition and intrinsic toroidal rotation reversals.

3.1.1 Non-local Heat Transport

Definition of "non-locality"

There has been vagueness in the definition of "non-locality". In this thesis, "non-locality" is defined as the breakdown of the local transport relation (the radial flux is a function of local plasma parameters and their gradients at the same position). Following this definition, the transport can be generally classified into 4 categories [163]: (a) local and diffusive, (b) local and non-diffusive, (c) non-local and diffusive, (d) non-local and non-diffusive. Particle and momentum transport is typically non-diffusive due to the existence of a pinch term. A purely diffusive relation (Fick's law) is generally adopted to model the heat transport, but there is evidence of inward electron heat flow with off-axis electron cyclotron heating in DIII-D tokamaks [92, 93].

Breakdown of Local Transport Model

The transport theories in Section 2.1 follow the local transport paradigm, i.e. the fluxes (particle, momentum and heat) can be accurately described by local plasma parameters and a set of local transport coefficients (diffusivities and conductivties). This paradigm formulates the fluxes in forms of a generalized Fick's law such as Eqs. 2.4, 2.5 and 2.6. A more general description of local transport considers the cross-field interaction and transport matrix [168] (for example, momentum flux driven by temperature gradient). A widely accepted basis of local transport is that successive transport events are either independent or weakly correlated so that transport events should be random and can be accurately described by a Markov process. Large scale, avalanche-like and temporally intermittent transport due to the acumulation of small transport events is forbidden by the belief that turbulence regulating $E \times B$ sheared flow will efficiently suppress the large-scale eddies and self-organized transport events. As a result, a local and diffusive transport paradigm is preferred in the heat transport channel.

A number of experiments indicates the breakdown of this local flux-gradient

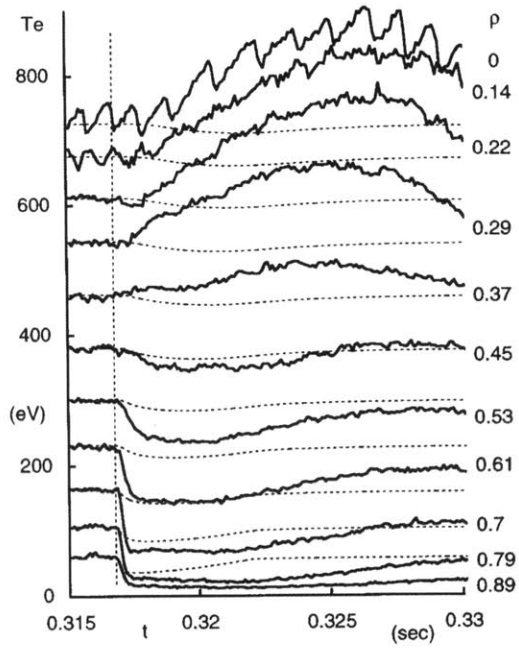

Figure 3-1: Time traces of electron temperature at various minor radii following impurity injection. The solid lines are measured electron temperature. The dashed lines illustrate the failure of a local model to simulate the electron temperature. Figure is from [9].

relation in heat transport. Analysis of sawtooth heat pulse propagation shows a ballistic response in the TFTR and DIII-D tokamaks [169, 170], which contradicts the purely diffusive picture of heat transport. Simulations of L-H transitions in the JET tokamak show a global reduction of diffusivity in a large region of the plasma [171]. The most striking evidence of the existence of non-local heat transport is the cold pulse experiment in TEXT tokamak [154, 155, 9]. In this experiment, small injection of carbon pellets into the edge plasma induces temperature perturbations throughout the plasma. Large, rapid temperature decreases are observed in the edge plasma, while the temperature in the core promptly begins to rise, as is shown in Fig. 3-1.

The cold pulse experiment challenges the local heat transport model in two aspects: First the core temperature increase in response to the edge cooling, or "polarity inversion", cannot be expected by a local model. An immediate drop of the core diffusivity or an inward heat pinch in the core plasma following the cold

pulse is required to reproduce this non-local response. The other issue with the local model revealed in the cold pulse experiment is that the core response is faster than the cold pulse propagation process predicted by the local diffusive model [18, 167]. The non-local phenomena are observed in TFTR [156, 13], RTP [157, 14, 158], ASDEX Upgrade [15], Tore Supra [16], JET [159], LHD [160, 161, 162, 163], JT-60U [164, 165, 163], HL-2A [166, 17], and Alcator C-Mod [18, 167]. A popular and succesful method to model the effect is to use an *ad hoc* transient diffusivity model: the core diffusivity decreases simultaneously with the edge cooling. In other word, the cold pulse cools the edge and at the same time a transport barrier forms in the remote core.

Several theories are proposed on the study of non-local phenomena, of which three will be briefly discussed:

1. Self-Organized Criticality and Avalanches: In nature many systems are self-similar in spatial and temporal scales. Examples of self-similarity include the ubiquitous $1/f$ noise (background fluctuation) in dynamic systems and the fractal structures in spatially extended objects. The self-organized criticality is a physical explanation for the similarity phenomena in totally different systems [172, 173]. This self-organized criticality theory argues that dynamic systems with extended spatial structure will naturally evolve into a self-organized critical state which is marginally steady. The running sandpile is a commonly used prototypical realization of self-organized criticality [173]. In the sandpile model, transport of sand only happens when the local sand gradient exceeds a critical gradient. The sandpile will eventually build up to a "least stable" state that everywhere is at this critical gradient. Any additional sand will fall site to site and exit the system. This model exhibits the behavior that a small local perturbation can be communicated throughout the whole system and cause an avalanche. The avalanche is an analogy of a transport event in dynamic systems. The avalanche power spectrum is shown to be $1/f$, which means larger transport events happen more infrequently and smaller events happen more often. The frequency and wavenumber of the avalanches is

related through a "critical exponent" z, where $\omega = ck^z$ [174]. This exponent characterizes the pulse response of the dynamic system: $z = 2$ indicates a diffusive response, $z < 2$ is a "super-diffusive" response, and $z = 1$ suggests a ballistic response. A plasma transport model based on subcritical resistive pressure-gradient-driven turbulence [175] shows that a heat pulse propagates from the center to the edge diffusively ($\Delta x^2/\Delta t \sim$ constant), whereas the cold pulse propagates from the edge to the core ballistically ($\Delta x/\Delta t \sim$ constant). What is more, with the inclusion of flow shear, the cold pulse propagation cuts off at some radius where a transport barrier is formed, associated with confinement improvement in the core.

2. Turbulence Spreading: Another model attempt to explain the super-diffusive or ballistic propagation of mean field (density or temperature) fronts concerns turbulence spreading [176, 177, 178]. Turbulence spreading means the spatio-temporal propagation of a turbulence from a region where it is locally excited to a region of weaker excitation or even damping. The turbulence spreading model couples the mean field transport equation to the evolution equation of underlying turbulence intensity. Mathematically, an example of such model is [178, 163]

$$\partial_t T = D_0 \partial_{xx} (IT) \tag{3.1}$$

$$\partial_t I = \gamma_L \mathcal{H} (\partial_x T - \kappa_c) I - \gamma_{NL} I^2 + D_1 \partial_x (I \partial_x I) \tag{3.2}$$

where T is the temperature, I is the turbulence intensity, D_0 is the effective turbulent diffusivity and the collisional diffusivity $D_c \partial_{xx} T$ is ignored. γ_L is the linear growth rate with a critical gradient κ_c defined by the Heaviside function $\mathcal{H}$, γ_{NL} represents the non-linear damping rate (arising from cascades), and D_1 characterizes the turbulence spreading (or turbulence scattering). This spatial turbulence spreading is linked to large-scale transport. An example of turbulence spreading is that the SOL turbulence can penertrate into the transport barrier in H-mode and govern the trasport barrier fluctuations [179].

The model of Eqs. 3.1 and 3.2 is basically a local model because all the coefficients are functions of local parameters and solution of the system can represent ballistic response due to the high nonlinearity. This nonlinear coupling is shown to bifurcate: the response to perturbations is diffusive when the temperature gradient is well above the stability threshold, and ballistic when the gradient is close to the threshold [178]. Because the dominant turbulence in a region is not necessarily excited locally, turbulence spreading into a stable region can give rise to up-gradient transport, a "pinch flux" of heat and particles [180, 181]. In principle the "polarity inversion" observed in cold pulse experiments can be incorporated into the turbulence spreading theory.

3. Meso-scale and Macro-scale Fluctuations: Mesoscale refers to the scales larger than a mode or integral scale eddy size but smaller than the system size or profile scale length. There are some fluctuations with meso-scale or macro-scale correlation length such as zonal flows [182, 183], geodesic acousic mode (GAMs) [184] and streamers [185, 186, 187]. The local flux-gradient relation can be violated by these fluctuations. It should be made clear that meso-scale phenomena are not necessary to arise from meso-scale or macro-scale fluctuations. Micro-scale fluctuations can also induce meso-scale transport like avalanche and turbulence spreading.

As a consequence of "non-local" mechanisms mentioned above, an integral form of the diffusive flux-gradient relation is proposed based on continuous time random walks (CTRWs)[188, 189]:

$$q(r) = -\int \mathcal{K}_r(r, r') \nabla T(r') \, dr' \tag{3.3}$$

where $\mathcal{K}_r$ is a generalized diffusivity kernel whose form is assumed to be a Levy distribution in [188] or a Lorentz distribution in [189]. It is worth noting that a strongly localized kernel will lead to a local flux-gradient relation.

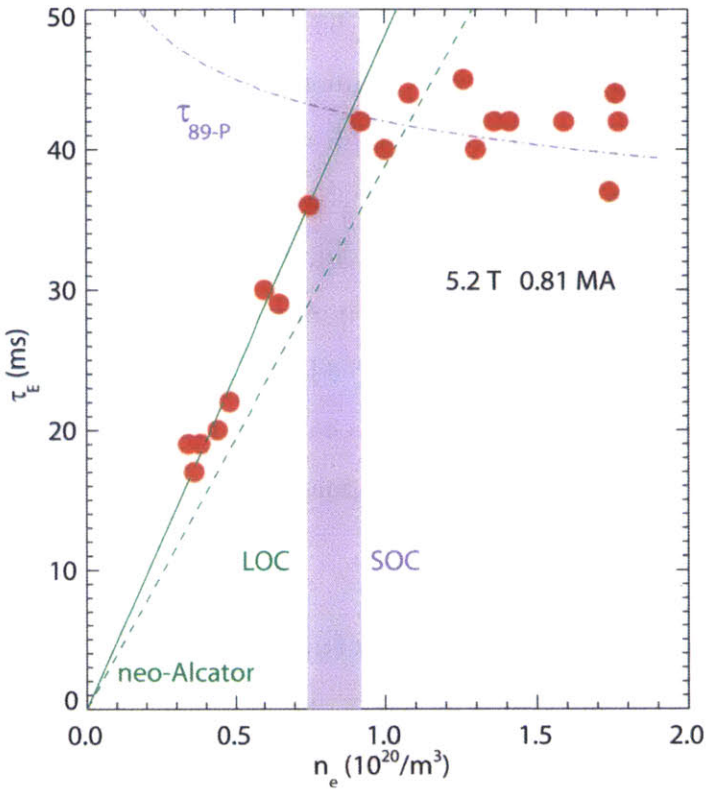

Figure 3-2: The energy confinement time τ_E as a function of averaged electron density for 5.4 T, 0.81 MA Ohmic discharges in Alcator C-Mod. The dashed line is the neo-Alcator scaling. The dash-dot line is the ITER-89p L-mode scaling. Figure is from [10].

3.1.2 Ohmic Confinement Regime and LOC/SOC Transition

The global energy confinement time τ_E in Ohmic plasmas has been a hot topic for decades. In Alcator A (1972 - 1978) experiments, τ_E increased linearly with the averaged electron density. The so-called neo-Alcator scaling is found to be $\tau_E \propto \overline{n}_e R^2 a$; while in Alcator C (1978-1987), the energy confinement time was observed to saturate at higher density [35]. This transition from the linear Ohmic confinement (LOC) regime at low density to the saturated Ohmic confinement (SOC) regime is also observed in other fusion devices [190, 191, 192, 193, 194, 195, 196].

Fig. 3-2 shows the energy confinement time τ_E as a function of averaged electron density for 5.4 T, 0.81 MA Ohmic discharges in Alcator C-Mod. In the LOC regime, the confinement time linearly increases with density, and is slightly higher than then neo-Alcator scaling prediction[197]

$$\tau_E^{\text{neo-Alcator}}\,[\text{ms}] = 70\overline{n}_{e,20}q\sqrt{\kappa}aR^2 \tag{3.4}$$

where $\overline{n}_{e,20}$ is the line averaged electron density in 10^{20}m^{-3}, q is the safety factor, κ is the elongation, a, R are minor and major radius in m.

In the SOC regime, the confinement time saturates with values close to the ITER89-p L-mode scaling [47]

$$\tau_E^{\text{ITER89-p}}\,[\text{ms}] = 48I_{\text{MA}}^{0.85}R^{1.2}a^{0.3}\kappa^{0.5}B_{\text{T}}^{0.2}A^{0.5}\overline{n}_{e,20}^{0.1}P_{\text{MW}}^{-0.5} \tag{3.5}$$

where I is the plasma current in MA, B_T is the magnetic field in tesla, A is the main ion mass number, and P_{MW} is the input power in MW.

The origin of the LOC/SOC transition is still an open question. One common hypothesis is that in the LOC regime, electron turbulence such as collisionless trapped electron modes (CTEMs) and electron temperature gradient (ETG) modes are the dominant instability that regulates the confinement; in the SOC regime with higher density, the trapped electrons are de-trapped due to collisions and ion temperature gradients tend to increas. The dominate instability then transits to the ion temperature gradient (ITG) mode. Several experiments were performed to investigate this assumption. In Alcator C, density fluctuations measured by CO_2 laser scattering showed that the group propagating velocity v_θ of fluctuations changed from the electron diamagnetic drift direction at low density to the ion diamagnetic drift direction at high density [198]. For Ohmic discharges in the TEXT tokamak, a distinct ion mode is observed at plasma densities at which there is a clear saturation in the global energy confinement time [199]. In DIII-D, a low-frequency turbulence feature is observed in the SOC regime, which is absent in the LOC regime. The turbulence has ITG characteristics and the onset of the turbulence is coincident with the onset of confinement saturation [196]. In ASDEX Upgrade, a clear ITG to TEM transition in the core $\rho_{\text{pol}} \leq 0.85$ turbulence has been observed when the collisionality decreases [200]. Analysis of reflectometry fluctuations in Tore Supra, TEXTOR and JET tokamaks shows that TEM

instabilities are responsible for Quasi-Coherent (QC) fluctuations which appear in LOC plasmas and disappear in SOC plasmas [201]. In Alcator C-Mod, PCI measurements showed that the intensity of density fluctuations propagating in the ion diamagnetic direction increases with density [202].

Ion scale ($k_\theta \rho_s \leq 1.0$) nonlinear GYRO simulations show that the simulated ion heat flux Q_i agrees with experiments within measurement uncertainty in both LOC and SOC plasmas; but the electron heat flux Q_e is always under-predicted [203]. The discrepancy between simulated and experimental Q_e tends to decrease with the transition from the LOC plasma to the SOC plasma. This "transport shortfall", where the heat flux is under-predicted by gyrokinetic codes, is observed in both the ion and electron channels in DIII-D plasmas [204, 205, 206, 207]. In C-Mod the shortfall is not seen, but ion-scale gyrokinetic simulation shows an under-predicted electron heat flux in Ohmic plasma [208]. Recent multi-scale ($k_\theta \rho_e$ up to 0.8) nonlinear GYRO simulations [97, 98] show that electron scale turbulence (ETG) has a significant contribution to the heat flux in marginal ITG stable plasmas. The inclusion of ETG modes can drive experimental levels of electron heat transport with an increase of 79%. The ion heat flux also increases by 31% due to the enhancement in low-k turbulence in these simulations, which sits at experimental levels within measurement uncertainty. With the increase of a/L_{T_i}, the ETG contribution tends to be less important and heat fluxes of multi-scale simulation converge to those of ion-scale simulations [209]. The original picture that LOC plasmas are CTEM-dominant and SOC plasmas are ITG-dominant is extended by these multi-scale simulations, which may suggest that a change from electron turbulence (ETG and TEMs) dominance to ion turbulence (ITG) dominance is responsible for the LOC-SOC transition.

3.1.3 Rotation Reversals in L-mode Plasmas

The core rotation in high confinement mode (H-mode) plasmas typically is in the co-current direction and scales with the plasma stored energy [65] or edge temperature gradients [210]. Unlikely, in Ohmic low confinement mode (L-mode) plasmas, the behavior of toroidal intrinsic rotation is more complicated. The

parametric dependence of rotation in this regime extends to electron density, plasma current, magnetic field and plasma shape. A special and hot topic of toroidal intrinsic rotation in Ohmic L-mode plasmas is the rotation reversal phenomenon, which is defined as an abrupt change in the rotation direction with small changes in other plasma parameters.

In Ohmic discharges, the direction of intrinsic toroidal rotation is observed to reverse abruptly with the change of electron density in multiple machines. In TCV limiter configuration plasmas [211, 212], the carbon toroidal rotation measured by charge exchange recombination spectroscopy (CXRS) is observed to reverse spontaneously from the counter-current to the co-current direction when the electron density exceeds a well-defined threshold. In the TCV diverter configuration [213, 214], the toroidal rotation is in the co-current direction at low density and reverses to counter-current direction when the density exceeds the threshold. In Alcator C-Mod L-mode discharges [215], there is an inversion of the rotation velocity from co-current to the counter-current as the electron density crosses a critical value, similar to the TCV result in the diverter configuration; changes in the plasma current or the magnetic field also lead to rotation reversals. In ASDEX Upgrade [216], at low density the toroidal rotation is in the co-current direction; at higher density the rotation has a hollow, counter-current profile; as the density increases further, a second reversal happens resulting in a co-current rotation profile. In C-Mod, the double reversal is not observed. In this chapter, by default we refer to rotation reversal as the change in the rotation direction from co-current at low density to counter-current at high density. Fig. 3-3 shows the sensitivity of toroidal rotation to the electron density in Alcator C-Mod. This discharge has two reversals (not the double reversal mentioned in [216]): first from counter- to co-current with a slight density decrease at 0.666 s; second from co- to counter-current with a slight density increase at 1.146 s. Fig. 3-4 shows that at the same current and magnetic field, the reversal density is almost identical regardless of how the density is ramping up.

In C-Mod, it is found that the critical density for rotation reversal has a strong

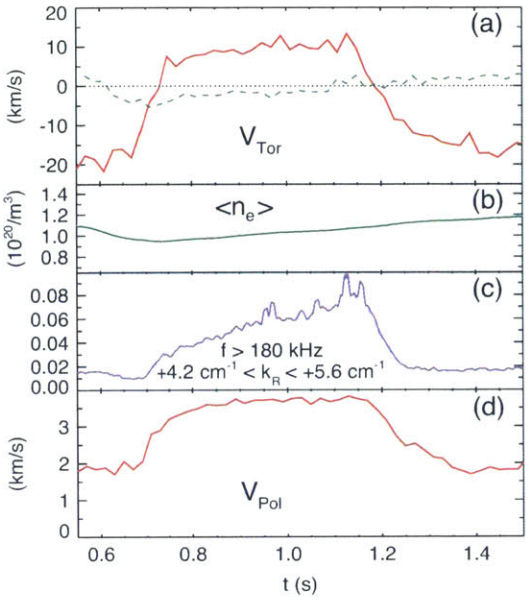

Figure 3-3: Time histories of (a) the toroidal rotation velocity in the center (solid line) and outside of $r/a = 0.75$ (dashed line), (b) average electron density, (c) density fluctuation intensity with k_R between 4.2 and 5.6 cm^{-1} and frequency above 180 kHz and (d) the poloidal propagation velocity of the turbulence for a 1.1 MA, 5.4 T ($q_{95} = 3.2$) discharge which underwent two rotation reversals. Figure is from [11].

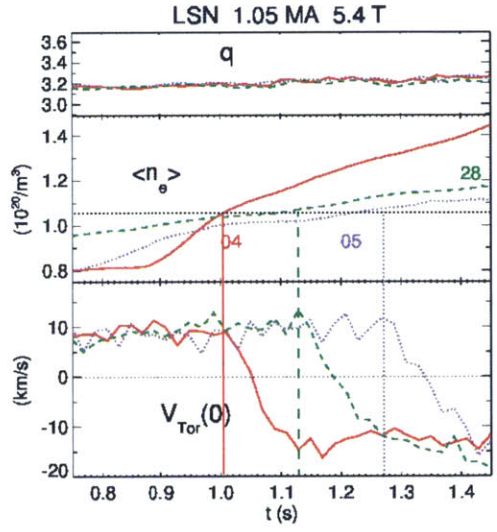

Figure 3-4: Time histories of the average electron density (top) and central toroidal rotation velocity (bottom) for LSN 1.05 MA 5.4 T ($q_{95} = 3.2$) discharges with different density ramps. The dotted horizontal line in the top frame represents an average density of 1.07×10^{20}m^3. Vertical lines indicate the initiation times of the three reversals. Figure is from [12].

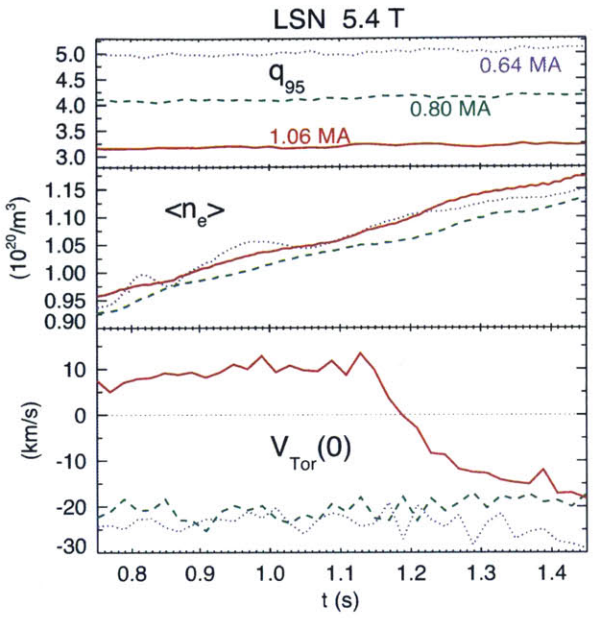

Figure 3-5: Time histories of q_{95} (top frame), average electron density (middle frame) and central toroidal rotation velocity (bottom frame) for 5.4 T LSN discharges with plasma currents of 0.64 MA (dotted), 0.80 MA (dashed) and 1.06 MA (solid). Figure is from [12].

dependence on plasma current and magnetic field. In the three discharges with the same magnetic field and density ramp but different currents, as is shown in Fig. 3-5, rotation reversals only happen for 1.06 MA discharge. The low current discharges don't experience the reversal. The best fit of the reversal critical density in C-Mod is $n_{e,\mathrm{crit}} q_{95} = 3.7$ [140], where $n_{e,\mathrm{crit}}$ is in 10^{20} m^{-3} and q_{95} is the safety factor at the 95% normalized poloidal flux surface ($\psi/\psi_a = 0.95$). This suggests the critical density scales with plasma current at fixed toroidal magnetic field: $n_{e,\mathrm{crit}} \propto I_p/B_t$, as is illustrated in Fig. 3-6.

The reversal critical density is reminiscent of the transition density from LOC to SOC as is mentioned in the previous section. It is actually observed [12, 11, 10, 18, 167] that in C-Mod these two phenomena are closely related. The rotation reversal occurs at a critical density, which coincides with the density separating the LOC and SOC regimes. Fig. 3-7 shows this correlation at two plasma currents: 0.62 MA and 1.0 MA. The critical density is higher for higher current. A unifying parameter, $\nu_* = \nu_{\mathrm{eff}}/\omega_{\mathrm{b}}$, is proposed that governs these two phenomena, where

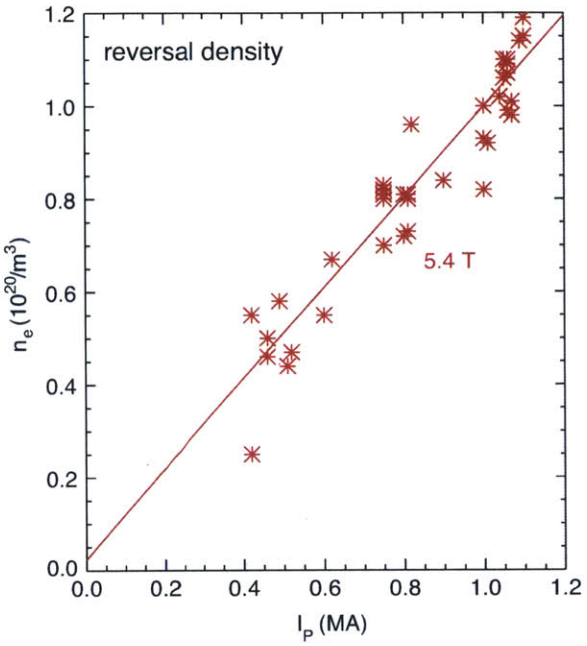

Figure 3-6: The density at the rotation reversal initiation time as a function of plasma current for 5.4 T discharges. Figure is from [11].

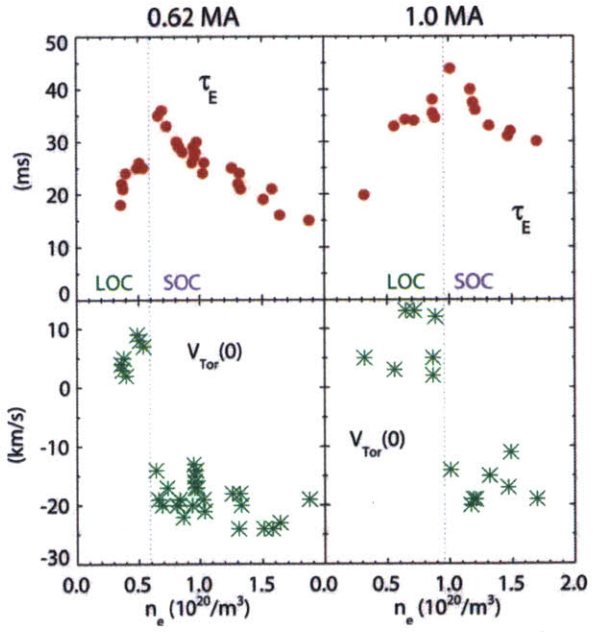

Figure 3-7: The energy confinement times from magnetics (top) and the core toroidal rotation velocities (bottom) as a function of line averaged electron density for 5.2 T discharges with plasma currents of 0.62 MA (left) and 1.0 MA (right). The vertical dashed lines indicate the locations of the co- to counter-current rotation boundaries. Figure is from [10].

$$\nu_{\text{eff}} = \frac{\nu}{\epsilon} \tag{3.6}$$

$$\epsilon = \frac{a}{R} \tag{3.7}$$

$$\omega_b = \frac{\sqrt{\epsilon} v_T}{qR} \tag{3.8}$$

$$\hat{\omega}_T = \frac{v_T}{qR} \tag{3.9}$$

$$\nu_* = \frac{\nu_{\text{eff}}}{\omega_b} = \frac{\nu}{\hat{\omega}_T \epsilon^{3/2}} \tag{3.10}$$

In practical units, $\nu_* = 0.0118 q R Z_{eff} n_e / T_e^2 \epsilon^{1.5} \propto n_e q R$. Fig. 3-8 shows the toroidal rotation as a function of ν_* at two currents. The ν_* is evaluated at the $q = 3/2$ surface inside which the rotation reversal occurs. For 0.62 MA the $q = 3/2$ surface is located at $r/a \sim 0.5$, and $r/a \sim 0.7$ for 1.0 MA. The ν_* values at the reversal are close, 0.41 at 0.61 MA and 0.45 at 1.0 MA, in support of ν_* being an important parameter. These values are also close to the $nu_* = 0.35$ at $\rho_{pol} \approx 0.7$ in ASDEX Upgrade, where the turbulence propagation reversal was observed [200]. But one should be cautious that the sensitivity of ν_* on electron temperature may cause fortuitous agreement at some specific locations.

An inter-machine comparison of the LOC/SOC transition was performed and the result supports the relation of $n_{\text{crit}} q \propto 1/R$ [10], as is demonstrated in Fig. 3-9. The dots from TCV and those from C-Mod without error bars are the rotation reversal critical density, suggesting that energy confinement saturation may occur in a range of collisionality with $\nu_* \propto n_e R q \approx$ const. The factor Z_{eff}/T_e^2 turns to vary slightly across the transition point [10], thus it is not considered in the scaling.

The residual stress in momentum flux Eq. 2.5 can change sign depending on the nature of the underlying turbulence, such as by a change in the mode propagation direction from the electron diamagnetic drift direction to the ion direction [217, 12]. This is considered to account for the rotation reversals. The correlation of the LOC/SOC transition density and rotation reversal critical density suggests the unifying hypothesis that dominant instabilities transition from electron turbulence

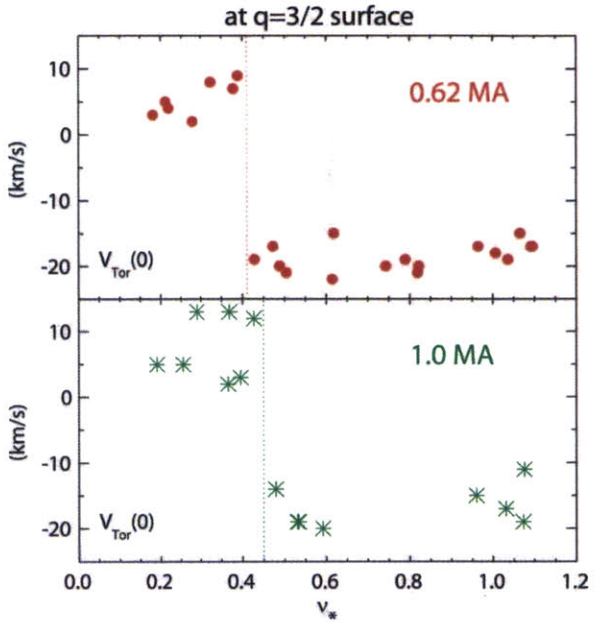

Figure 3-8: The core toroidal rotation velocities as a function of ν_* for plasma currents of 0.62 MA (top) and 1.0 MA (bottom). Vertical lines indicate the co- to counter-current rotation boundary. Figure is from [10].

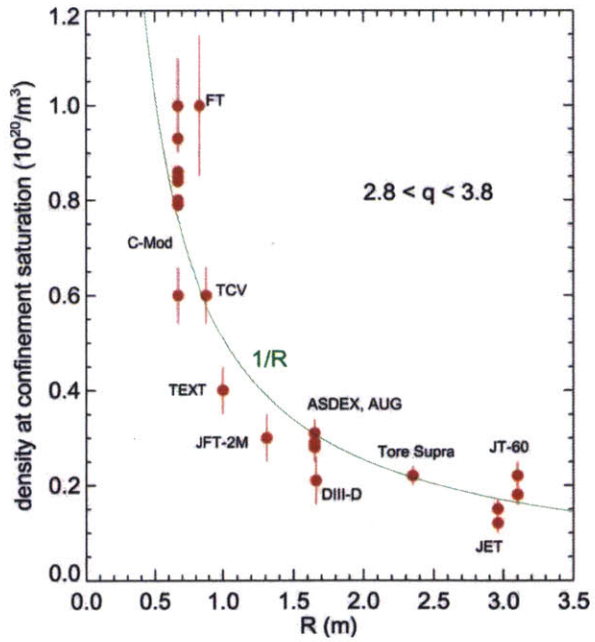

Figure 3-9: The transition density from LOC to SOC as a function of major radius for different devices at fixed values of q. The solid curve represents $1/R$. Figure is from [10].

at low collisionality to ion turbulence at high collisionality. Ion-scale linear GYRO simulations are performed for multiple C-Mod LOC and SOC discharges. In the core $r/a \leq 0.6$, the most unstable mode is always in the ion diamagnetic direction, suggesting ITG modes are the dominant turbulence [218, 219, 220, 167]. At $r/a > 0.6$, a general observation is that the turbulence has a trend from TEM dominance to ITG mode dominance as the plasma crosses the LOC/SOC boundary. But the simulation results do not consistently agree discharge by discharge, partially because of the extreme sensitivity on collisionality of both LOC/SOC transition, and rotation reversals cannot be fully captured by gyrokinetic simulations. In [10, 218] the sensitivity scans showed that at $r/a \sim 0.7$ the LOC plasma is on the TEM/ITG boundary, while the SOC plasma is ITG dominant; in [220] at $r/a \sim 0.8$ the LOC plasma is found to be TEM dominant, while SOC plasma is on the TEM/ITG boundary; in [167] at $r/a \sim 0.75$ the LOC plasma is TEM dominant, while SOC plasma is ITG mode dominant. It is worth noting that these simulations don't include the electron-scale turbulence, which was thought unlikely to drive significant transport. However recent nonlinear GYRO simulations including electron-scale turbulence show that the ETG instabilities have a significant contribution to the ion and electron transport [97, 98]. For this reason, multi-scale simulation, which requires extremely extensive computation resources, may be necessary to quantify correctly the roles of electron and ion turbulence in LOC and SOC plasmas.

3.1.4 "Non-locality" Revisit

As is mentioned in the beginning of this section, in general the transport phenomena can be categorized as (a) local and diffusive, (b) local and non-diffusive, (c) non-local and diffusive, (d) non-local and non-diffusive. It would be helpful to discuss here the experimental observations should fit into which category.

Momentum transport is generally non-diffusive because the momentum flux contains a pinch term and a residual stress term in addition to the diffusive term. If the non-diffusive terms and the diffusivity are function of local parameter, the

momentum transport can be categorized as (b) local and non-diffusive; otherwise the momentum transport will be (d) non-local and non-diffusive. For the heat transport, the cold pulse experiment does indicate a non-local transport due to the fast core response and the reversed polarity.

For heat transport, (c) non-local and diffusive model is widely used to simulate the non-local effect [155]. In this mode, the transport is diffusive, and the core diffusivity suddenly drops following the edge cooling, suggesting the non-locality in diffusive coefficient. (d) Non-local and non-diffusive models are also adopted in explaining the non-local effect, such as the model with a non-local diffusivity and a local pinch [157], and the model with a local diffusivity and a non-local pinch [167].

3.1.5 The Connections Among Non-local Transport, the LOC/SOC Transition and Rotation Reversals

An interesting observation in the cold pulse experiments is that the non-local effect disappears with increasing electron density. This critical cutoff density exists universally, although its value varies for different tokamaks depending on q and major radius. For example in TFTR [13] ($R_0 = 2.36$ m, $a = 0.71$ m, $B_t = 4.9$ T) the cutoff density was found to scale as $n_e(0)/\sqrt{T_e(0)} \leq 0.035 \times 10^{19}$ m^{-3}/eV$^{1/2}$, in RTP [14] ($R_0 = 0.72$ m, $a = 0.164$ m, $B_t \leq 2.4$ T, $I_p \leq 150$ kA) the cutoff line-averaged density is 2.7×10^{19}m^{-3}, in ASDEX Upgrade [15] ($R_0 = 1.65$ m, $a = 0.5$ m, $\kappa = 1.6$, $B_t = 2.46$ T, $I_p = 600$ kA) the value is 1.8×10^{19}m^{-3}, in Tore Supra [16] ($R_0 = 2.31$ m, $a = 0.75$ m, $B_t = 3.7$ T) the cutoff density was found to scale as $\langle n_e \rangle / I_p^2 \leq 1.0 \times 10^{19}$m^{-3}MA$^{-1/2}$, in HL-2A [17] ($R_0 = 1.65$ m, $a = 0.4$ m, $B_t = 1.45$ T, $I_p = 190$ kA) the value is 1.5×10^{19}m^{-3} and in Alcator C-Mod [18] ($R_0 = 0.67$ m, $a = 0.21$ m, $B_t = 5.4$ T), the critical density is $\sim 0.6 \times 10^{20}$m^{-3} for $I_p = 0.55$ MA ($q_{95} \sim 5.8$), $\sim 0.8 \times 10^{20}$m^{-3} for $I_p = 0.8$ MA ($q_{95} \sim 4.2$) and $\sim 1.3 \times 10^{20}$m^{-3} for $I_p = 1.1$ MA ($q_{95} \sim 3.3$). These parameters are listed in Table. 3.1.

The existence of a critical density for the non-local effect makes us consider the possible connection of non-locality with the LOC/SOC transition and intrinsic

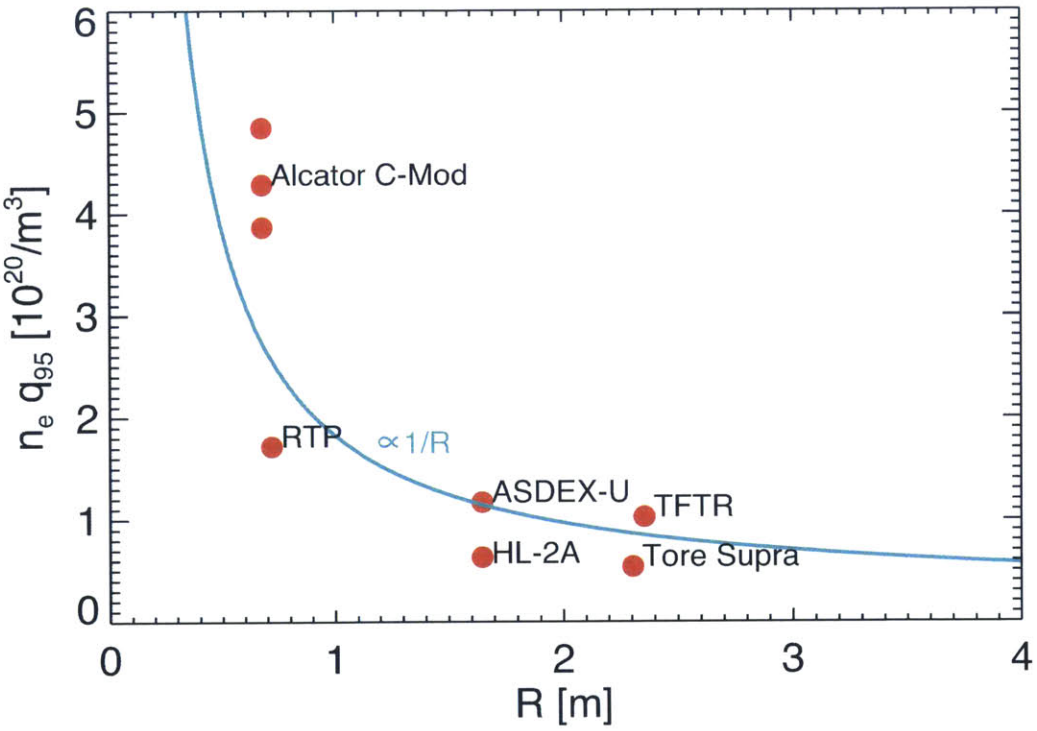

Figure 3-10: The product of cutoff density for non-local effect and q_{95} as a function of major radius for different devices [13, 14, 15, 16, 17, 18]. The solid line represents 1/R.

rotation reversal. One hypothesis for the saturated performance is the change from electron mode (TEM or ETG) dominant turbulent transport at low collisionality to ion mode (ITG) dominant turbulent transport at high collisionality. Shown in Fig. 3-10 is the product of non-locality cutoff density and boundary safety factor (q_{95} for diverted plasmas and $q\,(a)$ for limited plasmas) as a function of major radius for different devices. The boundary safety factor is estimated by $q_{95} = \frac{5a^2 B_T}{RI_{MA}} \frac{1+\kappa^2}{2} \frac{1.17-0.65\epsilon}{(1-\epsilon^2)^2}$ [221] where $\epsilon = a/R_0$ is the inverse aspect ratio. Fig. 3-10, together with Fig. 3-9, show that the collisionality $\nu_* \propto n_e q R$ could be a unifying parameter for the non-local effect, LOC/SOC transition and intrinsic rotation reversals. It is worth noting that the Z_{eff}/T_e^2 dependence is ignored here for the same reason mentioned in Section. 3.1.3. This motivates the cold pulse experiment in Alcator C-Mod to study the connection of these seemingly uncorrelated transport phenomena.

Table 3.1: Critical density for non-local effect on several takamaks.

Tokamak	R [m]	a [m]	κ	B_t [T]	I_p [MA]	q_{95}	$n_{e,\text{crit}}$ [10^{20} m^{-3}]	Reference
TFTR	2.36	0.71	1	4.9	1.2	5.14	~ 0.2	[13]
RTP	0.72	0.164	1	2.4	0.08	6.37	0.27	[14]
ASDEX Upgrade	1.65	0.5	1.6	2.46	0.6	6.52	0.18	[15]
Tore Supra	2.31	0.75	1	3.7	1.0	5.4	0.1	[16]
HL-2A	1.65	0.4	1	1.45	0.19	4.23	0.15	[17]
Alcator C-Mod	0.68	0.22	1.54	5.5	0.55	7.16	0.6	[18]
Alcator C-Mod	0.68	0.22	1.57	5.4	0.84	4.85	0.8	[18]
Alcator C-Mod	0.68	0.22	1.62	5.5	1.14	3.74	1.3	[18]

3.2 Experimental Setup

The experiments were carried out in Ohmic L-mode plasmas in the Alcator C-Mod. Typical Alcator C-Mod L-mode discharges are performed in lower single null (LSN) deuterium plasmas, $B_t = 5.4$ T, $I_p = 0.8$ MA, $\kappa \sim 1.7$, and line averaged electron density from 0.4 to 1.3×10^{20} m^{-3}. Fig. 3-11 shows the cross-section of Alcator C-Mod during a typical LSN discharge.

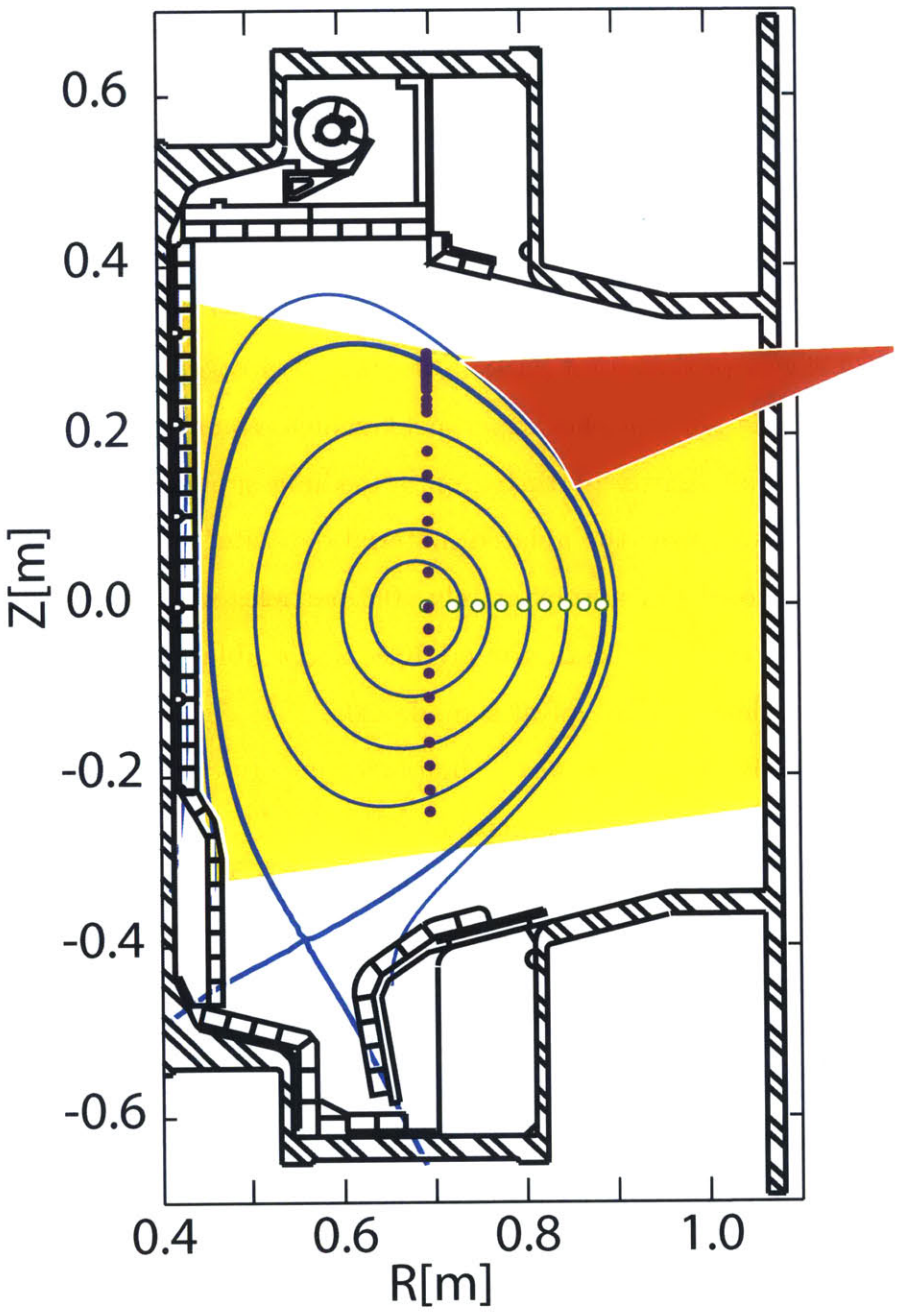

Figure 3-11: The cross section of Alcator C-Mod with lower single null equilibrium. Blue lines are poloidal magnetic flux contours; the red area indicates the approximate location of LBO injected impurities; the yellow area indicates the viewing range of a high resolution imaging x-ray spectrometer; horizontal green open circles represent the ECE measurement positions; vertical purple filled circles are Thomson scattering measurement positions.

3.2.1 Laser Blow-Off System

In Alcator C-Mod, a laser blow-off (LBO) system is used to study particle/impurity transport [20] by introducing non-intrinsic non-recycling impurities (red cone zone in Fig.3-11). The system includes a 0.68 J Nd Yag laser with pulse rate up to 10 Hz, coupled with fast beam steering via a 2D piezoelectric mirror mount able to move spot locations in the 100 ms between laser pulses. A remotely controllable optical train allows the ablated spot diameter to vary from 0.5 to 7.0 mm. A small spot size is preferred for particle/impurity transport studies to avoid perturbation of background plasmas. For experiments which require edge temperature perturbations, but minimal density perturbation, a medium spot size ($\sim$ 3 mm) is preferred. 2 μm of CaF_2 is used as the ablated material deposited on a thin film. A spot size of 2.5 mm will consist of approximately 10^{18} particles with a CaF_2 density of 3.18 g/cm^3. Previous results indicate around 10% of the ablated particles will actually make it into the plasma in a typical L-mode [20].

The LBO system is also valuable for energy transport studies. It induces a cold pulse into the edge of the plasmas. The energy transport properties can be inferred from the cold pulse propagation from the edge to the core. LBO produces the cooling perturbation for the non-local experiments discussed in this chapter.

3.2.2 Diagnostics

The electron temperature T_e profiles are measured by ECE systems, which is discussed in Section 1.4.2. Most of the T_e results presented here were from the GPC1 system, whose typical time resolution is 10 μs, with low noise levels of $\sim$ 10 eV [84], which is sufficient for the study. The electron density profiles are measured by a Thomson scattering system (Section 1.4.1). Line averaged density is measured by a two color interferometer as is discussed in Section 1.4.3. Ion temperature and plasma rotation profiles are measured by HiReX–Sr (Section 1.3). Fluctuation measurements presented in this chapter are made by phase contrast imaging (PCI) system (Section 1.4.4) and reflectometer system (Section 1.4.5).

3.3 Data Processing Methods

Two special data processing techniques are used for this study: the Fourier Analysis for repetitive cold pulse injection experiments, and the generalized singular value decomposition (GSVD) method for sawtooth removal.

3.3.1 Fourier Analysis

The Fourier transform is a general technique to determine the phase and amplitude profiles of perturbations in a modulation experiment [222]. It is a common method for the study of transient transport and provides a high signal to noise ratio. For slab geometry and purely diffusive transport, electron heat diffusivity can be calculated separately from amplitude and phase profiles [223]: $\chi_e^{HP,amp} = \frac{3}{4}\omega / \left(\frac{A'}{A}\right)^2$ and $\chi_e^{HP,phase} = \frac{3}{4}\omega / \left(\frac{\varphi'}{\varphi}\right)^2$, where ω is the modulation angular frequency, A is the Fourier transformed amplitude and φ is the phase. Due to damping [15] (from changes of local Ohmic power, electron-ion exchange and radiation), it usually obtains that $\chi_e^{HP,phase} > \chi_e^{HP,amp}$, and they converge at higher frequency. The convective effect can be observed in the amplitude profile and it will decrease with frequency. The phase profile is not sensitive to convection.

3.3.2 Generalized Singular Value Decomposition

One difficulty we encountered in the experiments is the presence of sawtooth activity. Large amplitude sawteeth of $\sim$ 100 eV in the core electron temperature occurred during the cold pulse experiments, which contaminates the quality of transient measurements. Repetitive injections and Fourier analysis improve the signal to noise level under the assumption that there is no strong interaction between sawtooth activity and the edge perturbations. The generalized singular value decomposition (GSVD) technique is used to verify this assumption. A detailed description of this method applied to perturbation experiments has been made in [224]. The basic idea is to separate the sawtooth and perturbation signals by reconstructing the data in phase space. Assume $\boldsymbol{U}(\boldsymbol{x}, t)$ is the electron temperature

signal measured from ECE before the perturbation which is dominated by sawtooth activity, and $\boldsymbol{Y}(\boldsymbol{x}, t)$ is that after the perturbation, whose evolution consists of both sawtooth activity and perturbation propagation. The GSVD gives $\boldsymbol{U}$ and $\boldsymbol{Y}$ a set of common bases. This set of bases is optimized such that some bases will best represent $\boldsymbol{Y}$ and have little information on $\boldsymbol{U}$. The set of bases consists of both spatial and temporal modes. Signals $\boldsymbol{U}$ and $\boldsymbol{Y}$ share the same spatial modes $V_k(\boldsymbol{x})$, but different temporal modes $A_t(t)$ for $\boldsymbol{U}$ and $B_k(t)$ for $\boldsymbol{Y}$. The choice of bases is made as follows:

$$\boldsymbol{U}(\boldsymbol{x}, t) = \sum_{k=1}^{K} \alpha_k \boldsymbol{A}_k^*(t)\, \boldsymbol{V}_k(\boldsymbol{x}) \tag{3.11}$$

$$\boldsymbol{Y}(\boldsymbol{x}, t) = \sum_{k=1}^{K} \beta_k \boldsymbol{B}_k^*(t)\, \boldsymbol{V}_k(\boldsymbol{x}) \tag{3.12}$$

The temporal modes are orthonormal and weights are normalized, i.e., $\langle \boldsymbol{A}_m^* \cdot \boldsymbol{A}_n \rangle = \langle \boldsymbol{B}_m^* \cdot \boldsymbol{B}_n \rangle = \delta_{mn}$ and $\alpha_m^2 + \beta_m^2 = 1$, where δ_{mn} is the Kronecker delta function. Spatial modes are not necessary to be orthonormal, generally $\langle \boldsymbol{V}_m^* \cdot \boldsymbol{V}_n \rangle \neq 0$ for $m \neq n$. If the sawtooth and perturbation are not strongly coupled, only a few modes will be able to recover the perturbation signal with removal of sawtooth activity. The GSVD method will quantitatively determine how strong the two signals are coupled, as well as separating them in a self-consistent way. A detailed discussion about GSVD is in Appendix. C.

3.4 Experimental Results

Fig. 3-12 shows selected time traces from a typical SOC L-mode discharge with a cold pulse: B_t = 5.4 T, I_p = 0.8 MA ($q_{95} \sim 4.2$), line averaged density $\langle n_e \rangle$ = 1.3×10^{20} m^{-3}. Notice the core plasma rotation is in the counter-current direction ($\sim$ -30 km/s). The CaF_2 injection time is 0.8 s (dashed line). Following the edge cooling, the edge electron temperature drops immediately, as expected. The core electron temperature gradually decreases on a time scale of around 20 ms, which is

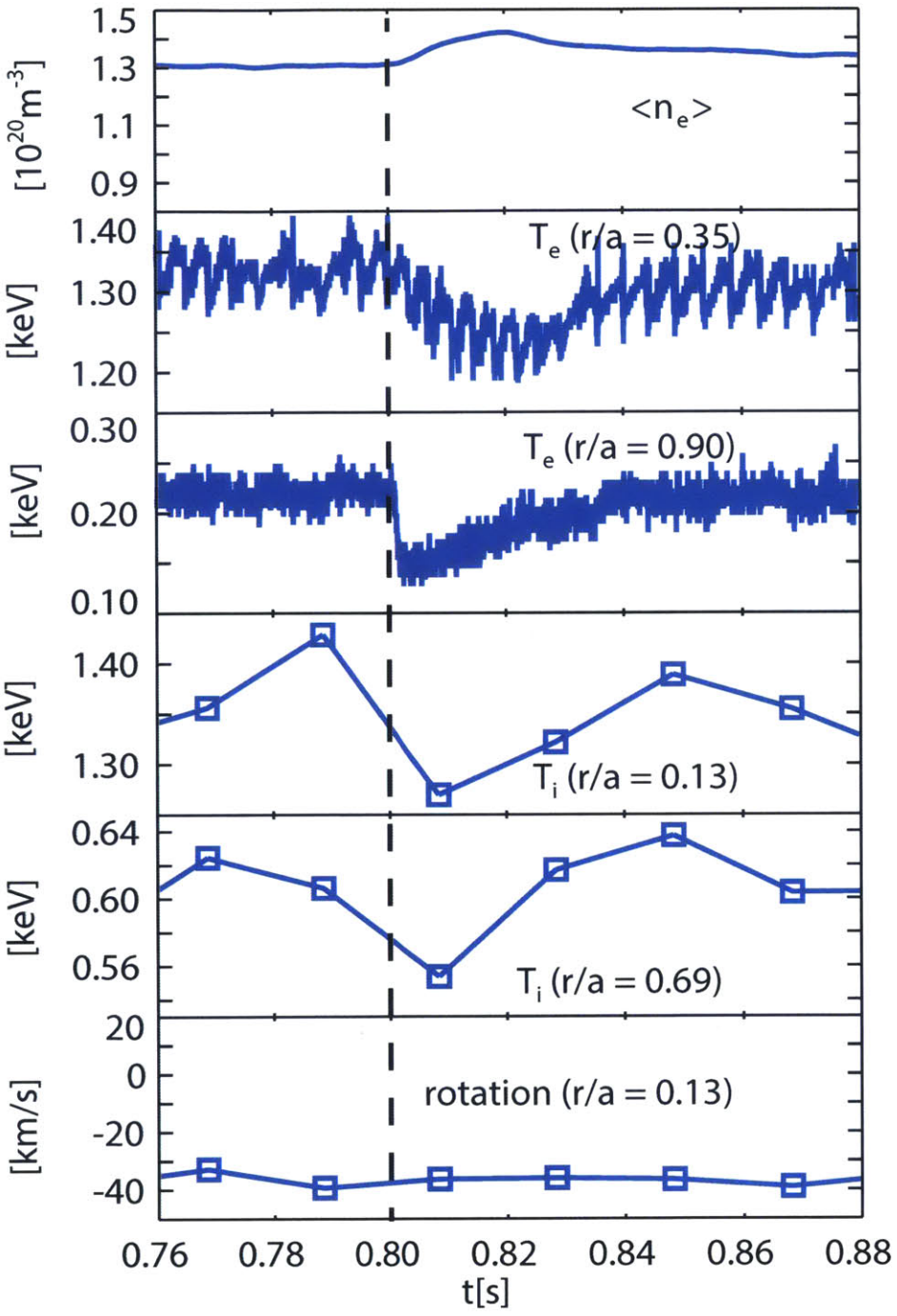

Figure 3-12: Time traces of line averaged electron density, electron temperatures at $r/a = 0.35$ and $r/a = 0.90$, ion temperatures at $r/a = 0.13$ and $r/a = 0.69$, core plasma rotation for an SOC discharge. The CaF_2 is injected at 0.8 s.

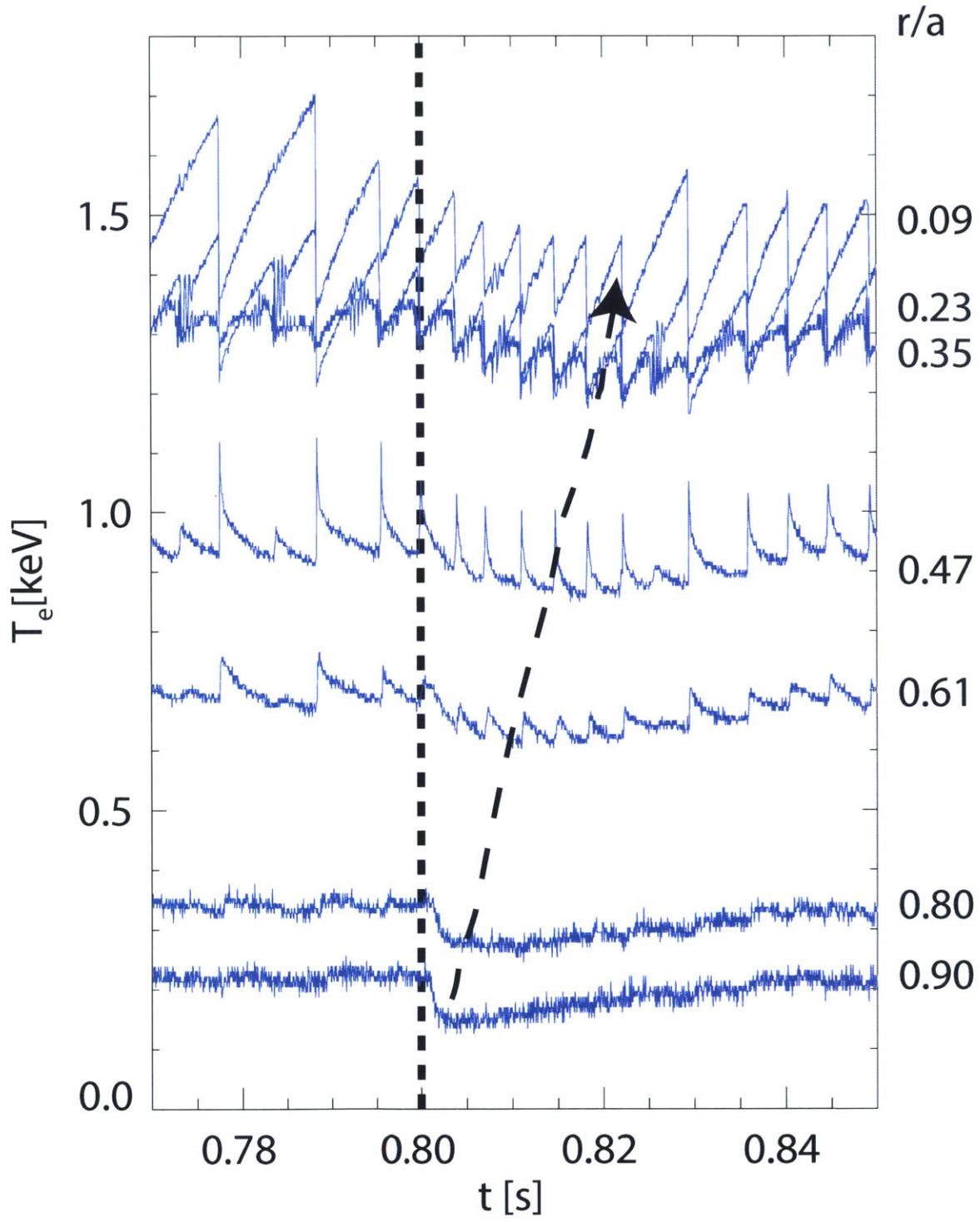

Figure 3-13: Same discharge as in Fig. 3-12. Time trace of electron temperatures at different radii measured by GPC1. The arrow shows the trajectory of minima in the electron temperature from each channel. The evolution of peaks at different radii clearly shows the diffusive behavior of the cold front propagation.

comparable to the energy confinement time $\sim$ 27 ms. In Fig. 3-13 the dashed line with the arrow shows the trajectory of minima in the electron temperature at different radii. The evolution of minima at different radii clearly shows the diffusive behavior of the cold front propagation. The core ion temperature also drops following the edge cooling, although the time resolution in this case is not good.

Fig. 3-14 is an LOC L-mode discharge with the same parameters as Fig. 3-12 except for a lower density of 0.6×10^{20} m^{-3}. The core plasma rotation is now in the co-current direction ($\sim$ 15 km/s). The CaF_2 injection time is 1.0 s. The core electron temperature begins to increase, rather than decrease, within 5 ms and peaks within 10 ms after the injection. This time scale is much less than the energy confinement time ($\sim$ 25 ms). The line averaged electron density is increased by 20% following the cold pulse injection, but the time evolution of n_e and T_e is very different: T_e begins to fall while n_e is still rising. LBO injection with smaller target size and minimal density perturbation in LOC plasmas also causes the core temperature increases (Fig. 3-18 and Fig. 3-22). The core T_e increase is unlikely due to a density dependence of confinement. The experiments on TEXT and TFR also suggest that either the rise in electron temperature [157] or the rise in radiation power [155] plays a role in the non-local transients. In Fig. 3-15, for the outer plasma region it takes a longer time to peak as the cold pulse propagates inwards; for the inner region, the time-to-peak decreases, which contradicts the pure diffusive transport. The core ion temperature also increases after the edge cooling, but peaks and decays on a longer time scale. Fig. 3-16 shows the profile evolution of the electron and ion temperatures during the LBO injection in the same LOC plasma. At 1.01 s the core ion temperature doesn't change within the uncertainty, while the core electron temperature peaks. At 1.03 s the core electron temperature drops, which is evidence that the cold front propagates to the core plasma; the edge electron temperature returns to its pre-injection value and the core ion temperature rises.

The rise in the core ion temperature doesn't necessarily indicate a non-local effect in the ion channel. The core ion temperature evolves on a longer time scale. It reaches the maximum approximately 30 ± 10 ms after the cold pulse injection, at

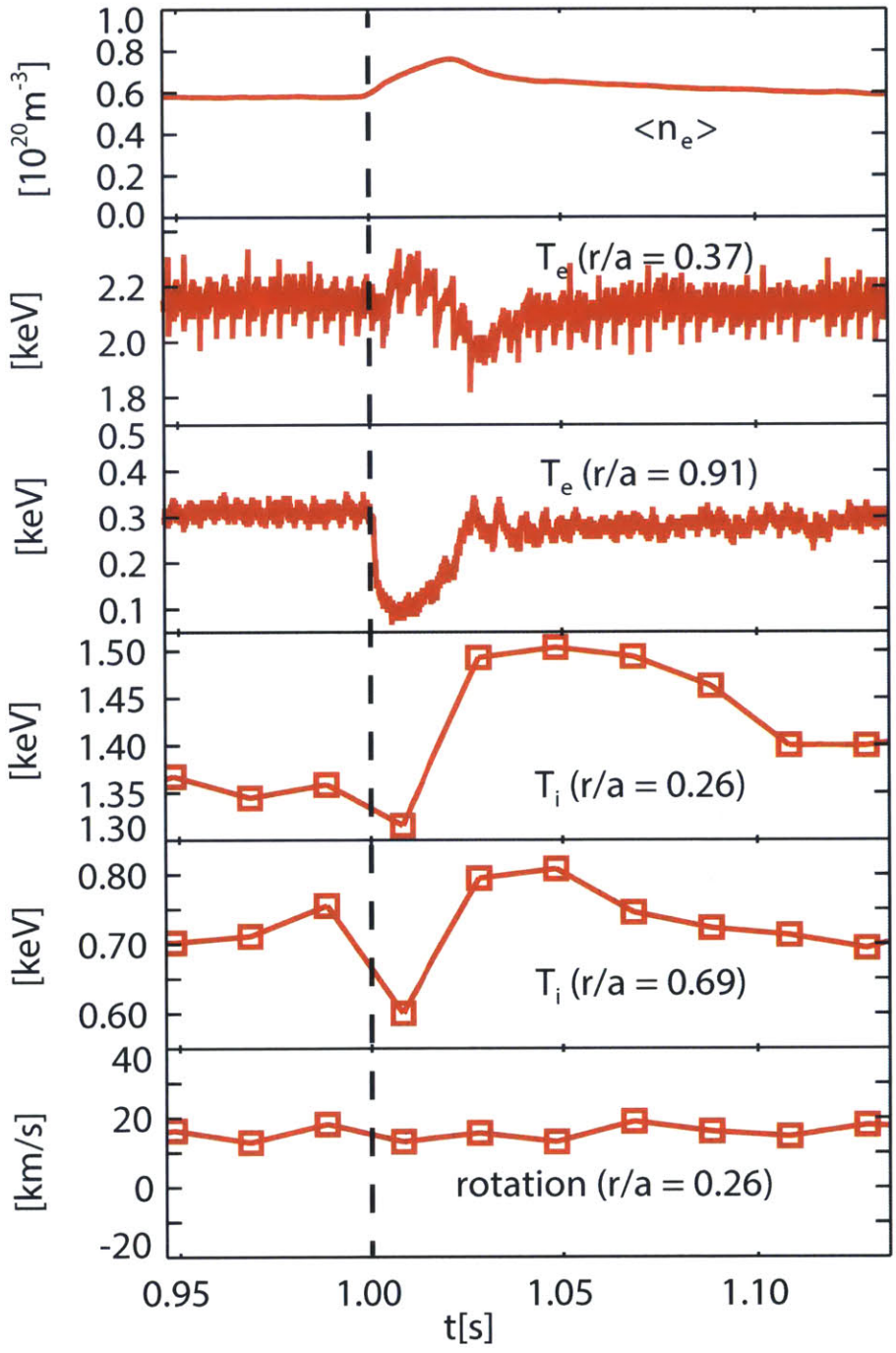

Figure 3-14: Time traces of line averaged electron density, electron temperatures at $r/a = 0.37$ and $r/a = 0.91$, ion temperatures at $r/a = 0.26$ and $r/a = 0.69$, core plasma rotation for an LOC discharge. The CaF_2 is injected at 1.0 s.

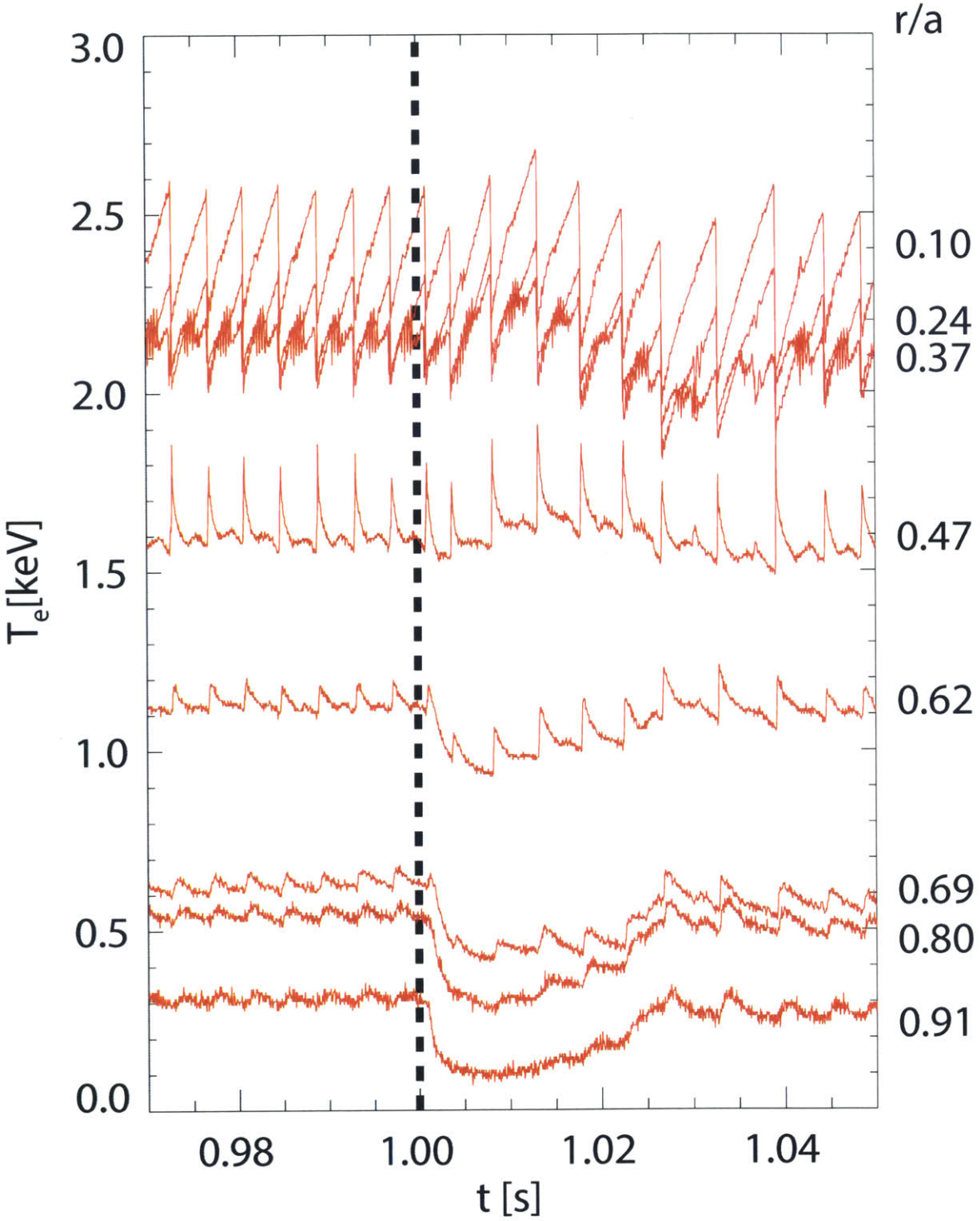

Figure 3-15: Same discharge as in Fig. 3-14. The evolution of peaks in core channels indicates the non-diffusive heat transport.

which time the core electron temperature increase has disappeared. The core ion temperature peaking time is close to the electron density peaking time. This suggests that the core T_i increase may be related to the ion-electron thermal coupling. For deuterium plasma, the ion-electron thermal equilibrium time is $\tau_{ie} \approx 0.019 \frac{T^{3/2}[\mathrm{keV}]}{n_e[10^{20}\mathrm{m}^{-3}]}[s]$ [1]. Before the cold pulse, $\tau_{ie} \sim 77$ ms with $r/a \sim 0.3$, $T_e \sim 2.0$ keV, $n_e \sim 0.7 \times 10^{20}$ m^{-3}; during the cold pulse τ_{ie} drops to 64 ms with the increased electron density. It is also observed that when the density perturbation is smaller, the rise in the core ion temperature is less significant. Within the current time resolution of ion temperature measurement (20 ms), the core ion temperature increase is at least in part due to an enhanced ion-electron collisional coupling.

Figs. 3-17 and 3-18 are repetitive LBO injection experiments with similar plasma parameters ($B_t = 5.4$ T, $I_p = 0.8$ MA, $q_{95} \sim 4.2$) as in Figs. 3-12 and 3-14, respectively. Fig. 3-17 is an SOC discharge with line averaged density $\sim 1.05 \times 10^{20}$ m^{-3} and counter-current directed rotation ($\sim$ -10 km/s). Fig. 3-18 is an LOC discharge with line averaged density $\sim 0.58 \times 10^{20}$ m^{-3} and co-current directed core plasma rotation ($\sim$ 7 km/s). The CaF_2 injection rate is 10 Hz. Although the core electron temperature signals are contaminated by sawtooth activity, it is visible that for the SOC discharge, the core T_e drops with edge cooling and for the LOC discharge, the core T_e increases. To verify this observation and to extract the amplitude and phase profiles, GSVD was applied to the raw data. Fig. 3-19 is the result of the decomposition applied to the LOC discharge between $0.85 - 0.95$ s with one injection event. Temporal modes $A_k(t)$, $B_k(t)$ and spatial modes $V_k(R)$ are calculated from electron temperatures with mean normalization, so they are dimensionless. It is shown that the first 2 modes can quantitatively represent the pulse process with sawtooth activity reduced by around 80% (the sawtooth amplitude reduced from $\sim$ 500 eV before GSVD was applied to $\sim$ 100 eV after GSVD was applied, as shown in Fig. 3-19(d)). Fig. 3-20 shows the LOC discharge (Fig. 3-18) temperature time traces with GSVD applied. Although it is impossible to remove totally the sawtooth activity, the increase of the core temperature is more clear for the three core channels. Fig. 3-21(a) is the result of

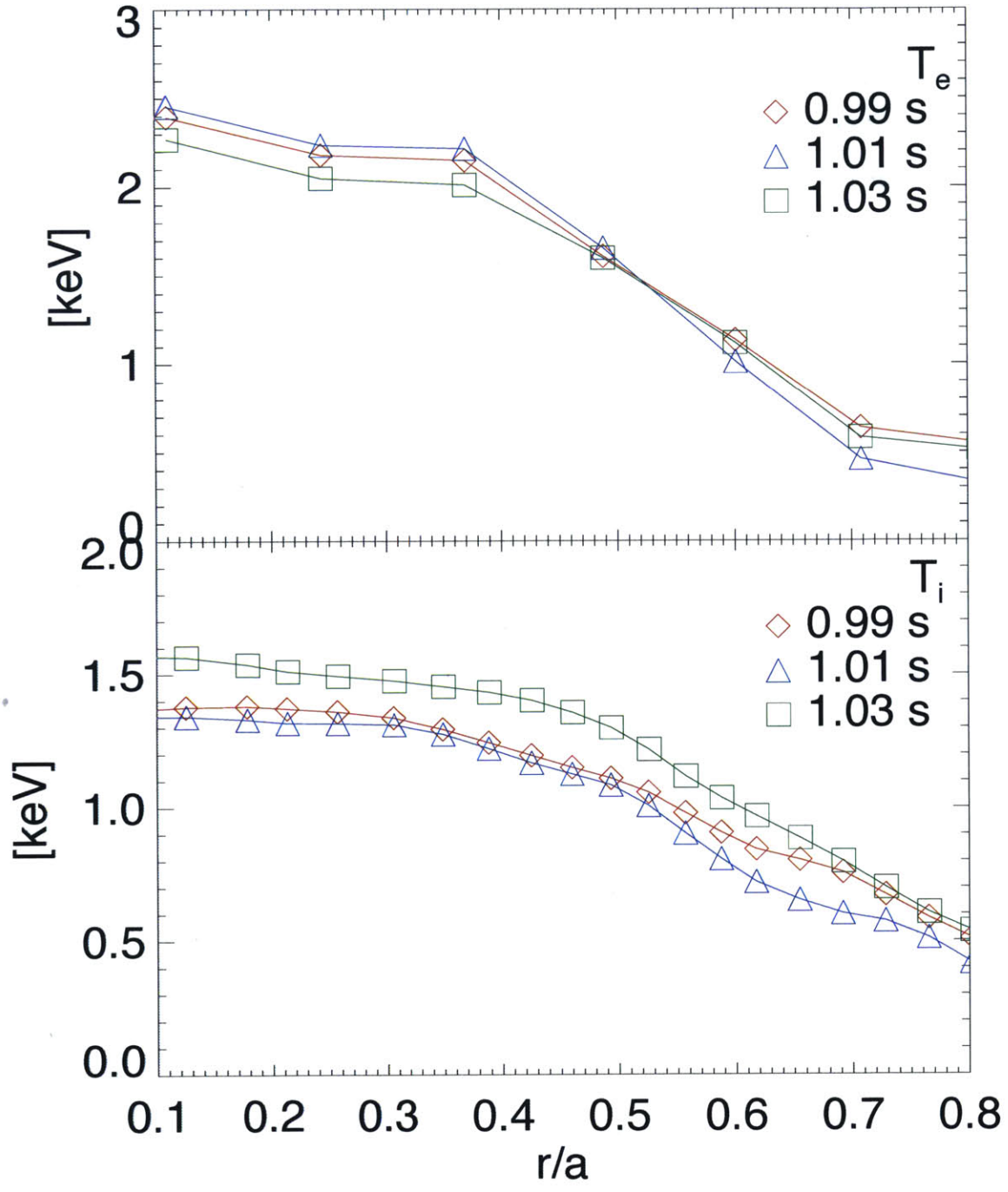

Figure 3-16: Same discharge as in Fig. 3-14. The profile evolution of the electron (top) and ion (bottom) temperatures for an LOC discharge. The injection time is 1.0 s.

Fourier transforms of the electron temperature for the discharge shown in Fig. 3-18 with GSVD applied. The first three harmonics of FFT profiles are shown. The location with minimum amplitude and phase crossing 90° indicates the "inversion radius", which is around 0.78 m in major radius ($r/a \sim 0.5$). The amplitude of the first harmonic increases towards the core. This increase contradicts the assumption of purely diffusive transport. This modulation experiment result in LOC plasmas differs from the previous single injection experiment (Figs. 3-14 and 3-15) in two regards. The first is that in the modulation experiment, there is no evidence that the cold front propagates into the core plasma. The other difference is the relative amplitude of changes in core and edge electron temperatures. In the modulation experiments, the amplitude of the core temperature increase is about twice the amplitude of the edge temperature drop (Figs. 3-20 and 3-21). For the single injection experiment (Figs. 3-14 and 3-15) the edge temperature has a larger perturbation than in the core. This discrepancy could be caused by the difference of ablated spot size. A larger injection would cause a larger perturbation in the edge and the cold pulse would propagate deeper into the core plasma. Fig. 3-21(b) is the FFT result of the SOC discharge shown in Fig. 3-17 with GSVD applied. The amplitude decreases as the cold pulse propagates into the core, which suggests a purely diffusive process.

For the LOC discharge, where the non-local effect of edge cooling exists, it is found from PCI that the density fluctuations are suppressed during the injections, as shown in the Fig. 3-22 (a). PCI provides a line integral measurement of density fluctuations. Fig. 3-23 is the time history of the spectral power integrated over $10 - 40$ kHz, which clearly shows the turbulence suppression associated with the cold pulses. To identify the location of turbulence suppression, density fluctuations measured by the reflectometer at $r/a \sim 0.9$ are shown in Fig. 3-22 (b). There is no clear correlation between the fluctuations from the reflectometer and CaF_2 injections, so it should be the turbulence at least inside $r/a \sim 0.9$ which is suppressed instead of the edge turbulence [17]. We did not observe the suppression in SOC discharges when the cold pulse propagates diffusively and local transport is valid.

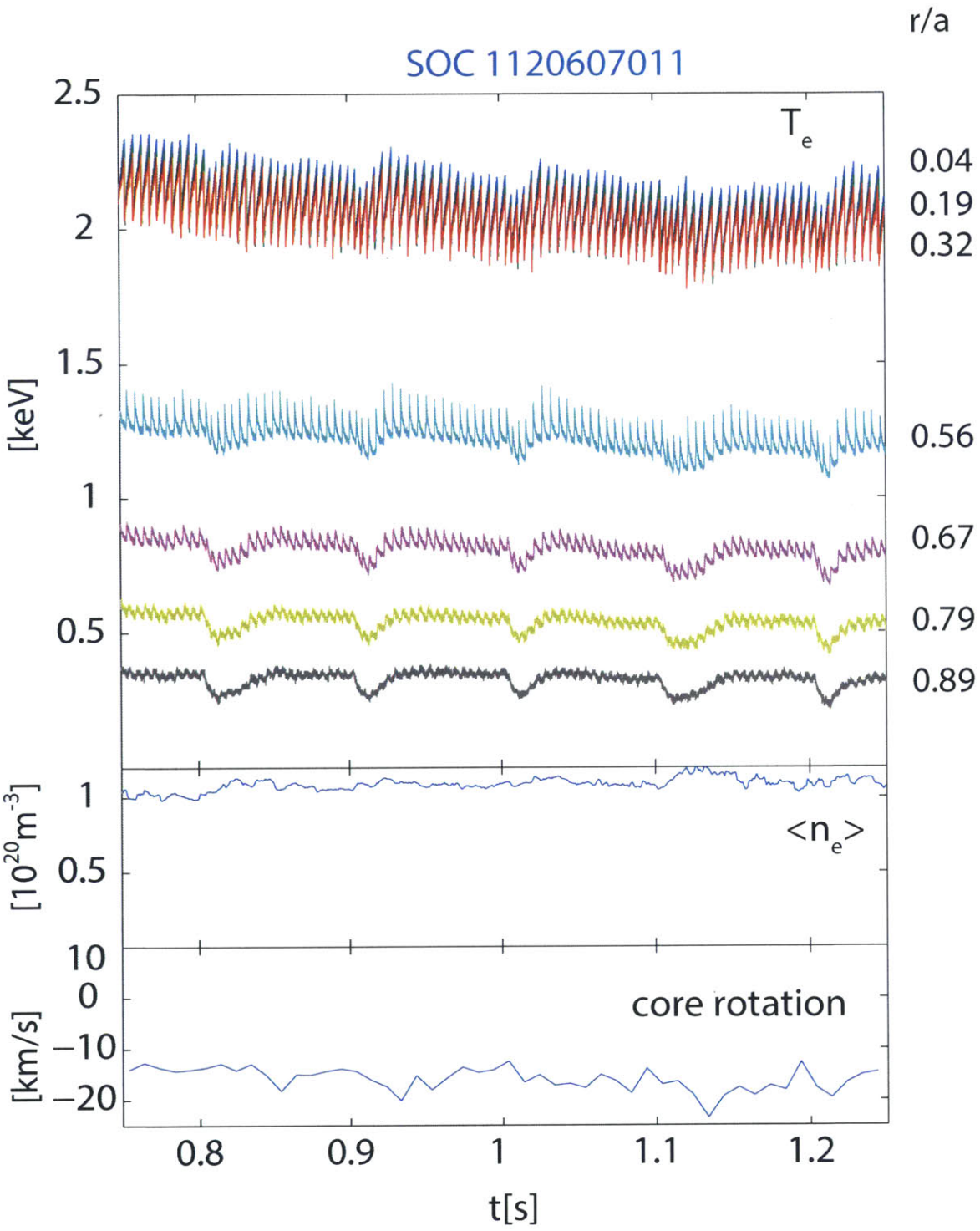

Figure 3-17: Time traces of electron temperatures, line averaged electron density and core plasma rotation for an SOC discharge with repetitive LBO injections at 0.8 s, 0.9 s, 1.0 s, 1.1 s and 1.2 s.

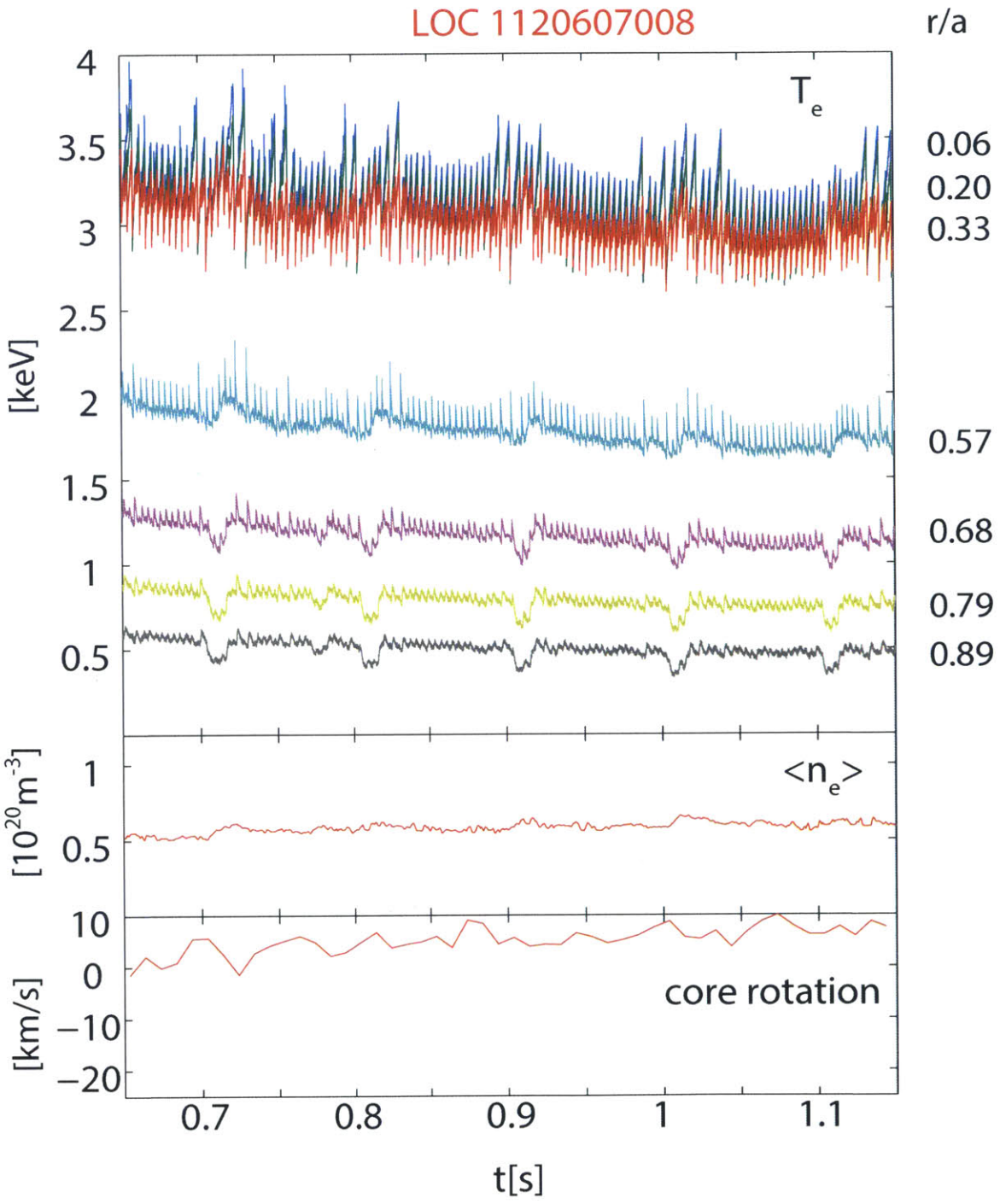

Figure 3-18: Time traces of electron temperatures, line averaged electron density and core plasma rotation for an LOC discharge with repetitive LBO injections at 0.7 s, 0.8 s, 0.9 s, 1.0 s and 1.1 s.

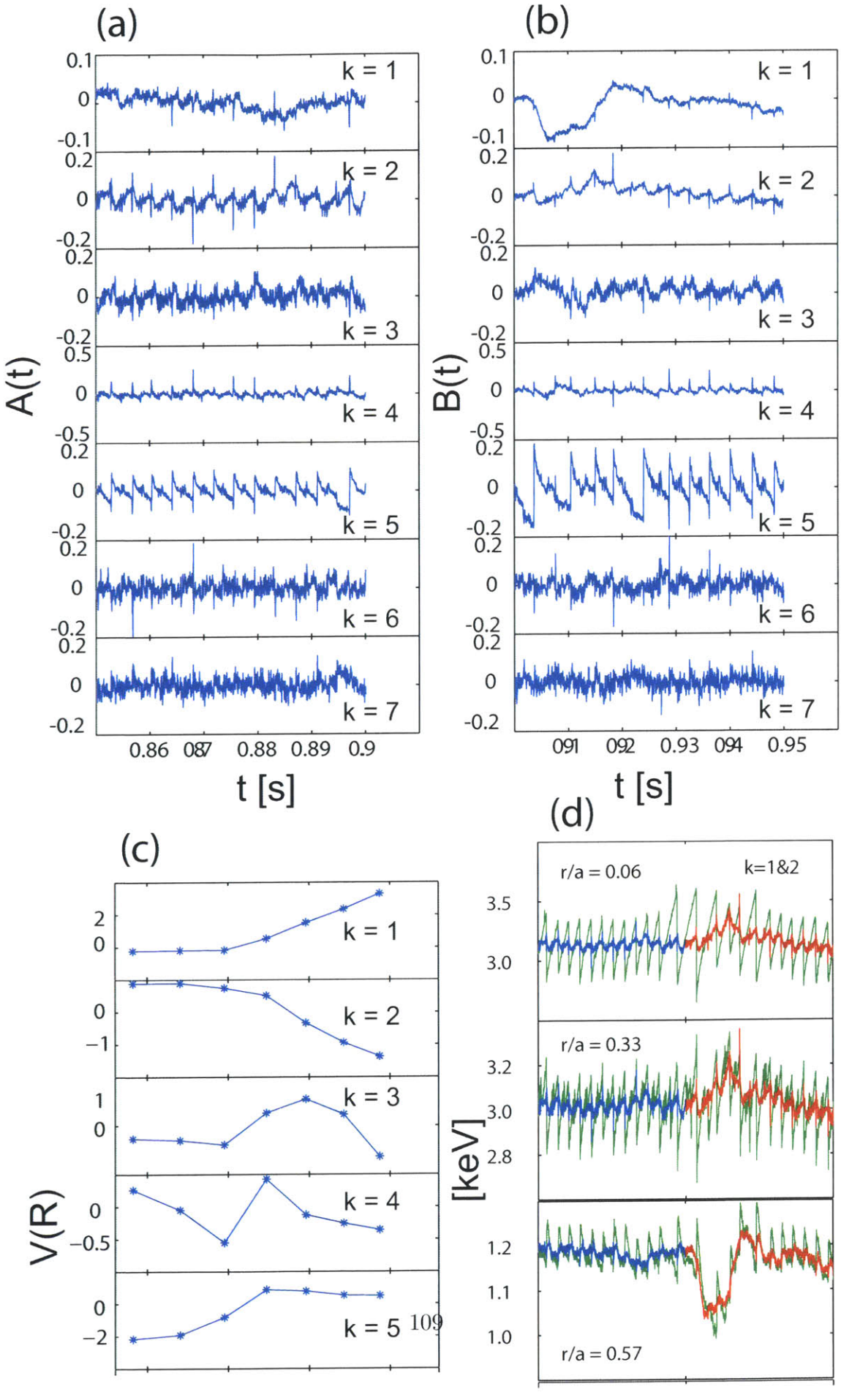
(a)
(b)
(c)
(d)
A(t)
B(t)
t [s]
t [s]
k = 1
k = 2
k = 3
k = 4
k = 5
k = 6
k = 7
V(R)
[keV]
r/a = 0.06
k=1&2
r/a = 0.33
r/a = 0.57

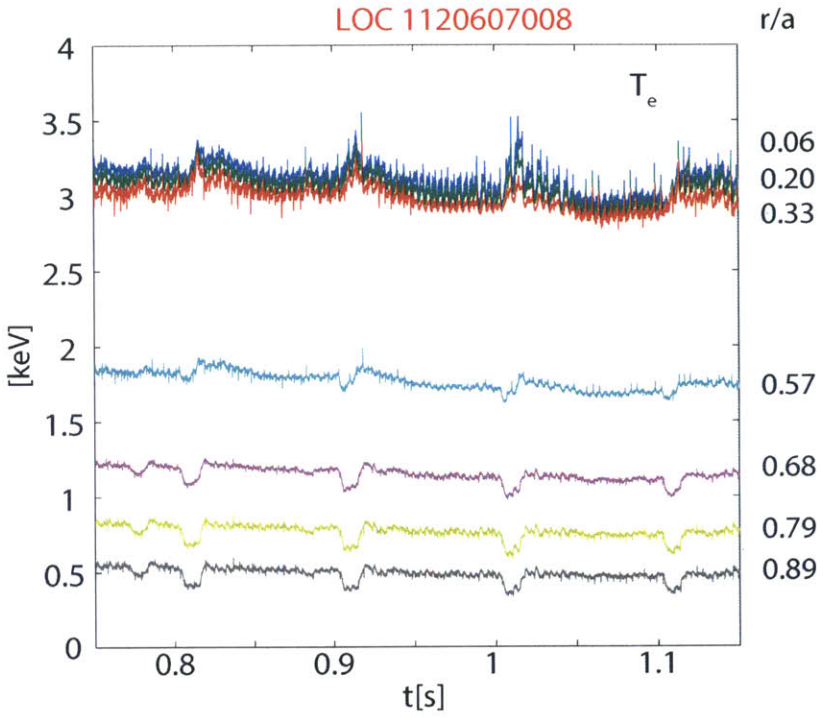

Figure 3-20: Time traces of electron temperatures in Fig. 3-18 with GSVD applied for LOC discharge.

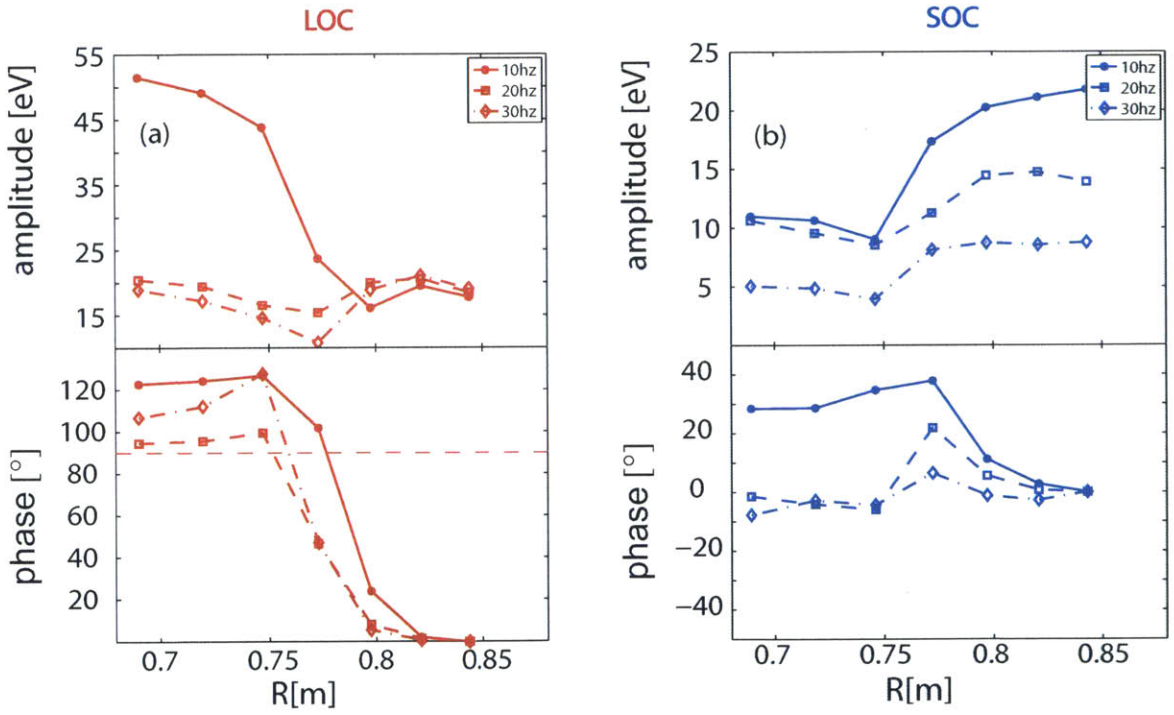

Figure 3-21: The FFT amplitude and phase profiles for (a) LOC discharge in Fig. 3-18 with GSVD applied , and (b) SOC discharge in Fig. 3-17 with GSVD applied.

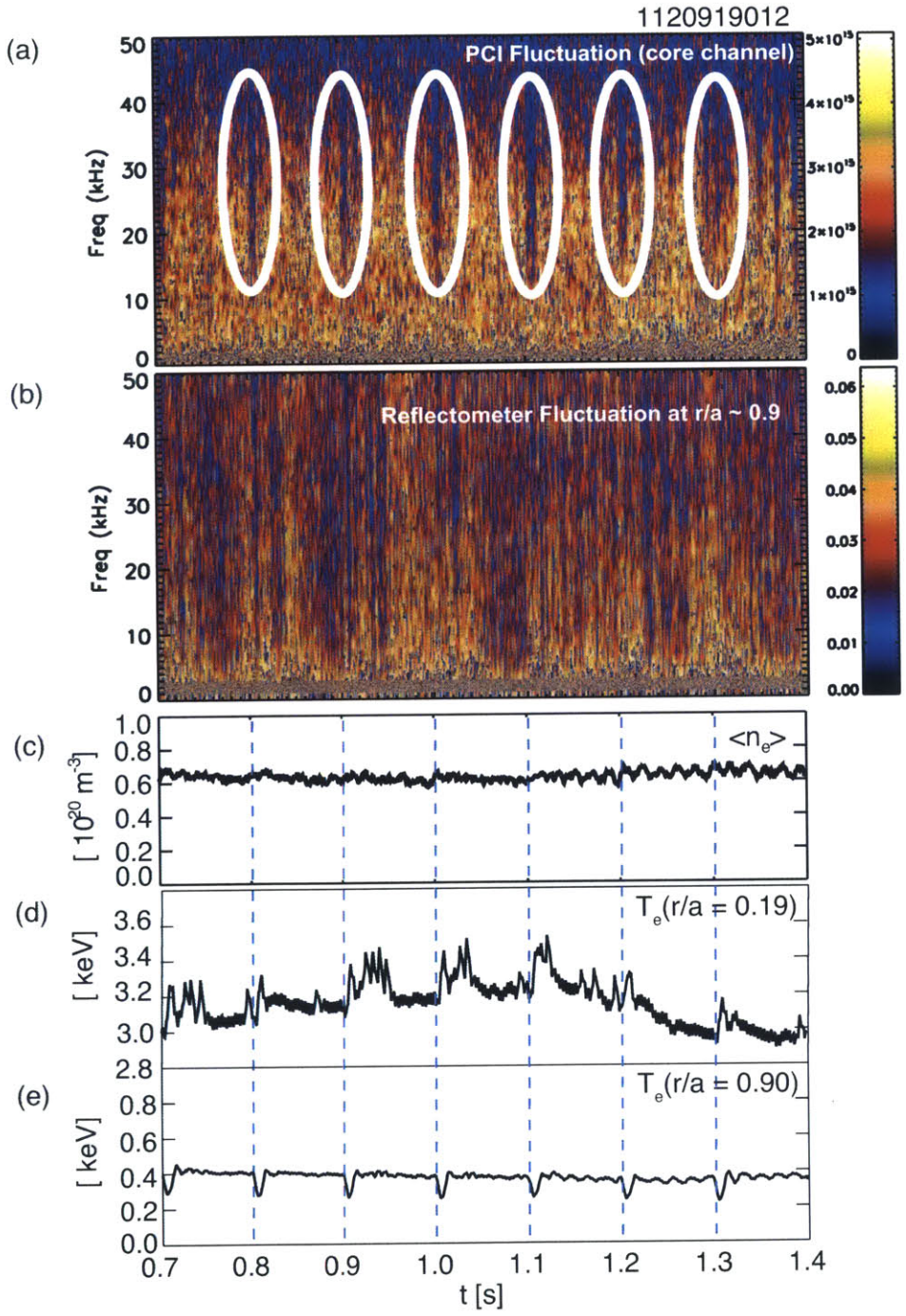

Figure 3-22: The LOC discharge with repetitive LBO injections: (a) density fluctuation measurement from PCI; (b) edge density fluctuation measurement from reflectometer; (c) line integrated electron density (d) core electron temperature; (e) edge electron temperature. The dashed lines indicating the LBO injection times.

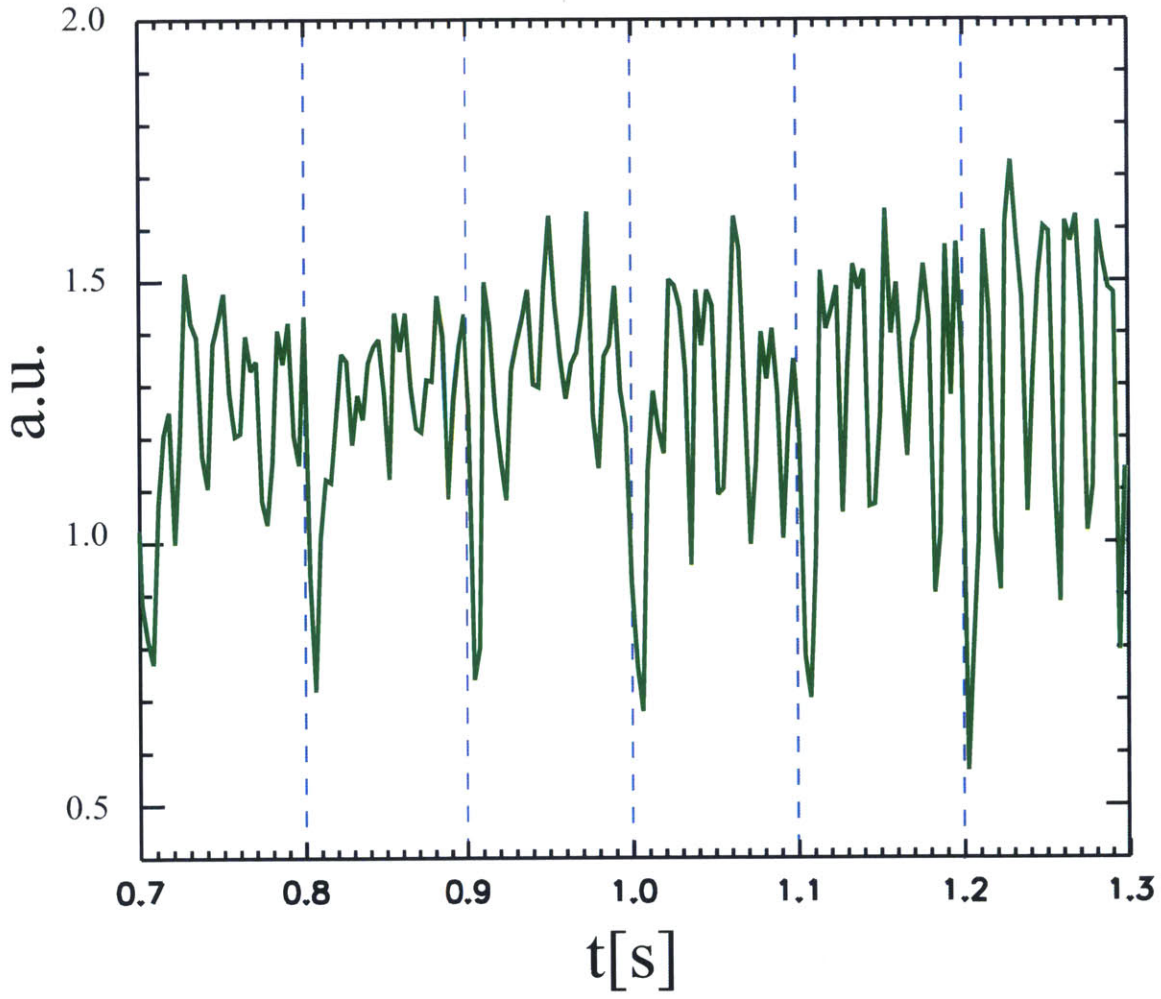

Figure 3-23: Time trace of the spectral power integrated over 10 - 40 kHz from PCI in Fig. 3-22. The spectral power trace is averaged over 1.6 ms.

Recent experiments in LHD [225] show that the amplitude of the electron temperature fluctuations decreased and their radial correlation lengths shortened during the transient phase induced by pellet injection. In Alcator C-Mod the electron temperature fluctuation and correlation length can be measured using upgraded multi-channel CECE [19]. This will be an interesting topic for future experiments.

For LOC plasmas the core electron temperature increases almost linearly with the edge cooling, as shown in Fig. 3-24(a), where the changes of the core T_e ($r/a \sim 0.3$) are plotted as a function of drops in the edge T_e ($r/a \sim 0.8$). For 0.8 MA discharges, the line averaged density is around 0.6×10^{20} m^{-3}. For 1.1 MA discharges, the line averaged density varies from 0.8 to 1.2×10^{20} m^{-3}. From Fig. 3-24(b) the core ion temperature ($r/a \sim 0.4$) also responds linearly to the cooling. The change of the core electron temperature is calculated as the temperature difference between before the cold pulse injection and around 5 ms after the cold pulse injection. The change of core ion temperature is calculated as the temperature difference between before and around 20 ms after the cold pulse injection.

The non-local effect is found to be correlated with the rotation reversal [18], shown in Fig. 3-25. For this 5.4 T, 0.8 MA discharge the line averaged density increased from 0.5×10^{20} m^{-3} to 1.0×10^{20} m^{-3}. This density range covers both the LOC and SOC regimes, roughly indicated in colors of yellow and blue, respectively, based on previous C-Mod results. The rotation reversal from the co-current to the counter-current direction happens at a density around 0.8×10^{20} m^{-3}. The interesting observation here is that the non-local effect disappears almost at the same density level. The core electron temperature increases as a result of the injection at 1.0 s, which is in the LOC regime and rotation is in the co-current direction. As the density rises, the core electron temperature decreases for the injection at 1.2 s. To illustrate the correlation, the energy confinement time, relative change of core electron temperature and absolute value of core plasma rotation are plotted as a function of line averaged density for 5.4 T, 0.8 MA discharges in Fig. 3-26.

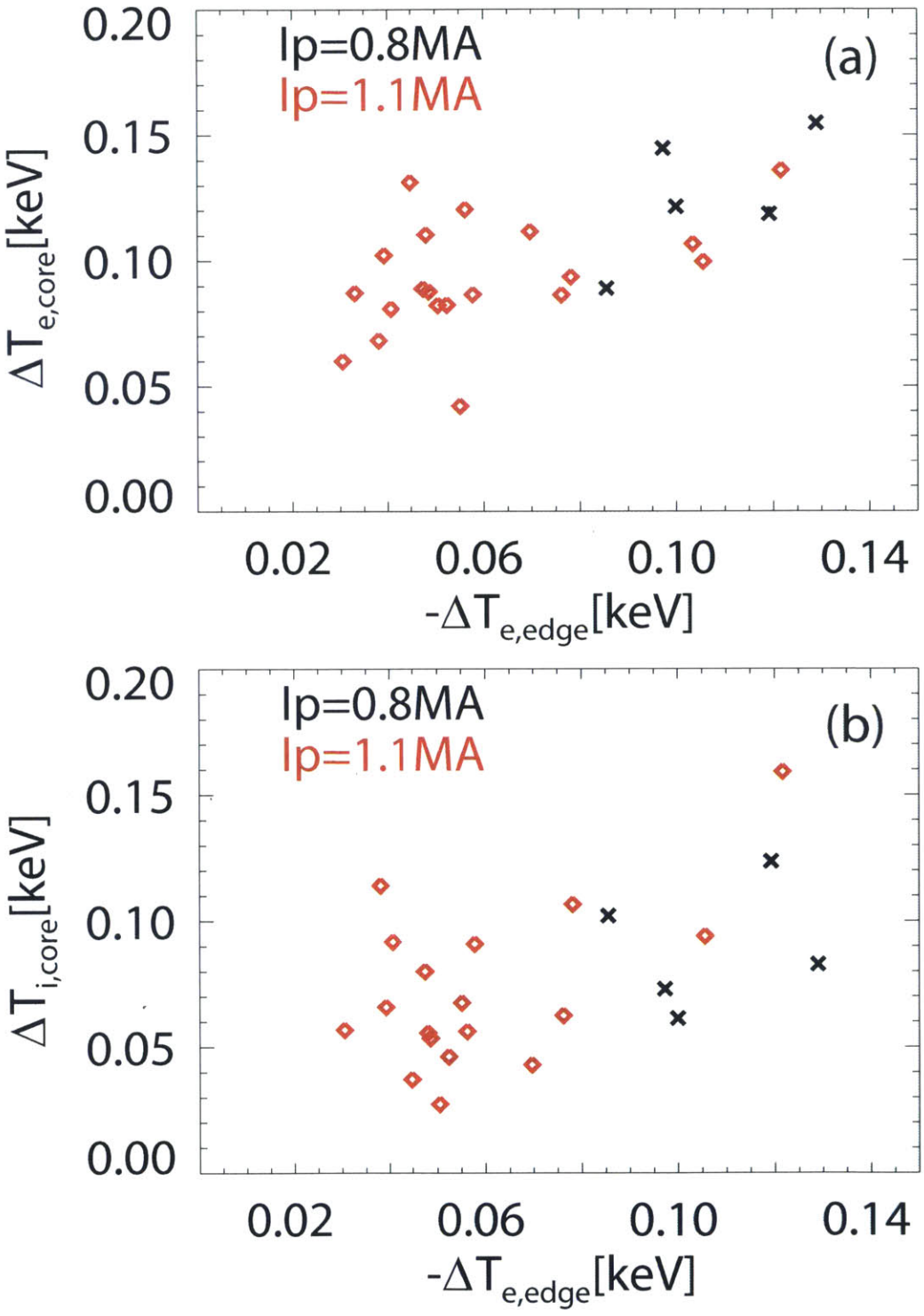

Figure 3-24: The changes of the core electron temperature (a) and core ion temperature (b) vs. the changes of edge electron temperature for 0.8 MA (black crosses) and 1.1 MA (red diamonds) in LOC plasmas.

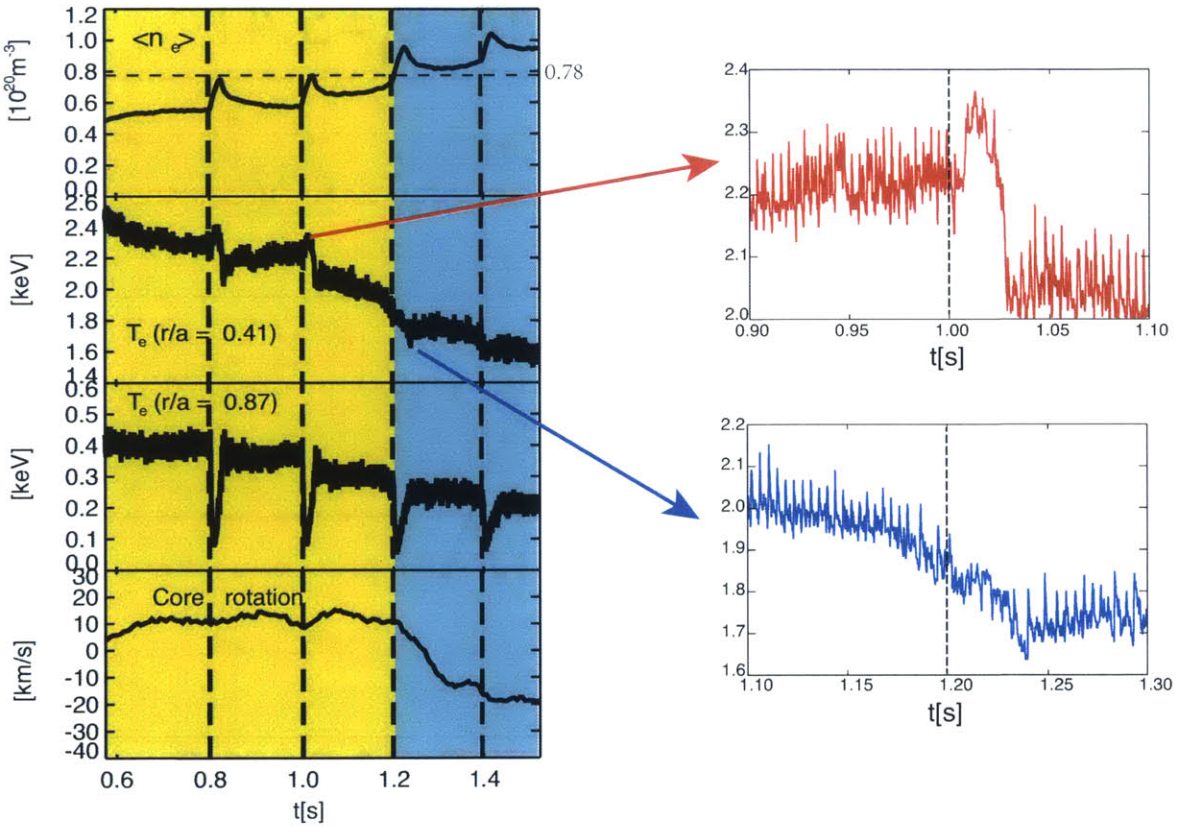

Figure 3-25: Left figure from top to bottom: time traces of line averaged electron density, core electron temperature, edge electron temperature and core rotation for a density ramp-up discharge. The yellow color indicates the LOC regime, and blue color indicates the SOC regime.

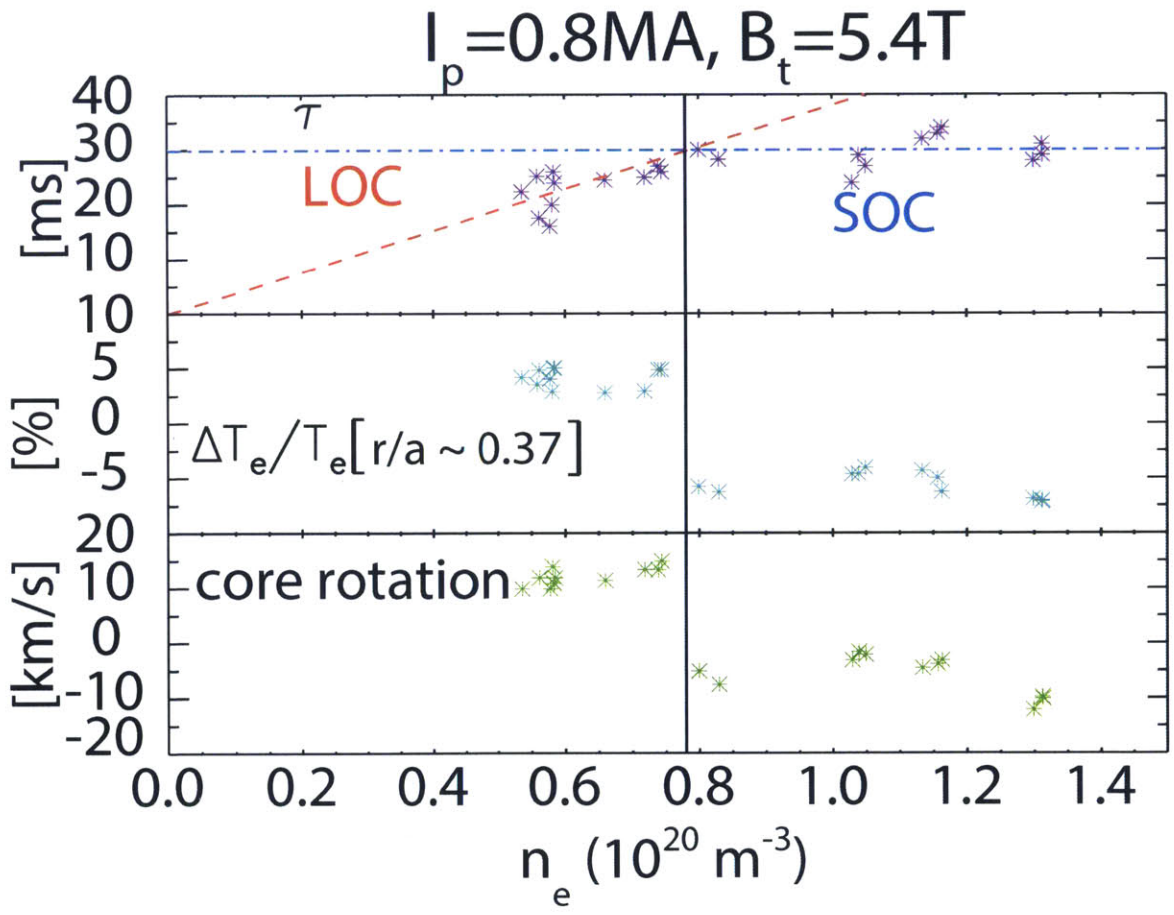

Figure 3-26: From top to bottom: energy confinement time, relative change of core electron temperature, absolute value of core rotation vs. line averaged electron density. The vertical line indicates the LOC-SOC transition density $n_{e,20} \sim 0.78$.

3.5 Transport Analysis

The electron heat diffusion coefficient χ_e has been calculated from power balance using TRANSP. Similar to the results in TEXT [154, 155, 9], RTP [157, 14, 158] etc, a rapid drop in the χ_e profile can explain the experimental results. Fig. 3-27(a) shows the LOC plasma diffusivity profiles averaged over three time intervals: before the injection, during the injection and after the injection. The CaF_2 was injected at 1.0 s for this discharge. The core diffusivity between $r/a = 0.3-0.8$ is reduced by $\sim$ 25% during the injection, and it returns to the previous level around 40 ms after the injection. Fig. 3-27(b),(c) are time traces of the simulated core and edge electron temperatures based on this diffusive model. The red lines are measured electron temperatures. This drop of core transport looks like the formation of an internal transport barrier (ITB) during the cold pulse injection, and we do observe a reduction of density fluctuations as discussed in the previous section. For SOC plasmas where the non-local effect disappears, the reduction of core transport is not observed from this analysis.

An alternative non-local non-diffusive model including a convection term in the heat flux ($q = -n_e\chi_e\nabla T_e + n_e V T_e$) can also match the observations and the result is shown in Fig. 3-28. The diffusivity is assumed to be constant during the cold pulse event, and the convection term is turned on right after the cold pulse injection. An inward pinch velocity profile (negative V) is obtained to match the experimental results. The simulated profiles agree with experiments as is shown in Fig. 3-28(b). Although one cannot distinguish between the two models, the Fourier analysis shown in Fig. 3-21 indicates that there should be a non-diffusive component in the transport model in LOC plasmas.

The reduction of core transport during cold pulse injection in LOC plasmas is also observed in the sawtooth induced heat pulse propagation, which is measured via the soft X-ray brightness and time-to-peak as a function of radius. Time-to-peak is defined as the time delay from the sawtooth crash to the time with maximum brightness. Shown in Fig. 3-29(a) is soft X-ray brightness from a select number of

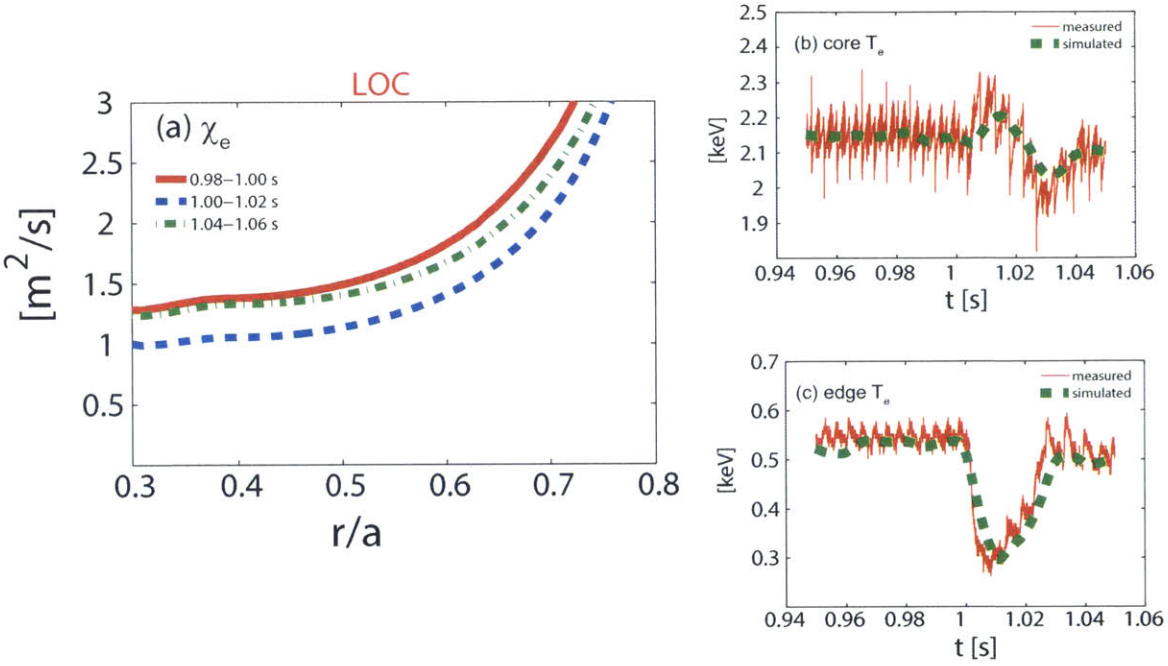

Figure 3-27: Left: The electron heat diffusivity profiles before (red solid line), during (blue dashed line) and 40 ms after (green dash-dot line) the LBO injection for a LOC plasma. Right: The time traces of measured (red solid lines) and simulated (green dashed lines) for core (b) and edge (c) electron temperatures.

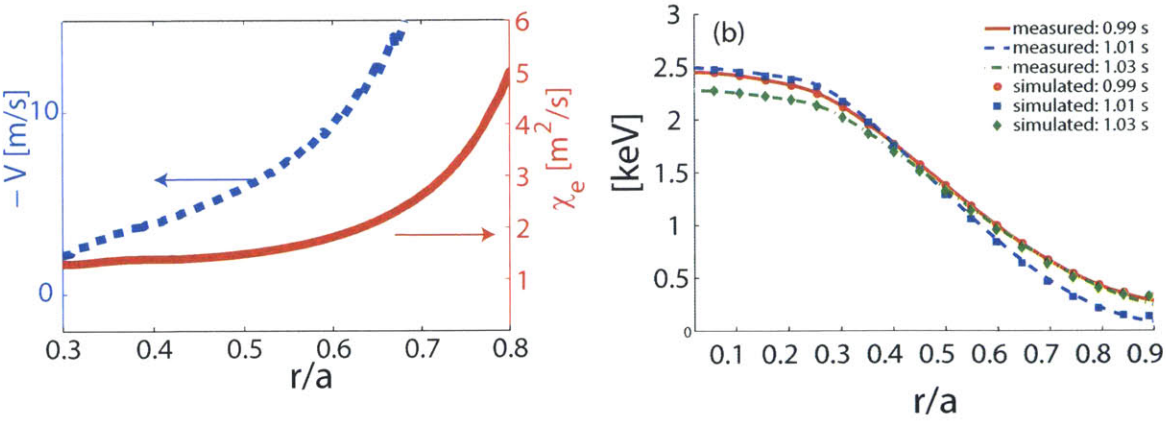

Figure 3-28: Left: The χ_e (red, solid line) and $-V$ (blue, dashed line) profiles. Right: The measured T_e profiles at 0.99 s (red, solid line), 1.013 s (blue dashed line) 1.03 s (green, dash-dot line); and the simulated T_e profiles at 0.99 s (red, circles), 1.013 s (blue squares) 1.03 s (green, diamonds). The LBO injection time is 1.0 s.

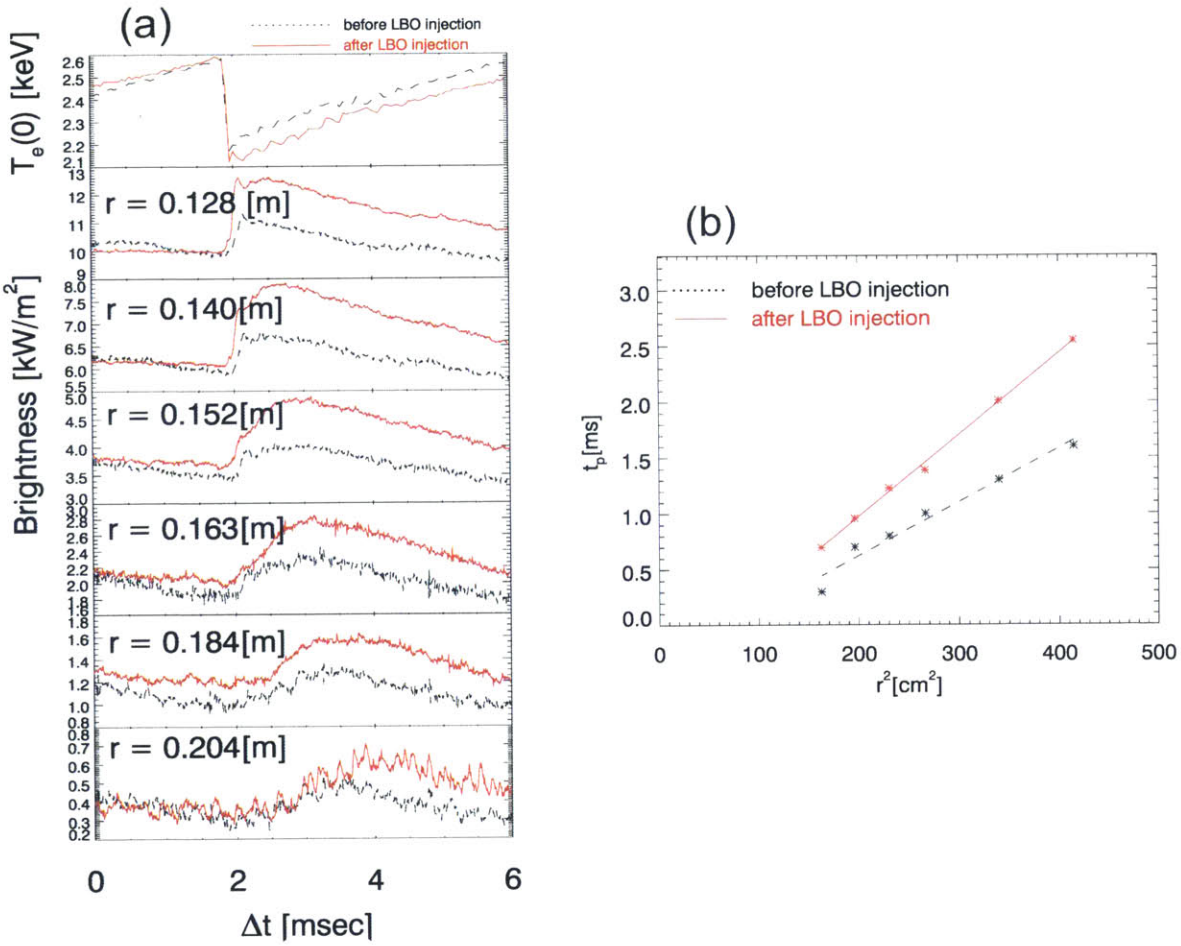

Figure 3-29: Comparison of (a) soft X-ray brightness chords and (b) time-to-peak during two sawtooth-induced heat pulses before (black, dashed lines) and after (red, solid lines) the LBO injection for an LOC plasma.

channels for two sawtooth events of one LOC plasma shot: one is before the cold pulse injection (black, dashed line) and the other is right after the cold pulse injection (red, solid line). The time-to-peak is found to be larger after cold pulse injection, as shown in Fig. 3-29(b) where the time-to-peak radial profile is presented. The heat pulse diffusivity $\chi^{hp} \propto r^2/t_p$ [226] is found to be reduced by $\sim 30\%$ after the cold pulse injection, which is consistent with the transport calculation above. It is worth noting that the analysis here assumes the heat pulse propagation as a diffusive process. The ballistic response is not considered.

3.6 Ion-scale Linear Gyrokinetic Analysis

Since the non-local effect is found to be correlated with the LOC/SOC transition, numerical studies of the turbulence characteristics for LOC and SOC plasmas were performed using the gyrokinetic code GYRO with $k_\theta \rho_s \leq 1.0$. Shown in Fig. 3-30 are the smoothed profiles of density (a), electron temperature (b) and ion temperature (c) in LOC (red solid lines) and SOC (blue dashed lines) plasmas. The gradients (d, e, f) are plotted as a/L, where L is the gradient length defined as $-X/\frac{\partial X}{\partial r}$, X could be n_e, T_e or T_i. The major difference in the gradients happens around $r/a = 0.8$, where a/L_{T_e} in LOC is slightly higher than in SOC; however a/L_{T_i} in LOC is significantly lower than in SOC. Linear gyrokinetic simulations are performed at two radii: $r/a = 0.5$ and $r/a = 0.75$. The input parameters of GYRO are listed in Table 3.2 and Table 3.3. Fig. 3-31 shows the results of real frequency (a) (c) and growth rate (b) (d) as a function of $k_\theta \rho_s$, for $r/a = 0.5$ (a) (b) and $r/a = 0.75$ (c) (d). k_θ is the poloidal wave number and $\rho_s = c_s/\Omega_i$ is the ion gryoradius with ion sound velocity $c_s = \sqrt{T_e/m_i}$. Red solid lines are for the LOC case and blue dashed lines are for the SOC case. Positive frequency indicates the modes propagate in the electron diamagnetic drift direction, and negative indicates the modes in the ion diamagnetic drift direction. At $r/a = 0.5$ both LOC and SOC plasmas are ITG dominant since the modes are in the ion diamagnetic direction for the range of $k_\theta \rho_s$ up to 1.0. At $r/a = 0.75$ for the LOC plasmas, the electron mode dominates. At this low wavenumber ($k_\theta \rho_s = 0 - 1.0$), it is TEM that will dominate for LOC plasmas. At $r/a = 0.75$ for the SOC plasmas, at lower $k_\theta \rho_s < 0.5$ it is electron mode dominant with smaller linear growth rate than that of LOC plasmas, and at higher $k_\theta \rho_s = 0.6 - 1.2$ it is ITG dominant. This indicates a mixed mode in SOC plasmas with a diminished TEM turbulence comparing to the LOC plasmas. Displayed in Fig. 3-32 are the coherence spectra of electron temperature fluctuations for the LOC and SOC discharges at $r/a \sim 0.8$ measured by CECE system [19], showing a reduction of electron temperature fluctuation across LOC/SOC transition, which is consistent with the diminished TEM turbulence in SOC plasmas.

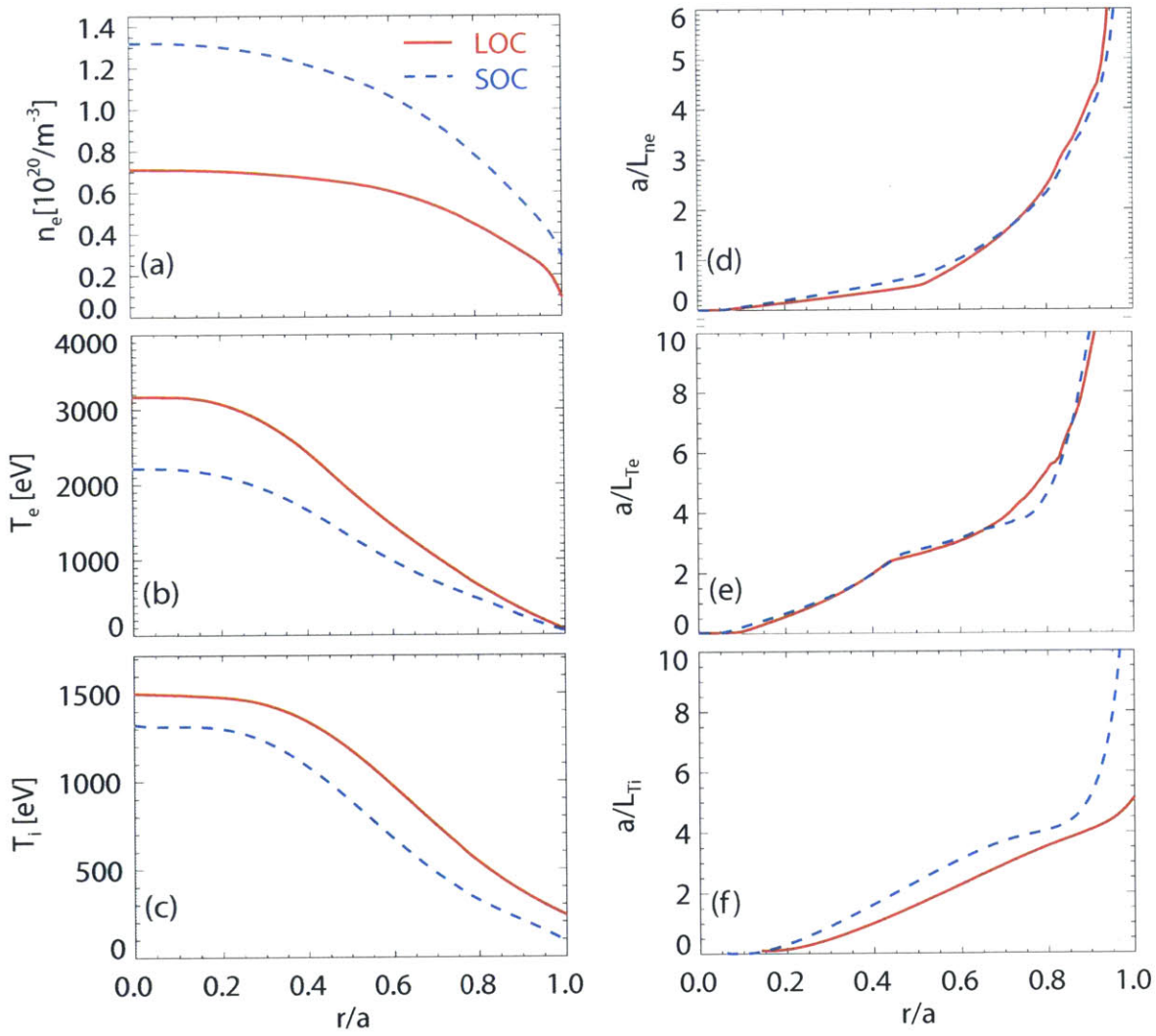

Figure 3-30: Profiles of electron density (a), electron temperature (b), ion temperature (c) and their gradients (d)(e)(f) for LOC (red solid lines) and SOC (blue dashed lines) discharges.

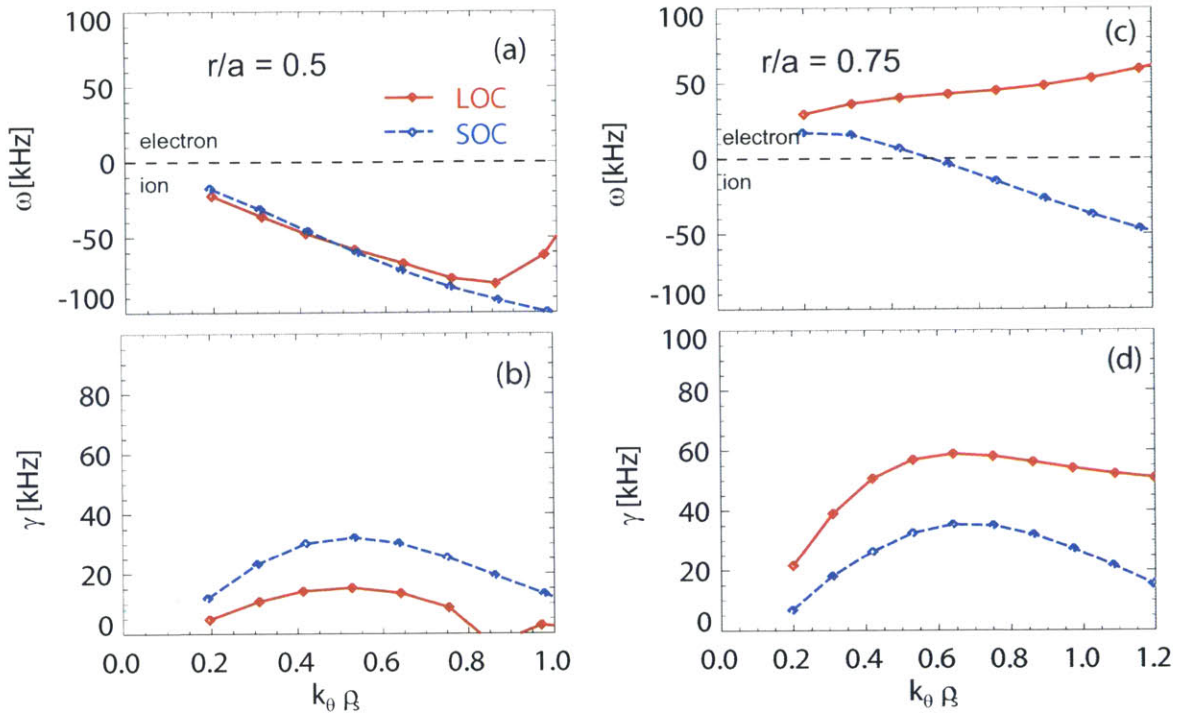

Figure 3-31: The real frequency (a)(c) and growth rate (b)(d) at $r/a = 0.5$ (a)(b) and $r/a = 0.75$ (c)(d) for LOC (red solid lines) and SOC (blue dashed lines) discharges. Positive real frequency indicates the modes in the electron diamagnetic direction, negative real frequency indicates the modes in the ion diamagnetic direction.

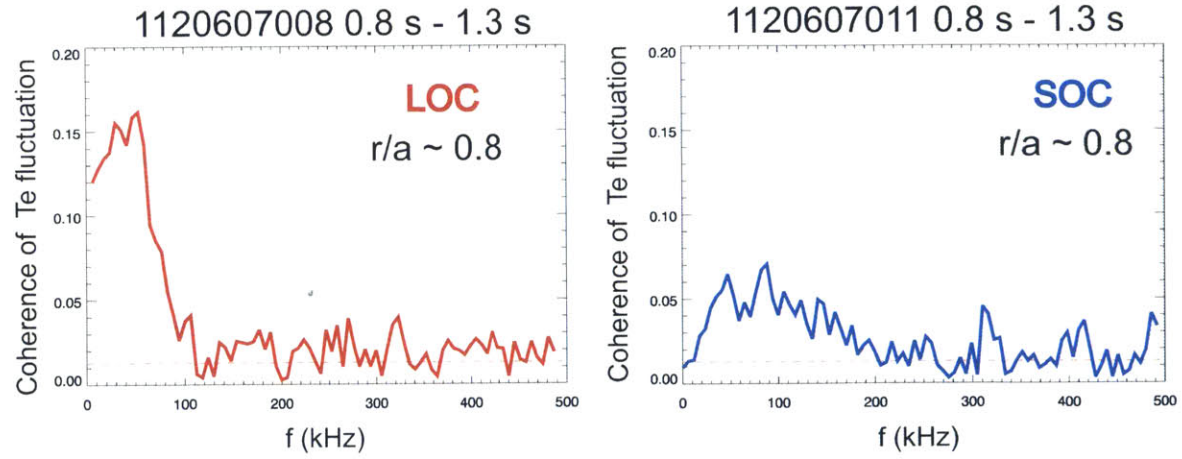

Figure 3-32: Coherence spectra of T_e fluctuations in (a) LOC and (b) SOC plasmas at $r/a \sim 0.8$ measured by CECE [19]. The fluctuation is time averaged over 0.8 s and 1.3 s.

Table 3.2: The input values for linear GYRO simulation at $r/a = 0.50$

Parameters	LOC	SOC
$\langle n_e \rangle$ (10^{20} m^{-3})	0.58	1.05
Aspect ratio (R/a)	3.095	3.094
Elongation κ	1.212	1.219
$s_\kappa = (r/\kappa)\,\partial\kappa/\partial r$	0.0551	0.0625
Triangularity δ	0.0596	0.0321
$s_\delta = (r/\delta)\,\partial\delta/\partial r$	0.0946	0.101
Safety factor q	1.230	1.271
$\hat{s} = (r/q)\,\partial q/\partial r$	0.944	0.947
$\nu_{e,i}/\,(c_s/a)$	0.035	0.131
Z_{eff}	3.6	1.75
T_i/T_e	0.615	0.677
n_i/n_e	0.688	0.878
a/L_{n_e}	0.485	0.673
a/L_{T_e}	2.619	2.753
a/L_{T_i}	1.674	2.466
$\eta_i = L_{n_i}/L_{T_i}$	3.449	3.641

Table 3.3: The input values for linear GYRO simulation at $r/a = 0.75$

Parameters	LOC	SOC
$\langle n_e \rangle$ (10^{20} m^{-3})	0.58	1.05
Aspect ratio (R/a)	3.082	3.080
Elongation κ	1.279	1.289
$s_\kappa = (r/\kappa)\,\partial\kappa/\partial r$	0.256	0.263
Triangularity δ	0.131	0.137
$s_\delta = (r/\delta)\,\partial\delta/\partial r$	0.324	0.328
Safety factor q	2.191	2.253
$\hat{s} = (r/q)\,\partial q/\partial r$	2.049	1.992
$\nu_{e,i}/\,(c_s/a)$	0.136	0.476
Z_{eff}	3.6	1.75
T_i/T_e	0.764	0.676
n_i/n_e	0.688	0.878
a/L_{n_e}	1.985	1.937
a/L_{T_e}	4.579	3.865
a/L_{T_i}	3.275	3.900
$\eta_i = L_{n_i}/L_{T_i}$	1.649	2.01

To demonstrate the sensitivity of the turbulence to the driving terms a/L_{n_e} and a/L_{T_i}, linear simulations were performed over a range of this parameter space at $r/a = 0.75$, as shown in Fig. 3-33. For each point of $[a/L_{n_e}, a/L_{T_i}]$ the linear growth

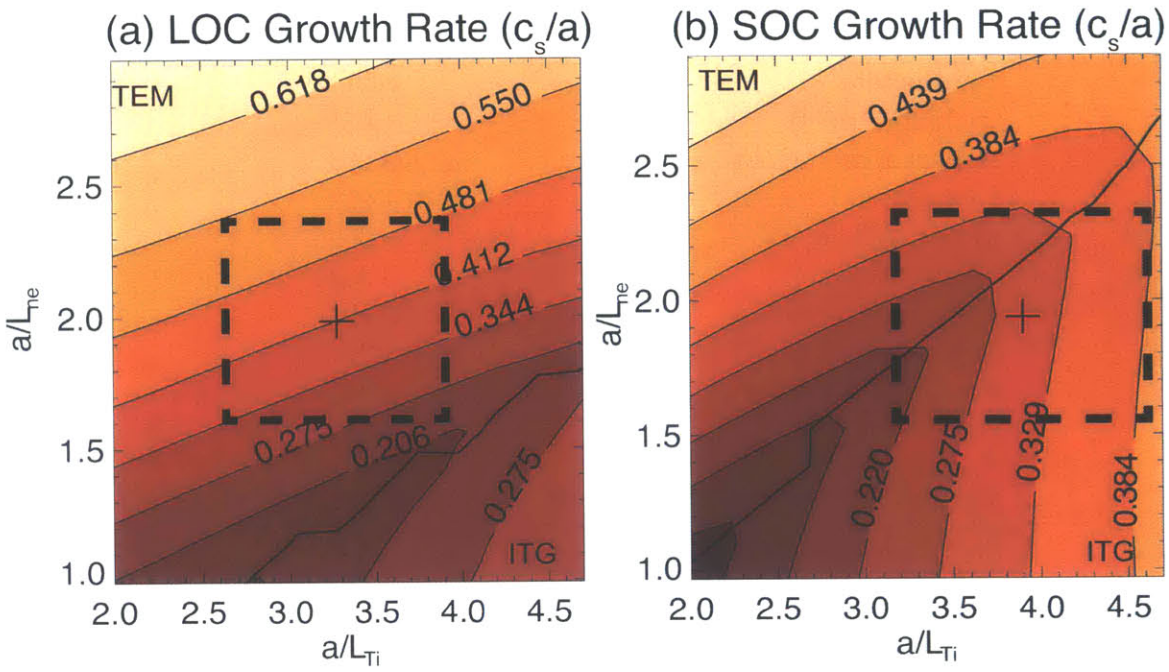

Figure 3-33: Contour plot of linear growth rate as a function of a/L_{T_i} and a/L_{n_e} for (a) an LOC plasma and (b) an SOC plasma at $r/a = 0.75$. The cross signs indicate the experimental values. The dashed square indicates the $\pm 20\%$ error bars for the gradient scale length.

rate is calculated over $k_\theta \rho_s = 0 - 0.75$ and the maximum growth rate (most unstable mode) is chosen. The growth rate values normalized to c_s/a (a is the machine minor radius) are indicated by the contour lines. For the left-upper part of the contour plot, the linear growth rate is sensitive to the change of electron density gradients, which is a feature of TEMs. For the right-lower part of the contour plot, the linear growth rate is sensitive to the change of ion temperature gradients, which indicates the dominance of ITG modes. The plus signs are experimental values of the gradients, and the dashed square indicates the typical $\pm 20\%$ error bars in gradient scale length. LOC plasmas (Fig. 3-33(a)) are in the TEM dominant regime, while SOC plasmas (Fig. 3-33(b)) are ITG dominant. But considering the error bars, the experimental point for SOC plasma is near the boundary of TEM and ITG modes, suggesting an ITG/TEM mixed mode, which is expected from Fig. 3-31(c). Fig. 3-34 shows the growth rate of the most unstable mode with the sensitivity scan of a/L_{T_e} and a/L_{T_i} at $r/a = 0.75$. The result is similar to the one in $[a/L_{n_e}, a/L_{T_i}]$ scan: at $r/a = 0.75$,

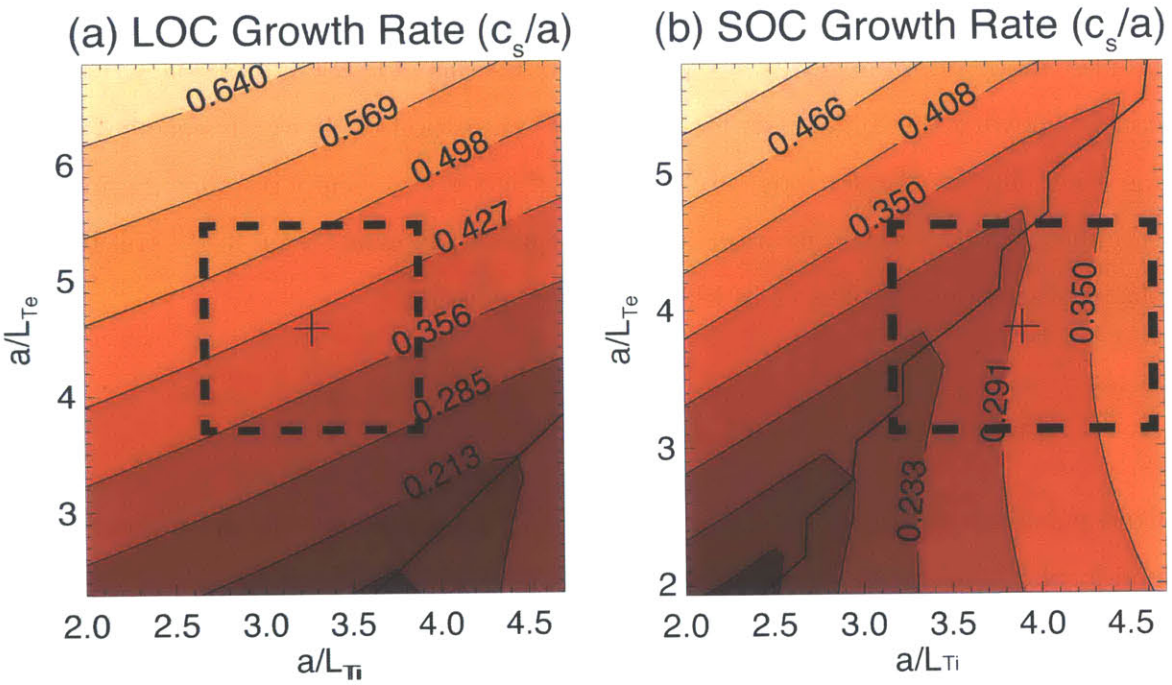

Figure 3-34: Contour plot of linear growth rate as a function of a/L_{T_i} and a/L_{T_e} for (a) an LOC plasma and (b) an SOC plasma at $r/a = 0.75$. The cross signs indicate the experimental values. The dashed square indicates the $\pm 20\%$ error bars for the gradient scale length.

LOC is TEM dominant, and SOC shows a mixed ITG/TEM mode feature.

As is mentioned in Section 3.1, in the outer plasma $r/a > 0.6$, the linear ion-scale simulation results do not consistently agree discharge by discharge. In [10, 218] the sensitivity scans showed that at $r/a \sim 0.7$ the LOC plasma is on the TEM/ITG boundary, while the SOC plasma is ITG dominant; in [220] at $r/a \sim 0.8$ the LOC plasma is found to be TEM dominant, while SOC plasma is on the TEM/ITG boundary. A diminished TEM turbulence is generally observed in experiments and simulations (i.e., the turbulence has a trend from TEM dominance to ITG mode dominance) as the plasma crosses the LOC/SOC boundary, which is consistent with the hypothesis for LOC/SOC transition. It is worth noting that the ion-scale linear simulations are crude evidences to support this hypothesis. Nonlinear multi-scale simulation may be required to correctly quantify the roles of electron and ion turbulences in LOC and SOC plasmas.

3.7 Summary and Discussion

Cold pulse injection experiments in Alcator C-Mod extend the understanding of the non-local phenomenon based on existing experiments from other machines. The measurement of ion temperature profiles could be used to verify various theoretical attempts to explain this non-local effect [227]. As seen with many other references, the transport analysis shows a reduction of core electron heat transport associated with the non-local effect, which is consistent with the fluctuation measurements. Fourier transformed profiles of the repetitive cold pulse injection experiments suggest the pure diffusive transport model is not valid for LOC discharges with the non-local effect, and an inward heat pinch should be responsible for this contradiction.

The non-local effect has a density/collisionality dependence. The results from Alcator C-Mod experiments suggest that this dependence is correlated with the LOC/SOC transition density and rotation reversal critical density. One unified explanation for the existence of a transition density for apparently unrelated

phenomena is the change of dominant turbulence types from electron modes (TEMs and ETG modes) in low collisionality plasmas to ion modes (ITG) in high collisionality plasmas. Experiments with direct electron heating (like ECRH on T-10 [228] and LH on Tore-Supra [229]) show that the confinement increases linearly with electron density when electron transport dominates. The dependence is weak with ion heating in ion transport loss dominant regimes [230]. This suggests the LOC regime is intrinsic to the electron mode, and the SOC regime is more likely to be ion mode dominant. The non-locality may be intrinsic in LOC where electron modes are dominant. As the collisionality increases and ion modes dominate the transport, the non-locality will diminish or disappear in electron transport channels. It is worth noting that the non-local effect is a transient phenomenon intrinsic in the LOC regime. The non-local phenomenon in the LOC regime is probably due to a transient ITB formed during the transient phase, which violates the local flux-gradient relation. The formation of a transient ITB during cold pulse injection may be related to turbulence spreading, or turbulence suppression by dilution. Turbulence was significantly reduced with impurity seeding in DIII-D L-mode discharge [231]. The dilution may play a role in the turbulence suppression shown in Fig. 3-22. For low density LOC plasma, Z_{eff} can be increased by $\sim 20\% - 30\%$ during LBO injection; the dilution effect is smaller for SOC plasma with an $\sim 10\%$ increase of Z_{eff}. Gyrokinetic simulations shown above are performed with time averaged profiles without considerations of the dilution due to LBO injection. Further non-linear simulations should be performed to identify the roles of dilution in these LOC plasma discharges.

The ion-scale linear gyrokinetic simulations show that at $r/a = 0.75$ the LOC plasma is TEM dominant; the SOC plasma is ITG/TEM mixed mode dominant with consideration of the measurement uncertainty. A diminished TEM turbulence is observed both from CECE measurement and the simulation near this radius, which is consistent with the unifying hypothesis. At $r/a = 0.5$, the linear simulation shows that both LOC and SOC plasmas are ITG mode dominant, which doesn't support the hypothesis. Two points should be emphasized here. First, it may not be proper to

simply connect the local turbulence at a specific location with the global phenomena. The Ohmic energy confinement time is obvious a global parameter; the core plasma rotation is shown to be strongly correlated with edge plasma parameters [210], which suggests a global effect in momentum transport; the non-local effect is naturally a global phenomenon. The simulations at one specific radius don't necessary prove or disprove the hypothesis. Secondly, the ITG-TEM interpretation in ion-scale linear simulations may be oversimplified. Nonlinear multi-scale simulation may be required to correctly quantify the roles of electron and ion turbulences in LOC and SOC plasmas. The most recent multi-scale gyrokinetic simulation [209] shows that the ETG mode is the dominant heat transport mechanism at low ion temperature gradient drive, and ITG modes take over the heat transport with the increase of the ion temperature gradient. This may be applied to explain the fast response of cold pulses in the LOC regime [232]: the large linear growth rate γ^{ETG} could play a role in the fast response, and the observed radially elongated streamer structure [98] suggests a spatially correlated transport paradigm.

The understanding for rotation reversal requires one to examine the turbulent momentum flux with residual stress term [233]

$$\Pi_{r,\phi} = \langle n \rangle \langle \tilde{v}_r \tilde{v}_\phi \rangle + \langle \tilde{v}_r \tilde{n} \rangle \langle v_\phi \rangle + \langle \tilde{n} \tilde{v}_r \tilde{v}_\phi \rangle \tag{3.13}$$

$$\langle \tilde{v}_r \tilde{v}_\phi \rangle = -\chi_\phi \frac{\partial \langle v_\phi \rangle}{\partial r} + V_{\mathrm{p}} \langle v_\phi \rangle + \Pi_\phi^{\mathrm{res}} \tag{3.14}$$

In Eq. 3.13 the first term is the toroidal Reynolds stress, the second is the convective flux and the third term represents the nonlinear flux driven by processes such as mode–mode coupling and turbulence spreading. Here only the Reynolds stress term will be discussed. The latter two terms are neglected, but the nonlinear flux term may be important when a strong nonlinear process is generating rotation. In the Reynolds stress flux Eq. 3.14, χ_ϕ is the momentum diffusivity, V_{p} is the momentum pinch, and Π_ϕ^{res} is the residual stress. A change in sign of any of these could give rise to a direction change in toroidal rotation. χ_ϕ is unlikely to invoke rotation reversals because it is positive definite. The turbulent pinch consists of two

parts: the turbulent equipartition pinch (TEP) V_p^{TEP} and thermoelectric pinch V_p^{th} [234]. For both ITG and TEM instabilities, the TEP pinch is inward and cannot change sign unless the density gradient changes sign. The thermoelectric pinch can change sign depending on the combination of temperature and density gradients, but it seems not to be the key player in the rotation reversal [12].

The residual stress Π_ϕ^{res} is a consequence of wave-particle momentum exchange enforced by outgoing wave boundary conditions. Physically the residual stress converts the energy flux Q_e or Q_i into a net flow. It is the only way to spin up a plasma from rest [233] because for $\Pi(0) = 0$

$$\begin{aligned} \partial_t \int_0^a \langle P_\phi \rangle \, dr &= -nm \left(-\chi_\phi \frac{\partial \langle v_\phi \rangle}{\partial r} + V_{\mathrm{p}} \langle v_\phi \rangle + \Pi_\phi^{\mathrm{res}} \right) \Big|_0^a \\ &\approx -nm \left(-\chi_\phi \frac{\partial \langle v_\phi \rangle}{\partial r} + V_{\mathrm{p}} \langle v_\phi \rangle + \Pi_\phi^{\mathrm{res}} \right) \Big|_{r=a} \end{aligned} \tag{3.15}$$

With $\langle v_\phi \rangle = 0$ and $\partial_r \langle v_\phi \rangle = 0$, we get

$$\partial_t \int_0^a \langle P_\phi \rangle \, dr \approx -nm \Pi^{\mathrm{res}}(a) \tag{3.16}$$

So the radial integration of momentum drive is determined by the edge temperature and density gradients through the residual stress. This is consistent with the observation in C-Mod [5, 210] that the rotation in H-mode and I-mode plasmas develops from the edge and scales with the edge temperature gradient. The residual stress can change sign depending on the nature of the underlying turbulence, such as by a change in the mode propagation direction from the electron diamagnetic drift direction to the ion direction [217, 12]. This is consistent with the hypothesis for the non-local effect and the LOC/SOC transition.

It is worth to mention the recent result on ASDEX Upgrade [235], which shows that the intrinsic rotation strongly dependents on the electron density gradient scale length R/L_{n_e}, and TEM to ITG transition is not observed during rotation reversal. A future systematical analysis of the C-Mod intrinsic rotation database to study the relations among toroidal rotation, rotation shear and other plasma parameters is

strongly desired.

Chapter 4

Study of Momentum Transport Coefficients in ICRF Modulation Experiments

4.1 Introduction

The ability of HiReX–SR to measure ion rotation and temperature profiles simultaneously makes it a powerful tool to study momentum transport, which is a hot area in fusion research. The radial transport of toroidal rotation and the momentum source determine the rotation profile. The toroidal rotation gradient, which is connected to the $E \times B$ shear, plays important roles in turbulence suppression and confinement improvement. It is believed to be responsible for the L–H transition [125, 126, 127, 128, 129] and internal transport barrier (ITB) formation [130, 131, 132, 133, 134, 135]. What is more, toroidal rotation also helps stabilize resistive wall modes (RWMs) [39, 136].

The significance of the momentum transport study is twofold. First, it is helpful to compare the momentum diffusivity and thermal diffusivity, especially in the ion temperature gradient (ITG) dominant regime where the two transport channels are predicted to be similar [142]. Secondly, the inferred momentum pinch can be

compared with theories, for example the momentum pinch predicted by a model based on the Coriolis effect [145]:

$$\frac{RV_{\text{pinch}}}{\chi_\phi} = -4 - \frac{R}{L_n} \tag{4.1}$$

A detailed derivation of this pinch can be found in Appendix. A.

The momentum transport coefficients can be determined with the momentum transport equation:

$$\frac{\partial}{\partial t}(nV_\phi) = -\nabla \cdot \Pi_\phi + S \tag{4.2}$$

$$\Pi_\phi = -\chi_\phi \frac{\partial}{\partial r}(nV_\phi) + V_{\text{pinch}} nV_\phi + \Pi^{\text{res}} \tag{4.3}$$

where V_ϕ is the toroidal rotation, Π_ϕ is the radial momentum flux, S is the momentum source, χ_ϕ is the momentum diffusivity, V_{pinch} is the momentum pinch, Π^{res} is the residual stress which describes the component of momentum flux that is independent of the rotation itself and its gradient (flow shear).

Because there are three unknowns χ_ϕ, V_{pinch} and Π^{res} in Eq. 4.3, perturbation experiments and some assumptions are necessary to determine the coefficients. In Alcator C-Mod, the rotation can be driven by ICRF in mode conversion experiments [44, 45, 46] and by LHCD [8, 138, 139, 140]. In other experiments, it is momentum source free in the core, $S = 0$. The rotation can be modulated with ICRF minority heating. By assuming the rotation is driven from the edge plasma and neglecting the residual stress in the core, it is possible to determine the χ_ϕ and V_{pinch} separately, which will be discussed in Section. 4.3.

4.2 ICRF Modulation Experiment

Fig. 4-1 shows the time traces of an ICRF minority heating experiment at three different plasma currents: 0.8 MA, 1.0 MA and 1.2 MA. For the high current shots 1120217026 and 1120217029, plasma density goes across the intrinsic rotation reversal density [11, 12, 10] and the core rotation changes direction from counter-current

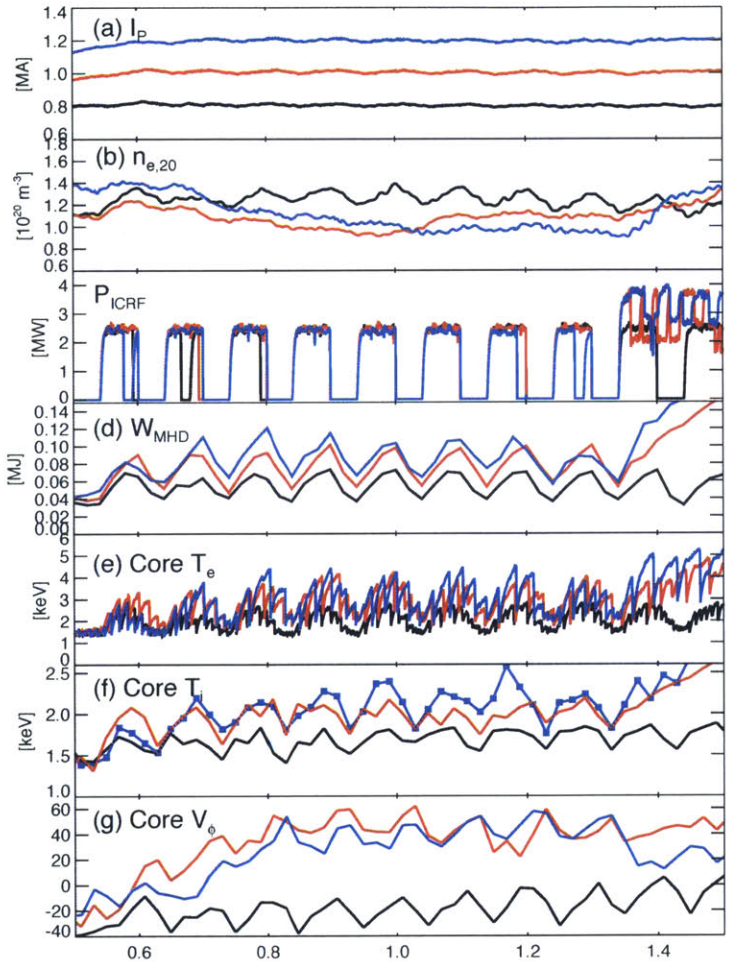

Figure 4-1: The time traces of (a) current, (b) ICRF power, (c) line averaged density, (d) stored energy, (e) core electron temperature, (f) core ion temperature and (g) core toroidal rotation for three C-Mod shots: 1110217026 (red, 1.0 MA) 1120217029 (blue, 1.2 MA) and 1110217032 (black, 0.8 MA).

(negative) to co-current (positive), as is shown in the last row of Fig. 4-1. This reversal can be due to the direction change in the residual stress, which is related to the regime change of dominant instabilities (ion modes to electron modes). For this reason, these two shots are not suitable to determine of momentum transport coefficients as the momentum source (residual stress) term is difficult to model. The shot 1120217032, whose density is relatively steady and is deeply in the high collisionality regime, or saturated Ohmic confinement (SOC) regime, is chosen for this study.

As a reminder, the electron and ion temperature profiles are modulated by the ICRF. This may hinder the validity of the modeling in the next section because the

χ_ϕ and V_{pinch} are assumed to be constant during ICRF.

4.3 "Toy" Model for Momentum Transport

The parallel momentum transport equation is

$$\frac{\partial}{\partial t}\left[n\left(r\right)V_\phi\left(r,t\right)\right] = -\frac{1}{r}\frac{\partial}{\partial r}\left[r\Pi_\phi\left(r,t\right)\right] + \cancel{S\left(r,t\right)} \tag{4.4}$$

where

$$\Pi_\phi\left(r,t\right) = -\chi_\phi\left(r\right)\frac{\partial}{\partial r}\left[n\left(r\right)V_\phi\left(r,t\right)\right] + V_{\text{pinch}}\left(r\right)n\left(r\right)V_\phi\left(r,t\right) \tag{4.5}$$

The momentum source $S\left(r,t\right)$ is neglected because we focus on the core where there is no direct momentum input, assuming that the momentum driving term is located in the edge of plasma. The residual stress Π^{res} is also neglected in the core region of interest $r/a \leq 0.5$, with the assumption that it is not modulated in the core, therefore it doesn't affect the perturbative analysis. One should notice the linear acceleration in the core rotation shown in Fig. 4-2. This can be accounted to a time-independent residual stress term: $\partial_t V_\phi \propto \partial_r \Pi^{\text{res}} \sim$ const. The density is assumed to be constant in time, based on the experiment in which the density modulation is smaller than the rotation modulation. The diffusive and pinch coefficients are also assumed to be constant in time. This assumption may have drawbacks because the temperature profile, whose gradient is considered to drive the momentum transport, varies with time.

The toroidal rotation $V_\phi\left(r,t\right)$ is modeled with a sinusoidal form

$$V_\phi = V_{\phi,0} + \tilde{V}_\phi\left(r,t\right) = V_{\phi,0} + A\left(r\right)\sin\left(\omega t - \phi\left(r\right)\right) \tag{4.6}$$

where $A\left(r\right)$ and $\phi\left(r\right)$ are the amplitude and phase information of modulated toroidal rotation, and $\omega/2\pi$ is the ICRF modulation frequency.

Integrating the oscillating part of Eq. 4.4 yields

$$\tilde{\Pi}_\phi(r,t) = -\frac{1}{r}\int_0^r r\frac{\partial(nV_\phi)}{\partial t}dr = \sin(\omega t)\left[-\frac{\omega}{r}Y(r)\right] + \cos(\omega t)\left[-\frac{\omega}{r}X(r)\right] \tag{4.7}$$

where

$$X = \int_0^r rn(r)A(r)\cos(\phi(r))\,dr \tag{4.8}$$

$$Y = \int_0^r rn(r)A(r)\sin(\phi(r))\,dr \tag{4.9}$$

Rearranging the oscillating part of Eq. 4.5 yields:

$$\begin{aligned}\tilde{\Pi}_\phi(r,t) = \sin(\omega t)&\left\{\cos\phi\left[-\chi_\phi\frac{\partial}{\partial r}(nA) + V_{\text{pinch}}nA\right] + \sin\phi\left[\chi_\phi nA\frac{\partial\phi}{\partial r}\right]\right\}\\ + \cos(\omega t)&\left\{-\sin\phi\left[-\chi_\phi\frac{\partial}{\partial r}(nA) + V_{\text{pinch}}nA\right] + \cos\phi\left[\chi_\phi nA\frac{\partial\phi}{\partial r}\right]\right\}\end{aligned} \tag{4.10}$$

By matching the sin and cos terms of Eq. 4.7 and Eq. 4.10, we can get the χ_ϕ and V_{pinch} in terms of $A(r)$ and $\phi(r)$:

$$\chi_\phi = -\frac{\omega(X\cos\phi + Y\sin\phi)}{nrA\frac{\partial\phi}{\partial r}} \tag{4.11}$$

$$V_{\text{pinch}} = \frac{1}{nA}\left[\chi_\phi\frac{\partial}{\partial r}nA + \frac{\omega}{r}(X\sin\phi - Y\cos\phi)\right] \tag{4.12}$$

In the limit $r \to 0$, Eqs. 4.11 and 4.12 are

$$\chi_\phi = -\frac{\omega r}{2\frac{\partial\phi}{\partial r}} \tag{4.13}$$

$$V_{\text{pinch}} = \frac{\chi_\phi}{nA}\frac{\partial(nA)}{\partial r} \tag{4.14}$$

Fig. 4-2 shows the sinusoidal fitting (red dashed lines) and experimental toroidal rotation (blue dash-dotted lines) at different radii. The fitting is based on Eq. 4.6, except that $V_{\phi,0}$ is replaced with $V_{\phi,0}+at$, because the toroidal rotation is observed to be a combination of sinusoidal oscillation and linear acceleration. The origin of this

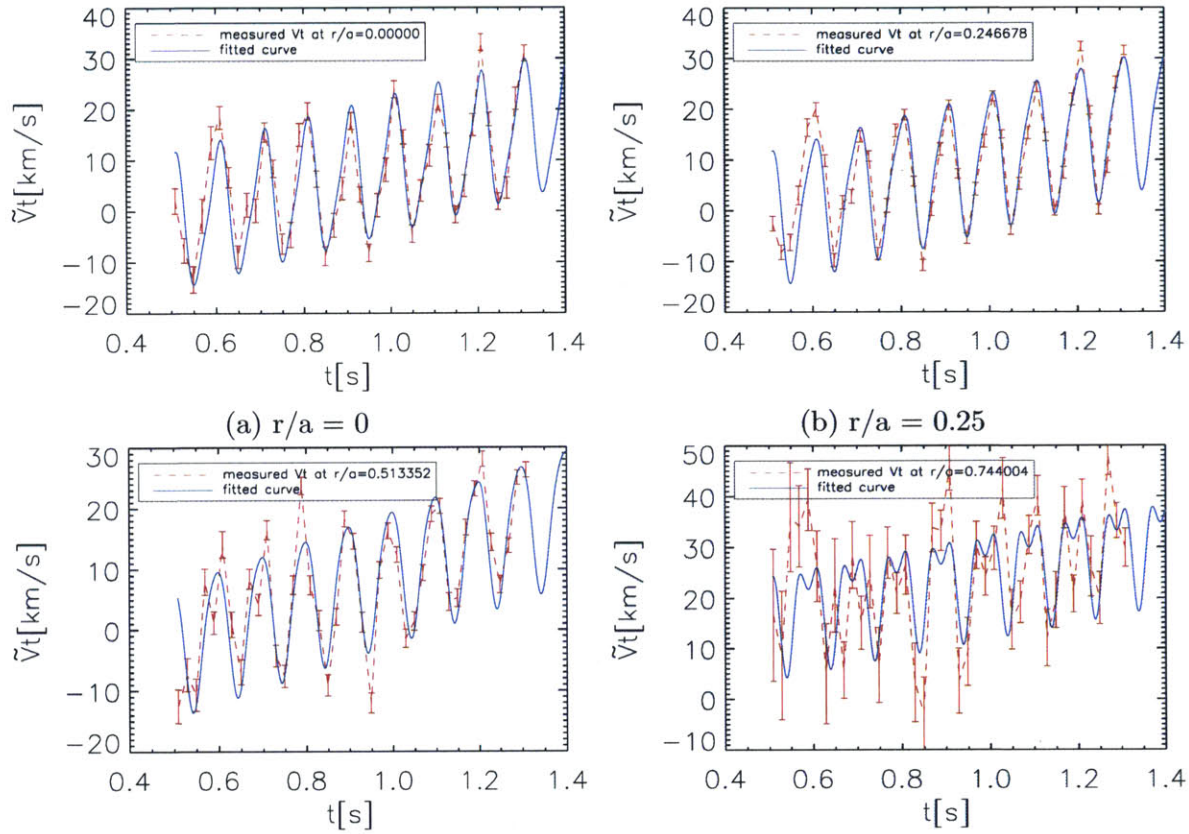

(a) r/a = 0 (b) r/a = 0.25

(c) r/a = 0.5 (d) r/a = 0.75

Figure 4-2: The sinusoidal fitting of toroidal rotation using the model in Eq. 4.6 at radii (a) r/a = 0.0, (b) r/a = 0.25, (c) r/a = 0.5, (d) r/a = 0.75.

acceleration is unclear. Assuming it is related to a constant residual stress and taking the oscillating part of Eq. 4.4, the diffusive and convective coefficients in Eqs. 4.11 and 4.12 still hold.

Fig. 4-3 shows the amplitude $A(r)$ and phase $\phi(r)$ profiles obtained from the sinusoidal model. The monotonically decreasing phase profile is consistent with the previous observations that the rotation change originates from the outer plasma [5, 210]. The decreasing amplitude profile (together with monotonically decreasing density profile) suggests an inward pinch, which can be easily seen from Eq. 4.14 at the limit $r \to 0$. The error bar indicates the 1σ error calculated from the covariance matrix for the fitting parameters.

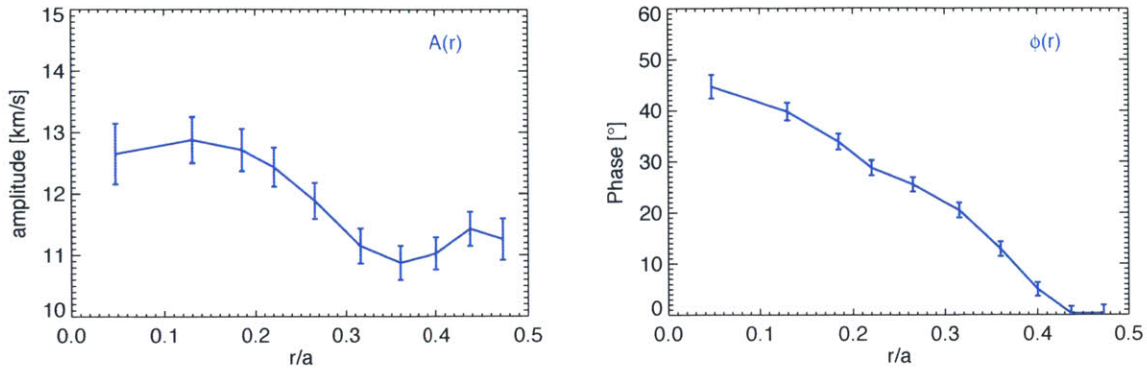

(a) $A(r)$ profile

(b) $\phi(r)$ profile

Figure 4-3: The amplitude $A(r)$ and phase $\phi(r)$ profiles of modulated toroidal rotation.

Error Analysis

The errors in parameters A and ϕ propagate into the calculated coefficients. The error in χ_ϕ and V_{pinch} are estimated based on Eq. 4.13 and Eq. 4.14

$$\frac{\delta\chi_\phi}{\chi_\phi} = \sqrt{\left(\frac{\delta r}{r}\right)^2 + \left(\frac{\delta\partial_r\phi}{\partial_r\phi}\right)^2} \tag{4.15}$$

$$\frac{\delta V_{\text{pinch}}}{V_{\text{pinch}}} = \sqrt{\left(\frac{\delta\chi_\phi}{\chi_\phi}\right)^2 + \left(\frac{\delta\partial_r \ln(nA)}{\partial_r \ln(nA)}\right)^2} \tag{4.16}$$

where δr is the variance of minor radius over 0.5 - 1.3 s, $\delta\partial_r\phi$ and $\delta\partial_r \ln(nA)$ are estimated as

$$\delta\partial_r\phi = \left|\frac{d(\partial_r\phi)}{d\phi}\right| \delta\phi \tag{4.17}$$

$$\delta\partial_r \ln(nA) = \sqrt{\left(\frac{d(\partial_r \ln(nA))}{dA}\delta A\right)^2 + \left(\frac{d(\partial_r \ln(nA))}{dn}\delta n\right)^2} \tag{4.18}$$

where the density error is assumed to be 5% ($\delta n \approx 0.05n$) in the error calculation.

Fig. 4-4 are the diffusive and convective coefficient profiles calculated using Eq. 4.11 and Eq. 4.12. A negative value of convection means an inward pinch. The

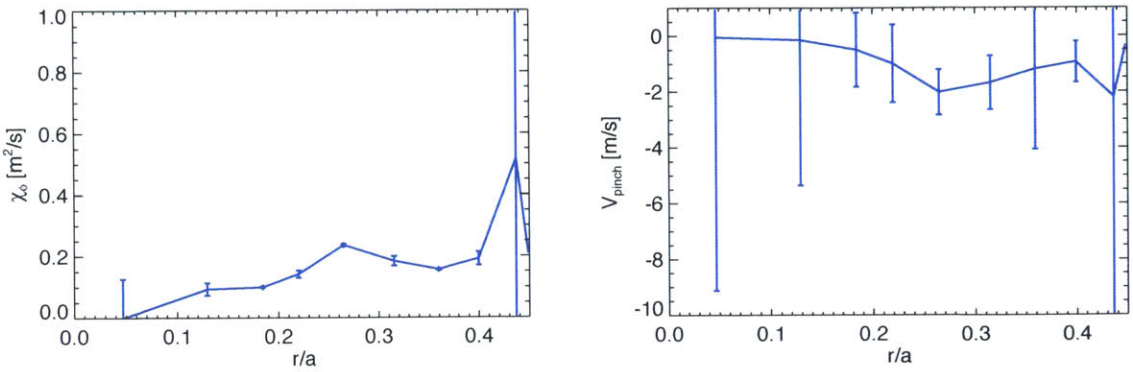

(a) χ_ϕ profile

(b) V_{pinch} profile

Figure 4-4: The diffusivity χ_ϕ and pinch V_{pinch} profiles.

error in the pinch is somehow large. This is due to the non-linear term $\delta\partial_r \ln(nA)$ as the denominator in Eq. 4.16.

4.4 Prandtl Number and Momentum Pinch

If ion temperature gradient (ITG) modes are the dominant instabilities, momentum and ion heat transport can be coupled tightly. The Prandtl number, defined as the ratio between momentum diffusivity and thermal diffusivity, χ_ϕ/χ_i, is a good measure of the connection between energy and momentum transport, which is expected to be order unity in ITG dominant plasmas. Fig. 4-5a is the profile of Prandtl number for the shot analyzed above. The ion thermal diffusivity χ_i is calculated by TRANSP from the power balance equation and averaged over the ICRF modulation time. As is shown, the Prandtl number is substantially below one between $0.1 < r/a < 0.5$, indicating weakly coupled momentum and ion thermal transport.

The momentum pinch profile is compared with the theoretical value based on Eq. 4.12, shown in Fig. 4-5b. A mismatch exists between the two profiles, but they agree in the order of magnitude and sign within uncertainty.

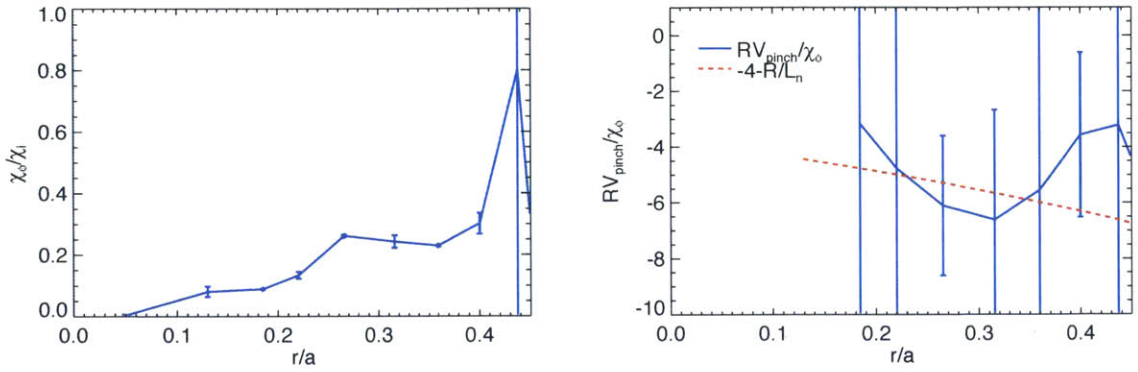

(a) Prandtl number χ_ϕ/χ_i

(b) $RV_{\text{pinch}}/\chi_\phi$ profile

Figure 4-5: The Prandtl number χ_ϕ/χ_i and momentum pinch $RV_{\text{pinch}}/\chi_\phi$. Theoretical value $-4 - R/L_n$ is also plotted.

4.5 Summary

In this chapter, a toy model is applied to the ICRF modulation experiment to extract the momentum diffusive and convective coefficients. The model is based on several assumptions:

- Momentum source and residual stress terms are neglected in the core plasma.
- The momentum transport coefficients are constant in time.
- The toroidal rotation follows a sinusoidal form.

It is found that within $0.1 < r/a < 0.5$, the momentum diffusivity is lower than the ion thermal diffusivity, indicating weakly coupled momentum and ion thermal transport. NBI modulation experiment on JET [41] shows Prandtl number $P_r \approx 1$ in ITG dominant H-mode plasmas. It is not unexpected here to get a Prandtl number smaller that 1 if the plasma is not ITG dominant. This should be verified with gyrokinetic analysis.

An inward momentum pinch is obtained on the same order of the Coriolis pinch as is predicted in [145]. The error bars are relatively large due to the nature of the perturbative analysis.

Lastly it is worth emphasizing the difficulty to perform rotation perturbation experiment in Alcator C-Mod, due to the lack of a well modeled momentum source such as a neutral beam, which is an efficient rotation modulation tool with well understood torque modeling. ICRF modulation in minority heating scheme is used to perturb the rotation, where the ion and electron temperature are also modulated. The momentum source and residual stress terms are assumed to be not perturbed. These limitations and assumptions challenge the validity of the perturbative analysis. ICRF mode conversion has proven to drive significant rotation [44, 45, 46]. The mode conversion modulation experiment will be helpful in the study of momentum transport, but it may require the implementation of flow drive theories on resonant wave-ion interactions [236, 237, 238, 239, 240].

Chapter 5

ICRF Induced Argon Pumpout

Accumulation of intermediate and high Z impurities is an important issue for fusion plasmas. Energy loss by impurity radiation could degrade energy confinement, sometimes even causing disruptions due to high impurity concentration. HiReX–Sr is a useful diagnostic for the impurity transport study by providing the spatially and temporally resolved impurity emission intensities. It has been actively used to study calcium impurity transport [20, 148, 241, 242]. Recently, a phenomenon potentially useful for active impurity control has been observed in Alcator C-Mod, which is discussed in this section.

5.1 Introduction

Impurities come into the plasma in two ways. First, the exhaust from high power plasmas will strike the wall and impurities from the wall material (boron, carbon, molybdenum, tungsten, etc.) will sputter into the plasma. These are intrinsic impurities. Secondly, some impurities are actively puffed into the plasma for diagnostic purposes or for as a radiating mantle to mitigate the power deposited onto the divertor; these are non-intrinsic impurities. In Alcator C-Mod, intrinsic impurities include molybdenum (full molybdenum wall) and boron (boronized wall). Non-intrinsic impurities include calcium (injected by the LBO system for impurity transport studies), argon (diagnostic gas for HiReX), nitrogen and neon for edge

radiation, etc.

The presence of high Z impurities leads to higher radiation which hinders the plasma performance. Tungsten ($^{184}_{74}W$) is the proposed wall material for ITER. A tungsten concentration of barely $10^{-5} \sim 10^{-4}$ of electron density translates is estimated as the allowable limit for ignited plasma [243]. What is more, neoclassical theory predicts that impurity density peaking is significant in the core plasma for high Z impurities. For this reason, the understanding of impurity transport and control is important for fusion research.

In the beginning of each C-Mod campaign, the ICRF system needs to be tested to ensure proper operation and the antennas need to be conditioned. Furthermore after each vessel opening, the hydrogen isotopic ratio in ^2D plasmas is high due to the water (H_2O) retained in the first wall. Wall conditioning is necessary to reduce the hydrogen level for normal operations, because the primary ICRF heating scheme is hydrogen minority heating which requires a n_H/n_D ratio between 5% - 10%.

Argon pumpout during ICRF has been observed recently in Alcator C-Mod ICRF test and conditioning experiments. This pumpout happens only when the H/D ratio is relatively high ($n_H/n_D \approx 35\% - 50\%$), at which level the H-D mode conversion layer is close to the Ar^{16+} (Ar^{16+} will be the dominant state for the experimental conditions) 2^{nd} harmonic resonance layer. However, it is still not clear if it is a resonant or peripheral/edge effect that dominates the pumpout process.

A similar phenomenon was first observed in the TFR tokamak[244], where the authors reported the experimental observation that a heavy impurity (argon) is efficiently pumped out of the two-ion-component plasma in the ICRF mode conversion regime. This was explained as the result of the two-ion hybrid layer overlaping with the second harmonic resonance layer of one of the argon ions.

In the TFR paper, the resonance charge state Ar^{16+} was not directly measured, but inferred by Ar^{15+} observations. Here we report the observation of argon pumpout during ICRF experiments at Alcator C-Mod with direct measurements of intensity and temperature profiles of Ar^{16+}, provided by HiReX–Sr.

5.2 Argon Pumpout during ICRF in H-D plasmas

Fig. 5-1 (a) shows the time traces of the plasma current (dark solid line) and argon puff (blue dashed line). The argon is puffed in the starting stage of the shot for 75 ms, from 0.3 s to 0.375 s. Argon is a recycling impurity because the argon ions, as a noble gas, are chemically inert and are backscattered by the first wall. Hence the observed argon emission intensities take $\sim$ 100s ms (ionization and transport) to build up and then become saturated (recycling), as shown in Fig. 5-1 from the core (b) and edge (c) Ar^{16+} w line $(1s2p\ ^1P_1 \rightarrow 1s^2\ ^1S_0, 3.9492\mathring{A})$ intensity, measured by HiReX–Sr. As a comparison, the time trace of a non-recycling impurity calcium (Ca^{18+} w line) is shown in 5-2, in which the intensity exponentially decays shortly after the LBO injection. In another shot (1140221015) with ICRF, the argon is strongly pumped out when ICRF is on, as shown in Fig. 5-1 (d) and (e). This effect is observed both in the core plasma $r/a \sim 0$ and outer plasma $r/a \sim 0.6$. For shot 1140221015, the ICRF E antenna is used from 1.0 s to 1.5 s with power of 0.6 MW, i.e. 0.3 MJ energy is delivered from the low field side. The ICRF frequency is 80 MHz, and the on-axis magnetic field B_0 is 5.4 T. With this ICRF frequency and magnetic field, the hydrogen (proton) fundamental resonance is located at $R_H = R_0 = 0.66$ m (Fig.5-10).

The pumpout happens only when the hydrogen level is relatively high. Fig. 5-3 is the ratio of core Ar^{16+} w line minimum intensity I_{min} and maximum intensity I_{max} as a function of H/D ratio for several shots where the H/D ratio is scanned between 1% and 70%. The data are taken over runs of 20101015, 20140221 and 20140225. I_{max} is calculated as the maximum intensity shortly before the ICRF, I_{min} is calculated as the minimum intensity within 200 ms after the ICRF is on. The H/D ratio n_H/n_D is measured by high resolution visible Balmer-α emission spectrometer [245] and is time averaged over $(t-0.1)$ s and $(t+0.4)$ s, where t is the pumpout starting time in second. The error bars on H/D ratio indicate the standard derivation of the time average. The discharges with only partial Balmer spectrometer data that don't cover the time t are not taken into account, because H/D ratio measured by Balmer spectrometer may not be steady within a discharge. This can be seen in Fig. 5-4.

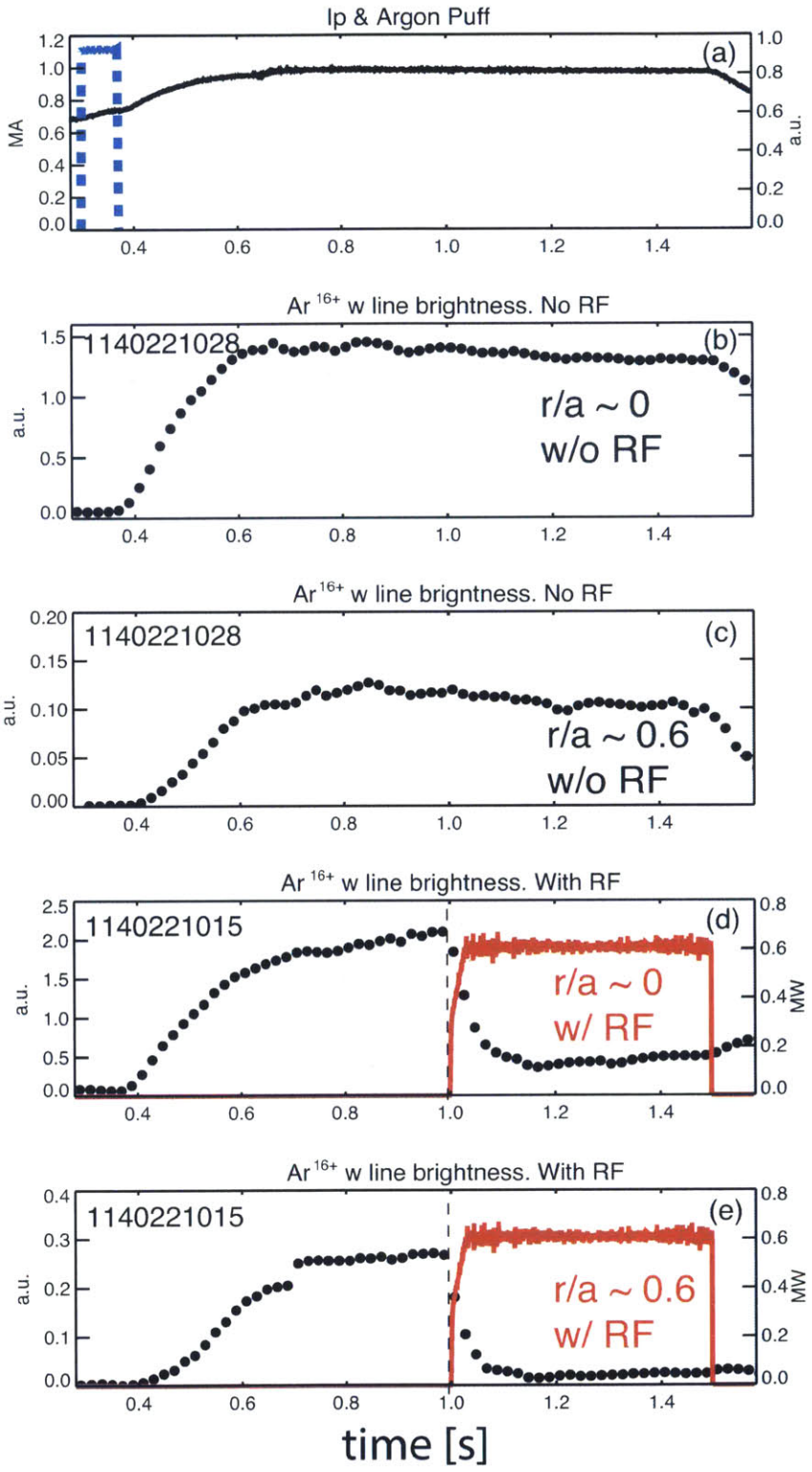

Figure 5-1: From top to bottom: time traces of (a) plasma current (dark solid line) and argon puff (blue dashed line); core (b, d) and edge (c, e) Ar^{16+} w line (resonance line) intensity without ICRF (b, c) and with ICRF (d,e). The ICRF trace is indicated in (d, e) by red lines. The argon intensities are normalized with the same constant. The H/D ratios of these two shots are both about 0.40.

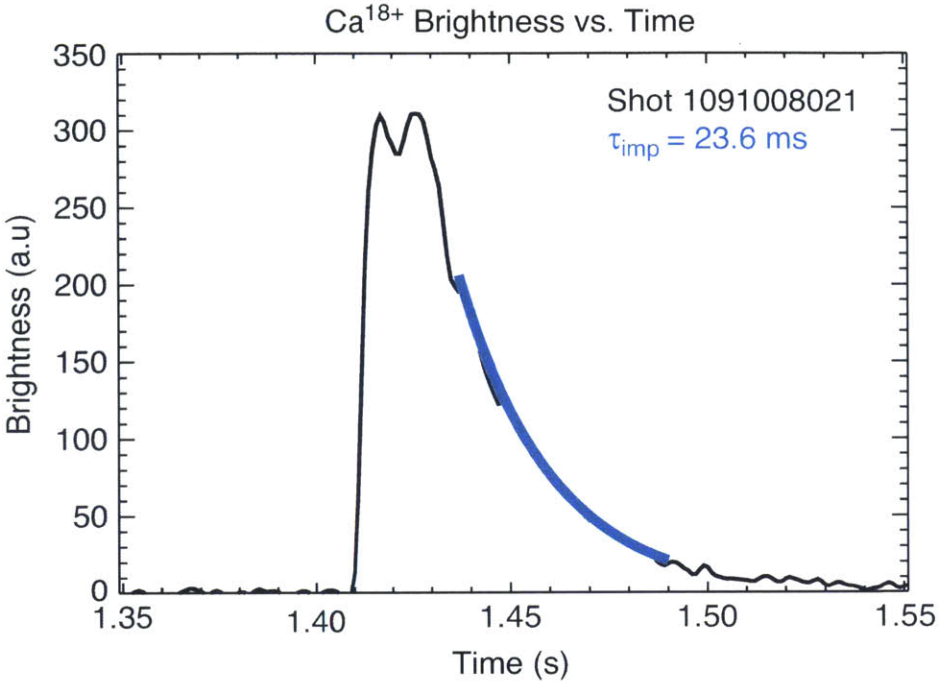

Figure 5-2: The time history of non-recycling Ca^{18+} w line (3.1763 Å) intensity after a CaF_2 injection measured by HiReX–Sr. The injection by LBO occurs at 1.41 s. Figure is adapted from [20].

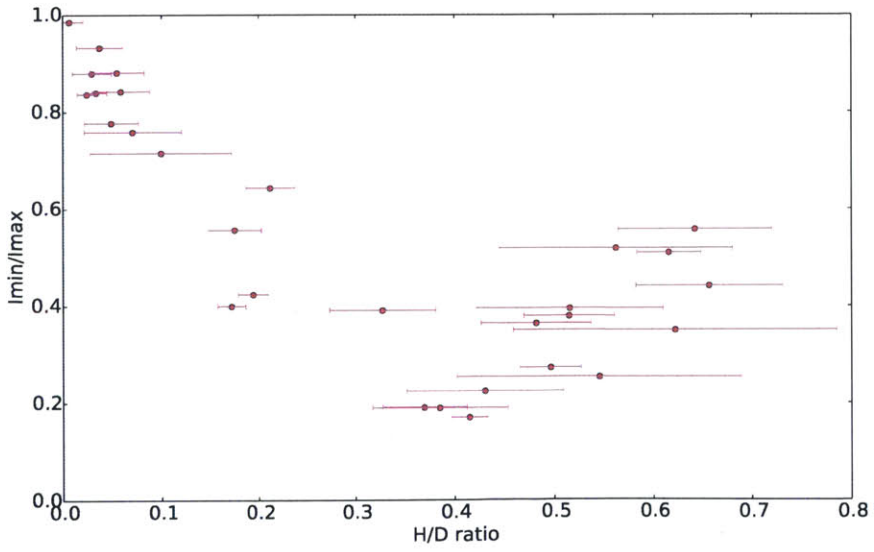

Figure 5-3: The I_{min}/I_{max} of core Ar^{16+} w line as a function of H/D ratio.

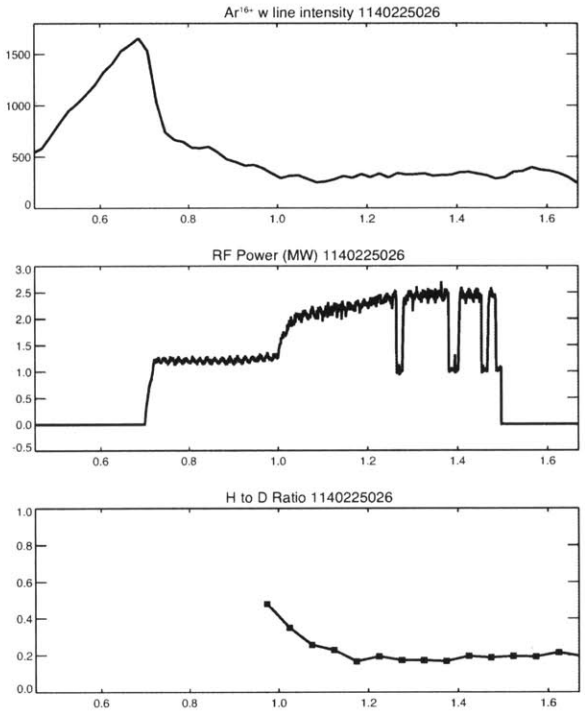

Figure 5-4: A discharge without Balmer spectrometer data around the pumpout time 0.7 s. Discharges like this are excluded from Fig. 5-3

From this scan, the pumpout effect has a preferred H/D ratio at $40 \pm 5\%$. At this H/D ratio the pumpout effect is maximal and the argon intensity is reduced to 20% of the level before ICRF.

A power threshold is observed for the argon pumpout effect. As is shown in Fig. 5-5, shot 1140221016 used two ICRF antennas: J4 antenna at 78 MHz launches with an averaged power of 0.4 MW from 0.6 s to 1.3 s; E antenna at 80 MHz launches with an averaged power of 0.6 MW from 1.0 s to 1.5 s. It can be seen that when the ICRF power is less than 0.5 MW before 1.0 s, there no pumpout effect; when the ICRF power is over 0.5 MW after 1.0 s, the argon is pumped out. This power threshold is not related to a specific antenna. In shots 1140221015 and 1140221016, argon is pumped out when the E antenna is turned on, as is shown in Fig. 5-5. In shot 1140221019, J3 & J4 antennas at 78 MHz are modulated with total power of 0.6 MW from 0.6 s to 1.3 s. The argon brightness is modulated by J3 & J4 antennas from 0.6 s to 1.0 s (Fig. 5-6). At 1.0 s, E antenna at 80 MHz launches with power of 0.6 MW. So the total ICRF is always above the threshold power and the argon brightness

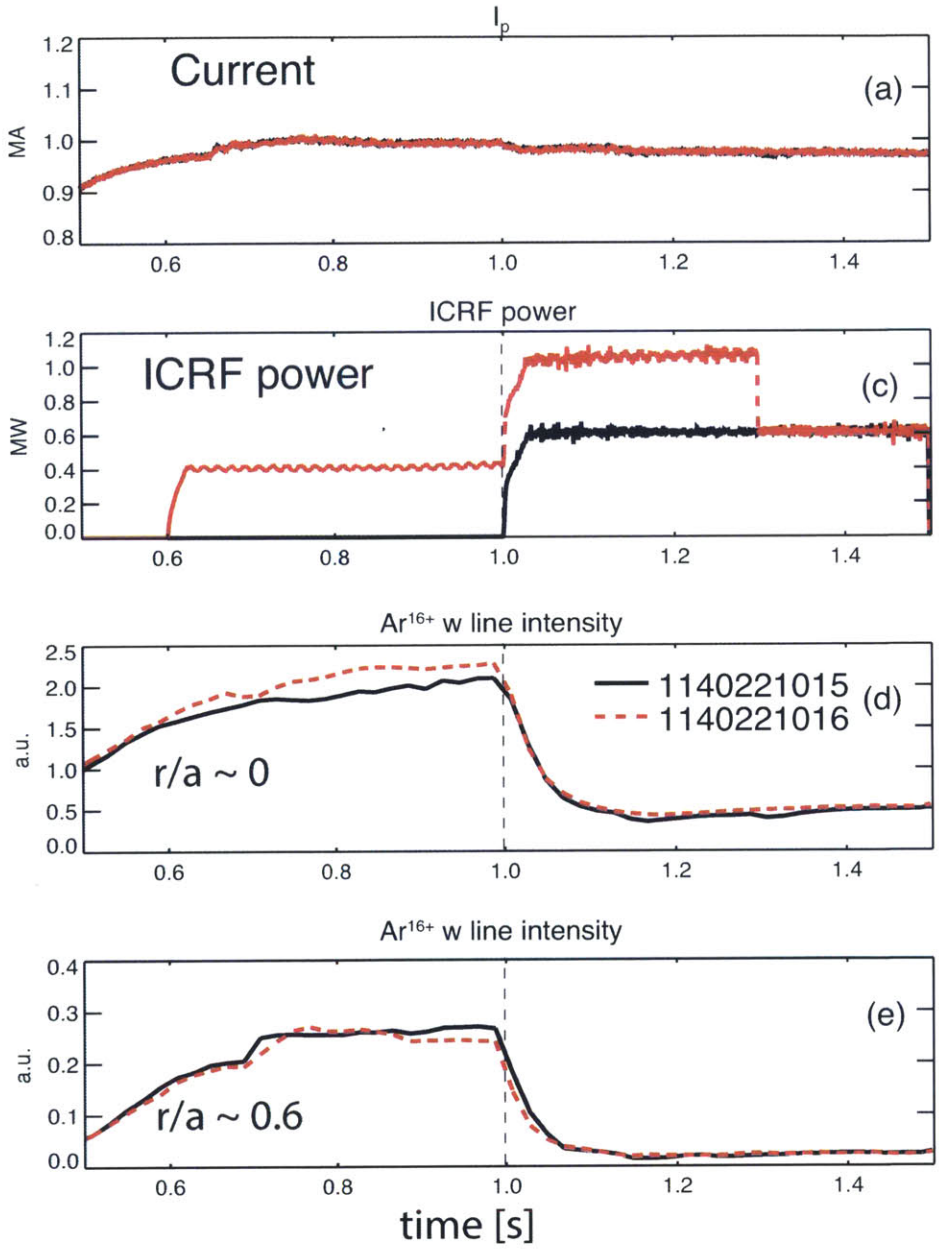

Figure 5-5: From top to bottom: Time traces of (a) plasma current; (b) line averaged electron density from TCI; (c) total ICRF power; Ar^{16+} w line brightness with tangential view at (d) $r/a \sim 0.0$ and (e) $r/a \sim 0.6$. The argon intensities are normalized with the same constant as in Fig. 5-1. The H/D ratios of these two shots are both about 0.40.

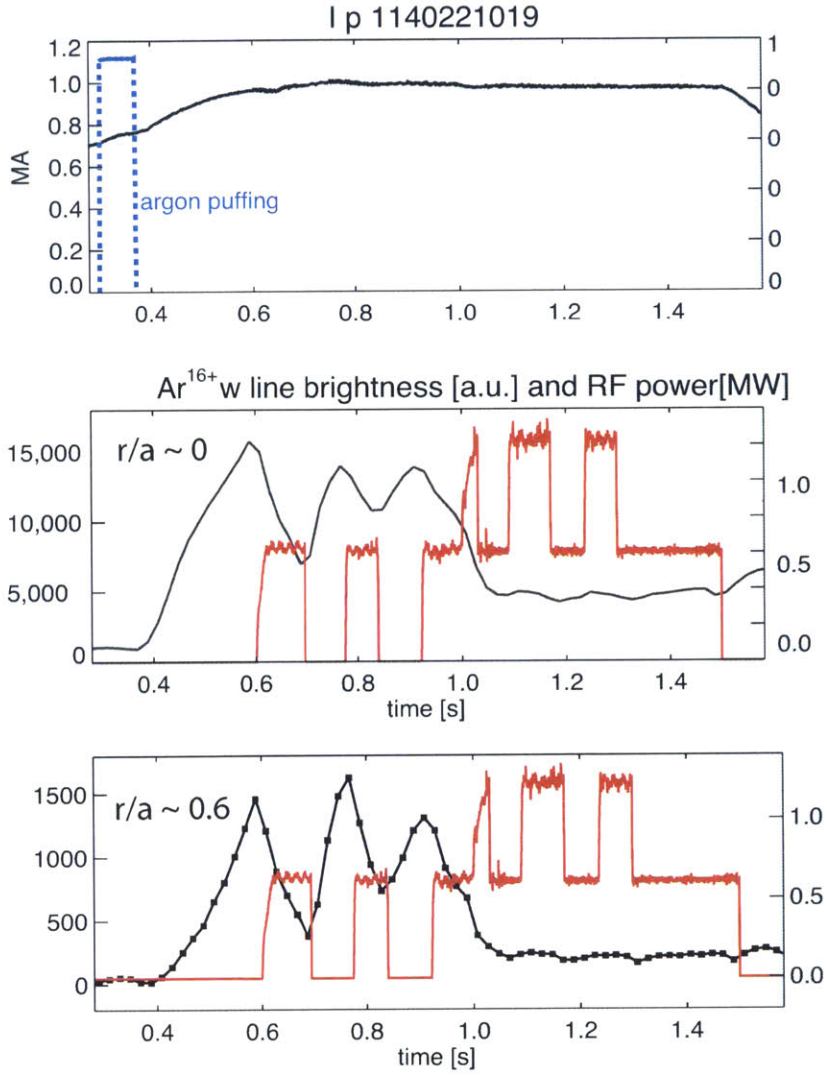

Figure 5-6: Argon brightness is modulated by ICRF.

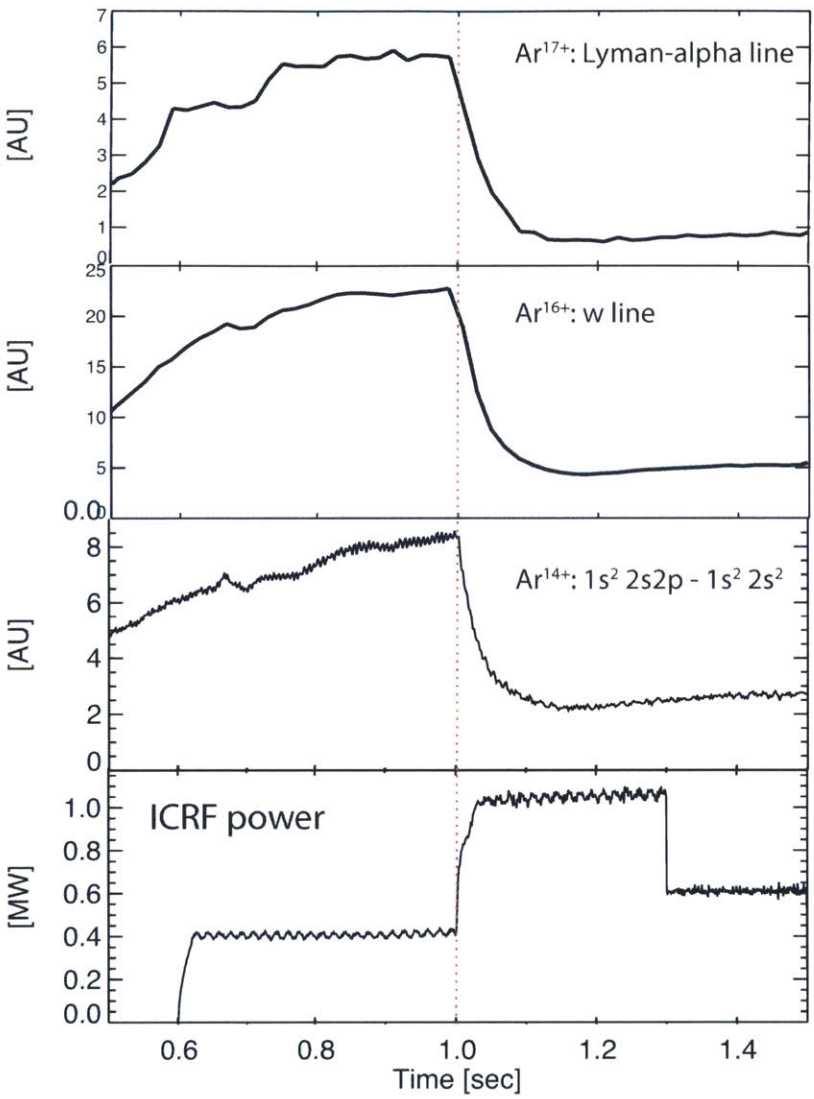

Figure 5-7: Ar^{17+}, Ar^{16+} and Ar^{14+} charge state transition line intensities during ICRF.

keeps a low level. The modulation at $r/a \sim 0.6$ is stronger, which indicates the origin of the pumpout effect may be close to the mid radius. A dedicated experiment with high time resolution HiReX–Sr measurement will help identify the original location of the pumpout effect using FFT phase information with ICRF modulation.

The line intensities from other charge states of argon (Ar^{17+}, Ar^{14+}) are observed to decrease as well. Fig. 5-7 shows the time trace of Ar^{17+} measured by HiReX–Sr and Ar^{14+} intensity measured by the flat-field grating spectrometer LoWEUS (Long Wavelength Extreme Ultraviolet Spectrometer) located on B-Port. For many shots,

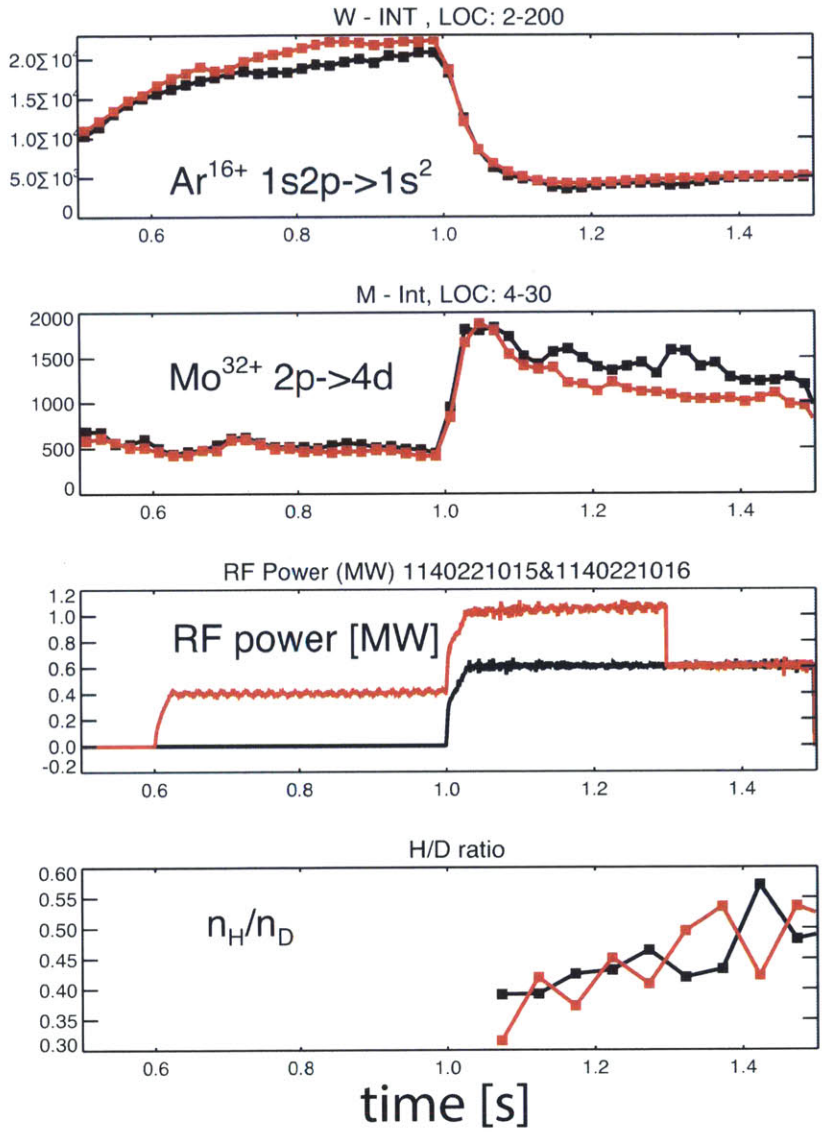

Figure 5-8: From top to bottom: time traces of (a) core Ar^{16+} w line intensity measured by HiReX–Sr; (b) core Mo^{32+} 2p→4d line intensity measured by HiReX–Sr; (c) ICRF power; (d) H/D ratio.

the molybdenum intensity shows the opposite behavior compared to the argon pumpout, as shown in Fig. 5-8. Due to this molybdenum increase, the electron temperature drops slightly.

5.3 Possible Mechanisms

5.3.1 Wave–Impurity Interaction

The fact that the argon pumpout effect happens only at relatively high hydrogen concentration suggests that some resonance mechanism plays a role. In theory it is the case that when $n_H/n_D \approx 46\%$, the Ar^{16+} 2^{nd} harmonic resonance layer overlaps with H–D hybrid resonance layer. As is derived in Section 2.3, the ion–ion hybrid resonance layer is located at a major radius of

$$R_{MC} = R_H \sqrt{\frac{1+\frac{1}{2}\frac{n_H}{n_D}}{1+2\frac{n_H}{n_D}}} \tag{5.1}$$

where R_H is the proton cyclotron resonance layer.

The Ar^{16+} 2^{nd} harmonic resonance layer is located at a major radius of

$$R_{resonant} = n\frac{Z}{A}\frac{eB_0}{m_p\omega_{RF}}R_0 = \frac{4}{5}R_H \tag{5.2}$$

The overlap happens when $R_{MC} = R_{resonant}$, i.e.

$$\gamma \equiv \frac{n_H}{n_D} = 0.46 \tag{5.3}$$

This theoretical value of γ is close to the observed optimal H–D ratio shown in Fig. 5-3, considering the uncertainty in local n_H/n_D measurement, which is inferred by a line integral measurement from the Balmer emission spectrometer. It is worth noting that the Balmer spectrometer is an edge measurement. The core n_H/n_D is unknown for these experiments.

The reason of choosing Ar^{16+} as the resonant species is that at the plasma

condition of interest, Ar^{16+} is the dominant charge state as is shown in Fig. 1-10. The required n_H/n_D values for other argon charge states are listed in Table 5.1.

Table 5.1: The required n_H/n_D of different argon charge states for the overlap of H-D hybrid resonance layer and argon 2^{nd} harmonic resonance layer.

Charge State	$\gamma = n_H/n_D$
Ar^{14+}	1.06
Ar^{15+}	0.70
Ar^{16+}	0.46
Ar^{17+}	0.29
Ar^{18+}	0.17

The idea that ICRF pumps out argon impurities is proposed as follows: at the ion-ion hybrid resonance layer, the left-handed polarized electric field E_+ is enhanced (Section 2.3). When the argon resonance layer is close to the hybrid layer, the argon impurity can gain energy from waves through resonance absorption. A simple illustration of how a resonant particle can gain energy from waves whose frequency is twice the particle's resonance frequency is shown in Fig. 5-9. If sufficient energy is absorbed, the energetic impurity particles can get de-confined ("pumpout").

The existence of an ICRF power threshold supports the wave–impurity interaction explanation. Eq. B.44 shows that the harmonic resonance power absorption is proportional to E_+^2, which is proportional to the launched ICRF power. At low ICRF power, the absorbed energy is not sufficient to de-confine the impurity particles. At higher power, the impurity can gain energy to get de-confined. It turns out that the strength of pumpout effect is independent of the ICRF power as long as it is above the threshold. This can be understood since there is only a small amount of argon in the plasma and increasing the ICRF power won't pump out more argon.

The TFR result [244] showed that argon pumped out of plasma did not recycle and the argon level did not recover when the ICRF was switched off, which was not understood by the authors. The result in Alcator C-Mod differs in that argon is still recycling during pumpout. It is more likely that argon impurities are just kept

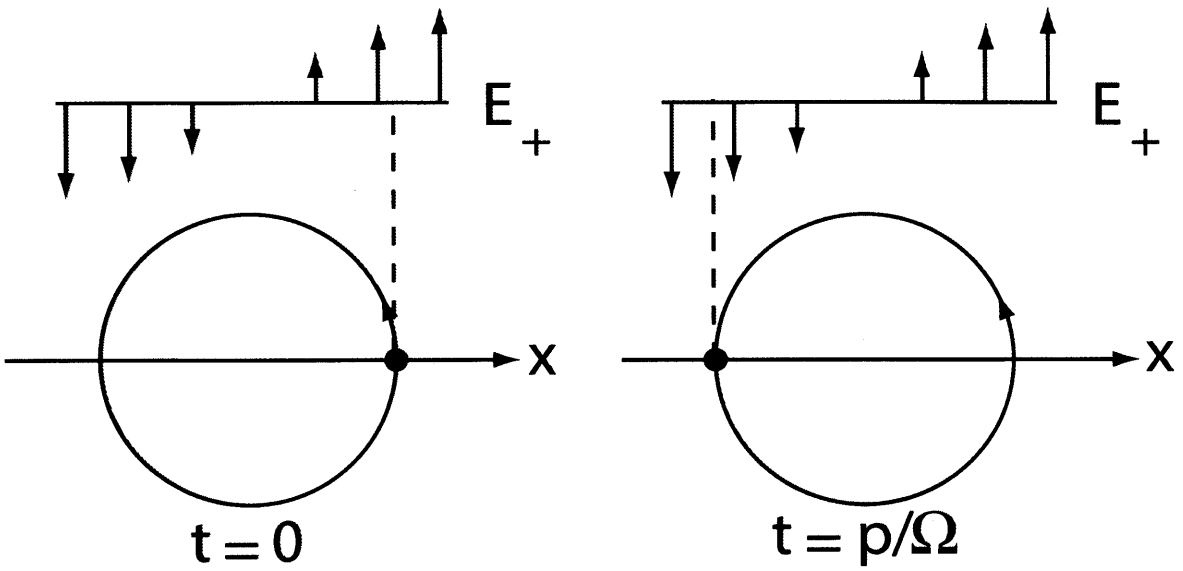

Figure 5-9: The simple physics picture of 2^{nd} harmonic resonance absorption. If the wavenumber k_x is order of the inverse of the particle Larmor radius $1/\rho_s$, the particle will always experience acceleration in the gyro-motion direction. Figure is adopted from [1].

out of the vicinity of the resonance layer. When ICRF is turned off, the "screening" disappears and argon influx recovers to previous levels, as is illustrated in Fig. 5-6.

Fig. 5-10 illustrates the position of the ion-ion hybrid (MC) and argon resonance layers, given $B_0 = 5.4$ T, $f = 80$ MHz and $n_H/n_D = 0.46$. This is the configuration for all shots analyzed in this chapter. At this magnetic field, the overlap is located on the high field side $R \approx 0.55$ m ($r/a \sim 0.6$). This is consistent with Fig. 5-6 in that the argon brightness modulation at $r/a \sim 0.6$ is stronger than that at $r/a \sim 0.0$. Higher magnetic field will push it to the low field side. At $B_0 = 6.5$ T, the resonance layer is close to the magnetic axis (Fig. 5-11). This magnetic field can be used in future experiments with the PCI diagnostic to detect the mode conversion layer, because the viewing range of PCI is 0.59 m $< R <$ 0.79 m in C-Mod.

5.3.2 Edge/Source Effect

Although some strong evidences indicate the argon pumpout is a resonant process, there are some obstacles in explaining the effect simply by resonance absorption.

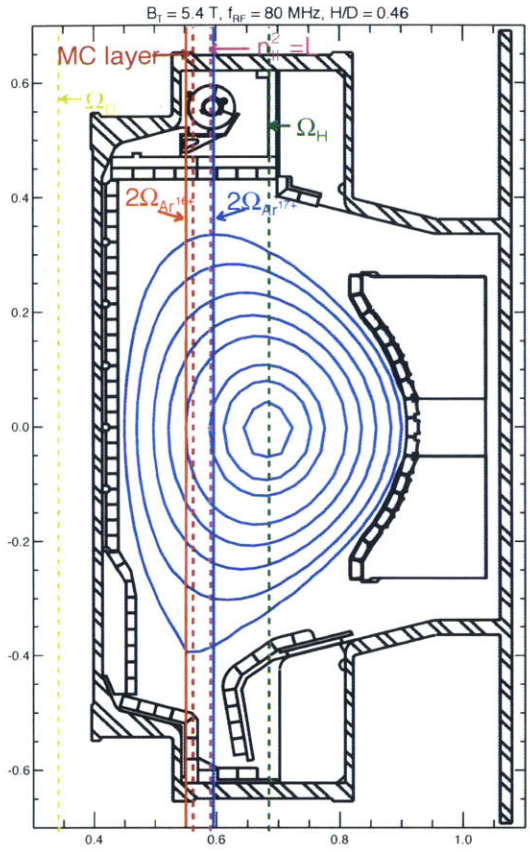

Figure 5-10: The equilibrium cross section of Alcator C-Mod at $B_0 = 5.4$ T, $n_H/n_D = 0.46$ and $f_{ICRF} = 80$ MHz. The 2^{nd} harmonic resonance layers of Ar^{16+} and Ar^{17+} are shown in red and blue solid vertical lines, respectively. The resonance layers of hydrogen and deuterium are shown in green and yellow dashed lines. The left cutoff layer ($n_\parallel^2 = L$) and mode conversion layer ($n_\parallel^2 = S$) are indicated with brown and purple dashed lines, which is calculated with experimental hot plasma parameters: $T_{e,0} = 2.5$ keV, $n_0 = 2.0 \times 10^{20}$ m^{-3}, $I_p = 1.0$ MA

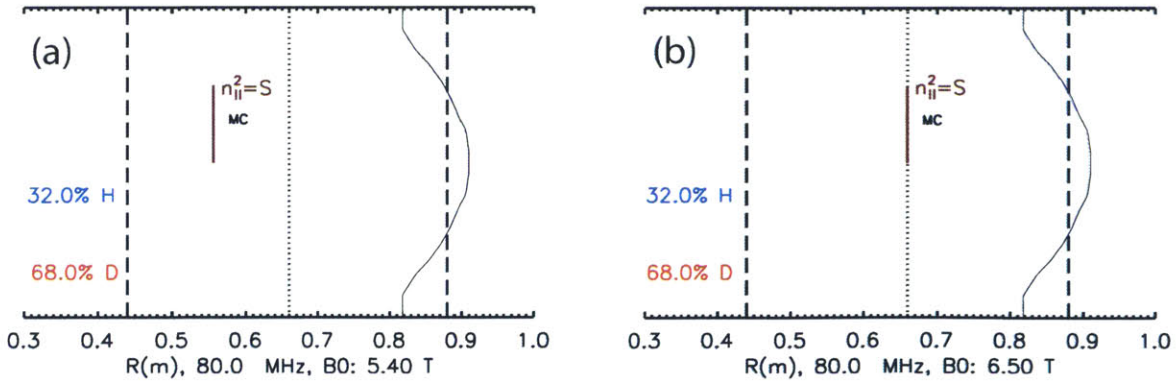

Figure 5-11: The location of H–D hybrid (MC) layer at (a) 5.4 T and (b) 6.5 T. The n_H/n_D is about 0.47.

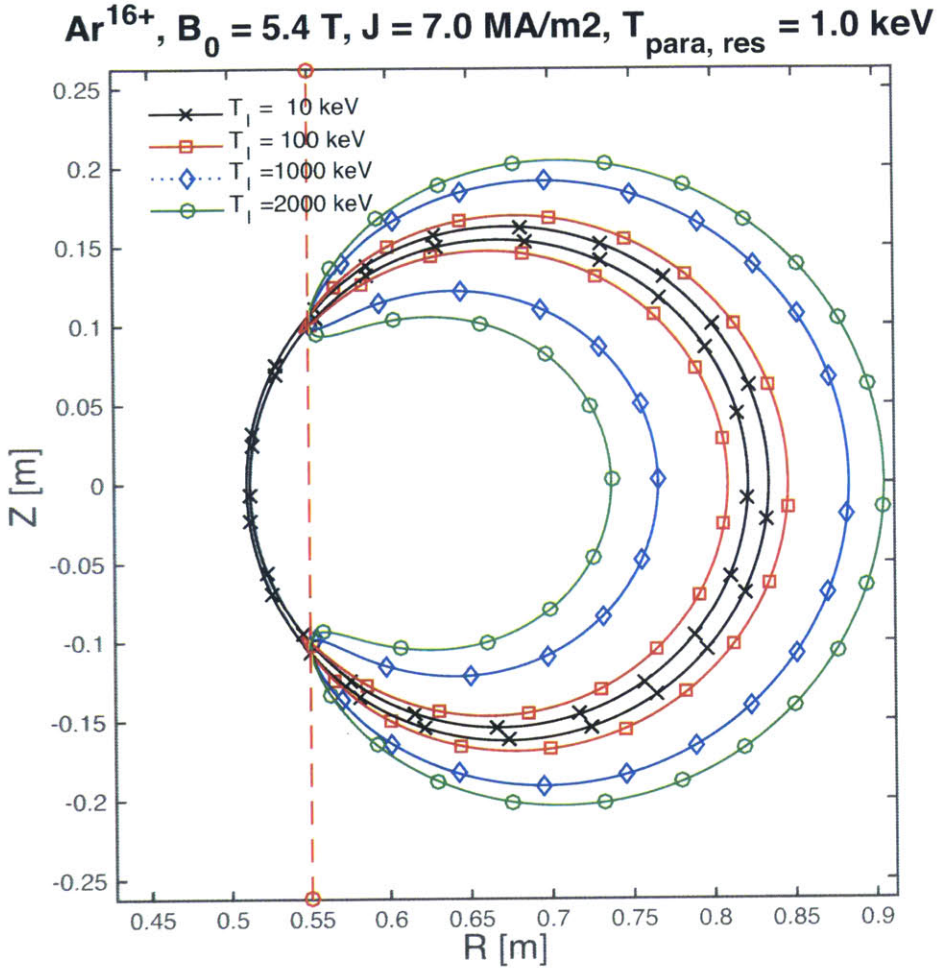

Figure 5-12: Banana orbits of Ar^{16+} at different energies. The $T_{\|}$ is fixed at 1 keV. The resonance layer is $R_{res} = 0.55$ m with $\frac{n_H}{n_D} \approx 46\%, B_0 = 5.4$ T. The orbits will intercept at the same place at the resonance layer, which is $R = 0.55$ m, $Z = 0.10$ m for this plot. A flat current density profile with $j = 7$ MA/m^2 is assumed, which corresponds to $I_p \sim 0.9$ MA with minor radius $a = 0.2$ m of a circular cross section.

First of all, it turns out that the required de-confinement energy is very large for impurities. Consider the trapped impurity with a banana orbit on the low field side (bad curvature), Fig. 5-12 shows that argon needs to acquire energy order of 1 MeV to get de-confined. This is a very high requirement. No fast ion measurement was available for this experiment. Impurity temperature measured by HiReX–Sr shows an increase of $\sim 10\%$ due to ICRF, far less than the de-confinement energy. It could be that the hybrid layer acts like a screening to prevent argon flux from going into the core, instead of directly heating the argon and kicking them out of the core.

The second obstacle in the resonance explanation is that non-resonance argon charge states are also pumped out, and the decay of the argon brightness seems to be widely spread, although not quite uniform, across a large region of the plasma, instead of localized around the ion-ion hybrid layer. Atomic processes should be considered. For example, a decrease of Ar^{16+} density should be followed by the ionization of Ar^{15+} and recombination of Ar^{17+}. The typical ionization time is estimated to be less than 1 ms [244]. A quantitative analysis of the atomic process is desired. But it is easier to assume the ICRF may introduce some "screening" effect that reduces the influx of all argon particles, instead of resonant charge states only. If the edge plasma potential is changed by the ICRF, it may modify the argon particle flux.

Lastly, the behavior of molybdenum complicates the situation. For many of the shots, argon pumpout coincides with a molybdenum increase. If the argon concentration can be modulated by molybdenum through such impurity interactions, we may attribute the pumpout to an edge effect which brings in molybdenum during ICRF.

5.3.3 Changes in Density and Temperature

Changes in electron density and temperature may affect the observed argon emissivity and brightness in two aspects. First, the emissivity of a given line is a function of electron density n_e, electron temperature T_e and the impurity charge state density

$$\epsilon = \sum_k n_k n_e F_k\left(T_e\right) \ \mathrm{phm}^{-3}\mathrm{s}^{-1} \tag{5.4}$$

where n_k is the k^{th} charge state and F_k is a function of the electron temperature considering all the atomic physics processes that give rise to the excited states. STRAHL is a good tool to examine this effect. As will be shown in next section, the pumpout effect cannot be fully accounted to the changes of atomic processes.

The changes in electron density, electron and impurity temperatures can also change the impurity transport properties. In Fig. 5-13, the electron temperature increases $\sim 10\%$ shortly after the ICRF is switched on (0.63 s), but later drops $\sim 10\%$

probably due to the cooling following the molybdenum increase. The ion/impurity temperature increases by $\sim$ 10% - 20%, and the electron density increase by $\sim$ 10%. It is an open question if the changes in profiles can lead to a significant change in transport which causes the pumpout effect. Neoclassical and turbulent transport calculations should be considered in the future work.

5.4 STRAHL Simulation

The modeling of wall recycling in STRAHL is not well tested in C-Mod plasmas, so for argon, the source is typically set to be constant to represent the recycling. STRAHL simulations can be used to test the role of the edge source effect on argon pumpout, with an *ansatz* that the argon source is significantly reduced when the ICRF is turned on.

A graphic user interface dedicated for predictive STRAHL simulations on argon impurities was developed, as shown in Fig. 5-14. Time-evolving electron temperature and density profiles can be used as input background parameters. The user can specify time-dependent sources, the diffusivity $D(r,t)$ and convective coefficient $V(r,t)$ interactively with the GUI. The GUI loads the experimental emissivity and brightness (line integral of emissivity) profiles from HiReX–Sr, and compares with the STRAHL simulated profiles.

Two scenarios are examined using STRAHL and compared with experimental measurements by HiReX–Sr:

1. Time evolving n_e and T_e profiles are provided. A time-independent diffusivity $D = 1 + 50\,(r/a - 0.3)^3$ m/s^2 is used. This diffusivity is chosen to match the simulated and experimental brightness profile before pumpout (0.8 - 1.0 s in Fig. 5-15c and Fig. 5-16d). A constant argon source is assumed to account for the recycling effect, which is consistent with the observation of constant argon brightness in steady state plasmas. This scenario is to examine if the pumpout is the result of the change in atomic processes due to the change in plasma temperature and density.

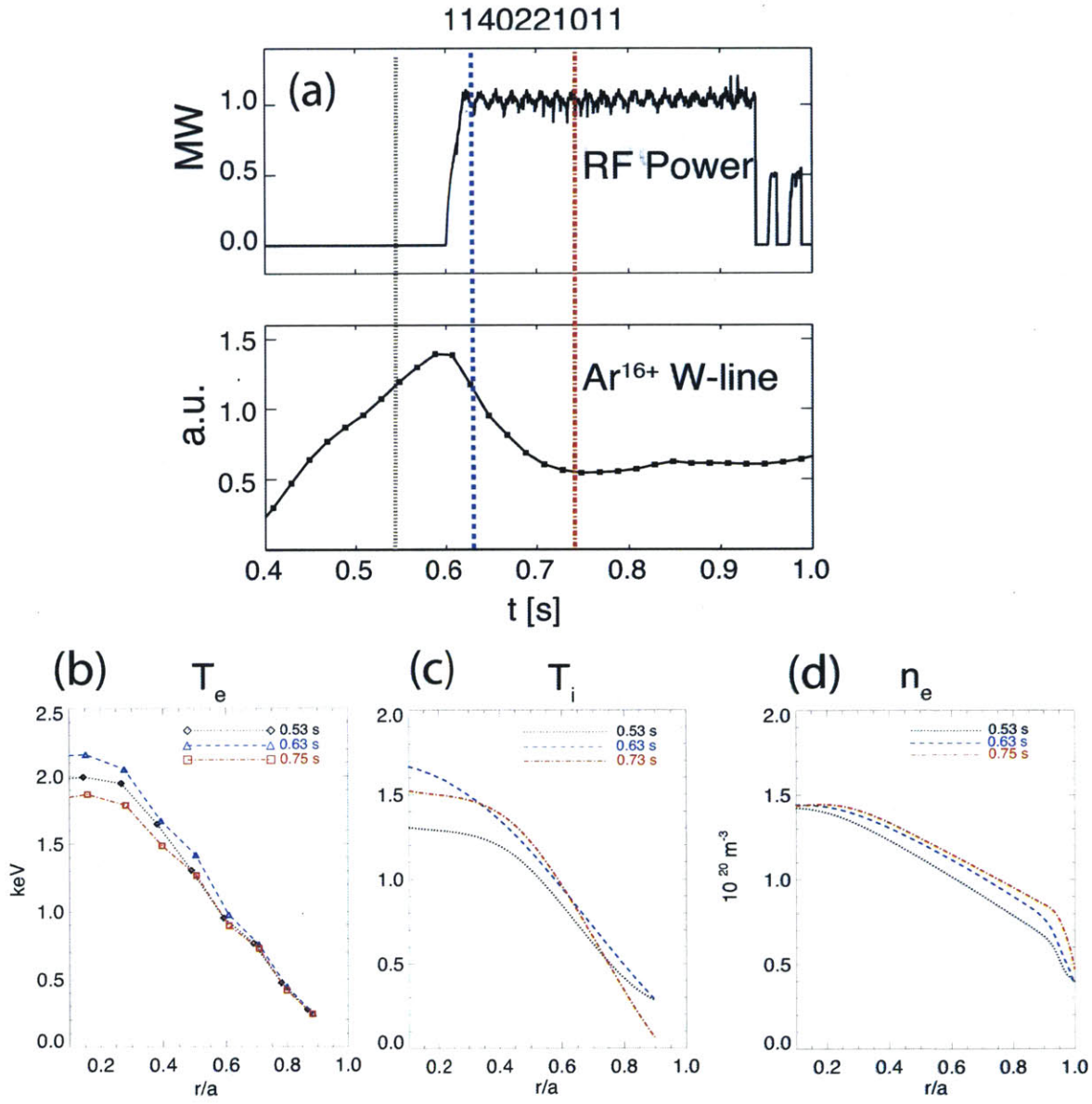

Figure 5-13: The (b) electron temperature, (c) ion/impurity temperature and (d) electron density profiles at three times: 0.53 s, 0.63 s and 0.75 s in (a).

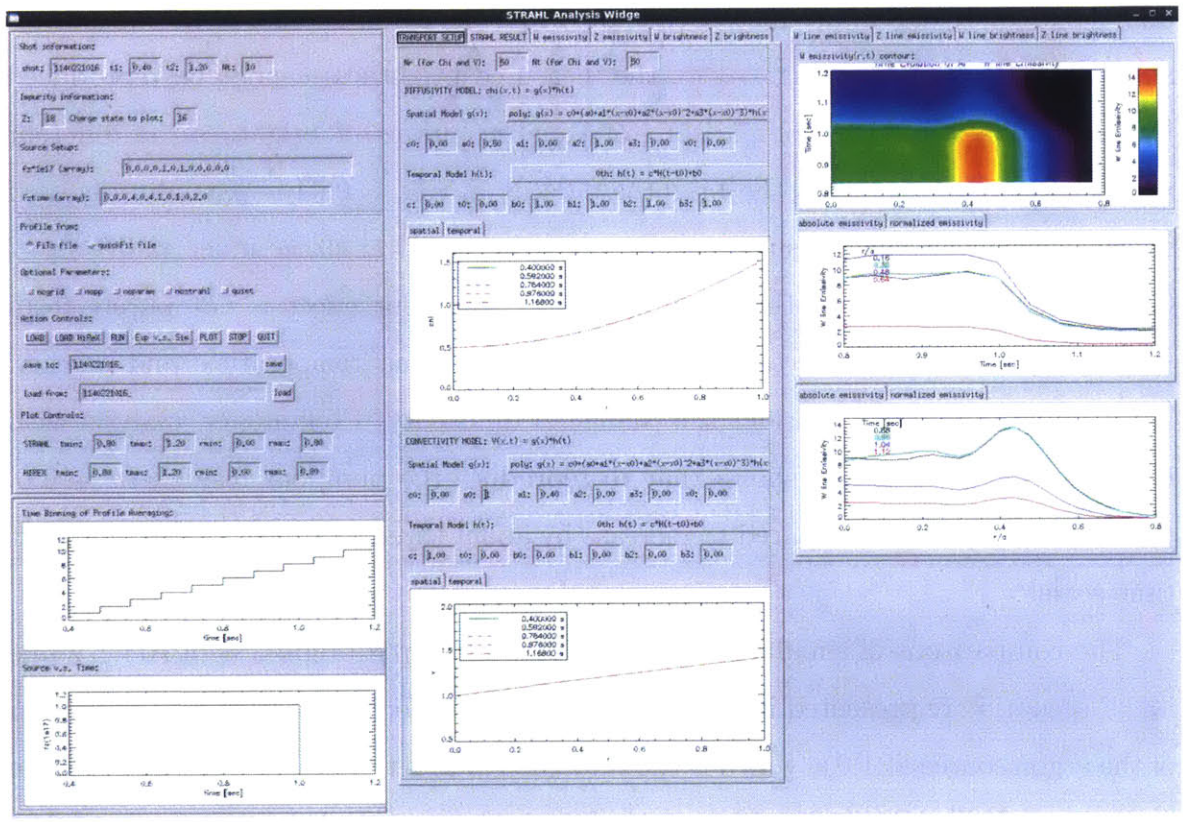

Figure 5-14: User interface of STRAHL simulation widget. Time-evolving source, background parameters, and transport coefficients can be switched on. The impurity source and transport coefficients can be specified interactively using the widget.

2. The same n_e, T_e and D profiles with scenarios 1, but a reduced argon source at the time of pumpout. This scenario is to examine if the pumpout can be reproduced by the source effect.

The comparisons of simulated and HiReX–Sr measured brightness of Ar^{16+} z line in 1^{st} scenario are presented in Fig. 5-15, where the first column are simulations and the second column are measurements. From the contour plots of the brightness shown in Fig. 5-15a and Fig. 5-15b, the measured brightness cannot be reproduced by the simulation. The comparisons of time evolutions of brightness at different radii in Fig.5-15 show that the brightness decay at $r/a = 0.64$ is partially revealed in the simulations, but is substantially underestimated at other inner radii $r/a = 0.16, 0.32, 0.48$. Based on the simulations, the pumpout effect is not purely from the change of atomic process due to changes in plasma temperature and density. The simulation doesn't consider the change of diffusivity. Preliminary analysis with time-dependent diffusivity shows that to reproduce the pumpout inside $r/a = 0.6$, the diffusivity profile is required to increase by about three times within the pumpout time scale.

The comparisons of simulated and HiReX–Sr measured brightness of Ar^{16+} z line in 2^{nd} scenario are presented in Fig. 5-16. The source effect is modeled by a reduction of the argon source at 1.0 s, which is the time the ICRF is turned on. The argon source is chosen as 30% of the level prior to 1.0 s. The contours of the brightness in Fig. 5-16a and Fig. 5-16b show qualitative agreement between simulation and experiment. This agreement can also be seen from the comparisons of time evolutions of brightness shown in Figs. 5-16c, 5-16d, 5-16e and 5-16f. It is also expected that a reduction in source will predict a reduction in all argon charge states.

To summarize this section, two scenarios are examined with STRAHL simulations. The change of atomic process caused by the changes in the plasma density and temperature, without a substantial increase of diffusivity, cannot reproduce the pumpout effect. Simulations based on an *ansatz* of source reduction (mechanism is unknown) agrees with the HiReX–Sr measurements.

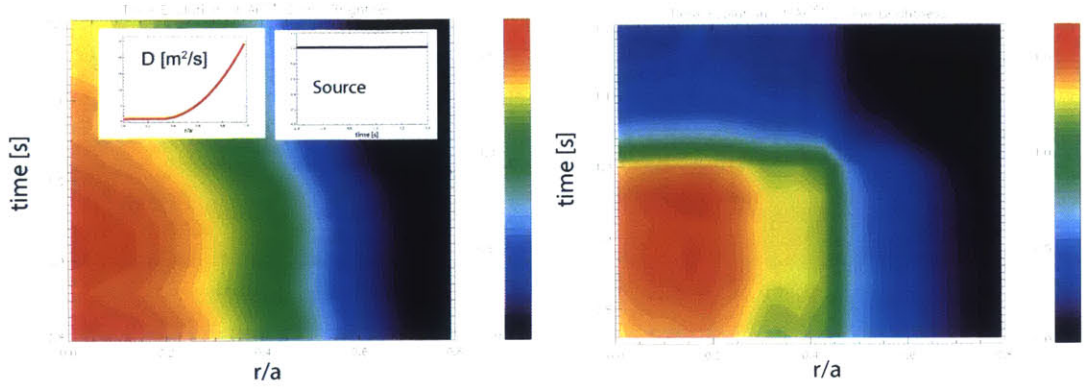

(a) STRAHL simulation

(b) HiReX–Sr measurement

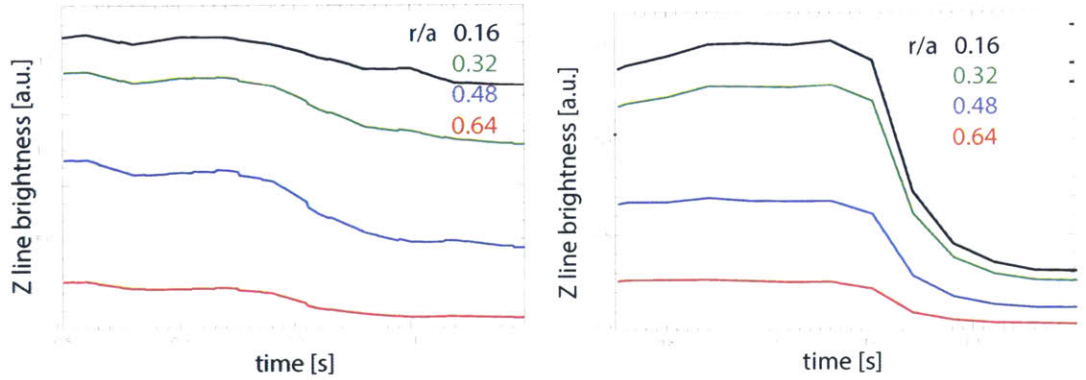

(c) STRAHL simulation

(d) HiReX–Sr measurement

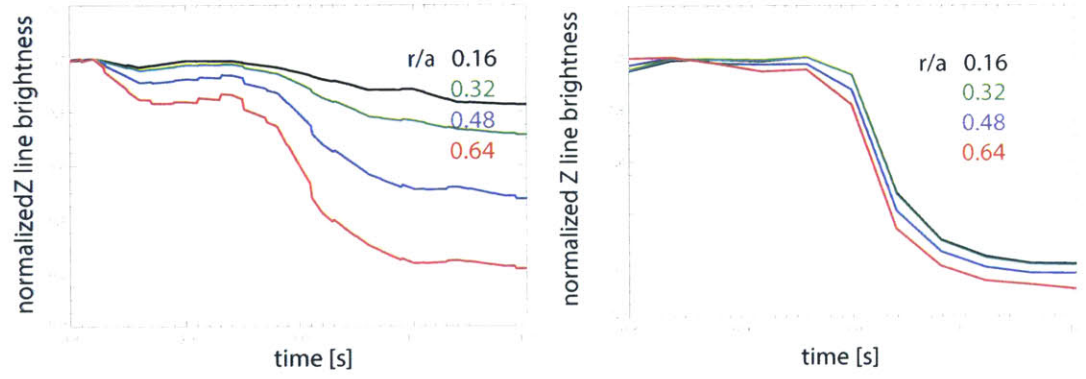

(e) STRAHL simulation

(f) HiReX–Sr measurement

Figure 5-15: Contours of (a) STRAHL simulated and (b) HiReX–Sr measured brightness of Ar^{16+} z line; and time evolutions of (c) (e) STRAHL simulated and (d) (f) HiReX–Sr measured brightness of Ar^{16+} z line at different radii. In the simulation, a constant diffusivity $D = 1$ m/s^2 is assumed. The source is assumed to be constant to represent the recycling. The time-dependent n_e and T_e profiles are taken from experimental measurements.

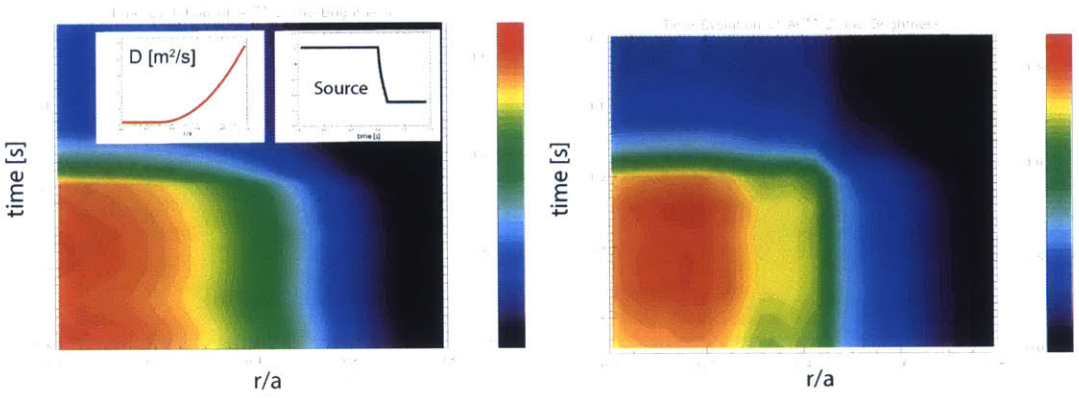

(a) STRAHL simulation (b) HiReX–Sr measurement

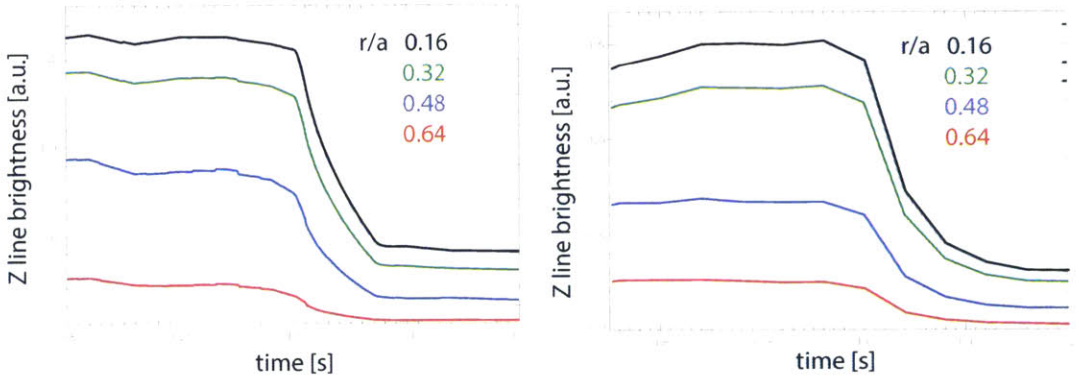

(c) STRAHL simulation (d) HiReX–Sr measurement

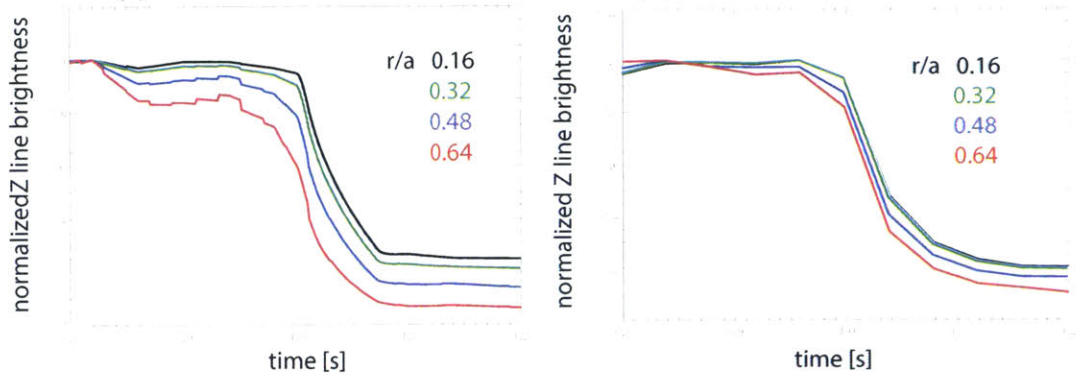

(e) STRAHL simulation (f) HiReX–Sr measurement

Figure 5-16: Contours of (a) STRAHL simulated and (b) HiReX–Sr measured brightness of Ar^{16+} z line; and time evolutions of (c) (e) STRAHL simulated and (d) (f) HiReX–Sr measured brightness of Ar^{16+} z line at different radii. In the simulation, a constant diffusivity $D = 1$ m/s^2 is assumed. The source is reduced to 30% of the one prior to the ICRF.

5.5 Summary

This chapter discussed the ICRF induced argon pumpout observed in Alcator C-Mod H–D plasmas. Three mechanisms are considered for this pumpout effect.

1. The resonance absorption is the probable mechanism due to the existence of an optimal H–D ratio and ICRF power threshold. But it has difficulty in explaining the pumpout of non-resonant impurities and uniform decay across the whole plasma region, and it is not clear if the electric field at the ion-ion hybrid layer can provide argon with sufficient de-confinement energy. This can be verified with without PCI measurements. The interplay between argon and molybdenum further complicates the explanation.

2. An *ansatz* of the edge effect: a reduction in argon recycling/influx source during ICRF can reproduce the pumpout effect, as well as matching the brightness profiles of different argon charge states. It could be unsatisfactory that the *ansatz* has a dependence on the H–D ratio and ICRF power due to an unknown mechanism.

3. The change in atomic processes due to changes in density and temperature cannot fully reproduce the pumpout effect. Preliminary analysis shows an additional increase of diffusivity by three times is required. It is still an open question if the changes in plasma profiles are able to drive significant outward transport. Future work should be done on the changes in neoclassical and turbulent transports in these experiments.

Most of the data shown in this chapter is collected in plasma conditioning experiments, which naturally provide a high n_H/n_D environment. However during these pre-physics operations, some diagnostics may not be available, of which PCI is the most desirable diagnostic to detect the mode conversion strength and location [44, 246]. A more dedicated experiment is proposed in Alcator C-Mod to study the pumpout effect. The experiment will be run at higher magnetic field $B_0 = 6.5$ T, which will move the ion-ion hybrid resonance layer close to the magnetic axis

(Fig. 5-11), within the PCI viewing range. The location and strength of the electric field near the hybrid layer will be inferred from the PCI and quantitative analysis of argon energy gained in this layer might be possible. The UV/visible spectrometer Chromex will also be equipped to monitor the lower charge states around the edge.

Chapter 6

Summary and Future Work

6.1 Non-local Heat Transport

Cold pulse experiments in Alcator C-Mod reveal the connection among non-local heat transport (the breakdown of a local expression of the heat flux), plasma intrinsic rotation reversals and the LOC/SOC transition. It extends the understanding of the non-local phenomenon on existing experiments from other machines. The non-local effect is observed in low collisionality LOC plasmas where the intrinsic rotation is in the co-current direction; it disappears in high collisionality plasmas where the plasma rotates in the counter-current direction. Transport analysis shows that a sudden drop of core diffusivity is required to model the non-local response (fast core temperature increase), which is consistent with density fluctuation measurements from PCI. Cold pulse modulation experiments suggest that an inward heat pinch may exist in the LOC plasmas.

The change of dominant turbulent modes is proposed as the underlying mechanism for the disappearance of the non-local effect, the intrinsic reversals and the LOC/SOC transition. Previous experiments showed that the LOC regime is intrinsic to electron modes, and the SOC regime is more likely to be ion mode dominant. The non-local effect may be intrinsic in the LOC regime, which is due to a transient ITB formed during the transient phase. The disappearance of electron channel non-local effects in SOC plasmas can be the consequence when the

electron-ion collisional thermal coupling power exceeds the electron mode transported power, which effectively eliminates the non-local effect in the electron channel. The most recent multi-scale gyrokinetic simulation [209] shows that the ETG mode is the dominant heat transport mechanism at low ion temperature gradient drive, and ITG modes take over the heat transport with the increase of the ion temperature gradient. This may be applied to explain the fast response of cold pulses in the LOC regime [232]: the large linear growth rate γ^{ETG} could play a role in the fast response, and the observed radially elongated streamer structure [98] suggests a spatially correlated transport paradigm. The rotation reversals can be induced by a sign change of the residual stress depending on the nature of the underlying turbulence, such as by a change in the mode propagation direction from the electron diamagnetic drift direction to the ion direction.

Ion-scale linear GYRO simulations performed in Chapter 3 only qualitatively demonstrate the trend of ion-scale turbulent modes across the LOC/SOC transition. It is shown in [97, 98] that ETG modes can drive significant heat transport in marginally ITG-stable plasmas. To quantitatively understand the turbulent transport in the non-local effect, the intrinsic rotation reversals and the LOC/SOC transitions, multi-scale nonlinear simulations are required.

It is still challenging to explain the cause of the non-local effect in LOC plasmas. As is mentioned in [163], two possible mechanisms for non-local effects are emphasized: (a) the fast front propagation of micro-scale turbulence (b) the coupling between micro-scale and meso/macro-scale turbulence. In the future, it will be helpful to investigate the micro-scale turbulence dynamics in the LOC regime. Reynolds stress generated meso-scale zonal flow can regulate the micro-scale fluctuations, which is worthy of investigation in these plasma conditions. Turbulence spreading can induce a wave-like heat propagation [247, 248]. Work on including the turbulence spreading induced transport into the transport modeling will be helpful in understanding its role in the non-local effect.

6.2 Momentum Transport Coefficients

Momentum transport coefficients (diffusivity and pinch) are calculated from ICRF modulation experiments using a "toy model". This model has some assumptions:

- Momentum source and residual stress are neglected in the core plasma $r \leq 0.5$.
- The momentum transport coefficients are assumed to be constant in time.

With these assumptions, it is found that within $0.1 < r/a < 0.5$, the momentum diffusivity is lower than the ion thermal diffusivity, and there is an inward momentum pinch on the same order of the Coriolis pinch predicted in [145]. Error analysis shows that the error bars on the momentum pinch are relatively large, due to the the nonlinear term $\partial_r \ln(nA)$ in Eq. 4.16.

It is difficult to perform rotation perturbation experiment in Alcator C-Mod, due to the lack of a well modeled momentum source such as a neutral beam, which is an efficient rotation modulation tool with well understood torque modeling. Lower hybrid waves can drive plasma rotation in Alcator C-Mod [8, 139]. The role of lower hybrid waves in flow driven is under investigation [249, 250], where the LH-induced torque [249] and intrinsic torque induced by magnetic shear effect [250] are calculated. Future work should be done to verify these theories. ICRF mode conversion has proven to drive significant rotation [44, 45, 46]. The mode conversion modulation experiment will be helpful in the study of momentum transport, but it may require the implementation of flow drive theories on resonant wave-ion interactions [236, 237, 238, 239, 240].

6.3 ICRF Induced Argon Pumpout

Argon pumpout during ICRF experiments in H-D plasmas is observed in Alcator C-Mod. This pumpout happens when the H/D ratio is relatively high ($n_H/n_D \approx 35\% - 50\%$). A scan of n_H/n_D shows that the pumpout effect is maximized at $n_H/n_D \approx 40 \pm 5\%$, at which about 80% of the argon is pumped out

within 50 ms. This pumpout effect has an ICRF power threshold of 0.5 MW. The ICRF modulation experiment shows that the argon intensity recovers to pre-ICRF levels if the ICRF is turned off. At $B_t = 5.4$ T, the pumpout effect is stronger at mid radius $r/a \sim 0.5 - 0.6$ than at the core $r/a \sim 0$.

Impurity-wave interaction is proposed as one mechanism for the pumpout effect. Theoretically at $n_H/n_D \approx 46\%$, the hydrogen–deuterium hybrid (mode conversion) layer overlaps with the Ar^{16+} 2^{nd} harmonic resonant layer. Argon may gain energy from waves and get de-confined from the plasma. At $B_t = 5.4$ T, the hybrid layer is located on the low field side $R \approx 0.55\text{m}\,(r/a \sim 0.5)$. This is consistent with the observation of a stronger pumpout effect at this radius.

There are some outstanding questions about the wave-impurity explanation. Firstly, preliminary analysis shows that the de-confinement energy of argon is fairly high ~ 1 MeV. No fast ion measurement was available for this experiment. Impurity temperature measured by HiReX–SR shows an increase of $\sim 10\%$ due to ICRF, far less than the de-confinement energy. Secondly, the intensities of non-resonant impurity charge states like Ar^{14+} and Ar^{17+} also decrease. It is reasonable that a decrease of Ar^{16+} density can be followed immediately by decreases of densities of other argon charge states due to the ionization and recombination, but a quantitative atomic process analysis is necessary. In the impurity transport simulation, one can set a transient flux for the resonant argon charge state to decrease the influx of the resonant charge state when ICRF is turned on. But to the author's knowledge, STRAHL may not be capable of specifying different transport coefficients for the different charge states of the same species. Lastly, the increase of the molybdenum density complicates the situation. The interplay between argon and molybdenum should be considered, which is currently out of the scope of this thesis.

For the future work, a dedicated experiment is proposed in Alcator C-Mod to study the pumpout effect. The experiment will be run at higher magnetic field $B_0 = 6.5$ T, which will move the ion-ion hybrid resonance layer close to the magnetic axis, within the PCI viewing range. The location and strength of the electron field near the

hybrid layer will be inferred from the PCI and quantitative analysis of argon energy gained in this layer might be possible. The ICRF modulation experiment with higher time resolution HiReX–Sr ($\Delta t \leq 10$ms) will be useful in determining the origin of the pumpout effect from the FFT phase information. The UV/visible spectrometer Chromex will also be equipped to monitor the lower charge states around the edge.

Transport simulation with modeling of pumpout or screening effects of a specified argon charge state Ar^{16+} should be performed. This may require a modification of the current available codes.

Another open question is if the changes in profiles can lead to a significant outward impurity transport in these experiments and, combining with the changes in atomic processes, cause the argon pumpout. Neoclassical and turbulent impurity transport simulations are necessary for this question.

The role of molybdenum can be studied by boronizing the molybdenum wall, thus the molybdenum content will be suppressed during ICRF. If argon pumpout is sill observed at a particular n_H/n_D level with boronization, the role of molybdenum can be excluded. If no pumpout is observed, it is either that molybdenum causes the pumpout, or some edge effect induces the molybdenum injection and argon pumpout. The interplay between molybdenum and argon should be studied. A full understanding of the argon pumpout effect will be helpful for impurity control in fusion devices.

6.4 Summary

This thesis studied several aspects of transport phenomena in Alcator C-Mod with HiReX–Sr as the primary diagnostic. The primary goal and contribution of the thesis is identifying the correlations between rotation reversals and the non-local effect across LOC and SOC regimes (Chapter 3), which suggests a common underlying mechanism for energy confinement, momentum transport and the non-local effect. Chapter 4 studied the core momentum transport in the ITG mode dominant regime in RF plasmas, which can be viewed as an analogy to the SOC

regime in Ohmic plasma. The core ($r/a \leq 0.5$) ITG mode dominance is determined from the observed counter-current rotation in the Ohmic phase, but linear GYRO simulation is desired to confirm the dominance in both Ohmic and RF phases. The existing simple momentum transport theoretical results in ITG mode dominant plasmas make for a good experimental regime for comparison with theories, and for this reason the ICRF modulation experiment in the "SOC" regime is chosen. Chapter 3 and Chapter 4 can be viewed as studies of energy and momentum transport in LOC and SOC plasmas, while Chapter 5 seems to be off the topic because it may be due to wave-impurity interaction or edge physics. But the transport effects are not excluded from the possible mechanisms. It is possible that the changes in impurity transport coefficients (turbulent or neoclassical) contribute to the observed argon pumpout. It is also worth mentioning that Scrape-Off Layer (SOL) flows and ICRF wave damping in the SOL may also play a role for the argon pumpout, which may be relevant to the edge transport. This section will discuss whether existing theories can be used to interpret the experimental observations in the thesis and possible verification work in the future.

For the non-local effect, the physical processes of producing the non-local response can be categorized as either local or global. Firstly, if the transport is governed by local microinstabilities, the non-local response can be produced by a fast propagation of turbulence from the edge to the core. Turbulence spreading mentioned in Section. 3.1.1 can be classified into this category. Turbulence spreading was demonstrated in self-consistent global gyrokinetic simulations [251, 176, 252, 253], where turbulence was found to spread from the linearly unstable region to the linearly stable region and influence transport in the stable region, but the reversed polarity (up-gradient transport) in the cold pulse experiment was not specifically studied in these simulations. To our knowledge, only empirical or semi-empirical models of turbulence spreading was applied to cold pulse experiments [181]. In these experiments, electron density fluctuation suppression is observed in C-Mod [167] and HL-2A [17], which indicates that the core turbulence is affected by edge profile changes, and the turbulence spreading is an attractive

candidate. The widely observed density dependence of the non-local effect could be related to that differences in turbulence spreading from the edge into the core which may behave differently for the core transport: down-gradient or up-gradient. A working hypothesis is that the non-local electron heat response may be intrinsic in electron mode dominant turbulence, and the response diminishes or disappears if the dominant turbulence changes. Due to the limitation of time resolution in the ion temperature measurement, it is not conclusive if the non-locality exists in the ion channel, but the rise in core ion temperature is at least in part due to an enhanced ion-electron thermal coupling. An open question is if the turbulence spreading in self-consistent global gyro-kinetic simulations can give rise to the up-gradient transport and the polarity-reversed response with the cold pulse experimental parameters. The cold pulse experiment provides a test bed for the validation of the gyrokinetic models. The non-local effect, the breakdown of local flux-gradient relations $q(r) = -n(r)\chi(r)\nabla T(r)$, doesn't necessarily invalidate the standard gyrokinetic modelings, and turbulence spreading may be the key component for the connection between the experiments and the simulations. Secondly, the plasma transport can be governed by global-type models such as integral flux equations. It is worth noting that the turbulence spreading discussed above can also lead to radially correlated turbulence and heat integral flux equations, but the global model is more relevant to physics issues such as magnetic processes. Electrons are tied to magnetic field lines via Ohm's law in low-resistivity plasmas, and the timescale for transmission of magnetic effects can be very short, on the Alfvén timescale [226]. However in C-Mod, the edge magnetic fluctuations seem to drop concomitantly with the cold pulse injections for plasmas with both non-local and local responses, which is probably a consequence of the edge T_e drop [155], and there is no significant change in sawtooth activity during cold pulse injections. Without the information of core magnetic fluctuations, it is difficult to tell if they are important for the non-local effect.

Under the framework of gyrokinetic theories, the correlation among non-locality, rotation reversals and LOC-SOC transitions can be related to the hypothesis of

changes of the turbulence propagation direction, as was discussed in Chapter 3. The ion-scale gyrokinetic simulations performed in Chapter 3 constitute a very preliminary study to investigate the possible changes of turbulence types. It may not be sufficient to examine the turbulence characteristics only at some specific locations, since these transient phenomena are basically global. Inclusions of global effects (including turbulence spreading) and multi-scale (including electron-scale) turbulence in the gyrokinetic simulations may be necessary to interpret correctly these phenomena and their connections. It is also worth mentioning that there are disagreements with the hypothesis, especially for rotation reversals. [254] showed that the correlation between intrinsic rotation and collisionality could be due to the collisionality dependence of diamagnetic flows in ITG mode dominant plasmas. Future work to perform the simulations with C-Mod rotation reversal parameters using GS2 (the code used in [254]) will be helpful.

The study of momentum transport coefficients in Chapter 4 has the caveats: (1) the assumptions of no core torque perturbation and constant χ_i and V_{pinch} may not be correct; (2) the modeling and calculation suffer from the time resolution of rotation measurements; (3) gyrokinetic simulation was not performed to confirm the ITG dominance. In theory the momentum diffusivity should be close to ion thermal diffusivity in ITG dominant plasmas. It is not unexpected that χ_i will be underestimated if there is core torque which is ignored in the modeling, or if the plasma is not ITG dominant which means the momentum and energy transport are not necessary strongly coupled. The pinch calculation seems to agree with the Coriolis pinch within uncertainty. However the pinch is normalized by R/χ_i, for this reason if χ_i is underestimated, the pinch will disagree with the Coriolis pinch theory, i.e. the normalized pinch will be smaller than the theory.

The argon pumpout effect has multiple explanations. The wave-impurity interaction is a possible mechanism based on the observed optimal n_H/n_D ratio, and a similar effect was observed in TFR [244]. The edge source effect is tested using an empirical source reduction in STRAHL simulations, which can reproduce the measured brightness. The changes of turbulent and neoclassical transport

coefficients are not considered in the study. It is true that the changes of plasma profiles can give rise to changes in impurity transport coefficients. Hollow carbon density profiles (impurity hole) were observed in LHD with dramatic changes of ion temperature profiles during NBI heating [255]. The profile changes during the argon pumpout in C-Mod are far less significant, but future work on neoclassical and turbulent calculations should be done to confirm this claim. Scrape-Off Layer (SOL) flows and ICRF wave damping in the SOL may also play a role, which requires further investigations.

THIS PAGE INTENTIONALLY LEFT BLANK

Appendix A

Toroidal Momentum Pinch Due to the Coriolis Drift Effect

This appendix discusses the Coriolis pinch effect on the toroidal momentum flux. It follows the derivations in [145, 256]. In Section A.1, the angular momentum pinch term will be derived using the gyro-fluid equation in a rigid body rotating, low β, large aspect ratio, circular cross-section tokamak with slab geometry. The toroidal momentum pinch factor is obtained as a function of density gradient. In Section A.2, a momentum pinch is derived for the total angular momentum. The result happens to be similar to the Coriolis pinch effect without consideration of the parallel dynamics. In Section A.3, the parallel dynamics are included in the equations and a reduced momentum pinch velocity is found due to a finite parallel wave vector. It is shown that with adiabatic electrons, the Coriolis pinch effect is completely compensated.

A.1 Coriolis Pinch Effect

A Coriolis pinch term of the momentum flux is derived in [145]. Unlike the diffusion term which is proportional to the flow shear, the pinch term depends on rotation itself. This pinch term comes from the Coriolis drift effect. A set of simplified slab geometry fluid equations is used to show the mechanism. The derivations are made in a rotating frame. The benefits are that in the lab frame we need to add a potential

Symbols	Meanings/Expressions
$\mathbf{X}$	guiding center
$\mathbf{u}_0$	background velocity
$v_\parallel$	parallel velocity in rotating frame
Γ	guiding-center phase-space Lagrangian
H	guiding-center Hamiltonian
$\{\ ,\ \}$	guiding-center Poisson bracket
$\mathbf{u}_0^*$	$\mathbf{u}_0^* = \mathbf{u}_0 + v_\parallel \mathbf{b}$
ϵ	$\epsilon = m/e$
$\mathbf{A}^*$	generalized magnetic vector potential $\mathbf{A}^* = \mathbf{A} + \epsilon \mathbf{u}_0^*$
$\mathbf{B}^*$	$\mathbf{B}^* = \nabla \times \mathbf{A}^*$
$B_\parallel^*$	$B_\parallel^* = \mathbf{b} \cdot \mathbf{B}^*$
μ	magnetic moment $\mu = mv_\perp^2/2B$
ω_D	drift frequency $\omega_D = -k_\theta T_0/eBR$
F_M	Maxwell distribution function $F_M = n\left(\frac{m}{2\pi T}\right)^{\frac{3}{2}} e^{-\frac{m\lvert \mathbf{V}-\mathbf{u}\rvert^2}{2T}}$
f	Perturbed distribution function $f = \left[\frac{\tilde{n}}{n} + \frac{\tilde{T}}{T}\left(\frac{mv^2}{2T} - \frac{3}{2}\right) + \frac{mv_\parallel \tilde{w}}{T}\right] F_M$

Table A.1: Table of symbols used in SectionA.1

(to provide background rotation) to the gyrokinetic equation. In a rotating frame the potential term turns into a drift velocity from the Coriolis force, which greatly simplifies the derivation. Symbols used in this section are listed in Table A.1.

The starting point is a set of equations for the time evolution of the ion guiding center $\mathbf{X}$ and its parallel velocity $v_\parallel$.

$$\frac{d\mathbf{X}}{dt} = v_\parallel \mathbf{b} + \frac{\mathbf{b}}{eB_\parallel^*} \times (e\nabla\phi + \mu\nabla B + m\mathbf{u}_0^* \cdot \nabla \mathbf{u}_0^*) \tag{A.1}$$

$$\frac{dv_\parallel}{dt} = -\frac{\mathbf{B}^*}{mB_\parallel^*} \cdot (e\nabla\phi + \mu\nabla B + m\mathbf{u}_0^* \cdot \nabla \mathbf{u}_0^*) \tag{A.2}$$

Eqs. A.1 and A.2 are derived in [257] using the phase-space Lagrangian method with expansion over $\epsilon = m/e$. To simplify the problem, some assumptions are made:

a) Rigid body toroidal rotation: $\mathbf{u}_0 = \mathbf{\Omega} \times \mathbf{X} = R^2 \Omega \nabla \zeta$.

b) $u_0 < v_{thi}$, that is $\frac{\Omega}{\omega_c} < \frac{\rho_i}{R} \sim \rho^*$. $\omega_c = \frac{eB}{M}$ is the ion gyro frequency.

c) Low beta. $B \sim$ constant. $\mathbf{b}\cdot\nabla\mathbf{b} \approx \nabla_\perp B/B$ and there is no magnetic fluctuation.

d) Neglect the centrifugal term and velocities in orders of the diamagnetic velocity.

e) Large aspect ratio, circular surface.

f) Slab geometry. $\mathbf{B} = B\mathbf{e}_y; \nabla B = -B/R\ \mathbf{e}_x$

g) All perturbed quantities are of the form $e^{\imath(k_\theta z - \omega t)}$

Under these assumptions, the nonlinear term in Eq. A.1 is

$$\begin{aligned}\mathbf{u}_0^* \cdot \nabla \mathbf{u}_0^* &= \left(R^2\Omega\nabla\zeta + v_\parallel \mathbf{b}\right) \cdot \nabla \left(R^2\Omega\nabla\zeta + v_\parallel \mathbf{b}\right) \\ &= v_\parallel^2 \frac{\nabla_\perp B}{B} + \Omega^2 R\hat{\zeta} \cdot \nabla\left(R\hat{\zeta}\right) + R^2\Omega v_\parallel \nabla\zeta \cdot \nabla\mathbf{b} + \Omega v_\parallel \mathbf{b} \cdot \nabla\left(R\hat{\zeta}\right)\end{aligned} \tag{A.3}$$

Using

$$\begin{aligned}\nabla\left(R\hat{\zeta}\right) &= \hat{R}\hat{\zeta} - \hat{\zeta}\hat{R} \\ \nabla \cdot \left(R\hat{\zeta}\right) &= \nabla \cdot \left(R^2\nabla\zeta\right) = 2R\nabla R \cdot \nabla\zeta + R^2\nabla \cdot \nabla\zeta = 0 \\ 0 = \nabla \times \nabla\psi &= \nabla \times \left(R^2\mathbf{B} \times \nabla\zeta\right) = \nabla \cdot \left(\nabla\zeta R^2\mathbf{B}\right) - \nabla \cdot \left(R^2\mathbf{B}\nabla\zeta\right) \\ &= \nabla \cdot \left(\nabla\zeta R^2\right)\mathbf{B} + R^2\nabla\zeta \cdot \nabla\mathbf{B} - \nabla \cdot \mathbf{B}R^2\nabla\zeta - \mathbf{B} \cdot \nabla\left(R^2\nabla\zeta\right) \\ &= R^2\nabla\zeta \cdot \nabla\mathbf{B} - \mathbf{B} \cdot \nabla\left(R^2\nabla\zeta\right) = BR\hat{\zeta} \cdot \nabla\mathbf{b} - B\mathbf{b} \cdot \nabla\left(R\hat{\zeta}\right) \\ R\hat{\zeta} \cdot \nabla\mathbf{b} &= \mathbf{b} \cdot \nabla\left(R\hat{\zeta}\right)\end{aligned} \tag{A.4}$$

we can get the centrifugal force and Coriolis force:

$$\Omega^2 R\hat{\zeta} \cdot \nabla\left(R\hat{\zeta}\right) = \Omega^2 R\hat{\zeta} \cdot \left(\hat{R}\hat{\zeta} - \hat{\zeta}\hat{R}\right) = -\Omega^2\mathbf{R} \tag{A.5}$$

$$\begin{aligned}\Omega v_\parallel \left[R\hat{\zeta} \cdot \nabla\mathbf{b} + \mathbf{b} \cdot \nabla\left(R\hat{\zeta}\right)\right] &= 2\Omega v_\parallel \mathbf{b} \cdot \nabla\left(R\hat{\zeta}\right) = 2\Omega v_\parallel \mathbf{b} \cdot \left(\hat{R}\hat{\zeta} - \hat{\zeta}\hat{R}\right) \\ &= 2\Omega v_\parallel \mathbf{b} \times \left(\hat{\zeta} \times \hat{R}\right) = 2\Omega v_\parallel \mathbf{b} \times (-\mathbf{e}_z) \\ &= 2v_\parallel \Omega \times \mathbf{b}\end{aligned} \tag{A.6}$$

Neglecting the centrifugal force (which is valid as long as $\frac{R\Omega}{v_{thi}} < 1$), we have

$$\begin{aligned}
\mathbf{u}_0^* \cdot \nabla \mathbf{u}_0^* &\approx v_\parallel^2 \frac{\nabla_\perp B}{B} + 2v_\parallel \boldsymbol{\Omega} \times \mathbf{b} \\
\mathbf{B}^* &= \mathbf{B} + \epsilon \nabla \times \left(v_\parallel \mathbf{b} + \mathbf{u}_0 \right) \\
&= \mathbf{B} + \frac{B}{\omega_c} \left[v_\parallel \nabla \times \frac{\mathbf{B}}{B} + \nabla \times \left(R^2 \Omega \nabla \zeta \right) \right] \\
&= \mathbf{B} + \frac{B}{\omega_c} \left(v_\parallel \frac{\mathbf{B} \times \nabla B}{B^2} + \frac{v_\parallel}{B} \cancelto{0}{\nabla \times \mathbf{B}} + 2\Omega R \nabla R \times \nabla \zeta \right) \\
&= \mathbf{B} + \frac{B}{\omega_c} \left(v_\parallel \frac{\mathbf{B} \times \nabla B}{B^2} + 2\boldsymbol{\Omega} \right) \\
&= B \left(\mathbf{b} + \frac{2\boldsymbol{\Omega}}{\omega_c} + \frac{v_\parallel}{\omega_c} \frac{\mathbf{B} \times \nabla B}{B^2} \right)
\end{aligned}$$

$\frac{v_\parallel}{B} \nabla \times \mathbf{B}$ term is neglected because $\beta \ll 1$. Since $B_\parallel^* \equiv \mathbf{b} \cdot \mathbf{B}^* = B \left(1 + \frac{2\Omega_\parallel}{\omega_c} \right)$, Eq. A.1 can be rewritten as:

$$\begin{aligned}
\frac{d\mathbf{X}}{dt} &= v_\parallel \mathbf{b} + \frac{\mathbf{b}}{eB \left(1 + \frac{2\Omega_\parallel}{\omega_c} \right)} \times \left[e \nabla \phi + \frac{m v_\perp^2}{2B} \nabla B + m \left(v_\parallel^2 \frac{\nabla_\perp B}{B} + 2 v_\parallel \boldsymbol{\Omega} \times \mathbf{b} \right) \right] \\
&= v_\parallel \mathbf{b} + \frac{\mathbf{b} \times \nabla \phi}{B} + \frac{v_\parallel^2 + \frac{v_\perp^2}{2}}{\omega_c} \frac{\mathbf{B} \times \nabla B}{B^2} + \frac{2 v_\parallel}{\omega_c} \boldsymbol{\Omega}_\perp \\
&= v_\parallel \mathbf{b} + \mathbf{v}_E + \mathbf{v}_d + \mathbf{v}_{dc}
\end{aligned} \tag{A.7}$$

With large aspect ratio assumption, we have

$$\begin{aligned}
\mathbf{v}_d + \mathbf{v}_{dc} &= \frac{v_\parallel^2 + \frac{v_\perp^2}{2}}{\omega_c} \frac{\mathbf{B} \times \nabla B}{B^2} + \frac{2 v_\parallel}{\omega_c} \boldsymbol{\Omega}_\perp \\
&\approx \left(\frac{v_\parallel^2 + \frac{v_\perp^2}{2}}{\omega_c} \frac{1}{R} + \frac{2 v_\parallel \Omega_\perp R}{\omega_c} \frac{1}{R} \right) \mathbf{e}_z \\
&= \frac{v_\parallel^2 + \frac{v_\perp^2}{2} + 2 v_\parallel R \Omega_\perp}{\omega_c R} \mathbf{e}_z
\end{aligned} \tag{A.8}$$

and

$$\mathbf{v}_E = \frac{\mathbf{b} \times \nabla \phi}{B} = \frac{i k_\theta \phi}{B} \mathbf{e}_x \tag{A.9}$$

Here small perturbation terms are assumed to have a linearized form of $\sim e^{e^{i(k_\theta z-\omega t)}}$. Since ϕ is the perturbed potential, $v_E \sim \delta v_d, \delta v_{dc}$. The parallel streaming term $v_\parallel$ is neglected by assuming $v_\parallel \mathbf{b}\cdot\nabla \approx 0$. The Fokker-Planck equation for ions in the moving frame becomes

$$\frac{\partial (F_M+f)}{\partial t}+(\mathbf{v}_E+\mathbf{v}_d+\mathbf{v}_{dc})\cdot\nabla(F_M+f)+\frac{e}{m}(-\nabla\phi)\cdot\nabla_v(F_M+f)=0 \quad \text{(A.10)}$$

By ordering $f\sim\delta F_M, v_E\sim\delta v_d\sim\delta v_{dc}$, we have

$$\frac{\partial f}{\partial t}+(\mathbf{v}_d+\mathbf{v}_{dc})\cdot\nabla f=-\mathbf{v}_E\cdot\nabla F_M-\frac{eF_M}{T}(\mathbf{v}_d+\mathbf{v}_{dc})\cdot\nabla\phi \quad \text{(A.11)}$$

For the spatial derivative of a Maxwellian distribution in the rotating frame, it is $\mathbf{V}$ (velocity in lab frame) instead of $\mathbf{v}$ (velocity in rotating frame) that should be kept constant. So the spatial derivative is:

$$\nabla F_M=\left[\left(\frac{3}{2}-\frac{mv^2}{2T}\right)\frac{1}{L_T}-\frac{1}{L_N}-\frac{mu'v_\parallel}{T}\right]F_M \quad \text{(A.12)}$$

where $u'=-R\nabla\Omega$, and f is the perturbed Maxwell distribution shown in Table A.1.

Integrating Eq. A.11 over $\left(1, v_\parallel, v^2\right)$ gives

- 0^{th} moment

$$\begin{aligned}
\int\frac{\partial f}{\partial t}\mathrm{d}\mathbf{v}&=-i\omega\tilde{n}\\
\int(\mathbf{v}_d+\mathbf{v}_{dc})\cdot\nabla f\mathrm{d}\mathbf{v}&=\int\frac{v_\parallel^2+\frac{v_\perp^2}{2}+2v_\parallel R\Omega}{\omega_c R}\mathbf{e}_z\cdot ik_\theta\mathbf{e}_z f\mathrm{d}\mathbf{v}\\
&=\frac{imk_\theta}{eBR}\int\left(v_\parallel^2+\frac{v_\perp^2}{2}+2v_\parallel R\Omega\right)f\mathrm{d}\mathbf{v}\\
&=\frac{imk_\theta}{eBR}\left[\frac{2\left(n\tilde{T}+\tilde{n}T\right)}{m}+2R\Omega n\tilde{w}\right]\\
&=-i\omega_D\left[2\left(n\frac{\tilde{T}}{T}+\tilde{n}\right)+\frac{4R\Omega n\tilde{w}}{v_{thi}^2}\right]
\end{aligned}$$

$$\begin{aligned}
\int -\mathbf{v}_E \cdot \nabla F_M \mathrm{d}\mathbf{v} &= \int -\frac{ik_\theta \phi}{B}\mathbf{e}_x \cdot F_M \left[\left(\frac{3}{2} - \frac{mv^2}{2T}\right)\frac{1}{L_T} - \frac{1}{L_n} - \frac{mu'v_\parallel}{T}\right]\mathbf{e}_x \mathrm{d}\mathbf{v} \\
&= \frac{ik_\theta \phi}{B}\frac{n}{L_n} = -i\omega_D n \frac{e\phi}{T}\frac{R}{L_n} \\
\int -\frac{eF_M}{T}\left(\mathbf{v}_d + \mathbf{v}_{dc}\right)\cdot \nabla \phi \mathrm{d}\mathbf{v} &= -\frac{e}{T}\int F_M \frac{v_\parallel^2 + \frac{v_\perp^2}{2} + 2v_\parallel R\Omega}{\omega_c R}\mathbf{e}_z \cdot ik_\theta \phi \mathbf{e}_z \mathrm{d}\mathbf{v} \\
&= -\frac{em}{T}\int ik_\theta \phi F_M \frac{v_\parallel^2 + \frac{v_\perp^2}{2} + 2v_\parallel R\Omega}{eBR}\mathrm{d}\mathbf{v} \\
&= 2i\omega_D n \frac{e\phi}{T}
\end{aligned}$$

And the 0^{th} moment equation is

$$-i\omega\tilde{n} - i\omega_D\left[2\left(n\frac{\tilde{T}}{T} + \tilde{n}\right) + \frac{4R\Omega n\tilde{w}}{v_{thi}^2}\right] = -i\omega_D n\frac{e\phi}{T}\frac{R}{L_N} + 2i\omega_D n\frac{e\phi}{T}$$

Nondimensionalization is applied to all quantities by:

$$\begin{aligned}
\omega &\leftarrow \frac{\omega}{\omega_D} \\
u &\leftarrow \frac{u}{v_{th}} = \frac{R\Omega}{v_{th}} \\
\tilde{w} &\leftarrow \frac{\tilde{w}}{v_{th}} \\
\tilde{w} &\leftarrow \frac{\tilde{w}}{v_{th}} \\
u' &\leftarrow -\frac{R^2\nabla\Omega}{v_{th}} \\
\tilde{n} &\leftarrow \frac{\tilde{n}}{n} \\
\tilde{T} &\leftarrow \frac{\tilde{T}}{T} \\
\phi &\leftarrow \frac{e\phi}{T} \\
v_E = \frac{i}{2}k_\theta \rho \phi &\leftarrow \frac{v_E}{v_{th}} = \frac{ik_\theta}{B}\frac{e\phi}{T}\frac{T}{ev_{th}}
\end{aligned}$$

Here $v_{th} = \sqrt{\frac{2T}{m}}$ is the thermal velocity. After normalization, the dimensionless

0^{th} moment equation becomes

$$\omega\tilde{n} + 2\left(\tilde{n} + \tilde{T}\right) + 4u\tilde{w} = \left[\frac{R}{L_n} - 2\right]\phi \tag{A.13}$$

- 1^{st} moment

$$\begin{aligned}
\int \frac{\partial f}{\partial t} v_\parallel \mathrm{d}\mathbf{v} &= -i\omega n\tilde{w} \\
\int \mathbf{v}_d \cdot \nabla f v_\parallel \mathrm{d}\mathbf{v} &= \int v_\parallel \frac{v_\parallel^2 + \frac{v_\perp^2}{2}}{\omega_c R}\mathbf{e}_z \cdot ik_\theta \mathbf{e}_z f \mathrm{d}\mathbf{v} \\
&= \frac{imk_\theta}{eBR}\int \left(v_\parallel^3 + \frac{v_\parallel v_\perp^2}{2}\right) f \mathrm{d}\mathbf{v} \\
&= \frac{imk_\theta}{eBR}\int \left(\frac{v_\parallel^3}{2} + \frac{v_\parallel v^2}{2}\right) f \mathrm{d}\mathbf{v} \\
&= -4i\omega_D n\tilde{w} \\
\int \mathbf{v}_{dc} \cdot \nabla f v_\parallel \mathrm{d}\mathbf{v} &= \int v_\parallel \frac{2v_\parallel R\Omega}{\omega_c R}\mathbf{e}_z \cdot ik_\theta \mathbf{e}_z f \mathrm{d}\mathbf{v} \\
&= \frac{imk_\theta}{eBR}\int 2v_\parallel^2 R\Omega f \mathrm{d}\mathbf{v} \\
&= \frac{imk_\theta}{eBR}\frac{2R\Omega\left(n\tilde{T} + \tilde{n}T\right)}{m} \\
&= -2i\omega_D R\Omega\left(n\frac{\tilde{T}}{T} + \tilde{n}\right) \\
\int -\mathbf{v}_E \cdot \nabla F_M v_\parallel \mathrm{d}\mathbf{v} &= \int -\frac{ik_\theta\phi}{B}\mathbf{e}_x \cdot \\
&\quad \left[\left(\frac{3}{2} - \frac{mv^2}{2T}\right)\frac{1}{L_T} - \frac{1}{L_n} - \frac{mu'v_\parallel}{T}\right] F_M \mathbf{e}_x v_\parallel \mathrm{d}\mathbf{v} \\
&= \frac{ik_\theta\phi}{B} n u' \\
&= -i\omega_D n R u' \frac{e\phi}{T} \\
\int -\frac{eF_M}{T}\left(\mathbf{v}_d + \mathbf{v}_{dc}\right) \cdot \nabla\phi v_\parallel \mathrm{d}\mathbf{v} &= -\frac{e}{T}\int F_M \frac{v_\parallel^2 + \frac{v_\perp^2}{2} + 2v_\parallel R\Omega}{\omega_c R}\mathbf{e}_z \cdot ik_\theta\phi\mathbf{e}_z v_\parallel \mathrm{d}\mathbf{v} \\
&= -\frac{em}{T}\int ik_\theta\phi F_M \frac{v_\parallel^2 + \frac{v_\perp^2}{2} + 2v_\parallel R\Omega}{eBR} v_\parallel \mathrm{d}\mathbf{v} \\
&= 2i\omega_D n R\Omega\frac{e\phi}{T}
\end{aligned}$$

The dimensionless 1st moment equation is

$$\omega\tilde{w} + 4\tilde{w} + 2u\tilde{n} + 2u\tilde{T} = [u' - 2u]\,\phi \tag{A.14}$$

- 2nd moment

$$\begin{aligned}
\int \frac{\partial f}{\partial t} v^2 \mathrm{d}\mathbf{v} &= -3i\omega\frac{\tilde{P}}{m} = -\frac{3i\omega}{m}\left(n\tilde{T} + \tilde{n}T\right) \\
\int \mathbf{v}_d \cdot \nabla f v^2 \mathrm{d}\mathbf{v} &= \int v^2 \frac{v_\parallel^2 + \frac{v_\perp^2}{2}}{\omega_c R}\mathbf{e}_z \cdot ik_\theta \mathbf{e}_z f \mathrm{d}\mathbf{v} \\
&= \frac{imk_\theta}{eBR}\int v^2\left(v_\parallel^2 + \frac{v_\perp^2}{2}\right) f \mathrm{d}\mathbf{v} \\
&= -i\frac{10\omega_D}{m}\left(2n\tilde{T} + \tilde{n}T\right) \\
\int \mathbf{v}_{dc} \cdot \nabla f v^2 \mathrm{d}\mathbf{v} &= \int v^2 \frac{2v_\parallel R\Omega}{\omega_c R}\mathbf{e}_z \cdot ik_\theta \mathbf{e}_z f \mathrm{d}\mathbf{v} \\
&= \frac{imk_\theta}{eBR}\int 2v^2 v_\parallel R\Omega f \mathrm{d}\mathbf{v} \\
&= -i10\omega_D R\Omega\tilde{w} \\
\int -\mathbf{v}_E \cdot \nabla F_M v^2 \mathrm{d}\mathbf{v} &= \int -\frac{ik_\theta\phi}{B}\mathbf{e}_x \cdot \\
&\quad \left[\left(\frac{3}{2} - \frac{mv^2}{2T}\right)\frac{1}{L_T} - \frac{1}{L_n} - \frac{mu'v_\parallel}{T}\right] F_M \mathbf{e}_x v^2 \mathrm{d}\mathbf{v} \\
&= -\frac{ik_\theta\phi}{B}\left[\left(\frac{3}{2L_T} - \frac{1}{L_n}\right)\frac{3nT}{m} - \frac{m}{2T}\frac{1}{L_T}\frac{15nT^2}{m^2}\right] \\
&= -\frac{ik_\theta\phi}{B}\frac{3nT}{m}\left(\frac{1}{L_T} + \frac{1}{L_n}\right) \\
&= -i\omega_D\frac{e\phi}{T}\frac{3nT}{m}\left(\frac{R}{L_T} + \frac{R}{L_n}\right) \\
\int -\frac{eF_M}{T}\left(\mathbf{v}_d + \mathbf{v}_{dc}\right)\cdot\nabla\phi v^2 \mathrm{d}\mathbf{v} &= -\frac{e}{T}\int F_M \frac{v_\parallel^2 + \frac{v_\perp^2}{2} + 2v_\parallel R\Omega}{\omega_c R}\mathbf{e}_z \cdot ik_\theta\phi\mathbf{e}_z v^2 \mathrm{d}\mathbf{v} \\
&= -\frac{em}{T}\int ik_\theta\phi F_M \frac{v_\parallel^2 + \frac{v_\perp^2}{2} + 2v_\parallel R\Omega}{eBR} v^2 \mathrm{d}\mathbf{v} \\
&= i\omega_D\frac{e\phi}{T}\frac{10nT}{m}
\end{aligned}$$

We have

$$3\omega\left(\tilde{T}+\tilde{n}\right)+10\left(2\tilde{T}+\tilde{n}\right)+20u\tilde{w}=\left[3\left(\frac{R}{L_T}+\frac{R}{L_n}\right)-10\right]\phi$$

It is worth noting that $20u\tilde{w}$ comes from definition of $v_{th}=\sqrt{\frac{2T}{m}}$. Combining with Eq. A.14 yields

$$\omega\tilde{T}+\frac{4}{3}\tilde{n}+\frac{14}{3}\tilde{T}+\frac{8}{3}u\tilde{w}=\left[\frac{R}{L_T}-\frac{4}{3}\right]\phi \tag{A.15}$$

The integrations use the formulas

$$\int v^N F_M \mathrm{d}\mathbf{v}=\frac{2n}{\sqrt{\pi}}\left(\frac{2T}{m}\right)^{\frac{N}{2}}\Gamma\left(\frac{N+3}{2}\right)$$

$$=\begin{cases} n\left(N+1\right)!!\left(\frac{T}{m}\right)^{\frac{N}{2}} & \text{if n is even.} \\ \frac{2n}{\sqrt{\pi}}\left(\frac{2T}{m}\right)^{\frac{N}{2}}\left(\frac{N+1}{2}\right)! & \text{if n is odd.} \end{cases}$$

$$\int v_{\parallel}^M v_{\perp}^N v^L F_M \mathrm{d}\mathbf{v}=\frac{n}{\sqrt{\pi}}\left(\frac{2T}{m}\right)^{\frac{M+N+L}{2}}\Gamma\left(\frac{M+N+L+3}{2}\right)\int_0^{\pi}\cos^M\theta\sin^{N+1}\theta\mathrm{d}\theta$$

$$=\begin{cases} \frac{n}{2}\left(M+N+L+1\right)!!\left(\frac{T}{m}\right)^{\frac{M+N+L}{2}}\int_0^{\pi}\cos^M\theta\sin^{N+1}\theta\mathrm{d}\theta & \text{if M is even and N+L is even.} \\ \frac{n}{\sqrt{\pi}}\left(\frac{2T}{m}\right)^{\frac{M+N+L}{2}}\left(\frac{M+N+L+1}{2}\right)!\int_0^{\pi}\cos^M\theta\sin^{N+1}\theta\mathrm{d}\theta & \text{if M is even and N+L is odd.} \\ 0 & \text{if M is odd.} \end{cases}$$

The perturbed distribution is assumed to be

$$f=\left[\frac{\tilde{n}}{n}+\frac{\tilde{T}}{T}\left(\frac{mv^2}{2T}-\frac{3}{2}\right)+\frac{mv_{\parallel}\tilde{w}}{T}\right]F_M$$

Apply them to the moments integration,

$$\int f\mathrm{d}\mathbf{v}=\tilde{n}$$

$$\int v_\parallel^2 f \mathrm{d}\mathbf{v} = \frac{\tilde{n}T + n\tilde{T}}{m}$$

$$\int v_\perp^2 f \mathrm{d}\mathbf{v} = \frac{2\left(\tilde{n}T + n\tilde{T}\right)}{m}$$

$$\int v_\parallel f \mathrm{d}\mathbf{v} = \frac{m\tilde{w}}{T}\int v_\parallel F_M = n\tilde{w}$$

$$\int v^2 F_M \mathrm{d}\mathbf{v} = \frac{3nT}{m}$$

$$\int v_\parallel^2 F_M \mathrm{d}\mathbf{v} = \frac{nT}{m}$$

$$\int v_\perp^2 F_M \mathrm{d}\mathbf{v} = \frac{2nT}{m}$$

$$\int v_\parallel F_M \mathrm{d}\mathbf{v} = 0$$

$$\int v_\parallel^3 f \mathrm{d}\mathbf{v} = \frac{m\tilde{w}}{T}\int v_\parallel^4 F_M \mathrm{d}\mathbf{v} = \frac{3nT\tilde{w}}{m}$$

$$\int v_\parallel v^2 f \mathrm{d}\mathbf{v} = \frac{m\tilde{w}}{T}\int v_\parallel^2 v^2 F_M \mathrm{d}\mathbf{v} = \frac{5nT\tilde{w}}{m}$$

$$\int v_\parallel^3 F_M \mathrm{d}\mathbf{v} = 0$$

$$\int v_\parallel v_\perp^2 F_M \mathrm{d}\mathbf{v} = 0$$

$$\int v^2 f \mathrm{d}\mathbf{v} = \frac{3\left(\tilde{n}T + n\tilde{T}\right)}{m}$$

$$\int v_\parallel^2 v^2 f \mathrm{d}\mathbf{v} = \frac{\tilde{n}}{n}\int v_\parallel^2 v^2 F_M \mathrm{d}\mathbf{v} + \frac{\tilde{T}}{T}\int \left(\frac{mv^2}{2T} - \frac{3}{2}\right) v_\parallel^2 v^2 F_M \mathrm{d}\mathbf{v} = \frac{5T^2}{m^2}\tilde{n} + \frac{10nT}{m^2}\tilde{n}$$

$$\int v_\perp^2 v^2 f \mathrm{d}\mathbf{v} = \frac{10T^2}{m^2}\tilde{n} + \frac{20nT}{m^2}\tilde{n}$$

$$\int v_\parallel^2 v^2 F_M \mathrm{d}\mathbf{v} = \frac{5nT^2}{m^2}$$

$$\int v_\perp^2 v^2 F_M \mathrm{d}\mathbf{v} = \frac{10nT^2}{m^2}$$

Eq. A.13$\times u$ - Eq. A.14, neglect the u^2 term, assume $T_i = T_e$ and adiabatic electrons $\tilde{n} = \phi\frac{T_i}{T_e} = \phi$:

$$(\omega + 4)\,\tilde{w} = \left[u' - \left(\frac{R}{L_n} - \omega\right)u\right]\phi \tag{A.16}$$

The quasi-linear parallel momentum flux (normalized with ion heat flux) is:

$$\Gamma_\phi = \left\langle \int \mathbf{v}_E v_\parallel f \mathrm{d}\mathbf{v} \right\rangle = \frac{1}{2}\mathrm{Re}\left[-\frac{i}{2}k_\theta \rho \phi^* \tilde{w}\right] = \frac{1}{4}k_\theta \rho \mathrm{Im}\left[\phi^* \tilde{w}\right] \tag{A.17}$$

where

$$\begin{aligned}
\tilde{w} &= \frac{\left[u' - \left(\frac{R}{L_n} - \omega\right)u\right]\phi}{\omega + 4} = \frac{A + iB}{C}\phi \\
A &= \left[u' - \left(\frac{R}{L_n} - \omega_R\right)u\right](\omega_R + 4) + \gamma^2 u \\
B &= \gamma\left[\left(\frac{R}{L_n} + 4\right)u - u'\right] \\
C &= (\omega_R + 4)^2 + \gamma^2
\end{aligned}$$

Now it is straightforward to calculate the momentum diffusivity χ_ϕ and pinch V_{pinch}:

$$\begin{aligned}
\Gamma_\phi &= \frac{1}{4}k_\theta \rho \mathrm{Im}\left[\phi^* \tilde{w}\right] = \frac{1}{4}k_\theta \rho \frac{B}{C}|\phi|^2 = \frac{1}{4}\frac{k_\theta \rho \gamma |\phi|^2}{(\omega_R + 4)^2 + \gamma^2}\left[\left(\frac{R}{L_n} + 4\right)u - u'\right] \\
&= \chi_\phi\left[u' - \left(\frac{R}{L_n} + 4\right)u\right] \\
&= \chi_\phi u' + V_{\text{pinch}} u \\
\chi_\phi &= -\frac{1}{4}k_\theta \rho \frac{\gamma}{(\omega_R + 4)^2 + \gamma^2}|\phi|^2 \\
V_{\text{pinch}} &= -\chi_\phi\left(\frac{R}{L_n} + 4\right)
\end{aligned}$$

It is worth noting that χ_ϕ is positive, because γ, which is normalized to $\omega_D = k_\theta T_0/eBR$, is negative. As a reminder, by definition $u' = -\frac{R^2 \nabla \Omega}{v_{th}}$, $\Gamma_\phi > 0$ means outward flux. Back to real units, the momentum pinch predicted by this fluid model will be:

$$\frac{R V_{\text{pinch}}}{\chi_\phi} = -4 - \frac{R}{L_n} \tag{A.18}$$

A.2 Pinch in Total Angular Momentum

In the previous section, the diffusive and convective terms of the momentum flux Γ_ϕ for parallel momentum density $nU_\parallel$ is derived. Now we will consider the total angular momentum density $nU_\parallel R$ using the same set of moment equations Eq. A.13, A.14 and A.15. The perturbed total angular momentum density is:

$$\tilde{W} = R(\tilde{n}u + \tilde{w}) \tag{A.19}$$

Eq. A.13$\times Ru$ + Eq. A.14$\times R$ yields:

$$\omega\tilde{W} + 4\tilde{W} + 4Ru\tilde{T} + \cancel{4Ru^2\tilde{w}} = R\left[u' + \frac{R}{L_n}u - 4u\right]\phi \tag{A.20}$$

where the quadratic term in u is neglected.

The angular momentum flux Γ_Ω will be:

$$\Gamma_\Omega \propto \mathrm{Im}\left[\phi^*\tilde{W}\right] = \frac{\gamma|\phi|^2}{(\omega_R+4)^2+\gamma^2}\left[-u' - \frac{R}{L_n}u + 4u\right] - \mathrm{Im}\left[4Ru\frac{\phi^*\tilde{T}}{\omega+4}\right] \tag{A.21}$$

The 1$^{\text{st}}$ term on RHS is so-called turbulent equipartition (TEP) term, and the 2$^{\text{nd}}$ term is the thermoelectric pinch term. For adiabatic electrons

$$\tilde{n} = \frac{e\phi}{T_e} = \frac{\phi}{\tau} \tag{A.22}$$

where we relax the assumption $T_e = T_i$ and define $\tau = \frac{T_e}{T_i}$.

Rewrite Eq. A.13 and Eq. A.15:

$$2\tilde{T} + 4u\tilde{w} = \left[\frac{R}{L_n} - 2 - \frac{2}{\tau} - \frac{\omega}{\tau}\right]\phi \tag{A.23}$$

$$\omega\tilde{T} + \frac{14}{3}\tilde{T} + \frac{8}{3}u\tilde{w} = \left[\frac{R}{L_T} - \frac{4}{3} - \frac{4}{3\tau}\right]\phi \tag{A.24}$$

Substitute $\tilde{T}$ of Eq. A.24 into Eq. A.21 and neglect the $u\tilde{w}$ term:

$$\frac{\phi^* \tilde{T}}{\omega + 4} = \frac{|\phi|^2}{(\omega + 14/3)(\omega + 4)} \left(\frac{R}{L_T} - \frac{4}{3} - \frac{4}{3\tau} \right) \tag{A.25}$$

Combining Eq. A.23 and A.24 (neglect the $u\tilde{w}$ term) yields:

$$\frac{1}{\omega + 14/3} = \frac{R/L_n - 2 - \omega/\tau - 2/\tau}{2(R/L_T - 4/3 - 4/3\tau)}$$

The Eq. A.25 becomes

$$\mathrm{Im}\left[\frac{4\phi^* \tilde{T}}{\omega + 4} \right] = \mathrm{Im}\left[\frac{2|\phi|^2}{\omega + 4} \left(\frac{R}{L_n} - 2 - \frac{\omega}{\tau} - \frac{2}{\tau} \right) \right] \tag{A.26}$$

$$= \frac{\gamma |\phi|^2}{(\omega_R + 4)^2 + \gamma^2} \left(-2\frac{R}{L_n} - \frac{4}{\tau} + 4 \right) \tag{A.27}$$

The total angular momentum flux Γ_Ω is

$$\Gamma_\Omega = R\chi_\phi \left[u' + \left(-4 + \frac{R}{L_n} \right) u + \left(-2\frac{R}{L_n} - \frac{4}{\tau} + 4 \right) u \right] \tag{A.28}$$

$$\chi_\phi \propto -\frac{\gamma |\phi|^2}{(\omega_R + 4)^2 + \gamma^2} \tag{A.29}$$

In Eq. A.28 the 1st pinch term $-4 + \frac{R}{L_n}$ is TEP term, and the 2nd pinch term $-2\frac{R}{L_n} - \frac{4}{\tau} + 4$ is from thermoelectric term. Combining these two terms yields:

$$\Gamma_\Omega = R\chi_\phi u' + R^2 V_{\mathrm{pinch}} u$$

The momentum pinch is:

$$\frac{R V_{\mathrm{pinch}}}{\chi_\phi} = -\frac{R}{L_n} - \frac{4}{\tau} \tag{A.30}$$

This is in agreement with the result derived for the flux of parallel momentum, when $\tau = 1$.

A.3 Compensation of the Coriolis Pinch

In previous sections, we neglect the parallel streaming term $v_{\parallel}$ with the assumption $v_{\parallel}\mathbf{b}\cdot\nabla \approx 0$. If we relax this assumption and consider the parallel dynamics, Eqs. A.13, A.14 and A.15 still hold:

$$\omega\tilde{n} + 2\tilde{n} + 2\tilde{T} + 4\hat{u}\tilde{w} = \left[\frac{R}{L_n} - 2\right]\phi \tag{A.31}$$

$$\omega\tilde{w} + 4\tilde{w} + 2\hat{u}\tilde{n} + 2\hat{u}\tilde{T} = [u' - 2\hat{u}]\,\phi \tag{A.32}$$

$$\omega\tilde{T} + \frac{4}{3}\tilde{n} + \frac{14}{3}\tilde{T} + \frac{8}{3}\hat{u}\tilde{w} = \left[\frac{R}{L_T} - \frac{4}{3}\right]\phi \tag{A.33}$$

where $\hat{u}$ is:

$$\hat{u} = u + k_{\parallel N} \tag{A.34}$$

and $k_{\parallel N}$ is the normalized parallel wave vector:

$$k_{\parallel N} = \frac{k_{\parallel}R}{2k_\theta\rho},\ \rho = \frac{mv_{th}}{eB} \tag{A.35}$$

The choice of $k_{\parallel}$ can be made by selecting the most unstable mode. We will investigate the growth rate of ITG modes with adiabatic electrons and assume $\hat{u} \ll 1$. Rearrange Eqs. A.31 and A.33 as:

$$2\tilde{T} + 4\hat{u}\tilde{w} = \left[\frac{R}{L_n} - 2 - \frac{2}{\tau} - \frac{\omega}{\tau}\right]\phi \tag{A.36}$$

$$\omega\tilde{T} + \frac{14}{3}\tilde{T} + \frac{8}{3}\hat{u}\tilde{w} = \left[\frac{R}{L_T} - \frac{4}{3} - \frac{4}{3\tau}\right]\phi \tag{A.37}$$

Again we assume $\tau = 1$. Eliminate the perturbed temperature $\tilde{T}$ in Eqs. A.36 and A.37:

$$\omega^2 + \left(\frac{26}{3} - \frac{R}{L_n}\right)\omega + \left(\frac{2R}{L_T} - \frac{14R}{3L_n}\right) + \frac{40}{3} + 4\left(\omega + \frac{10}{3}\right)\frac{\hat{u}\tilde{w}}{\phi} = 0 \tag{A.38}$$

An approximated solution for Eq. A.38 at $\hat{u} = \gamma = 0$ is

$$\omega = \omega_R = \frac{1}{2}\left(\frac{R}{L_n} - \frac{26}{3}\right) \tag{A.39}$$

From Eq. A.32 we have:

$$\frac{\hat{u}\tilde{w}}{\phi} = \frac{1}{\omega + 4}\left[\hat{u}u' - 4\hat{u}^2 - 2\hat{u}^2\frac{\tilde{T}}{\phi}\right] \tag{A.40}$$

Substituting into Eq.A.40 with $\tilde{T}$ obtained in Eq. A.36 and ω obtained in Eq.A.39 results in the estimation of term $4\left(\omega + 10/3\right)\frac{\hat{u}\tilde{w}}{\phi}$ in Eq. A.38:

$$\frac{\tilde{T}}{\phi} = \frac{1}{4}\left(\frac{R}{L_n} + \frac{2}{3}\right) - 2\frac{\hat{u}\tilde{w}}{\phi} \tag{A.41}$$

$$\begin{aligned} 4\left(\omega + 10/3\right)\frac{\hat{u}\tilde{w}}{\phi} &= \frac{\omega + \frac{10}{3}}{\omega + 4}\left[4\hat{u}u' - 16\hat{u}^2 - 2\hat{u}^2\left(\left(\frac{R}{L_n} + \frac{3}{2}\right) - 8\frac{\hat{u}\tilde{w}}{\phi}\right)\right] \\ &\approx \frac{R/L_n - 2}{R/L_n - 2/3}\left[4\hat{u}u' - 2\hat{u}^2\left(\frac{R}{L_n} + \frac{26}{3}\right)\right] \end{aligned} \tag{A.42}$$

From Eq. A.38 the growth rate γ can be estimated as:

$$\gamma^2 \propto 4\left(\omega + \frac{10}{3}\right)\frac{\hat{u}\tilde{w}}{\phi} = \frac{R/L_n - 2}{R/L_n - 2/3}\left[4\hat{u}u' - 2\hat{u}^2\left(\frac{R}{L_n} + \frac{26}{3}\right)\right] \tag{A.43}$$

- For $\frac{2}{3} < \frac{R}{L_n} < 2$, $\gamma \propto c + -au'\hat{u} + \hat{u}^2$, the most unstable mode corresponds to infinite $\hat{u}$, which breaks the $\hat{u} \ll 1$ assumption. This range of parameter will not be considered.

- For $\frac{R}{L_n} < \frac{2}{3}$ or $\frac{R}{L_n} > 2$, $\gamma \propto c + au'\hat{u} - \hat{u}^2$ and the most unstable mode corresponds

to $\hat{u} = 0$, that is

$$k_{\|N} = -u \tag{A.44}$$

This suggests that the parallel dynamics effectively eliminate the Coriolis drift from the equations. The so-called "compensation" effect is expected to remove the Coriolis pinch in parallel momentum flux, according to the derivations in this section based on the fluid model with adiabatic electrons.

Numerical simulations [256] show that with adiabatic electrons and parallel dynamics, there is no pinch in the parallel momentum flux. However if kinetic electrons are considered, a finite momentum pinch appears as a function of root of the inverse aspect ratio $\sqrt{\epsilon}$, i.e. the fraction of trapped particles.

$$\frac{RV_{\text{pinch}}}{\chi_\phi} \propto \sqrt{\epsilon} \approx \sqrt{\frac{r}{R}} \tag{A.45}$$

Appendix B

ICRF Waves

B.1 Plasma Wave Theory

The charged particles (electrons and ions) can respond to electric and magnetic fields, which can be described by Maxwell's equations:

$$\nabla \cdot \mathbf{E} = \frac{\rho}{\varepsilon_0} \tag{B.1}$$

$$\nabla \cdot \mathbf{B} = 0 \tag{B.2}$$

$$\nabla \times \mathbf{E} = -\frac{\partial \mathbf{B}}{\partial t} \tag{B.3}$$

$$\nabla \times \mathbf{B} = \mu_0 \mathbf{j} + \frac{1}{c^2}\frac{\partial \mathbf{E}}{\partial t} \tag{B.4}$$

The charge density ρ and current density $\mathbf{j}$ can be described individually by equation of motion or kinetically by the Fokker-Planck equation.

B.1.1 Plasma Dielectric and Dispersion Relation

Small fluctuations (waves) can be studied as perturbations around the background equilibrium, $\mathbf{E} = \mathbf{E}_0 + \mathbf{E}_1$, where $\mathbf{E}_0$ is the background equilibrium electric field, and $\mathbf{E}_1$ is the perturbed electric field. The same notation is applied to magnetic field $\mathbf{B}$. By equilibrium it means $\partial/\partial t = 0$. Taking the perturbed terms of Eqs. B.3 and B.4,

we can get

$$\nabla \times (\nabla \times \mathbf{E}_1) + \frac{1}{c^2}\frac{\partial^2 \mathbf{E}_1}{\partial t^2} = -\mu_0 \frac{\partial}{\partial t}\mathbf{j}_1 \tag{B.5}$$

Now we will linearize the equation by assuming all perturbed quantities have the form of $e^{i(\mathbf{k}\cdot\mathbf{r}-\omega t)}$, Eq.B.5 becomes:

$$\mathbf{k} \times (\mathbf{k} \times \mathbf{E}_1) + \frac{\omega^2}{c^2}\mathbf{E}_1 = -i\mu_0\omega\mathbf{j}_1 \tag{B.6}$$

We define the plasma conductivity tensor $\overleftrightarrow{\sigma}$, refractive index $\mathbf{n}$ and plasma dielectric tensor $\overleftrightarrow{\mathbf{K}}$ as

$$\mathbf{j}_1 = \overleftrightarrow{\sigma}\mathbf{E}_1 \tag{B.7}$$

$$\mathbf{n} = \frac{c\mathbf{k}}{\omega} \tag{B.8}$$

$$\overleftrightarrow{\mathbf{K}} = \overleftrightarrow{\mathbf{I}} + \overleftrightarrow{\chi} = \overleftrightarrow{\mathbf{I}} + \frac{i}{\omega\varepsilon_0}\overleftrightarrow{\sigma} \tag{B.9}$$

Eq.B.6 can be rewritten as

$$\overleftrightarrow{\mathbf{D}} \cdot \mathbf{E}_1 \equiv \left(\mathbf{nn} - n^2 + \overleftrightarrow{\mathbf{K}}\right) \cdot \mathbf{E}_1 = 0 \tag{B.10}$$

The condition for existence of non-trivial electric field solution gives the plasma dispersion relation

$$\det \overleftrightarrow{\mathbf{D}} = 0 \tag{B.11}$$

B.1.2 Cold Plasma Dispersion Relation

For the rest of this chapter, I will drop the subscript 1 on $\mathbf{E}$ for simplicity. Under the cold plasma assumption, finite thermal effects on particle motion can be neglected. The response of s-species particles to waves can be written as

$$m_s \frac{\partial \mathbf{v}_s}{\partial t} = q_s \left(\mathbf{E} + \mathbf{v_s} \times \mathbf{B}_0\right) \tag{B.12}$$

Assume the equilibrium magnetic field $\mathbf{B}_0$ is in the z-axis direction. By solving

Eq.B.12, we can get the perturbed current $\mathbf{j}_s = q_s n_{j0} \mathbf{v}_s$ for each species. Substitute the current into the definition of the dielectric tensor, and we get

$$\overleftrightarrow{\mathbf{K}} = \begin{pmatrix} S & -iD & 0 \\ iD & S & 0 \\ 0 & 0 & P \end{pmatrix} \tag{B.13}$$

where

$$S = 1 - \sum_s \frac{\omega_{ps}^2}{\omega^2 - \Omega_s^2} = \frac{R+L}{2} \tag{B.14}$$

$$D = \sum_s \frac{\Omega_s}{\omega} \frac{\omega_{ps}^2}{\omega^2 - \Omega_s^2} = \frac{R-L}{2} \tag{B.15}$$

$$P = 1 - \sum_s \frac{\omega_{ps}^2}{\omega^2} \tag{B.16}$$

$$L = 1 - \sum_s \frac{\omega_{ps}^2}{\omega(\omega - \Omega_s)} \tag{B.17}$$

$$R = 1 - \sum_s \frac{\omega_{ps}^2}{\omega(\omega + \Omega_s)} \tag{B.18}$$

$$\omega_{ps} = \sqrt{\frac{q_s^2 n_{s0}}{\varepsilon_0 m_s}} \tag{B.19}$$

$$\Omega_s = \frac{q_s B_0}{m_s} \tag{B.20}$$

The dispersion relation for cold plasma waves can be written as

$$\begin{aligned} 0 &= \det\left(\mathbf{nn} - n^2 + \overleftrightarrow{\mathbf{K}}\right) \\ &= \begin{vmatrix} S - n_\parallel^2 & -iD & n_\perp n_\parallel \\ iD & S - n^2 & 0 \\ n_\perp n_\parallel & 0 & P - n_\perp^2 \end{vmatrix} \end{aligned} \tag{B.21}$$

where $n_\parallel = \mathbf{n} \cdot \mathbf{B}_0 / B_0 = n\cos\theta$ is the parallel refractive index, and $n_\perp = n\sin\theta$ is the perpendicular refractive index.

For propagation perpendicular to $\mathbf{B_0}$ $(n_\parallel \to 0)$, two dispersions are

$$\text{O-mode: } n_\perp^2 = P \tag{B.22}$$

$$\text{X-mode: } n_\perp^2 = \frac{RL}{S} \tag{B.23}$$

O-mode means ordinary mode because its electric field $\mathbf{E} = E_z\hat{z}$ is linearly polarized and parallel to $\mathbf{B_0}$. The magnetic field doesn't play a role in the wave propagation. For tokamak geometry, O-mode is accessible to the plasma from both the high field side (HFS) and low field side (LHS), as long as $\omega_{pe}^2 \leq \Omega_e^2$. This is used by the reflectometer for plasma density measurement.

X-mode means extraordinary mode. It has accessibility to the plasma only from the HFS. X-mode is elliptically polarized as

$$\frac{E_x}{E_y} = i\frac{D}{S} \neq \pm i \tag{B.24}$$

For propagation parallel to $\mathbf{B_0}$ $(n_\perp \to 0)$, two dispersions are

$$\text{R-wave: } n_\parallel^2 = R \tag{B.25}$$

$$\text{L-wave: } n_\parallel^2 = L \tag{B.26}$$

The R-wave has right-hand polarization, and L-wave has left-hand polarization,

$$\text{R-wave: } \frac{E_x}{E_y} = i\frac{D}{S - N^2} = -i \tag{B.27}$$

$$\text{L-wave: } \frac{E_x}{E_y} = i\frac{D}{S - N^2} = i \tag{B.28}$$

B.1.3 1-D Wave Propagation in Inhomogeneous Plasmas

The dispersion relation Eq.B.21 can be rearranged as

$$An^4 - Bn^2 + C = 0 \tag{B.29}$$

where

$$A = S\sin^2\theta + P\cos^2\theta \tag{B.30}$$

$$B = RL\sin^2\theta + PS\left(1+\cos^2\theta\right) \tag{B.31}$$

$$C = PRL \tag{B.32}$$

In Alcator C-Mod, the ICRF antennas are located at the outboard periphery of the plasma. The parallel refractive index $n_\parallel$ is fixed by the ICRF launcher structure, and the perpendicular refractive index $n_\perp$ can be solved as

$$n^2 = \frac{B \pm \sqrt{B^2 - 4AC}}{2A} \tag{B.33}$$

For ion cyclotron range of frequencies (ICRF), $\omega \sim \Omega_i$ and $P \gg S, n_\perp^2$, the dispersion relation becomes

$$A \approx P\cos^2\theta \tag{B.34}$$

$$B \approx PS\left(1+\cos^2\theta\right) \tag{B.35}$$

$$C = PRL \tag{B.36}$$

$$n_\perp^2 \approx \frac{\left(n_\parallel^2 - R\right)\left(n_\parallel^2 - L\right)}{S - n_\parallel^2} \tag{B.37}$$

Eq.B.37 is called the ICRF equation. From it we can get the cut-off ($n_\perp^2 = 0$) and resonance ($n_\perp^2 = \infty$) conditions.

Cut-offs: $n_\perp^2 = 0$

There are two cut-offs:

Right-handed cut-off

$$n_\parallel^2 = R = 1 - \sum_i \frac{\omega_{pi}^2}{\omega\left(\omega + \Omega_i\right)} \tag{B.38}$$

Left-handed cut-off

$$n_{\parallel}^2 = L = 1 - \sum_i \frac{\omega_{pi}^2}{\omega\left(\omega - \Omega_i\right)} \tag{B.39}$$

The summation over i includes all ion species. For ion cyclotron frequency range $\omega \sim \Omega_i \ll \Omega_e$, we can ignore the electron contribution to R, L and S.

Resonance: $n_{\perp}^2 = \infty$

$$n_{\parallel}^2 = S = 1 - \sum_i \frac{\omega_{pi}^2}{\omega^2 - \Omega_i^2} \tag{B.40}$$

For single ion species plasma and $\omega < \Omega_i$, at the same plasma location we have

$$R < S < L \tag{B.41}$$

Therefore we have

$$n\left(x_L\right) < n\left(x_S\right) < n\left(x_R\right) \tag{B.42}$$

where $n\left(x_L\right), n\left(x_R\right), n\left(x_S\right)$ are the plasma right-handed cut-off, left-handed cut-off and resonance density, respectively.

For single ion species plasma and $\omega > \Omega_i$, there is no resonance since $S < 0$.

It is worth noting that for a single ion species plasma, there is no fundamental cyclotron resonance absorption because the left-handed circularly polarized electric field is perfectly screened $E_+ \equiv E_x + iE_y \to 0$ when $(\omega = \Omega_i)$. This will be discussed in the next section.

For two-ion species plasmas (for example deuterium majority with hydrogen minority), with a small minority of fraction $(n_H/n_D \sim 1\text{s}\%)$, the minority cyclotron resonance $(\omega = \Omega_m)$ layer is close to the hybrid resonance $\left(n_{\parallel}^2 = S\right)$ layer. The ICRF waves are absorbed by minority ions through minority cyclotron damping, which is called minority heating. The distance between the minority cyclotron resonance layer and the hybrid resonance layer becomes larger as the minority fraction increases $(n_H/n_D > 10\%)$, in this regime the waves are mode–converted into ion Bernstein waves (IBW) and absorbed by electrons through Landau

damping. This is called the mode conversion regime. This will also be discussed in the next section. From now on in this chapter, the subscript m denotes the minority species, and subscript M denotes the majority species.

B.2 Cyclotron Resonance Heating

The ICRF power dissipation due to fundamental and second harmonic cyclotron resonance in tokamaks is [258, Chapter 6]:

$\omega = \omega_{ci}$:

$$P_1 = \frac{\pi^{1/2}\omega_{pi}^2}{4k_\parallel v_{ti}}\varepsilon_0 |E_+|^2 exp\left[-\left(\frac{\omega-\omega_{ci}}{k_\parallel v_{ti}}\right)^2\right] \tag{B.43}$$

$\omega = 2\omega_{ci}$:

$$P_2 = \frac{\pi^{1/2}\omega_{pi}^2}{4k_\parallel v_{ti}}\varepsilon_0 |E_+|^2 (k_\perp \rho_i)^2 exp\left[-\left(\frac{\omega-2\omega_{ci}}{k_\parallel v_{ti}}\right)^2\right] \tag{B.44}$$

It is worth noting that only the left-handed circularly polarized component of electric field $E_+ \equiv E_x + iE_y$ is absorbed by ions.

B.2.1 Single Ion Species Plasma

In the cold plasma limit, we have

$$\left|\frac{E_+}{E_y}\right|^2 = \frac{\left(\frac{\omega}{\Omega_i}-1\right)^2\left(\frac{\omega}{\Omega_i}-\cos^2\theta\right)^2}{\left(\frac{\omega}{\Omega_i}\right)^2(1+\cos^2\theta)^2} \tag{B.45}$$

For $\cos\theta \to 0$, the polarizations at fundamental and 2^{nd} harmonic are

$$\frac{E_+}{E_y} \to 0 \quad \text{at} \quad \omega = \Omega_i \tag{B.46}$$

$$\frac{E_+}{E_y} \to 1 \quad \text{at} \quad \omega = 2\Omega_i \tag{B.47}$$

If we consider the hot plasma effect, the polarization at the fundamental and 2^{nd}

harmonic will be

$$\frac{E_+}{E_y} \to 0 \quad \text{at} \quad \omega = \Omega_i \tag{B.48}$$

$$\frac{E_+^2}{E_y^2} \approx \frac{1}{1+\sigma_2^2} \quad \text{at} \quad \omega = 2\Omega_i \tag{B.49}$$

where

$$\sigma_2 = \frac{3}{4}\sqrt{\frac{\pi}{2}}\frac{k_\perp}{k_\parallel}k_\perp \rho_i \tag{B.50}$$

For a single species plasma, there is no fundamental cyclotron resonance absorption either in the cold plasma limit or with finite temperature effects. 2^{nd} harmonic resonance heating is possible when σ_2 is small. The corresponding transmission coefficient per pass is

$$T = e^{-2\eta} \tag{B.51}$$

where 2η is the transmission coefficient exponent

$$2\eta \approx \frac{\pi}{4}\frac{\beta_i k_\perp R}{1+\sigma_2^2} \tag{B.52}$$

$$\beta_i = \frac{2\mu_0 n_0 T_i}{B^2} \tag{B.53}$$

and the 2^{nd} harmonic resonance absorption coefficient per pass is

$$A = 1 - T = 1 - e^{-2\eta} \tag{B.54}$$

For Alcator C-Mod parameters, $f = 80$ MHz, $B_0 = 5.4$ T, $T_i = 4$ keV, $n_D = 2 \times 10^{20}$ m^{-3},

if $n_\parallel = 8$:

$$\sigma_2 = 0.891$$

$$2\eta = 0.276$$

$$T = e^{-2\eta} = 0.759$$

$$A = 1 - T = 0.241$$

if $n_{\parallel} = 4$:

$$\sigma_2 = 1.782$$

$$2\eta = 0.119$$

$$T = e^{-2\eta} = 0.888$$

$$A = 1 - T = 0.112$$

B.2.2 Two-ion Species Plasma

If a minority ion species (m) is present in a majority plasma (M), there is an evanescent layer between the ion-ion hybrid resonance layer $\left(n_{\parallel}^2 = S\right)$ and minority species cyclotron resonance layer ($\omega = \Omega_m$). Fig.B-1 shows the locations of H(minority)–D(majority) hybrid resonance (mode conversion, labeled as MC in figure) layer $n_{\parallel}^2 = S$, minority fundamental resonance and majority 2^{nd} harmonic resonance layer $\omega = 2\Omega_M = \Omega_m$, the left-handed cut-off $n_{\parallel}^2 = L$ and the right-handed cut-off $n_{\parallel}^2 = R$, at given electron density and temperature profiles, and $B_0 = 5.4$ T, $\omega = 80$ MHz with Alcator C-Mod geometry. It can be seen that the width of this evanescent layer is small for small hydrogen fraction, and becomes larger as n_H/n_D increases.

At minority resonance layer where $\omega = \Omega_m$, the absorbed power by minority ions in Eq.B.43 can be rewritten as

$$P_1 = \frac{\pi^{1/2}\omega_{pM}^2}{4k_{\parallel}v_{ti}}\frac{n_m}{n_M}\frac{M}{m}\varepsilon_0 |E_+|^2 exp\left[-\left(\frac{\omega - \omega_{ci}}{k_{\parallel}v_{ti}}\right)^2\right] \tag{B.55}$$

The transmission coefficient exponent can be derived as

$$2\eta = \frac{\pi}{4}\frac{2\omega_{pM}}{c}\frac{n_m}{n_M}\frac{Z_m}{Z_M}R\left(\frac{E_+}{E_y}\right)^2 \tag{B.56}$$

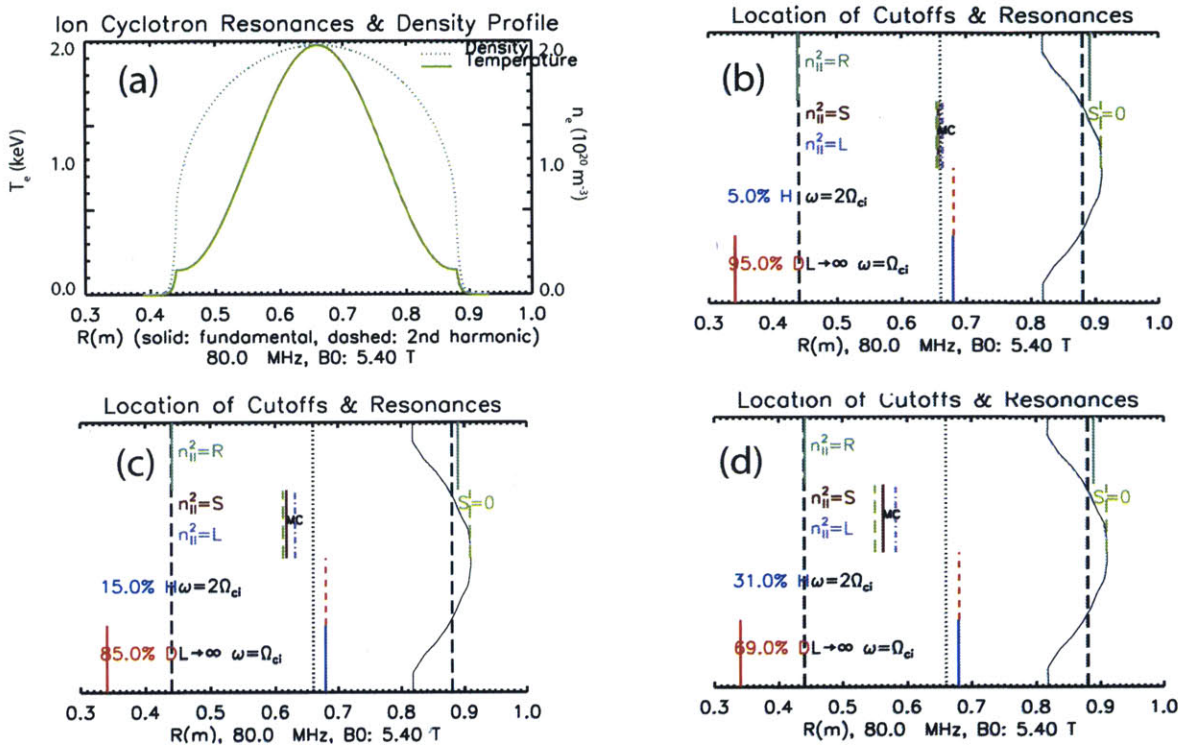

Figure B-1: (a) Density and temperature profiles; resonance and cut-off layers with (b) 5% (c) 15% and (d) 31% hydrogen concentration.

and the polarization is

$$\left(\frac{E_+}{E_y}\right)^2 = \frac{1}{1+\sigma_1^2}\left(1-\frac{Z_m}{Z_M}\frac{M}{m}\right)^2 \tag{B.57}$$

where

$$\sigma_1 = \frac{\sqrt{\pi}}{2}\frac{n_m}{n_M}\frac{M}{m}\frac{Z_m^2}{Z_M^2}\left(1-\frac{\Omega_M}{\omega^2}\right)\frac{\omega}{k_\parallel v_{th}} \tag{B.58}$$

We can see that the minority power absorption efficient is proportional to the minority concentration n_m/n_M and the polarization E_+^2 (Eqs.B.55, B.56). The latter is determined by n_m/n_M through σ_1^2 (Eqs.B.57, B.58). If n_m/n_M is moderate (a few percentage), then $\sigma_1^2 \ll 1$, $\frac{E_+}{E_y} \sim 1$, $2\eta \sim 1$ and $A \sim 1$. If n_m/n_M is large ($\geq 10\%$), then $\sigma_1^2 \gg 1$, $\frac{E_+}{E_y} \to 0$, $2\eta \to 0$ and $A \to 0$.

For D–H plasma with Alcator C-Mod parameters, $f = 80$ MHz, $B_0 = 5.4$ T, $T_H = 4$ keV, $n_e = 2 \times 10^{20}$ m^{-3} and $n_\parallel = 9$,

if $n_H/n_e = 5\%$:

$$2\eta = 0.303$$
$$T = e^{-2\eta} = 0.738$$
$$A = 1 - T = 0.262$$

if $n_H/n_e = 10\%$:

$$2\eta = 0.159$$
$$T = e^{-2\eta} = 0.853$$
$$A = 1 - T = 0.147$$

if $n_H/n_e = 30\%$:

$$2\eta = 0.042$$
$$T = e^{-2\eta} = 0.958$$
$$A = 1 - T = 0.042$$

The waves are not absorbed by the minority ion cyclotron resonance layer at high minority concentration. This is due to the small left-handed polarized electric field E_+ at the resonance layer far away from the hybrid layer. In this so-called mode conversion regime, the waves are converted into ion Bernstein waves (IBW). These waves can be damped by electrons with sufficiently large $k_\parallel$. However, if the resonance layer of impurity minority is close to the ion-ion hybrid layer, it is possible that impurity ions absorb power and get energetic. This is what we observed in Alcator C-Mod, which is discussed in Section 2.3 and Chapter 5.

THIS PAGE INTENTIONALLY LEFT BLANK

Appendix C

Generalized Singular Value Decomposition

As is mentioned in Chapter 3, one outstanding difficulty in the cold pulse experiment is the presence of sawtooth activity. Large amplitude sawteeth of $\sim$ 100 eV in the core electron temperature occurred during the cold pulse experiments, which contaminates the quality of transient measurements. An example of this sawtooth activity is shown in Fig. C-1. There are several sawtooth removal techniques, such as time averaging method, peak-finding method. In this thesis, GSVD (generalized singular value decomposition) method [224] is used to remove the sawtooth oscillation. It will be introduced in this appendix.

C.1 Phase Space of Multidimensional Data

Consider an experiment with d time-serial measurements $\{Y_1(t), Y_2(t), \cdots, Y_d(t)\}$. The d-dimension vector $\mathbf{Y}(s) \equiv [Y_1(s), Y_2(s), \cdots, Y_d(s)]$ represents a point in the d-dimension phase space at time s, and $\mathbf{Y}(t)$ will draw a trajectory in this phase space. Fig. C-2 (a)(b) are the trajectories in a 3-D phase space. Each axis corresponds to a measurement channel: $x = T_e(r/a = 0.44)$, $y = T_e(r/a = 0.57)$, $x = T_e(r/a = 0.68)$, where the normalized electron temperatures in Fig. C-1 are used. Fig. C-2 (a) is the trajectory with $t \in [0.85, 0.90]$ s, when the temperature evolution is stationary

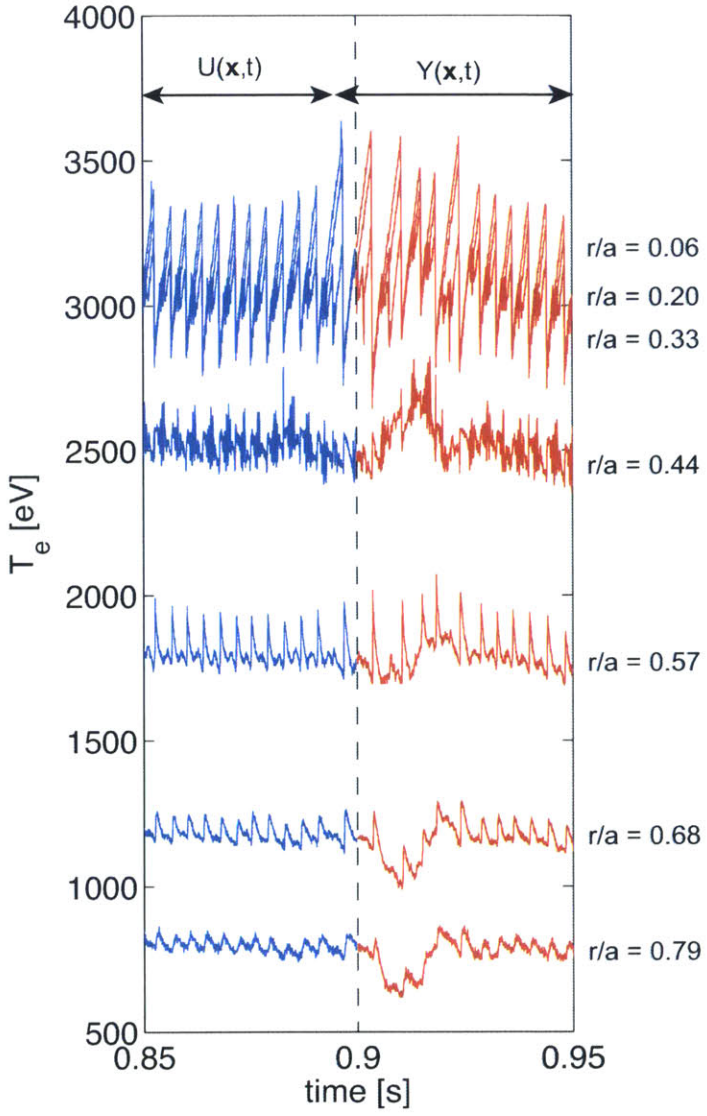

Figure C-1: The evolutions of electron temperatures during a cold pulse injection. The cold pulse injection happens at 0.9 s.

with sawtooth oscillation. Fig. C-2 (b) is the trajectory with $t \in [0.90, 0.95]$ s, when the sawtooth oscillation and cold pulse perturbation coexist. It can be seen that the dynamics of the trajectories before (blue) and after (red) the cold pulse injection (0.9 s) are very different. Ideally if the trajectory after cold pulse (red in Fig. C-2 (b)) is perpendicular to the plane made by the trajectory before the cold pulse (blue in Fig. C-2 (b)), the projection to the plane will perfectly reveal the slow evolution with few oscillations from sawtooth activities, which is demonstrated with Tore Supra data in [224]. The perpendicular relation of the data studied here is not as good as the one in Tore Supra, but one can still distinguish the slow evolution with this projection. GSVD method can be used to such projecting directions (basis). Fig. C-2 (c) shows the trajectory on three leading basis chosen by GSVD, showing that the sawtooth oscillation is well confined around $[0, 0, 0]$.

C.2 GSVD

Two assumptions need to be made to apply GSVD technique on sawtooth removal [224]:

- The sawtooth oscillation and cold pulse propagation follow different dynamics.
- The sawtooth oscillation is not strongly affected by the cold pulse injection.

With these assumptions, consider $\boldsymbol{U}(\boldsymbol{x}, t)$ is the electron temperature signal measured from ECE before the perturbation which is dominated by sawtooth activity, and $\boldsymbol{Y}(\boldsymbol{x}, t)$ is that after the perturbation, whose evolution consists of both sawtooth activity and perturbation propagation. The GSVD gives $\boldsymbol{U}$ and $\boldsymbol{Y}$ a set of common bases. This set of bases is optimized such that some bases will best represent $\boldsymbol{Y}$ and have little information on $\boldsymbol{U}$. The set of bases consists of both spatial and temporal modes. Signals $\boldsymbol{U}$ and $\boldsymbol{Y}$ share the same spatial modes $V_k(\boldsymbol{x})$, but different temporal modes $A_t(t)$ for $\boldsymbol{U}$ and $B_k(t)$ for $\boldsymbol{Y}$. The choice of bases is made as follows:

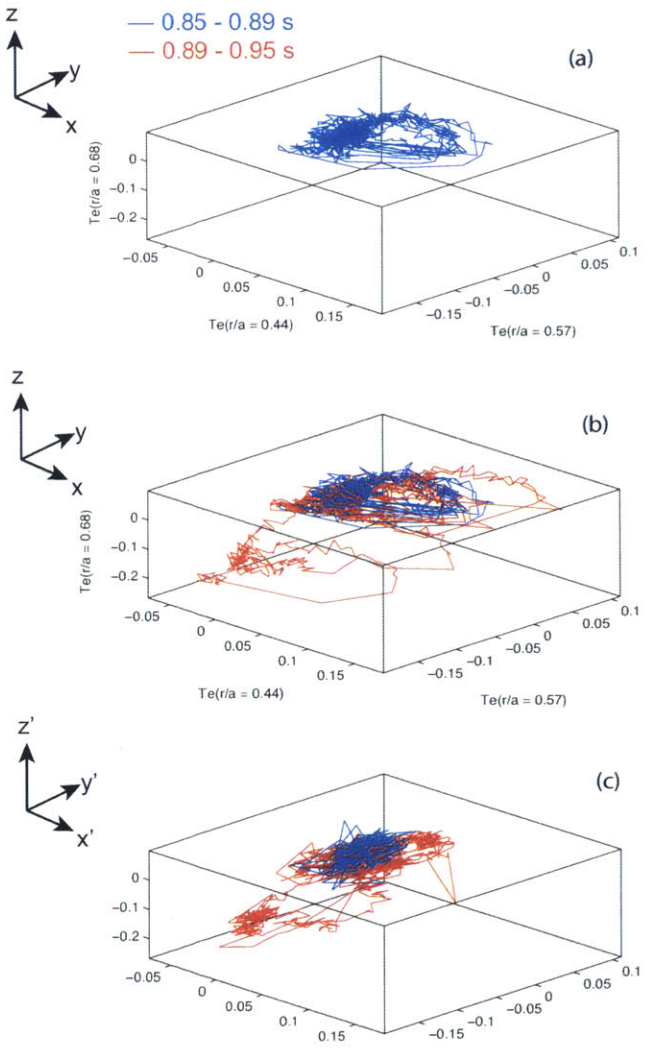

Figure C-2: The 3-D representation of the trajectories in a 3-D phase space with coordinates $x = T_e\,(r/a = 0.44)$, $y = T_e\,(r/a = 0.57)$, $x = T_e\,(r/a = 0.68)$. (a) The trajectory between 0.85 s and 0.89 s when the temperature evolution is stationary with sawtooth oscillation. (b) The trajectory between 0.89 s and 0.95 s when the sawtooth oscillation and cold pulse perturbation coexist. (c) The trajectory projected to the 3 leading basis of GSVD.

$$\boldsymbol{U}(\boldsymbol{x},t) = \sum_{k=1}^{K} \alpha_k \boldsymbol{A}_k^*(t)\, \boldsymbol{V}_k(\boldsymbol{x}) \tag{C.1}$$

$$\boldsymbol{Y}(\boldsymbol{x},t) = \sum_{k=1}^{K} \beta_k \boldsymbol{B}_k^*(t)\, \boldsymbol{V}_k(\boldsymbol{x}) \tag{C.2}$$

The temporal modes are orthonormal and eigenvalues are normalized, i.e.,

$$\langle \boldsymbol{A}_m^* \cdot \boldsymbol{A}_n \rangle = \delta_{mn} \tag{C.3}$$

$$\langle \boldsymbol{B}_m^* \cdot \boldsymbol{B}_n \rangle = \delta_{mn} \tag{C.4}$$

$$\alpha_m^2 + \beta_m^2 = 1 \tag{C.5}$$

Spatial modes are not necessary to be orthonormal, i.e., for $m \neq n$

$$\langle \boldsymbol{V}_m^* \cdot \boldsymbol{V}_n \rangle \neq 0 \tag{C.6}$$

If the sawtooth and perturbation are not strongly coupled, the first L leading modes will be able to recover the perturbation signal with removal of sawtooth activity.

$$\hat{\boldsymbol{Y}}(\boldsymbol{x},t) = \sum_{k=1}^{L} \beta_k \boldsymbol{B}_k^*(t)\, \boldsymbol{V}_k(\boldsymbol{x}) \tag{C.7}$$

Fig. C-3 shows the GSVD eigenvalues $\alpha(k)$ and $\beta(k)$ of data in Fig. C-1. Notice that β is finite at higher k mode number, which is consistent with the observation that the trajectory after cold pulse is not perfectly perpendicular with the sawtooth trajectory plane. The tradeoff of choosing a few leading modes (for example, $L = 3$) is some cold pulse propagation information will be lost. The eigenvectors $A_k(t), B_k(t), V_k(R)$, and reconstructed electron temperatures using the first 2 leading modes are shown in Fig. 3-18. Fig. C-5 is another comparison of the raw ECE data and the GSVD processed data.

To summarize, the GSVD technique is applied to remove the sawtooth oscillations in electron temperatures in Alcator C-Mod cold pulse experiments. This

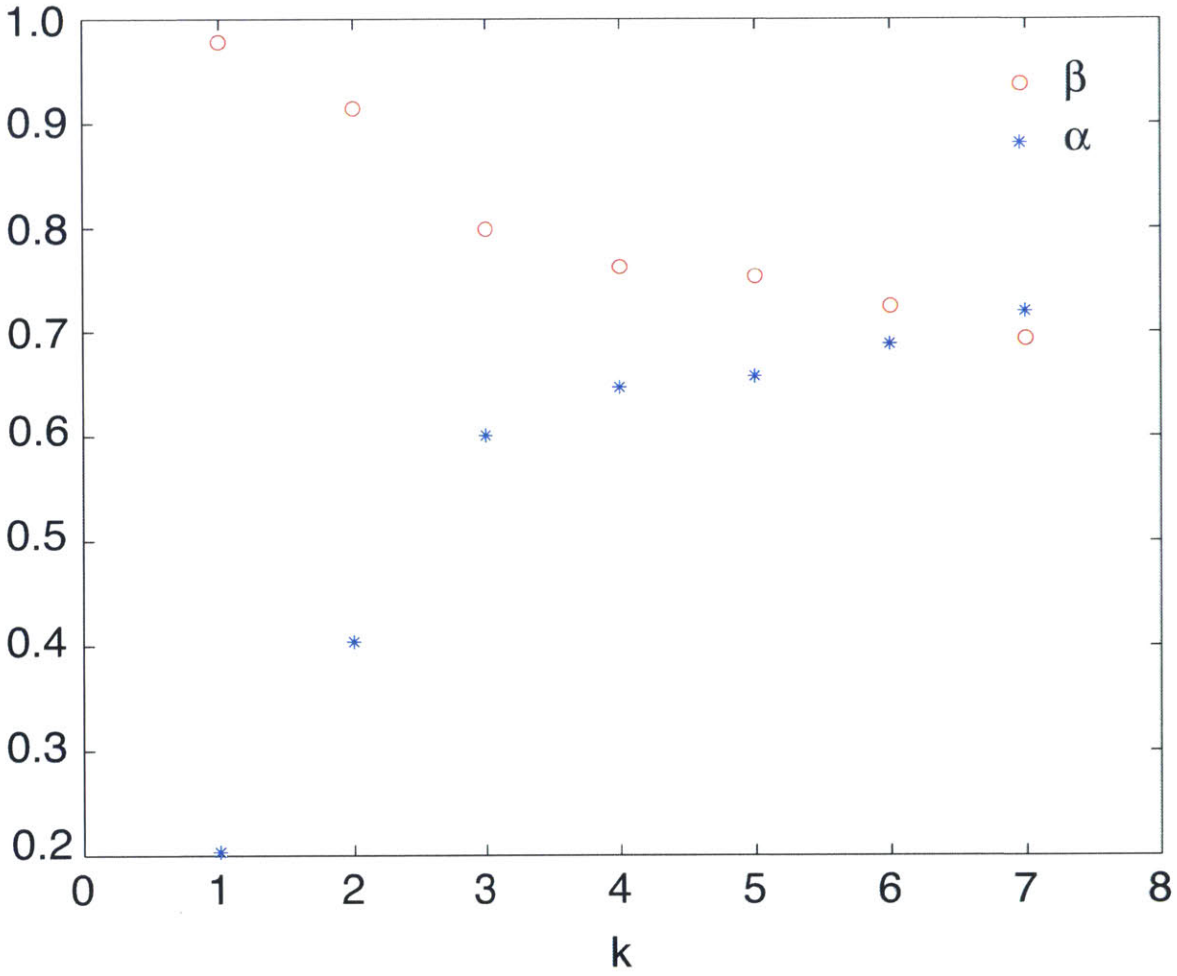

Figure C-3: The GSVD eigen values $\alpha(k)$ and $\beta(k)$.

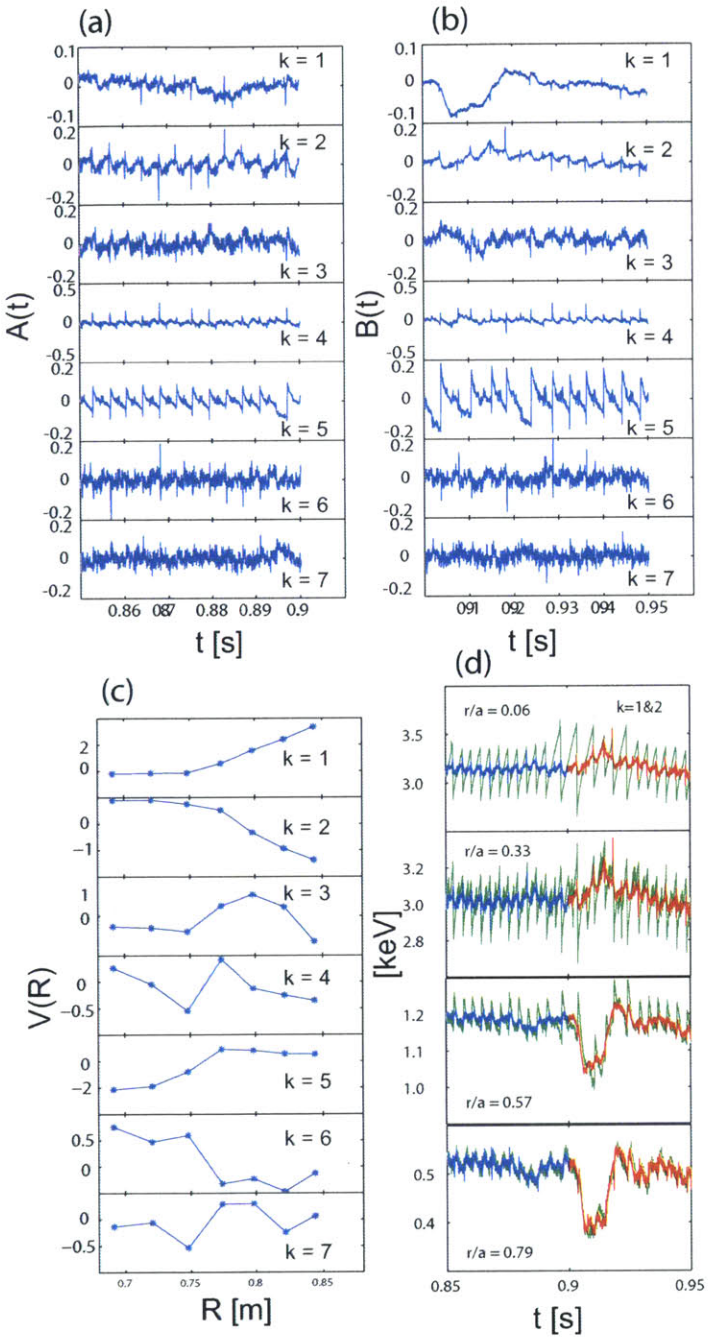

Figure C-4: The seven modes associated with the GSVD for the LOC discharge of Fig. 3-18. (a): the temporal modes $A_k(t)$ of sawtooth subset; (b): the temporal modes $B_k(t)$ of perturbation subset; (c) the common spatial modes $V_k(R)$; (d) the evolution of reconstructed electron temperatures by choosing the first two dominant modes (k=1,2) at different radii. Green lines are original signals, blue and red lines are reconstructed signals before and after the cold pulse injection, respectively.

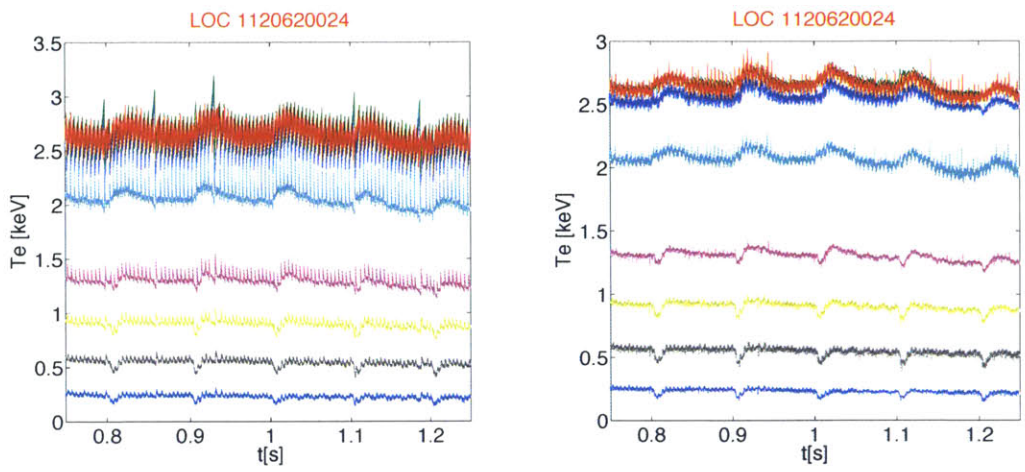

(a) Raw ECE data (b) GSVD processed data

Figure C-5: Comparison of (a) raw ECE data and (b) GSVD processed data.

self-consistent method improves the raw data qualify. However, based on the analyzed data, the cold pulse propagation and sawtooth oscillation are not perfectly separately. The current analysis uses GPC1 data only. Future work can be done with GPC2 and FRCECE data, which will allow more eigenvectors in the phase space. GSVD technique can also be applied to remove sawteeth during L–H transitions. It provides a quantitative method to study the interactions between the perturbation and sawtooth oscillations.

Appendix D

List of Shots and Codes Used in the Thesis

D.1 List of shots

Table D.1: List of shots used in Chapter 3.

Figure	Shot
Figure 3-12, 3-13	1120106010
Figure 3-14 – 3-16	1120106020
Figure 3-17	1120607011
Figure 3-18 – 3-20	1120607008
Figure 3-21	1120607008, 1120607011
Figure 3-22, 3-23	1120919012
Figure 3-24	Run 1120106, 1120216, 1120607
Figure 3-25	1120106025
Figure 3-26	Run 1120106, 1120607
Figure 3-27, 3-28	1120106020
Figure 3-29	1120106020 (SXR3)
Figure 3-30 - 34	1120607008, 1120607011

Table D.2: List of shots used in Chapter 4.

Figure	Shot
Figure 4-1	1110217026 (1.0MA), 1110217029 (1.2MA), 1120217032 (0.8MA)
Figure 4-2 – 4-5	1120217032

Table D.3: List of shots used in Chapter 5.

Figure	Shot
Figure 5-1	1140221028, 1140221015
Figure 5-2	1091008021
Figure 5-3	Run 1101015, 1140221, 1140225
Figure 5-4	1140225026
Figure 5-5, 5-8	1140221015, 1140221016
Figure 5-6	1140221019
Figure 5-7	1140221016
Figure 5-13	1140221011
Figure 5-15, 5-16	1140221016

D.2 Codes used in the thesis

D.2.1 Codes for coronal equilibrium

The code used to calculate argon charge states in coronal equilibrium in Figure 1-10:
/home/cgao/idl/corona/arcoron.pro

D.2.2 Codes used for GSVD analysis

The GSVD codes used to process ECE data (Figure 3-19, 3-20, 3-21):
/home/cgao/matlab/GSVD/GSVD_GPC.m

/home/cgao/matlab/GSVD/GSVD_FFT.m

D.2.3 Codes used for transport analysis

Transport analysis code (Matlab) used in Figure 3-27, 3-28:

/home/cgao/research/2012/te_model/Te_prediction/te_model.m

/home/cgao/research/2012/te_model/Te_prediction/scripts.m

TRANSP run 88267 is used in the analysis. GPC electron temperature profile is used, which is fitted using quickfit_gpc procedure:

/home/cgao/idl/quickfit_gpc.pro

The TRANSP source code to load quickfit_gpc profile is:

/home/cgao/transp/source_nathan/load_te_gpc_cg.pro

D.2.4 Codes used for sawtooth heat pulse analysis

The codes for sawtooth heat pulse analysis in Figure 3-29:

/home/cgao/idl/xtomo/xtomo_tp_array3.pro

D.2.5 Codes used for GYRO simulation

The comparison of profiles in Figure 3-30 is plotted with:

/home/cgao/idl/hirex/compare_profile.pro

The used TRANSP runs are 88191 for 1120607008; 88188 for 1120607011. For both TRANSP run, the T_e, T_i, n_e and rotation profiles are averaged over 0.8 s and 1.2 s. The averaged profiles are inserted to profiles at 1.0 s.

The codes used to load experiment data into TRANSP:

/home/cgao/transp/source_nathan/

/home/cgao/transp/source_nathan/load_te_cg.pro

/home/cgao/transp/source_nathan/load_ne_cg.pro

/home/cgao/transp/source_nathan/load_ti_cg.pro
/home/cgao/transp/source_nathan/load_rot_cg.pro

The codes used to load TRANSP results for GYRO simulations:
/home/cgao/GYRO/gyro_input/gyro_input_tools.pro
/home/cgao/GYRO/gyro_input/log.txt

The steps to run GYRO simulation for the two discharges (88191 and 88188) are logged in:
/home/cgao/GYRO/lin_stability.txt
/home/cgao/GYRO/gyro_input/log.txt

The GYRO simulation results are stored in LOKI cluster:
loki:/home/cgao/gacode/gyro/sim/88188.r0500_xxx/...
loki:/home/cgao/gacode/gyro/sim/88188.r0750_xxx/...
loki:/home/cgao/gacode/gyro/sim/88191.r0500_xxx/...
loki:/home/cgao/gacode/gyro/sim/88191.r0750_xxx/...

The code to plot linear frequencies and growth rates in Figure 3-31:
/home/cgao/GYRO/gyro_output/plot_lin_gyro.pro

The code to plot the contours of linear growth rates in Figure 3-33, 3-34:
/home/cgao/GYRO/gyro_output/plot_stability.pro

D.2.6 Codes used for momentum modulation analysis

The codes used for momentum modulation analysis in Chapter 4 and to plot the Figures 4-2–4-5:
/home/cgao/idl/hirex/hirex_rotation_modulation/hirex_rotation_modulation_v4.pro

D.2.7 Codes used in argon pumpout analysis

The codes (piScope) used to analyze the data shown Figure 5-3:
/home/cgao/piscope/hirex_delta.pfz

The ICRF mode conversion code (Figure 5-11):
/home/cgao/people/ylin/icrf_physics/scenario_widget/

The codes (Matlab) used to calculate the argon de-confinement energy:
/home/cgao/matlab/argon_pumpout_banana_orbit/

The codes to analysis the profiles in Figure 5-13:
/home/cgao/research/2014 Research/Argon pumpout/1140221011/1140221011.pro

The codes of STRAHL widget shown in Figure 5-14:
/home/cgao/strahl/widget/w_strahl.pro
/home/cgao/strahl/widget/w_strahl.bat

The inputs and outputs for STRAHL simulation shown in Figure 5-15:
/home/cgao/strahl/widget/result/1140221016_42_timeEnvolving_constantSource_noflatDiff/

The inputs and outputs for STRAHL simulation shown in Figure 5-16:
/home/cgao/strahl/widget/result/1140221016_43_timeEnvolving_reduceSource_noflatDiff/

D.2.8 HiReX–Sr calibration widget

A widget for post-locked-mode calibration is developed. It is located in:
/home/cgao/idl/hirex/hirex_analysis_para/

D.2.9 HiReX–Sr ray-tracing widget

A raytracing widget for vignetting analysis is developed. It is located in :

/home/cgao/idl/widget/raytracing/w_hirexsr_raytracing_v13.pro

/home/cgao/idl/widget/raytracing/w_hirexsr_raytracing_v13.bat

Bibliography

[1] J. P. Freidberg, *Plasma Physics and Fusion Energy.* Cambridge University Press, 2007.

[2] J. Mlynavr, "Focus on: Jet, the european centre of fusion research," *EFDA website*, 2007.

[3] S. J. Wukitch, R. L. Boivin, P. Bonoli, J. A. Goetz, J. Irby, I. Hutchinson, Y. Lin, A. Parisot, M. Porkolab, E. Marmar, *et al.*, "Investigation of performance limiting phenomena in a variable phase icrf antenna in alcator c-mod," *Plasma physics and controlled fusion*, vol. 46, no. 9, p. 1479, 2004.

[4] Y. Ma, *Study of H-mode access conditions on the Alcator C-Mod Tokamak.* PhD thesis, Massachusetts Institute of Technology, 2013.

[5] W. D. Lee, *Experimental investigation of toroidal rotation profiles in the Alcator C-Mod tokamak.* PhD thesis, Massachusetts Institute of Technology, Department of Nuclear Engineering, 2003.

[6] M. Bitter, K. Hill, A. Roquemore, P. Beiersdorfer, S. Kahn, S. Elliott, and B. Fraenkel, "Imaging x-ray crystal spectrometers for the national spherical torus experiment," *Review of scientific instruments*, vol. 70, no. 1, pp. 292–295, 1999.

[7] A. Ince-Cushman, J. Rice, M. Bitter, M. Reinke, K. Hill, M. Gu, E. Eikenberry, C. Broennimann, S. Scott, Y. Podpaly, *et al.*, "Spatially resolved high resolution x-ray spectroscopy for magnetically confined fusion plasmas," *Review of Scientific Instruments*, vol. 79, no. 10, pp. 10E302–10E302, 2008.

[8] A. Ince-Cushman, J. Rice, M. Reinke, M. Greenwald, G. Wallace, R. Parker, C. Fiore, J. Hughes, P. Bonoli, S. Shiraiwa, *et al.*, "Observation of self-generated flows in tokamak plasmas with lower-hybrid-driven current," *Physical review letters*, vol. 102, no. 3, p. 035002, 2009.

[9] K. Gentle, R. Bravenec, G. Cima, G. Hallock, P. Phillips, D. Ross, W. Rowan, A. Wootton, T. Crowley, A. Ouroua, *et al.*, "The evidence for nonlocal transport in the texas experimental tokamak," *Physics of Plasmas*, vol. 4, p. 3599, 1997.

[10] J. Rice, M. Greenwald, Y. Podpaly, M. Reinke, P. Diamond, J. Hughes, N. Howard, Y. Ma, I. Cziegler, B. Duval, *et al.*, "Ohmic energy confinement saturation and core toroidal rotation reversal in alcator c-mod plasmas," *Physics of Plasmas*, vol. 19, p. 056106, 2012.

[11] J. Rice, I. Cziegler, P. Diamond, B. Duval, Y. Podpaly, M. Reinke, P. Ennever, M. Greenwald, J. Hughes, Y. Ma, *et al.*, "Rotation reversal bifurcation and energy confinement saturation in tokamak ohmic l-mode plasmas," *Physical Review Letters*, vol. 107, no. 26, p. 265001, 2011.

[12] J. Rice, B. Duval, M. Reinke, Y. Podpaly, A. Bortolon, R. Churchill, I. Cziegler, P. Diamond, A. Dominguez, P. Ennever, *et al.*, "Observations of core toroidal rotation reversals in alcator c-mod ohmic l-mode plasmas," *Nuclear Fusion*, vol. 51, no. 8, p. 083005, 2011.

[13] M. Kissick, J. Callen, and E. Fredrickson, "Conditions and behaviour related to non-local electron heat transport on tftr," *Nuclear fusion*, vol. 38, no. 6, p. 821, 1998.

[14] P. Galli, G. Gorini, P. Mantica, G. Hogeweij, J. De Kloe, N. L. Cardozo, and R. Team, "'non-local'response of rtp ohmic plasmas to peripheral perturbations," *Nuclear fusion*, vol. 39, no. 10, p. 1355, 1999.

[15] F. Ryter, R. Neu, R. Dux, H.-U. Fahrbach, F. Leuterer, G. Pereverzev, J. Schweinzer, J. Stober, W. Suttrop, A. U. Team, *et al.*, "Propagation of cold pulses and heat pulses in asdex upgrade," *Nuclear fusion*, vol. 40, no. 11, p. 1917, 2000.

[16] X. Zou, A. Geraud, P. Gomez, M. Mattioli, J. Ségui, F. Clairet, C. De Michelis, P. Devynck, T. D. de Wit, M. Erba, *et al.*, "Edge cooling experiments and non-local transport phenomena in tore supra," *Plasma physics and controlled fusion*, vol. 42, no. 10, p. 1067, 2000.

[17] H. Sun, P. Diamond, Z. Shi, C. Chen, L. Yao, X. Ding, B. Feng, X. Huang, Y. Zhou, J. Zhou, *et al.*, "Experimental evidence of the non-local response of transport to peripheral perturbations," *Nuclear Fusion*, vol. 51, no. 11, p. 113010, 2011.

[18] J. Rice, C. Gao, M. Reinke, P. Diamond, N. Howard, H. Sun, I. Cziegler, A. Hubbard, Y. Podpaly, W. Rowan, *et al.*, "Non-local heat transport, rotation reversals and up/down impurity density asymmetries in alcator c-mod ohmic l-mode plasmas," *Nuclear Fusion*, vol. 53, no. 3, p. 033004, 2013.

[19] C. Sung, A. White, J. Irby, R. Leccacorvi, R. Vieira, C. Oi, W. Peebles, and X. Nguyen, "Design of a correlation electron cyclotron emission diagnostic for alcator c-mod," *Review of Scientific Instruments*, vol. 83, no. 10, pp. 10E311–10E311, 2012.

[20] N. Howard, M. Greenwald, and J. Rice, "Characterization of impurity confinement on alcator c-mod using a multi-pulse laser blow-off system," *Review of Scientific Instruments*, vol. 82, no. 3, pp. 033512–033512, 2011.

[21] J. E. Rice, E. Marmar, E. Källne, and J. Källne, "Radial profiles of ground-state transitions of heliumlike argon from the alcator-c tokamak," *Physical Review A*, vol. 35, no. 7, p. 3033, 1987.

[22] E. S. Marmar, J. Rice, K. Kallne, J. Kallne, and R. LaVilla, "Precision measurement of the 1s lamb shift in hydrogenlike argon," *Physical Review A*, vol. 33, no. 1, p. 774, 1986.

[23] J. E. Rice, K. Fournier, M. Graf, L. Terry, M. Finkenthal, F. Bombarda, E. Marmar, and W. Goldstein, "X-ray observations of 2l-nl' transitions in mo30+ – mo33+ from tokamak plasmas," *Physical Review A*, vol. 51, no. 5, p. 3551, 1995.

[24] M. Greenwald, D. Andelin, N. Basse, S. Bernabei, P. Bonoli, B. Böse, C. Boswell, R. Bravenec, B. Carreras, I. Cziegler, *et al.*, "Overview of the alcator c-mod program," *Nuclear fusion*, vol. 45, no. 10, p. S109, 2005.

[25] E. S. Marmar, "The alcator c-mod program," *Fusion science and technology*, vol. 51, no. 3, pp. 261–265, 2007.

[26] M. Greenwald, A. Bader, S. Baek, H. Barnard, W. Beck, W. Bergerson, I. Bespamyatnov, M. Bitter, P. Bonoli, M. Brookman, *et al.*, "Overview of experimental results and code validation activities at alcator c-mod," *Nuclear Fusion*, vol. 53, no. 10, p. 104004, 2013.

[27] M. Greenwald, A. Bader, S. Baek, M. Bakhtiari, H. Barnard, W. Beck, W. Bergerson, I. Bespamyatnov, P. Bonoli, D. Brower, *et al.*, "20 years of research on the alcator c-mod tokamak a)," *Physics of Plasmas (1994-present)*, vol. 21, no. 11, p. 110501, 2014.

[28] G. Boxman, L. de Kock, B. Meddens, A. Oomens, L. Ornstein, B. Coppi, D. Pappas, R. Parker, L. Pieroni, and S. Segre, "Low and high density operation of alcator," in *Controlled Fusion and Plasma Physics*, vol. 1, pp. 14–23, 1976.

[29] E. Apgar, B. Coppi, A. Gondhalekar, H. Helava, D. Komm, F. Martin, B. Montgomery, D. Pappas, R. Parker, and D. Overskei, "High-density and collisional plasma regimes in the alcator programme," in *Plasma Physics and Controlled Nuclear Fusion Research 1976, Volume 1*, vol. 1, pp. 247–256, 1977.

[30] M. Gaudreau, A. Gondhalekar, M. Hughes, D. Overskei, D. t. Pappas, R. Parker, S. Wolfe, E. Apgar, H. Helava, I. Hutchinson, *et al.*, "High-density discharges in the alcator tokamak," *Physical Review Letters*, vol. 39, no. 20, p. 1266, 1977.

[31] A. Gondhalekar, R. Granetz, D. Gwinn, I. Hutchinson, B. Kusse, E. Marmar, D. Overskei, D. Pappas, R. Parker, and M. Pickrell, "Study of the energy balance in alcator," in *Plasma Physics and Controlled Nuclear Fusion Research 1978, Volume 1*, vol. 1, pp. 199–209, 1979.

[32] B. Blackwell, C. Fiore, and R. Gandy, "Energy and impurity transport in the alcator c tokamak," in *Plasma physics and controlled nuclear fusion research 1982*, 1983.

[33] M. Greenwald, D. Gwinn, S. Milora, J. Parker, R. Parker, S. Wolfe, M. Besen, F. Camacho, S. Fairfax, C. Fiore, *et al.*, "Energy confinement of high-density pellet-fueled plasmas in the alcator c tokamak," *Physical review letters*, vol. 53, no. 4, p. 352, 1984.

[34] E. S. Marmar, J. Rice, J. Terry, and F. Seguin, "Impurity injection experiments on the alcator c tokamak," *Nuclear Fusion*, vol. 22, no. 12, p. 1567, 1982.

[35] R. R. Parker, M. Greenwald, S. Luckhardt, E. Marmar, M. Porkolab, and S. Wolfe, "Progress in tokamak research at mit," *Nuclear fusion*, vol. 25, no. 9, p. 1127, 1985.

[36] M. Ono, S. Kaye, Y.-K. Peng, G. Barnes, W. Blanchard, M. Carter, J. Chrzanowski, L. Dudek, R. Ewig, D. Gates, *et al.*, "Exploration of spherical torus physics in the nstx device," *Nuclear Fusion*, vol. 40, no. 3Y, p. 557, 2000.

[37] F. Wagner, G. Becker, K. Behringer, D. Campbell, A. Eberhagen, W. Engelhardt, G. Fussmann, O. Gehre, J. Gernhardt, G. v. Gierke, *et al.*, "Regime of improved confinement and high beta in neutral-beam-heated divertor discharges of the asdex tokamak," *Physical Review Letters*, vol. 49, no. 19, p. 1408, 1982.

[38] K. Burrell, S. Ejima, D. Schissel, N. Brooks, R. Callis, T. Carlstrom, A. Colleraine, J. DeBoo, H. Fukumoto, R. Groebner, *et al.*, "Observation of an improved energy-confinement regime in neutral-beam–heated divertor discharges in the diii-d tokamak," *Physical review letters*, vol. 59, no. 13, p. 1432, 1987.

[39] E. Strait, T. Taylor, A. Turnbull, J. Ferron, L. Lao, B. Rice, O. Sauter, S. Thompson, and D. Wróblewski, "Wall stabilization of high beta tokamak discharges in diii-d," *Physical review letters*, vol. 74, no. 13, p. 2483, 1995.

[40] K.-D. Zastrow, W. Core, L.-G. Eriksson, M. Von Hellermann, A. Howman, and R. König, "Transfer rates of toroidal angular momentum during neutral beam injection," *Nuclear fusion*, vol. 38, no. 2, p. 257, 1998.

[41] T. Tala, K.-D. Zastrow, J. Ferreira, P. Mantica, V. Naulin, A. Peeters, G. Tardini, M. Brix, G. Corrigan, C. Giroud, *et al.*, "Evidence of inward toroidal momentum convection in the jet tokamak," *Physical review letters*, vol. 102, no. 7, p. 075001, 2009.

[42] D. Nishijima, A. Kallenbach, S. Günter, M. Kaufmann, K. Lackner, C. Maggi, A. Peeters, G. Pereverzev, B. Zaniol, *et al.*, "Experimental studies of toroidal momentum transport in asdex upgrade," *Plasma physics and controlled fusion*, vol. 47, no. 1, p. 89, 2005.

[43] W. Solomon, S. Kaye, R. Bell, B. LeBlanc, J. Menard, G. Rewoldt, W. Wang, F. Levinton, H. Yuh, and S. Sabbagh, "Momentum-transport studies in high e× b shear plasmas in the national spherical torus experiment," *Physical review letters*, vol. 101, no. 6, p. 065004, 2008.

[44] Y. Lin, J. Rice, S. Wukitch, M. Greenwald, A. Hubbard, A. Ince-Cushman, L. Lin, M. Porkolab, M. Reinke, and N. Tsujii, "Observation of ion-cyclotron-frequency mode-conversion flow drive in tokamak plasmas," *Physical review letters*, vol. 101, no. 23, p. 235002, 2008.

[45] Y. Lin, J. Rice, S. Wukitch, M. Greenwald, A. Hubbard, A. Ince-Cushman, L. Lin, E. Marmar, M. Porkolab, M. Reinke, *et al.*, "Observation of ion cyclotron range of frequencies mode conversion plasma flow drive on alcator c-mod," *Physics of Plasmas*, vol. 16, p. 056102, 2009.

[46] Y. Lin, J. Rice, S. Wukitch, M. Reinke, M. Greenwald, A. Hubbard, E. Marmar, Y. Podpaly, M. Porkolab, N. Tsujii, *et al.*, "Icrf mode conversion flow drive on alcator c-mod," *Nuclear Fusion*, vol. 51, no. 6, p. 063002, 2011.

[47] P. Yushmanov, T. Takizuka, K. Riedel, O. Kardaun, J. Cordey, S. Kaye, and D. Post, "Scalings for tokamak energy confinement," *Nuclear Fusion*, vol. 30, no. 10, p. 1999, 1990.

[48] R. McDermott, B. Lipschultz, J. Hughes, P. Catto, A. Hubbard, I. Hutchinson, R. Granetz, M. Greenwald, B. LaBombard, K. Marr, *et al.*, "Edge radial electric field structure and its connections to h-mode confinement in alcator c-mod plasmasa)," *Physics of Plasmas (1994-present)*, vol. 16, no. 5, p. 056103, 2009.

[49] D. Whyte, A. Hubbard, J. Hughes, B. Lipschultz, J. Rice, E. Marmar, M. Greenwald, I. Cziegler, A. Dominguez, T. Golfinopoulos, *et al.*, "I-mode: an h-mode energy confinement regime with l-mode particle transport in alcator c-mod," *Nuclear Fusion*, vol. 50, no. 10, p. 105005, 2010.

[50] E. Källne, J. Källne, E. Marmar, and J. Rice, "High resolution x-ray spectroscopy diagnostics of high temperature plasmas," *Physica Scripta*, vol. 31, no. 6, p. 551, 1985.

[51] M. Bitter, K. Hill, B. Stratton, A. Roquemore, D. Mastrovito, S. Lee, J. Bak, M. Moon, U. Nam, G. Smith, *et al.*, "Spatially resolved spectra from a new x-ray imaging crystal spectrometer for measurements of ion and electron temperature profiles," *Review of scientific instruments*, vol. 75, no. 10, pp. 3660–3665, 2004.

[52] K. Hill, M. Bitter, S. Scott, A. Ince-Cushman, M. Reinke, J. Rice, P. Beiersdorfer, M.-F. Gu, S. Lee, C. Broennimann, *et al.*, "A spatially resolving x-ray crystal spectrometer for measurement of ion-temperature and rotation-velocity profiles on the alcator¡ equation¿ c¡/equation¿-mod tokamak," *Review of Scientific Instruments*, vol. 79, no. 10, pp. 10E320–10E320, 2008.

[53] A. C. Ince-Cushman, *Rotation studies in fusion plasmas via imaging x-ray crystal spectroscopy.* PhD thesis, Massachusetts Institute of Technology, 2008.

[54] M. Reinke, Y. Podpaly, M. Bitter, I. Hutchinson, J. Rice, L. Delgado-Aparicio, C. Gao, M. Greenwald, K. Hill, N. Howard, *et al.*, "X-ray imaging crystal spectroscopy for use in plasma transport research," *Review of Scientific Instruments*, vol. 83, no. 11, pp. 113504–113504, 2012.

[55] L. Hamos, "Röntgenspektroskopie und abbildung mittels gekrümmter kristallreflektoren. i. geometrisch-optische betrachtungen," *Annalen der Physik*, vol. 409, pp. 716–724, 1933.

[56] J. E. Rice, E. Marmar, F. Bombarda, and L. Qu, "X-ray observations of central toroidal rotation in ohmic alcator c-mod plasmas," *Nuclear Fusion*, vol. 37, no. 3, p. 421, 1997.

[57] C. Chang, C. Phillips, R. White, S. Zweben, P. Bonoli, J. Rice, M. Greenwald, *et al.*, "Generation of plasma rotation by ion cyclotron resonance heating in tokamaks," *Physics of Plasmas*, vol. 6, p. 1969, 1999.

[58] J. E. Rice, P. Bonoli, J. Goetz, M. Greenwald, I. Hutchinson, E. Marmar, M. Porkolab, S. Wolfe, S. Wukitch, and C. Chang, "Central impurity toroidal rotation in icrf heated alcator c-mod plasmas," *Nuclear Fusion*, vol. 39, no. 9, p. 1175, 1999.

[59] J. Rice, J. Goetz, R. Granetz, M. Greenwald, A. Hubbard, I. Hutchinson, E. Marmar, D. Mossessian, T. S. Pedersen, J. Snipes, *et al.*, "Impurity toroidal rotation and transport in alcator c-mod ohmic high confinement mode plasmas," *Physics of Plasmas*, vol. 7, p. 1825, 2000.

[60] J. Rice, R. Boivin, P. Bonoli, J. Goetz, R. Granetz, M. Greenwald, I. Hutchinson, E. Marmar, G. Schilling, J. Snipes, *et al.*, "Observations of impurity toroidal rotation suppression with itb formation in icrf and ohmic h mode alcator c-mod plasmas," *Nuclear fusion*, vol. 41, no. 3, p. 277, 2001.

[61] A. Rogister, J. Rice, A. Nicolai, A. Ince-Cushman, S. Gangadhara, C. Alcator, *et al.*, "Theoretical interpretation of the toroidal rotation velocity observed in alcator c-mod ohmic h-mode discharges," *Nuclear fusion*, vol. 42, no. 9, p. 1144, 2002.

[62] J. E. Rice, W. Lee, E. Marmar, N. Basse, P. Bonoli, M. Greenwald, A. Hubbard, J. Hughes, I. Hutchinson, A. Ince-Cushman, *et al.*, "Toroidal rotation and

momentum transport in alcator c-mod plasmas with no momentum input," *Physics of Plasmas*, vol. 11, p. 2427, 2004.

[63] Y. Lin, S. Wukitch, P. Bonoli, E. Nelson-Melby, M. Porkolab, J. Wright, N. Basse, A. Hubbard, J. Irby, L. Lin, *et al.*, "Investigation of ion cyclotron range of frequencies mode conversion at the ion–ion hybrid layer in alcator c-mod," *Physics of Plasmas (1994-present)*, vol. 11, no. 5, pp. 2466–2472, 2004.

[64] J. E. Rice, A. E. Hubbard, J. W. Hughes, M. Greenwald, B. LaBombard, J. H. Irby, Y. Lin, E. S. Marmar, D. Mossessian, S. M. Wolfe, *et al.*, "The dependence of core rotation on magnetic configuration and the relation to the h-mode power threshold in alcator c-mod plasmas with no momentum input," *Nuclear fusion*, vol. 45, no. 4, p. 251, 2005.

[65] J. Rice, A. Ince-Cushman, L.-G. Eriksson, Y. Sakamoto, A. Scarabosio, A. Bortolon, K. Burrell, B. Duval, C. Fenzi-Bonizec, M. Greenwald, *et al.*, "Inter-machine comparison of intrinsic toroidal rotation in tokamaks," *Nuclear Fusion*, vol. 47, no. 11, p. 1618, 2007.

[66] J. E. Rice, E. S. Marmar, P. Bonoli, R. S. Granetz, M. Greenwald, A. E. Hubbard, J. W. Hughes, I. H. Hutchinson, J. H. Irby, B. LaBombard, *et al.*, "Spontaneous toroidal rotation in alcator c-mod plasmas with no momentum input," *Fusion science and technology*, vol. 51, no. 3, pp. 288–302, 2007.

[67] C. L. Fiore, J. Rice, P. Bonoli, R. Boivin, J. Goetz, A. Hubbard, I. Hutchinson, R. Granetz, M. Greenwald, E. Marmar, *et al.*, "Internal transport barriers on alcator c-mod," *Physics of Plasmas*, vol. 8, p. 2023, 2001.

[68] J. E. Rice, P. Bonoli, E. Marmar, S. Wukitch, R. Boivin, C. Fiore, R. Granetz, M. Greenwald, A. Hubbard, J. Hughes, *et al.*, "Double transport barrier plasmas in alcator c-mod," *Nuclear fusion*, vol. 42, no. 5, p. 510, 2002.

[69] S. J. Wukitch, R. Boivin, P. Bonoli, C. Fiore, R. Granetz, M. Greenwald, A. Hubbard, I. Hutchinson, Y. In, J. Irby, *et al.*, "Double transport barrier experiments on alcator c-mod," *Physics of Plasmas (1994-present)*, vol. 9, no. 5, pp. 2149–2155, 2002.

[70] D. Ernst, P. Bonoli, P. Catto, W. Dorland, C. Fiore, R. Granetz, M. Greenwald, A. Hubbard, M. Porkolab, M. Redi, *et al.*, "Role of trapped electron mode turbulence in internal transport barrier control in the alcator c-mod tokamak," *Physics of Plasmas (1994-present)*, vol. 11, no. 5, pp. 2637–2648, 2004.

[71] C. Fiore, D. Ernst, J. Rice, K. Zhurovich, N. Basse, P. Bonoli, M. Greenwald, E. Marmar, and S. Wukitch, "C-mod review: Internal transport barriers in alcator c-mod," 2005.

[72] H. H. Johann, "Die erzeugung lichtstarker röntgenspektren mit hilfe von konkavkristallen," *Zeitschrift für Physik*, vol. 69, no. 3-4, pp. 185–206, 1931.

[73] A. Gabriel, "Dielectronic satellite spectra for highly-charged helium-like ion lines," *Monthly Notices of the Royal Astronomical Society*, vol. 160, no. 1, pp. 99–119, 1972.

[74] P. Helander and D. J. Sigmar, "Collisional transport in magnetized plasmas," *Collisional Transport in Magnetized Plasmas, by Per Helander, Dieter J. Sigmar, Cambridge, UK: Cambridge University Press, 2005*, vol. 1, 2005.

[75] M. Reinke, Y. Podpaly, and C. Gao, "Operation and validation of the hirexsr analysis code (thaco)," tech. rep., PSFC-RR-11-9, 2013.

[76] B. Grierson, K. Burrell, W. Heidbrink, M. Lanctot, N. Pablant, and W. Solomon, "Measurements of the deuterium ion toroidal rotation in the diii-d tokamak and comparison to neoclassical theorya)," *Physics of Plasmas (1994-present)*, vol. 19, no. 5, p. 056107, 2012.

[77] R. Watterson and K.-i. Chen, "Status of the alcator c-mod scanning two-dimensional thomson scattering diagnostic," *Review of Scientific Instruments*, vol. 61, no. 10, pp. 2867–2869, 1990.

[78] D. A. Mossessian, A. Hubbard, and J. Irby, "Performance of alcator c-mod core thomson scattering system," *Review of scientific instruments*, vol. 70, no. 1, pp. 759–762, 1999.

[79] J. W. Hughes, D. Mossessian, A. Hubbard, E. Marmar, D. Johnson, and D. Simon, "High-resolution edge thomson scattering measurements on the alcator c-mod tokamak," *Review of Scientific Instruments*, vol. 72, no. 1, pp. 1107–1110, 2001.

[80] J. W. Hughes, D. Mossessian, K. Zhurovich, M. DeMaria, K. Jensen, and A. Hubbard, "Thomson scattering upgrades on alcator c-mod," *Review of scientific instruments*, vol. 74, no. 3, pp. 1667–1670, 2003.

[81] T. C. Hsu, "The submillimeter wave electron cyclotron emission diagnostic for the alcator c-mod tokamak.," 1993.

[82] P. J. L. O'Shea, "Measurements of icrf power deposition and thermal transport with an ece grating polychromator on the alcator c-mod tokamak," 1997.

[83] G. Taylor, C. Phillips, G. Schilling, J. Wilson, A. Hubbard, S. Wukitch, and E. Nelson-Melby, "First measurements with a 19-channel ece polychromator on c-mod," in *APS Division of Plasma Physics Meeting Abstracts*, vol. 1, 1998.

[84] N. Basse, A. Dominguez, E. Edlund, C. Fiore, R. Granetz, A. Hubbard, J. Hughes, I. Hutchinson, J. Irby, B. LaBombard, *et al.*, "Diagnostic systems on alcator c-mod," *Fusion science and technology*, vol. 51, no. 3, pp. 476–507, 2007.

[85] J. Heard, C. Watts, R. Gandy, P. Phillips, G. Cima, R. Chatterjee, A. Blair, A. Hubbard, C. Domier, and N. Luhmann Jr, "High resolution electron cyclotron emission temperature profile and fluctuation diagnostic for alcator c-mod," *Review of scientific instruments*, vol. 70, no. 1, pp. 1011–1013, 1999.

[86] J. Irby, E. Marmar, E. Sevillano, and S. Wolfe, "Two-color interferometer system for alcator c-mod," *Review of Scientific Instruments*, vol. 59, no. 8, pp. 1568–1570, 1988.

[87] C. Kasten, J. Irby, R. Murray, A. White, N. Howard, C. Sung, Y. Lin, and P. Bonoli, "Turbulence measurements with fast two-color interferometry on alcator c-mod," in *Proc. 54th Annual Meeting of the APS Division of Plasma Physics (Providence, RI, 29 October–2 November)*, 2012.

[88] M. Porkolab, J. C. Rost, N. Basse, J. Dorris, E. Edlund, L. Lin, Y. Lin, and S. Wukitch, "Phase contrast imaging of waves and instabilities in high temperature magnetized fusion plasmas," *Plasma Science, IEEE Transactions on*, vol. 34, no. 2, pp. 229–234, 2006.

[89] L. Lin, E. Edlund, M. Porkolab, Y. Lin, and S. Wukitch, "Vertical localization of phase contrast imaging diagnostic in alcator c-mod," *Review of scientific instruments*, vol. 77, no. 10, pp. 10E918–10E918, 2006.

[90] Y. Lin, *Experimental application and numerical study of reflectometry in the Alcator C-Mod tokamak.* Plasma Science and Fusion Center, Massachusetts Institute of Technology, 2001.

[91] B. Coppi and N. Sharky, "Model for particle transport in high-density plasmas," *Nuclear Fusion*, vol. 21, no. 11, p. 1363, 1981.

[92] T. Luce, C. Petty, and J. De Haas, "Inward energy transport in tokamak plasmas," *Physical review letters*, vol. 68, no. 1, p. 52, 1992.

[93] C. Petty and T. Luce, "Inward transport of energy during off-axis heating on the diii-d tokamak," *Nuclear fusion*, vol. 34, no. 1, p. 121, 1994.

[94] C. Greenfield, D. Schissel, B. Stallard, E. Lazarus, G. Navratil, K. Burrell, T. Casper, J. DeBoo, E. Doyle, R. Fonck, *et al.*, "Transport and performance in diii-d discharges with weak or negative central magnetic shear," *Physics of Plasmas (1994-present)*, vol. 4, no. 5, pp. 1596–1604, 1997.

[95] A. Brizard and T. Hahm, "Foundations of nonlinear gyrokinetic theory," *Reviews of modern physics*, vol. 79, no. 2, p. 421, 2007.

[96] X. Garbet, Y. Idomura, L. Villard, and T. Watanabe, "Gyrokinetic simulations of turbulent transport," *Nuclear Fusion*, vol. 50, no. 4, p. 043002, 2010.

[97] N. Howard, C. Holland, A. White, M. Greenwald, and J. Candy, "Synergistic cross-scale coupling of turbulence in a tokamak plasma," *Physics of Plasmas (1994-present)*, vol. 21, no. 11, p. 112510, 2014.

[98] N. Howard, C. Holland, A. White, M. Greenwald, and J. Candy, "Fidelity of reduced and realistic electron mass ratio multi-scale gyrokinetic simulations of tokamak discharges," *Plasma Physics and Controlled Fusion*, vol. 57, no. 6, p. 065009, 2015.

[99] F. Hinton and R. Hazeltine, "Theory of plasma transport in toroidal confinement systems," *Reviews of Modern Physics*, vol. 48, no. 2, p. 239, 1976.

[100] M. Rosenbluth, R. Hazeltine, and F. L. Hinton, "Plasma transport in toroidal confinement systems," *Physics of Fluids (1958-1988)*, vol. 15, no. 1, pp. 116–140, 1972.

[101] A. Guthrie and R. K. Wakerling, *The characteristics of electrical discharge in magnetic fields*, vol. 5. McGraw-Hill, 1949.

[102] L. Spitzer Jr, "Particle diffusion across a magnetic field," *Physics of Fluids (US)*, vol. 3, 1960.

[103] M. Greenwald, J. Schachter, W. Dorland, R. Granetz, A. Hubbard, J. Rice, J. Snipes, P. Stek, and S. Wolfe, "Transport phenomena in alcator c-mod h-modes," *Plasma physics and controlled fusion*, vol. 40, no. 5, p. 789, 1998.

[104] F. Ryter, F. Imbeaux, F. Leuterer, H.-U. Fahrbach, W. Suttrop, and A. U. Team, "Experimental characterization of the electron heat transport in low-density asdex upgrade plasmas," *Physical review letters*, vol. 86, no. 24, p. 5498, 2001.

[105] J. Candy and R. Waltz, "Anomalous transport scaling in the diii-d tokamak matched by supercomputer simulation," *Physical review letters*, vol. 91, no. 4, p. 045001, 2003.

[106] J. Conner and H. Wilson, "Survey of theories of anomalous transport," *Plasma physics and controlled fusion*, vol. 36, no. 5, p. 719, 1994.

[107] W. Horton, "Drift waves and transport," *Reviews of Modern Physics*, vol. 71, no. 3, p. 735, 1999.

[108] L. Rudakov and R. Sagdeev, "On the instability of a nonuniform rarefied plasma in a strong magnetic field," in *Soviet Physics Doklady*, vol. 6, p. 415, 1961.

[109] A. Mikhailovskii and M. Leontovich, "Reviews of plasma physics," *Reviews of Plasma Physics*, vol. 3, 1967.

[110] B. Coppi, M. Rosenbluth, and R. Sagdeev, "Instabilities due to temperature gradients in complex magnetic field configurations," *Physics of Fluids*, vol. 10, no. 3, p. 582, 1967.

[111] C. Horton Jr and R. Varma, "Electrostatic stability theory of tokamaks from two-component fluid equations," *Physics of Fluids (1958-1988)*, vol. 15, no. 4, pp. 620–631, 1972.

[112] F. Romanelli, "Ion temperature-gradient-driven modes and anomalous ion transport in tokamaks," *Physics of Fluids B: Plasma Physics (1989-1993)*, vol. 1, no. 5, pp. 1018–1025, 1989.

[113] A. Hassam, T. Antonsen Jr, J. Drake, and P. Guzdar, "Theory of ion temperature gradient instabilities: Thresholds and transport," *Physics of Fluids B: Plasma Physics (1989-1993)*, vol. 2, no. 8, pp. 1822–1832, 1990.

[114] T. Hahm and W. Tang, "Weak turbulence theory of ion temperature gradient modes for inverted density plasmas," tech. rep., Princeton Univ., NJ (USA). Plasma Physics Lab, 1989.

[115] W. Horton and R. Estes, "Fluid simulation of ion pressure gradient driven drift modes," *Plasma Physics*, vol. 22, no. 7, p. 663, 1980.

[116] S. Hamaguchi and W. Horton, "Ion temperature gradient driven turbulence in the weak density gradient limit," *Physics of Fluids B: Plasma Physics (1989-1993)*, vol. 2, no. 12, pp. 3040–3046, 1990.

[117] S. Parker, W. Dorland, R. Santoro, M. Beer, Q. Liu, W. Lee, and G. Hammett, "Comparisons of gyrofluid and gyrokinetic simulations*," *Physics of Plasmas (1994-present)*, vol. 1, no. 5, pp. 1461–1468, 1994.

[118] W. Horton Jr, D.-I. Choi, and W. Tang, "Toroidal drift modes driven by ion pressure gradients," *Physics of Fluids (1958-1988)*, vol. 24, no. 6, pp. 1077–1085, 1981.

[119] B. Kadomtsev and O. Pogutse, "Plasma instability due to particle trapping in a toroidal geometry," *Soviet Journal of Experimental and Theoretical Physics*, vol. 24, p. 1172, 1967.

[120] B. Kadomtsev and O. Pogutse, "Trapped particles in toroidal magnetic systems," *Nuclear Fusion*, vol. 11, no. 1, p. 67, 1971.

[121] B. Coppi and G. Rewoldt, "New trapped-electron instability," *Physical Review Letters*, vol. 33, no. 22, p. 1329, 1974.

[122] F. Romanelli, W. Tang, and R. White, "Anomalous thermal confinement in ohmically heated tokamaks," *Nuclear fusion*, vol. 26, no. 11, p. 1515, 1986.

[123] F. Jenko and W. Dorland, "Prediction of significant tokamak turbulence at electron gyroradius scales," *Physical review letters*, vol. 89, no. 22, p. 225001, 2002.

[124] J. Candy, R. Waltz, M. Fahey, and C. Holland, "The effect of ion-scale dynamics on electron-temperature-gradient turbulence," *Plasma Physics and Controlled Fusion*, vol. 49, no. 8, p. 1209, 2007.

[125] K.-C. Shaing and E. Crume Jr, "Bifurcation theory of poloidal rotation in tokamaks: A model for l-h transition," *Physical Review Letters*, vol. 63, no. 21, p. 2369, 1989.

[126] H. Biglari, P. Diamond, and P. Terry, "Influence of sheared poloidal rotation on edge turbulence," *Physics of Fluids B: Plasma Physics (1989-1993)*, vol. 2, no. 1, pp. 1–4, 1990.

[127] R. Groebner, K. Burrell, and R. Seraydarian, "Role of edge electric field and poloidal rotation in the l-h transition," *Physical review letters*, vol. 64, no. 25, p. 3015, 1990.

[128] K. Ida, S. Hidekuma, Y. Miura, T. Fujita, M. Mori, K. Hoshino, N. Suzuki, T. Yamauchi, *et al.*, "Edge electric-field profiles of h-mode plasmas in the jft-2m tokamak," *Physical review letters*, vol. 65, no. 11, p. 1364, 1990.

[129] P. Terry, "Suppression of turbulence and transport by sheared flow," *Reviews of Modern Physics*, vol. 72, no. 1, p. 109, 2000.

[130] T. S. Hahm, "Rotation shear induced fluctuation decorrelation in a toroidal plasma," *Physics of Plasmas (1994-present)*, vol. 1, no. 9, pp. 2940–2944, 1994.

[131] E. Synakowski, "Formation and structure of internal and edge transport barriers," *Plasma physics and controlled fusion*, vol. 40, no. 5, p. 581, 1998.

[132] K. Burrell, "Effects of e× b velocity shear and magnetic shear on turbulence and transport in magnetic confinement devices," *Physics of Plasmas (1994-present)*, vol. 4, no. 5, pp. 1499–1518, 1997.

[133] R. Wolf, "Internal transport barriers in tokamak plasmas," *Plasma Physics and Controlled Fusion*, vol. 45, no. 1, p. R1, 2003.

[134] C. L. Fiore, P. Bonoli, D. Ernst, A. Hubbard, M. Greenwald, A. Lynn, E. Marmar, P. Phillips, M. Redi, J. Rice, *et al.*, "Control of internal transport barriers on alcator c-mod," *Physics of Plasmas (1994-present)*, vol. 11, no. 5, pp. 2480–2487, 2004.

[135] C. Fiore, D. Ernst, Y. Podpaly, D. Mikkelsen, N. Howard, J. Lee, M. Reinke, J. Rice, J. Hughes, Y. Ma, *et al.*, "Production of internal transport barriers via self-generated mean flows in alcator c-moda)," *Physics of Plasmas (1994-present)*, vol. 19, no. 5, p. 056113, 2012.

[136] L.-J. Zheng, M. Kotschenreuther, and M. Chu, "Rotational stabilization of resistive wall modes by the shear alfvén resonance," *Physical review letters*, vol. 95, no. 25, p. 255003, 2005.

[137] Y. Liu, A. Bondeson, Y. Gribov, and A. Polevoi, "Stabilization of resistive wall modes in iter by active feedback and toroidal rotation," *Nuclear fusion*, vol. 44, no. 2, p. 232, 2004.

[138] J. Rice, A. Ince-Cushman, P. Bonoli, M. Greenwald, J. Hughes, R. Parker, M. Reinke, G. Wallace, C. Fiore, R. Granetz, *et al.*, "Observations of counter-current toroidal rotation in alcator c-mod lhcd plasmas," *Nuclear Fusion*, vol. 49, no. 2, p. 025004, 2009.

[139] J. Rice, Y. Podpaly, M. Reinke, R. Mumgaard, S. Scott, S. Shiraiwa, G. Wallace, B. Chouli, C. Fenzi-Bonizec, M. Nave, *et al.*, "Effects of magnetic shear on toroidal rotation in tokamak plasmas with lower hybrid current drive," *Physical review letters*, vol. 111, no. 12, p. 125003, 2013.

[140] J. Rice, Y. Podpaly, M. Reinke, C. Gao, S. Shiraiwa, J. Terry, C. Theiler, G. Wallace, P. Bonoli, D. Brunner, *et al.*, "Effects of lhrf on toroidal rotation in alcator c-mod plasmas," *Nuclear Fusion*, vol. 53, no. 9, p. 093015, 2013.

[141] N. Mattor and P. Diamond, "Momentum and thermal transport in neutral-beam-heated tokamaks," *Physics of Fluids (1958-1988)*, vol. 31, no. 5, pp. 1180–1189, 1988.

[142] A. Peeters, C. Angioni, *et al.*, "Linear gyrokinetic calculations of toroidal momentum transport in a tokamak due to the ion temperature gradient mode," *Physics of Plasmas (1994-present)*, vol. 12, no. 7, p. 072515, 2005.

[143] M. Barnes, F. Parra, E. Highcock, A. Schekochihin, S. Cowley, and C. Roach, "Turbulent transport in tokamak plasmas with rotational shear," *Physical review letters*, vol. 106, no. 17, p. 175004, 2011.

[144] M. Yoshida, Y. Kamada, H. Takenaga, Y. Sakamoto, H. Urano, N. Oyama, G. Matsunaga, *et al.*, "Role of pressure gradient on intrinsic toroidal rotation in tokamak plasmas," *Physical review letters*, vol. 100, no. 10, p. 105002, 2008.

[145] A. Peeters, C. Angioni, and D. Strintzi, "Toroidal momentum pinch velocity due to the coriolis drift effect on small scale instabilities in a toroidal plasma," *Physical review letters*, vol. 98, no. 26, p. 265003, 2007.

[146] K. Behringer, "Description of the impurity transport code'strahl'," tech. rep., Commission of the European Communities, Abingdon (UK). JET Joint Undertaking, 1987.

[147] R. Dux and I. Garching, "Strahl user manual," *IPP Garching, Germany http://www. rzg. mpg. de/˜ rld/strahl. ps*, 2006.

[148] N. Howard, M. Greenwald, D. Mikkelsen, M. Reinke, A. White, D. Ernst, Y. Podpaly, and J. Candy, "Quantitative comparison of experimental impurity transport with nonlinear gyrokinetic simulation in an alcator c-mod l-mode plasma," *Nuclear Fusion*, vol. 52, no. 6, p. 063002, 2012.

[149] R. Hawryluk *et al.*, "An empirical approach to tokamak transport," *Physics of plasmas close to thermonuclear conditions*, vol. 1, pp. 19–46, 1980.

[150] J. Ongena, M. Evrard, and D. McCune, "Numerical transport codes," *Fusion Technology*, vol. 33, no. 2 T, pp. 181–191, 1998.

[151] J. Schachter, M. Greenwald, *et al.*, "Local transport analysis for alcator c-mod," in *APS Division of Plasma Physics Meeting Abstracts*, vol. 1, 1996.

[152] R. Waltz, J. Candy, and M. Rosenbluth, "Gyrokinetic turbulence simulation of profile shear stabilization and broken gyrobohm scaling," *Physics of Plasmas*, vol. 9, p. 1938, 2002.

[153] J. Candy and R. Waltz, "An eulerian gyrokinetic-maxwell solver," *Journal of Computational Physics*, vol. 186, no. 2, pp. 545–581, 2003.

[154] K. Gentle, W. Rowan, R. Bravenec, G. Cima, T. Crowley, H. Gasquet, G. Hallock, J. Heard, A. Ouroua, P. Phillips, *et al.*, "Strong nonlocal effects in a tokamak perturbative transport experiment," *Physical review letters*, vol. 74, no. 18, pp. 3620–3623, 1995.

[155] K. Gentle, R. Bravenec, G. Cima, H. Gasquet, G. Hallock, P. Phillips, D. Ross, W. Rowan, A. Wootton, T. Crowley, *et al.*, "An experimental counter-example to the local transport paradigm," *Physics of Plasmas*, vol. 2, p. 2292, 1995.

[156] M. Kissick, J. Callen, E. Fredrickson, A. Janos, and G. Taylor, "Non-local component of electron heat transport in tftr," *Nuclear fusion*, vol. 36, no. 12, p. 1691, 1996.

[157] P. Mantica, P. Galli, G. Gorini, G. Hogeweij, J. De Kloe, N. Lopes Cardozo, and R. Team, "Nonlocal transient transport and thermal barriers in rijnhuizen tokamak project plasmas," *Physical review letters*, vol. 82, no. 25, pp. 5048–5051, 1999.

[158] G. Hogeweij, P. Mantica, G. Gorini, J. de Kloe, N. L. Cardozo, *et al.*, "Recording non-local temperature rise in the rtp tokamak," *Plasma physics and controlled fusion*, vol. 42, no. 10, p. 1137, 2000.

[159] P. Mantica, G. Gorini, F. Imbeaux, J. Kinsey, Y. Sarazin, R. Budny, I. Coffey, R. Dux, X. Garbet, L. Garzotti, *et al.*, "Perturbative transport experiments in jet low or reverse magnetic shear plasmas," *Plasma physics and controlled fusion*, vol. 44, no. 10, p. 2185, 2002.

[160] N. Tamura, S. Inagaki, K. Ida, T. Shimozuma, S. Kubo, T. Tokuzawa, K. Tanaka, S. Neudatchin, K. Itoh, D. Kalinina, *et al.*, "Observation of core electron temperature rise in response to an edge cooling in toroidal helical plasmas," *Physics of plasmas*, vol. 12, p. 110705, 2005.

[161] K. Ida, S. Inagaki, R. Sakamoto, K. Tanaka, H. Funaba, Y. Takeiri, K. Ikeda, C. Michael, T. Tokuzawa, H. Yamada, *et al.*, "Slow transition of energy transport in high-temperature plasmas," *Physical review letters*, vol. 96, no. 12, p. 125006, 2006.

[162] N. Tamura, S. Inagaki, K. Tanaka, C. Michael, T. Tokuzawa, T. Shimozuma, S. Kubo, R. Sakamoto, K. Ida, K. Itoh, *et al.*, "Impact of nonlocal electron heat transport on the high temperature plasmas of lhd," *Nuclear fusion*, vol. 47, no. 5, p. 449, 2007.

[163] K. Ida, Z. Shi, H. Sun, S. Inagaki, K. Kamiya, J. Rice, N. Tamura, P. Diamond, G. Dif-Pradalier, X. Zou, *et al.*, "Towards an emerging understanding of non-locality phenomena and non-local transport," *Nuclear Fusion*, vol. 55, no. 1, p. 013022, 2015.

[164] K. Ida, Y. Sakamoto, H. Takenaga, N. Oyama, K. Itoh, M. Yoshinuma, S. Inagaki, T. Kobuchi, A. Isayama, T. Suzuki, *et al.*, "Transition between internal transport barriers with different temperature-profile curvatures in jt-60u tokamak plasmas," *Physical review letters*, vol. 101, no. 5, p. 055003, 2008.

[165] K. Ida, Y. Sakamoto, S. Inagaki, H. Takenaga, A. Isayama, G. Matsunaga, R. Sakamoto, K. Tanaka, S. Ide, T. Fujita, *et al.*, "Dynamic transport study of the plasmas with transport improvement in lhd and jt-60u," *Nuclear Fusion*, vol. 49, no. 1, p. 015005, 2009.

[166] H.-J. Sun, X.-T. Ding, L.-H. Yao, B.-B. Feng, Z.-T. Liu, X.-R. Duan, and Q.-W. Yang, "Experiment of non-local effect with smbi on hl-2a," *Plasma Physics and Controlled Fusion*, vol. 52, no. 4, p. 045003, 2010.

[167] C. Gao, J. Rice, H. Sun, M. Reinke, N. Howard, D. Mikkelson, A. Hubbard, M. Chilenski, J. Walk, J. Hughes, *et al.*, "Non-local heat transport in alcator c-mod ohmic l-mode plasmas," *Nuclear Fusion*, vol. 54, no. 8, p. 083025, 2014.

[168] P. Mantica and F. Ryter, "Perturbative studies of turbulent transport in fusion plasmas," *Comptes Rendus Physique*, vol. 7, no. 6, pp. 634–649, 2006.

[169] E. Fredrickson, K. McGuire, A. Cavallo, R. Budny, A. Janos, D. Monticello, Y. Nagayama, W. Park, G. Taylor, and M. Zarnstorff, "Ballistic contributions to heat-pulse propagation in the tftr tokamak," *Physical review letters*, vol. 65, no. 23, p. 2869, 1990.

[170] E. Fredrickson, M. Austin, R. Groebner, J. Manickam, B. Rice, G. Schmidt, and R. Snider, "Heat pulse propagation studies on diii-d and the tokamak fusion test reactor," *Physics of Plasmas (1994-present)*, vol. 7, no. 12, pp. 5051–5063, 2000.

[171] J. Cordey, D. Muir, S. Neudachin, V. Parail, E. Springmann, and A. Taroni, "A numerical simulation of the lh transition in jet with local and global models of anomalous transport," *Nuclear fusion*, vol. 35, no. 1, p. 101, 1995.

[172] P. Bak, C. Tang, and K. Wiesenfeld, "Self-organized criticality: An explanation of the 1/f noise," *Physical review letters*, vol. 59, no. 4, p. 381, 1987.

[173] P. Bak, C. Tang, and K. Wiesenfeld, "Self-organized criticality," *Physical review A*, vol. 38, no. 1, p. 364, 1988.

[174] P. H. Diamond and T. Hahm, "On the dynamics of turbulent transport near marginal stability," *Physics of Plasmas (1994-present)*, vol. 2, no. 10, pp. 3640–3649, 1995.

[175] B. Carreras, D. Newman, V. Lynch, and P. Diamond, "A model realization of self-organized criticality for plasma confinement," *Physics of Plasmas (1994-present)*, vol. 3, no. 8, pp. 2903–2911, 1996.

[176] T. S. Hahm, P. Diamond, Z. Lin, K. Itoh, and S. Itoh, "Turbulence spreading into the linearly stable zone and transport scaling," *Plasma physics and controlled fusion*, vol. 46, no. 5A, p. A323, 2004.

[177] Ö. Gürcan, P. Diamond, T. Hahm, and Z. Lin, "Dynamics of turbulence spreading in magnetically confined plasmas," *Physics of Plasmas (1994-present)*, vol. 12, no. 3, p. 032303, 2005.

[178] X. Garbet, Y. Sarazin, F. Imbeaux, P. Ghendrih, C. Bourdelle, Ö. Gürcan, and P. Diamond, "Front propagation and critical gradient transport models," *Physics of Plasmas (1994-present)*, vol. 14, no. 12, p. 122305, 2007.

[179] P. Ghendrih, Y. Sarazin, G. Ciraolo, G. Darmet, X. Garbet, V. Grangirard, P. Tamain, S. Benkadda, and P. Beyer, "Transport barrier fluctuations governed by sol turbulence spreading," *Journal of nuclear materials*, vol. 363, pp. 581–585, 2007.

[180] V. Naulin, J. Nycander, and J. J. Rasmussen, "Equipartition and transport in two-dimensional electrostatic turbulence," *Physical review letters*, vol. 81, no. 19, p. 4148, 1998.

[181] J. J. Rasmussen, V. Naulin, P. Mantica, J. Lönnroth, V. Parail, and J.-E. Contributors, "Turbulence spreading transport simulations of jet plasmas," in *33rd European Physical Society Conference on Plasma Physics, Rome, Italy*, 2006.

[182] P. Diamond, S. Itoh, K. Itoh, and T. Hahm, "Zonal flows in plasma: a review," *Plasma Physics and Controlled Fusion*, vol. 47, no. 5, p. R35, 2005.

[183] A. Fujisawa, "A review of zonal flow experiments," *Nuclear Fusion*, vol. 49, no. 1, p. 013001, 2009.

[184] K. Hallatschek and D. Biskamp, "Transport control by coherent zonal flows in the core/edge transitional regime," *Physical review letters*, vol. 86, no. 7, p. 1223, 2001.

[185] J. Drake, A. Zeiler, and D. Biskamp, "Nonlinear self-sustained drift-wave turbulence," *Physical review letters*, vol. 75, no. 23, p. 4222, 1995.

[186] P. Diamond, S. Champeaux, M. Malkov, A. Das, I. Gruzinov, M. Rosenbluth, C. Holland, B. Wecht, A. Smolyakov, F. Hinton, *et al.*, "Secondary instability in drift wave turbulence as a mechanism for zonal flow and avalanche formation," *Nuclear fusion*, vol. 41, no. 8, pp. 1067–1080, 2001.

[187] T. Yamada, S.-I. Itoh, T. Maruta, N. Kasuya, Y. Nagashima, S. Shinohara, K. Terasaka, M. Yagi, S. Inagaki, Y. Kawai, *et al.*, "Anatomy of plasma turbulence," *Nature Physics*, vol. 4, no. 9, pp. 721–725, 2008.

[188] G. Dif-Pradalier, P. Diamond, V. Grandgirard, Y. Sarazin, J. Abiteboul, X. Garbet, P. Ghendrih, A. Strugarek, S. Ku, and C. Chang, "On the validity of the local diffusive paradigm in turbulent plasma transport," *Physical Review E*, vol. 82, no. 2, p. 025401, 2010.

[189] G. M. Zaslavsky, "Chaos, fractional kinetics, and anomalous transport," *Physics Reports*, vol. 371, no. 6, pp. 461–580, 2002.

[190] R. Bravenec, K. Gentle, P. Phillips, T. Price, W. Rowan, K. Empson, W. Hodge, C. Klepper, T. Kochanski, D. Patterson, *et al.*, "Confinement time scaling in text," *Plasma physics and controlled fusion*, vol. 27, no. 11, p. 1335, 1985.

[191] Y. Shimomura, N. Suzuki, and M. Sugihara, "Empirical scaling of energy confinement time of l-mode and optimized mode and some consideration of reactor core plasma in tokamak," */Rep./Japan atomic energy inst.*, vol. 1000, pp. 87–080, 1987.

[192] F. Söldner, E. Müller, F. Wagner, H. Bosch, A. Eberhagen, H. Fahrbach, G. Fussmann, O. Gehre, K. Gentle, J. Gernhardt, *et al.*, "Improved confinement in high-density ohmic discharges in asdex," *Physical review letters*, vol. 61, no. 9, pp. 1105–1108, 1988.

[193] X. Garbet, J. Payan, C. Laviron, P. Devynck, S. Saha, H. Capes, X. Chen, J. Coulon, C. Gil, G. Harris, *et al.*, "Turbulence and energy confinement in tore supra ohmic discharges," *Nuclear fusion*, vol. 32, no. 12, p. 2147, 1992.

[194] F. Ryter, K. Buchl, C. Fuchs, O. Gehre, O. Gruber, A. Herrmann, A. Kallenbach, M. Kaufmann, W. Koppendorfer, F. Mast, *et al.*, "H-mode results in asdex upgrade," *Plasma physics and controlled fusion*, vol. 36, no. 7A, p. A99, 1994.

[195] G. Bracco and K. Thomsen, "Analysis of a global energy confinement database for jet ohmic plasmas," *Nuclear fusion*, vol. 37, no. 6, p. 759, 1997.

[196] C. Rettig, T. Rhodes, J. Leboeuf, W. Peebles, E. Doyle, G. Staebler, K. Burrell, and R. Moyer, "Search for the ion temperature gradient mode in a tokamak plasma and comparison with theoretical predictions," *Physics of Plasmas*, vol. 8, p. 2232, 2001.

[197] R. J. Goldston, "Energy confinement scaling in tokamaks: some implications of recent experiments with ohmic and strong auxiliary heating," *Plasma Physics and Controlled Fusion*, vol. 26, no. 1A, p. 87, 1984.

[198] R. Watterson, R. Slusher, and C. Surko, "Low-frequency density fluctuations in a tokamak plasma," *Physics of Fluids (1958-1988)*, vol. 28, no. 9, pp. 2857–2867, 1985.

[199] D. Brower, W. Peebles, S. Kim, N. Luhmann Jr, W. Tang, and P. Phillips, "Observation of a high-density ion mode in tokamak microturbulence," *Physical review letters*, vol. 59, no. 1, p. 48, 1987.

[200] G. Conway, C. Angioni, R. Dux, F. Ryter, A. Peeters, J. Schirmer, C. Troester, *et al.*, "Observations on core turbulence transitions in asdex upgrade using doppler reflectometry," *Nuclear fusion*, vol. 46, no. 9, p. S799, 2006.

[201] H. Arnichand, J. Citrin, R. Sabot, S. Hacquin, A. Krämer-Flecken, J. Bernardo, C. Bourdelle, X. Garbet, J. Giacalone, R. Guirlet, *et al.*, "Evidence of trapped electron mode contribution to fluctuation spectra and first applications to turbulence studies,"

[202] L. Lin, M. Porkolab, E. Edlund, J. Rost, M. Greenwald, N. Tsujii, J. Candy, R. Waltz, and D. Mikkelsen, "Studies of turbulence and transport in alcator c-mod ohmic plasmas with phase contrast imaging and comparisons with gyrokinetic simulations," *Plasma Physics and Controlled Fusion*, vol. 51, no. 6, p. 065006, 2009.

[203] C. Sung, *Experimental study of turbulent heat transport in Alcator C-Mod.* PhD thesis, Massachusetts Institute of Technology, 2015.

[204] T. Rhodes, C. Holland, S. Smith, A. White, K. Burrell, J. Candy, J. DeBoo, E. Doyle, J. Hillesheim, J. Kinsey, *et al.*, "L-mode validation studies of gyrokinetic turbulence simulations via multiscale and multifield turbulence measurements on the diii-d tokamak," *Nuclear Fusion*, vol. 51, no. 6, p. 063022, 2011.

[205] A. White, L. Schmitz, G. McKee, C. Holland, W. Peebles, T. Carter, M. Shafer, M. Austin, K. Burrell, J. Candy, *et al.*, "Measurements of core electron temperature and density fluctuations in diii-d and comparison to nonlinear gyrokinetic simulationsa)," *Physics of Plasmas (1994-present)*, vol. 15, no. 5, p. 056116, 2008.

[206] C. Holland, A. White, G. McKee, M. Shafer, J. Candy, R. Waltz, L. Schmitz, and G. Tynan, "Implementation and application of two synthetic diagnostics for validating simulations of core tokamak turbulence," *Physics of Plasmas (1994-present)*, vol. 16, no. 5, p. 052301, 2009.

[207] C. Holland, L. Schmitz, T. Rhodes, W. Peebles, J. Hillesheim, G. Wang, L. Zeng, E. Doyle, S. Smith, R. Prater, *et al.*, "Advances in validating gyrokinetic turbulence models against l-and h-mode plasmas a)," *Physics of Plasmas (1994-present)*, vol. 18, no. 5, p. 056113, 2011.

[208] N. Howard, A. White, M. Greenwald, M. Reinke, J. Walk, C. Holland, J. Candy, and T. Görler, "Investigation of the transport shortfall in alcator c-mod l-mode plasmas," *Physics of Plasmas (1994-present)*, vol. 20, no. 3, p. 032510, 2013.

[209] N. Howard, "Cross-scale coupling of ion and electron-scale turbulence in experimental tokamak discharges," 2015 US/EU Transport Task Force Workshop, 2015.

[210] J. Rice, J. Hughes, P. Diamond, Y. Kosuga, Y. Podpaly, M. Reinke, M. Greenwald, Ö. Gürcan, T. Hahm, A. Hubbard, *et al.*, "Edge temperature gradient as intrinsic rotation drive in alcator c-mod tokamak plasmas," *Physical Review Letters*, vol. 106, no. 21, p. 215001, 2011.

[211] A. Scarabosio, A. Bortolon, B. Duval, A. Karpushov, and A. Pochelon, "Toroidal plasma rotation in the tcv tokamak," *Plasma physics and controlled fusion*, vol. 48, no. 5, p. 663, 2006.

[212] A. Bortolon, B. P. Duval, A. Pochelon, and A. Scarabosio, "Observation of spontaneous toroidal rotation inversion in ohmically heated tokamak plasmas," *Physical review letters*, vol. 97, no. 23, p. 235003, 2006.

[213] B. Duval, A. Bortolon, A. Karpushov, R. Pitts, A. Pochelon, A. Scarabosio, *et al.*, "Bulk plasma rotation in the tcv tokamak in the absence of external momentum input," *Plasma Physics and Controlled Fusion*, vol. 49, no. 12B, p. B195, 2007.

[214] B. Duval, A. Bortolon, A. Karpushov, R. Pitts, A. Pochelon, O. Sauter, A. Scarabosio, G. Turri, *et al.*, "Spontaneous l-mode plasma rotation scaling in the tcv tokamak," *Physics of Plasmas*, vol. 15, p. 056113, 2008.

[215] J. Rice, A. Ince-Cushman, M. Reinke, Y. Podpaly, M. Greenwald, B. LaBombard, and E. Marmar, "Spontaneous core toroidal rotation in alcator c-mod l-mode, h-mode and itb plasmas," *Plasma Physics and Controlled Fusion*, vol. 50, no. 12, p. 124042, 2008.

[216] C. Angioni, R. McDermott, F. Casson, E. Fable, A. Bottino, R. Dux, R. Fischer, Y. Podoba, T. Pütterich, F. Ryter, *et al.*, "Intrinsic toroidal rotation, density peaking, and turbulence regimes in the core of tokamak plasmas," *Physical review letters*, vol. 107, no. 21, p. 215003, 2011.

[217] P. Diamond, C. McDevitt, Ö. Gürcan, T. Hahm, and V. Naulin, "Transport of parallel momentum by collisionless drift wave turbulence," *Physics of Plasmas (1994-present)*, vol. 15, no. 1, p. 012303, 2008.

[218] Y. A. Podpaly, *Rotation generation and transport in tokamak plasmas.* PhD thesis, Massachusetts Institute of Technology, 2012.

[219] A. White, N. Howard, M. Greenwald, M. Reinke, C. Sung, S. Baek, M. Barnes, J. Candy, A. Dominguez, D. Ernst, *et al.*, "Multi-channel transport experiments at alcator c-mod and comparison with gyrokinetic simulations," *Physics of Plasmas*, vol. 20, p. 056106, 2013.

[220] C. Sung, A. White, N. Howard, C. Oi, J. Rice, C. Gao, P. Ennever, M. Porkolab, F. Parra, *et al.*, "Changes in core electron temperature fluctuations across the ohmic energy confinement transition in alcator c-mod plasmas," *Nuclear fusion*, vol. 53, p. 083010, 2013.

[221] N. Uckan, *ITER physics design guidelines: 1989.* International Atomic Energy Agency, 1990.

[222] N. Lopes Cardozo, "Perturbative transport studies in fusion plasmas," *Plasma physics and controlled fusion*, vol. 37, no. 8, pp. 799–852, 1995.

[223] A. Jacchia, P. Mantica, F. De Luca, and G. Gorini, "Determination of diffusive and nondiffusive transport in modulation experiments in plasmas," *Physics of Fluids B: Plasma Physics*, vol. 3, no. 11, pp. 3033–3040, 1991.

[224] T. D. de Wit, M. Erba, M. Mattioli, and J.-L. Ségui, "Self-consistent removal of sawtooth oscillations from transient plasma data by generalized singular value decomposition," *Physics of Plasmas*, vol. 5, p. 1360, 1998.

[225] S. Inagaki, N. Tamura, T. Tokuzawa, K. Ida, T. Kobayashi, T. Shimozuma, S. Kubo, H. Tsuchiya, Y. Nagayama, K. Kawahata, *et al.*, "Fluctuations with long-distance correlation in quasi-stationary and transient plasmas of lhd," *Nuclear Fusion*, vol. 52, no. 2, p. 023022, 2012.

[226] J. Callen and G. Jahns, "Experimental measurement of electron heat diffusivity in a tokamak," *Physical Review Letters*, vol. 38, pp. 491–494, 1977.

[227] J. Kinsey, R. Waltz, and H. S. John, "Theoretical transport modeling of ohmic cold pulse experiments," *Physics of Plasmas*, vol. 5, p. 3974, 1998.

[228] V. B. Alikaev, N. Vasin, Y. Esipchuk, A. Kislov, G. Noikin, and K. Razamova, "Energy confinement in the plasma of the t-10 tokamak," *Sov. J. Plasma Phys*, vol. 13, pp. 1–10, 1987.

[229] G. T. Hoang, C. Gil, E. Joffrin, D. Moreau, A. Becoulet, P. Bibet, J. Bizarro, R. Budny, J. Carrasco, J. Coulon, *et al.*, "Improved confinement in high li lower hybrid driven steady state plasmas in tore supra," *Nuclear fusion*, vol. 34, no. 1, p. 75, 1994.

[230] M. Wakatani, V. Mukhovatov, K. Burrell, J. Connor, J. Cordey, Y. V. Esipchuk, X. Garbet, S. Lebedev, M. Mori, K. Toi, *et al.*, "Chapter 2: Plasma confinement and transport," *Nuclear Fusion*, vol. 39, no. 12, pp. 2175–2249, 1999.

[231] G. McKee, K. Burrell, R. Fonck, G. Jackson, M. Murakami, G. Staebler, D. Thomas, and P. West, "Impurity-induced suppression of core turbulence and transport in the diii-d tokamak," *Physical review letters*, vol. 84, no. 9, p. 1922, 2000.

[232] N. Howard. personal communication.

[233] P. Diamond, C. McDevitt, Ö. Gürcan, T. Hahm, W. Wang, E. Yoon, I. Holod, Z. Lin, V. Naulin, and R. Singh, "Physics of non-diffusive turbulent transport of momentum and the origins of spontaneous rotation in tokamaks," *Nuclear Fusion*, vol. 49, no. 4, p. 045002, 2009.

[234] T. Hahm, P. Diamond, O. Gurcan, and G. Rewoldt, "Nonlinear gyrokinetic theory of toroidal momentum pinch," *Physics of Plasmas (1994-present)*, vol. 14, no. 7, p. 072302, 2007.

[235] R. McDermott, C. Angioni, G. Conway, R. Dux, E. Fable, R. Fischer, T. Pütterich, F. Ryter, E. Viezzer, *et al.*, "Core intrinsic rotation behaviour in asdex upgrade ohmic l-mode plasmas," *Nuclear Fusion*, vol. 54, no. 4, p. 043009, 2014.

[236] L. Berry, E. Jaeger, and D. Batchelor, "Wave-induced momentum transport and flow drive in tokamak plasmas," *Physical review letters*, vol. 82, no. 9, p. 1871, 1999.

[237] J. Myra and D. D'Ippolito, "Toroidal formulation of nonlinear-rf-driven flows," *Physics of Plasmas (1994-present)*, vol. 9, no. 9, pp. 3867–3873, 2002.

[238] E. Jaeger, L. Berry, J. Myra, D. Batchelor, E. D'Azevedo, P. Bonoli, C. Phillips, D. Smithe, D. DIppolito, M. Carter, *et al.*, "Sheared poloidal flow driven by mode conversion in tokamak plasmas," *Physical review letters*, vol. 90, no. 19, p. 195001, 2003.

[239] J. Myra, L. Berry, D. D'ippolito, and E. Jaeger, "Nonlinear fluxes and forces from radio-frequency waves with application to driven flows in tokamaks," *Physics of Plasmas (1994-present)*, vol. 11, no. 5, pp. 1786–1798, 2004.

[240] J. C. Wright, P. Bonoli, M. Brambilla, F. Meo, E. DAzevedo, D. B. Batchelor, E. Jaeger, L. A. Berry, C. Phillips, and A. Pletzer, "Full wave simulations of fast wave mode conversion and lower hybrid wave propagation in tokamaks," *Physics of Plasmas (1994-present)*, vol. 11, no. 5, pp. 2473–2479, 2004.

[241] N. T. Howard, *Experimental and gyrokinetic studies of impurity transport in the core of Alcator C-Mod Plasmas.* PhD thesis, Massachusetts Institute of Technology, 2012.

[242] J. Rice, M. Reinke, C. Gao, N. Howard, M. Chilenski, L. Delgado-Aparicio, R. Granetz, M. Greenwald, A. Hubbard, J. Hughes, *et al.*, "Core impurity transport in alcator c-mod l-, i-and h-mode plasmas," *Nuclear Fusion*, vol. 55, no. 3, p. 033014, 2015.

[243] D. Post, "A review of recent developments in atomic processes for divertors and edge plasmas," *Journal of nuclear materials*, vol. 220, pp. 143–157, 1995.

[244] TFR-Group, "Impurity pump-out at the two-ion hybrid resonance during icrf experiments in tfr tokamak plasmas," *Nuclear Fusion*, vol. 22, no. 7, p. 956, 1982.

[245] T. E. Tutt, *H-[alpha]/D-[alpha] Spectroscopy on Alcator C-Mod.* PhD thesis, Massachusetts Institute of Technology, Department of Nuclear Engineering, 2000.

[246] N. Tsujii, *Studies of ICRF mode conversion with phase contrast imaging and full-wave simulations in Alcator C-Mod.* PhD thesis, Massachusetts Institute of Technology, 2012.

[247] Y. Kosuga, P. Diamond, and Ö. Gürcan, "How the propagation of heat-flux modulations triggers e× b flow pattern formation," *Physical review letters*, vol. 110, no. 10, p. 105002, 2013.

[248] Ö. Gürcan, L. Vermare, P. Hennequin, V. Berionni, P. Diamond, G. Dif-Pradalier, X. Garbet, P. Ghendrih, V. Grandgirard, C. McDevitt, *et al.*, "Structure of nonlocality of plasma turbulence," *Nuclear Fusion*, vol. 53, no. 7, p. 073029, 2013.

[249] J. Lee, M. Barnes, F. Parra, E. Belli, and J. Candy, "The effect of diamagnetic flows on turbulent driven ion toroidal rotationa)," *Physics of Plasmas (1994-present)*, vol. 21, no. 5, p. 056106, 2014.

[250] Z. Lu, W. Wang, P. Diamond, G. Tynan, S. Ethier, C. Gao, and J. Rice, "Intrinsic torque reversals induced by magnetic shear effects on the turbulence spectrum in tokamak plasmasa)," *Physics of Plasmas (1994-present)*, vol. 22, no. 5, p. 055705, 2015.

[251] Z. Lin and T. Hahm, "Turbulence spreading and transport scaling in global gyrokinetic particle simulations," *Physics of Plasmas (1994-present)*, vol. 11, no. 3, pp. 1099–1108, 2004.

[252] W. Wang, T. Hahm, W. Lee, G. Rewoldt, J. Manickam, and W. Tang, "Nonlocal properties of gyrokinetic turbulence and the role of e× b flow shear," *Physics of Plasmas (1994-present)*, vol. 14, no. 7, p. 072306, 2007.

[253] W. Wang, P. Diamond, T. Hahm, S. Ethier, G. Rewoldt, and W. Tang, "Nonlinear flow generation by electrostatic turbulence in tokamaks," *Physics of Plasmas (1994-present)*, vol. 17, no. 7, p. 072511, 2010.

[254] M. Barnes, F. Parra, J. Lee, E. Belli, M. Nave, and A. White, "Intrinsic rotation driven by non-maxwellian equilibria in tokamak plasmas," *Physical review letters*, vol. 111, no. 5, p. 055005, 2013.

[255] K. Ida, M. Yoshinuma, M. Osakabe, K. Nagaoka, M. Yokoyama, H. Funaba, C. Suzuki, T. Ido, A. Shimizu, I. Murakami, *et al.*, "Observation of an impurity hole in a plasma with an ion internal transport barrier in the large helical devicea)," *Physics of Plasmas (1994-present)*, vol. 16, no. 5, p. 056111, 2009.

[256] A. Peeters, C. Angioni, Y. Camenen, F. J. Casson, W. Hornsby, A. Snodin, and D. Strintzi, "The influence of the self-consistent mode structure on the coriolis pinch effect," *Physics of Plasmas*, vol. 16, p. 062311, 2009.

[257] A. J. Brizard, "Nonlinear gyrokinetic vlasov equation for toroidally rotating axisymmetric tokamaks," *Physics of Plasmas*, vol. 2, p. 459, 1995.

[258] M. Kikuchi, K. Lackner, and M. Q. Tran, *Fusion physics*. 2012.